

DISSERTATION

submitted to the
Combined Faculties for the Natural Sciences and for Mathematics
of the Ruperto-Carola University of Heidelberg, Germany
for the degree of
Doctor of Natural Sciences

Put forward by
Kirill Boguslavski

Born in: Kiev, Ukraine

Oral examination: 27.07.2016

Universality classes far from equilibrium:
From heavy-ion collisions to superfluid
Bose systems

Referees: Prof. Dr. Jürgen Berges
Prof. Dr. Jan Pawłowski

*Universality classes far from equilibrium:
From heavy-ion collisions to superfluid Bose systems*

Abstract

Quantum many-body systems far from equilibrium can approach a nonthermal fixed point during their real-time evolution. One example is scalar field theory, which occurs in models of cosmological inflation, and similar examples are found for non-Abelian plasmas relevant for heavy-ion collisions and for ultracold Bose gases. Investigating nonthermal fixed points of different microscopic theories, we present two novel universality classes that provide links between these systems.

One of them involves nonrelativistic, N -component relativistic and expanding scalar systems. It occurs in the deep infrared regime of very high occupancies and is governed by a self-similar evolution. Its nonequilibrium dynamics leads to the formation of a Bose-Einstein condensate. The scaling properties of this region can be described by a vertex-resummed kinetic theory that is based on a systematic large- N expansion at next-to-leading order.

The other novel universality class encompasses scalar field theories and non-Abelian plasmas in a longitudinally expanding background and corresponds to an early dynamical stage of heavy-ion collisions in the high-energy limit. We show that these systems share the same self-similar scaling properties for a wide range of momenta in a limit where particles are weakly coupled but their occupancy is high.

Both universality classes are found in separate momentum regions in a longitudinally expanding N -component scalar field theory. We argue that the important role of the infrared dynamics ensures that key features of our results for scalar and gauge theories cannot be reproduced consistently in conventional kinetic theory frameworks. Moreover, the observed universality connects different physics disciplines from heavy-ion collisions to ultracold atoms, making a remarkable link between the world's hottest and coldest matter.

*Universalitätsklassen fern des Gleichgewichts:**Von Schwerionenkollisionen bis zu superfluiden bosonischen Systemen***Zusammenfassung**

Quantenvielteilchensysteme fern des Gleichgewichts können sich während ihrer Realzeitentwicklung einem nichtthermischen Fixpunkt nähern. Ein Beispiel dafür ist die skalare Feldtheorie, die in Modellen zur kosmologischen Inflation auftritt, und ähnliche Beispiele werden für Schwerionenkollisionen-relevante nicht-Abelsche Plasmen und ultrakalte Bosegas gefunden. Wir untersuchen nichtthermische Fixpunkte verschiedener mikroskopischer Theorien und stellen zwei neue Universalitätsklassen vor, die Verbindungen zwischen den verschiedenen Systemen herstellen.

Eine von ihnen beinhaltet nichtrelativistische, N -komponentige relativistische und sogar expandierende skalare Systeme. Sie befindet sich im tiefen Infrarotbereich mit sehr hohen Besetzungszahlen und folgt einer selbstähnlichen Zeitentwicklung. Ihre Nichtgleichgewichtsdynamik führt zur Entstehung eines Bose-Einstein-Kondensats. Die Skalierungseigenschaften dieses Bereichs lassen sich mit einer Vertex-resummierten kinetischen Theorie beschreiben, die auf einer systematischen groß- N Entwicklung zu nächstführender Ordnung basiert.

Die andere neue Universalitätsklasse umfasst skalare Systeme und nicht-Abelsche Plasmen in einem longitudinal expandierenden Hintergrund und entspricht einem frühen Stadium der Dynamik von Schwerionenkollisionen im Hochenergielimes. Wir zeigen, dass diese Systeme in einem weiten Impulsbereich dieselben selbstähnlichen Skalierungseigenschaften haben, wenn sie schwach gekoppelt aber hoch besetzt sind.

Beide Universalitätsklassen werden in separaten Impulsbereichen einer N -komponentigen longitudinal expandierenden skalaren Feldtheorie gefunden. Wir argumentieren, dass durch die wichtige Rolle des Infrarotbereichs wesentliche Merkmale unserer Resultate für skalare und Eichtheorien nicht konsistent innerhalb einer herkömmlichen kinetischen Theorie wiedergegeben werden können. Außerdem verbindet die beobachtete Universalität verschiedene Disziplinen der Physik miteinander, von Schwerionenkollisionen bis zu ultrakalten Quantengasen, und erstellt damit eine bemerkenswerte Verbindung zwischen der heißesten und der kältesten Materie der Welt.

List of Publications

The results of this thesis led to the following publications that have been written and published during the course of my doctoral studies:

- **J. Berges, K. Boguslavski, S. Schlichting and R. Venugopalan**, “Nonequilibrium fixed points in longitudinally expanding scalar theories: infrared cascade, Bose condensation and a challenge for kinetic theory”, *Phys. Rev. D* **92**, 096006 (2015).
- **A. Pieiro Orioli, K. Boguslavski and J. Berges**, “Universal self-similar dynamics of relativistic and nonrelativistic field theories near nonthermal fixed points”, *Phys. Rev. D* **92**, 025041 (2015).
- **J. Berges, K. Boguslavski, S. Schlichting and R. Venugopalan**, “Universality far from equilibrium: From superfluid Bose gases to heavy-ion collisions”, *Phys. Rev. Lett.* **114**, 061601 (2015), Editors’ suggestion.
- **J. Berges, K. Boguslavski, S. Schlichting and R. Venugopalan**, “Basin of attraction for turbulent thermalization and the range of validity of classical-statistical simulations”, *JHEP* **1405**, 054 (2014).
- **J. Berges, K. Boguslavski, S. Schlichting and R. Venugopalan**, “Universal attractor in a highly occupied non-Abelian plasma”, *Phys. Rev. D* **89**, 114007 (2014).

Contents

Abstract, Zusammenfassung	i
List of Publications	iii
1 Introduction	1
2 Theoretical background	9
2.1 Considered field theories	9
2.1.1 Coordinates and longitudinal expansion	10
2.1.2 Relativistic scalar field theory	11
2.1.3 Nonrelativistic scalar field theory	12
2.1.4 Non-Abelian gauge theory	12
2.2 Nonequilibrium quantum field theory	16
2.2.1 Quantum field theory on a closed time path	16
2.2.2 Distribution function in homogeneous systems	20
2.2.3 Initial conditions	24
2.3 Classical-statistical lattice simulations	26
2.3.1 Classical-statistical approximation	26
2.3.2 Numerical algorithm and lattice setup	30
2.3.3 Scalar fields on a lattice	31
2.3.4 Nonrelativistic scalars on a lattice	33
3 Nonthermal fixed points in Minkowski space-time	35
3.1 Nonthermal fixed points	36
3.1.1 Relations to critical phenomena in thermal equilibrium	38
3.1.2 Nonthermal fixed points and wave turbulence	41
3.2 Thermalization process in non-expanding systems	42
3.2.1 Non-Abelian plasmas	44
3.2.2 Relativistic scalars: scaling, cosmological context & basin of attraction .	48
3.2.3 $O(N)$ -symmetric scalar systems in more detail	51
3.3 Nonthermal fixed points from kinetic theory	56
3.3.1 Scalar systems	58
3.3.2 Non-Abelian plasmas	60
3.4 Summary	63
4 Universality class of condensation dynamics	65
4.1 Universality from lattice simulations	67
4.1.1 Self-similar dynamics from classical-statistical simulations	67

4.1.2	Universality with nonrelativistic Bose gases	71
4.1.3	Generation of a mass gap	73
4.1.4	Condensate formation	75
4.2	Universality from resummed kinetic approaches	77
4.2.1	Condensation in a perturbative kinetic theory	78
4.2.2	Vertex-resummed kinetic theory and scaling properties	79
4.2.3	Anomalous scaling beyond vertex-resummed kinetic theory	84
4.3	Summary	88
5	Universality class and thermalization in expanding systems	89
5.1	Nonthermal fixed points in expanding media	90
5.2	Universality class in expanding systems: From non-Abelian plasmas to superfluid scalars	92
5.2.1	Reduced distribution and conservation laws	92
5.2.2	Details of the universal scaling region	94
5.2.3	Scaling regions in expanding scalar and gauge theories	96
5.2.4	Basin of attraction	97
5.3	Non-Abelian plasmas and thermalization in more detail	98
5.3.1	Self-similar evolution and scaling exponents	98
5.3.2	Distinguishing between thermalization scenarios	100
5.3.3	Kinetic analysis for non-Abelian plasmas	101
5.3.4	A consistent picture of thermalization at weak couplings	104
5.4	Summary	107
6	Nonthermal fixed point in expanding scalars	109
6.1	The scaling regions of the nonthermal fixed point	110
6.1.1	Infrared cascade and Bose-Einstein condensation	112
6.1.2	Low momentum region from vertex-resummed kinetic theory	120
6.1.3	Intermediate momenta	123
6.1.4	Hard momentum region	127
6.2	Implications of self-similarity for bulk anisotropy	132
6.3	Summary	135
7	Conclusion and Outlook	137
	Acknowledgements	142
A	Mode functions and late-time asymptotics	143
B	Nonequilibrium lattice gauge theory	147
C	Detailed analysis of self-similarity	153
C.1	For isotropic systems	153
C.2	For longitudinally expanding anisotropic systems	154
D	Expanding non-Abelian plasmas: Scaling exponents	157
D.1	Gauge invariant analysis	157

D.2 Self-similarity analysis	161
E Range of validity of the classical approximation for expanding scalars	163
E.1 Parametric estimate of quantum large angle scattering	164
E.2 ‘Quantum’ contributions to observables	167
Bibliography	169

Chapter 1

Introduction

“Dream no small dreams for they have no power to stir the hearts of men.”

Johann Wolfgang von Goethe

Generations of physicists have sought and studied similarities among different physics disciplines and phenomena. Such universality provides new links between seemingly disparate physical systems and may allow for unified descriptions of the observations. In particular, the systems can be grouped into universality classes according to their shared behavior. This opens intriguing theoretical and experimental possibilities to access their properties by studying the simplest or the experimentally best accessible representative of a universality class [1, 2]. Prominent examples for universality are critical phenomena in or close to thermal equilibrium. These occur for instance close to the critical point in phase diagrams and have been extensively studied in the literature over the past decades [3–6].

In contrast, we consider here isolated quantum systems in far-from-equilibrium conditions that can exhibit unusually large occupancies per mode. Important examples include the initial stages in collisions of ultra-relativistic nuclei at large laboratory facilities, the reheating process in the early universe after inflation as well as table-top experiments with ultracold quantum gases. Even though the typical energy scales of these systems vastly differ, they can show very similar dynamical properties at weak couplings. In recent years there have been important advances in understanding them at weak couplings, which led to the concept of nonthermal fixed points [7–10].

A generic thermalization process of such systems is illustrated in Fig. 1.1. Starting far from equilibrium with a high over-population of soft modes, the system can approach a nonthermal fixed point during its space-time evolution. The dynamics is then governed by a *self-similar* evolution of the underlying correlation or distribution functions and is specified by scaling

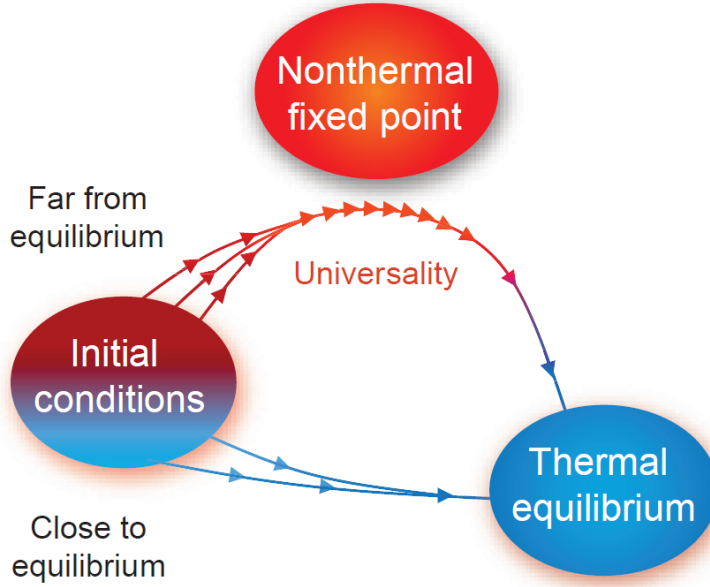
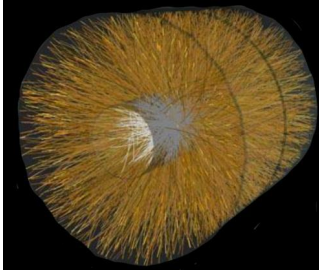


FIGURE 1.1: Visualization of different ways to approach thermal equilibrium. Starting with initial conditions close to equilibrium, the system relaxes to the thermal state. In contrast, far-from-equilibrium initial conditions may lead to a nonthermal fixed point where the dynamics slows down considerably and the memory of details of the initial state gets lost. Eventually, the system thermalizes, leaving the fixed point solution.

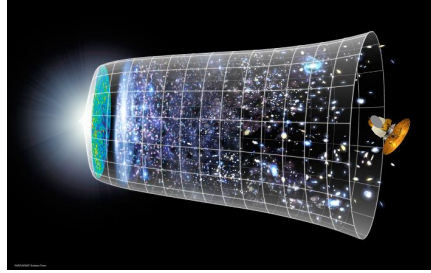
exponents and scaling functions. The same scaling properties occur for a wide range of initial conditions, which implies an emergent effective *memory loss* close to the nonthermal fixed point. If the same scaling properties can be observed for different field theories, with different microscopic interactions, then the scaling regions can even be grouped into universality classes.¹

In the considered highly occupied systems at weak couplings, the nonequilibrium quantum dynamics can be accurately mapped onto a classical-statistical problem [11–13]. The latter can be solved using real-time lattice simulation techniques, where the system is initialized with the full quantum initial conditions and the dynamics are approximated by a classical evolution for the fields. Numerical simulations in this context reveal that different physics disciplines spanning heavy-ion collisions [14–19], inflationary cosmology [8, 20, 21] and ultra-cold atoms [10, 22–24] exhibit nonthermal fixed points. These different physical systems are illustrated in Fig. 1.2 and are discussed in the following.

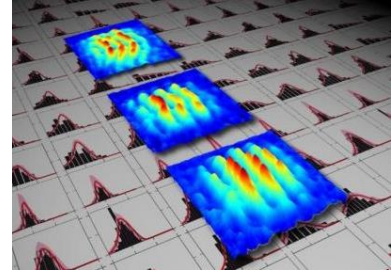
¹To better compare different physical systems, three spatial dimensions are considered and natural units will be employed in the entire thesis, where the reduced Planck constant (\hbar), the speed of light (c) and Boltzmann’s constant (k_B) are set to one.

Heavy-ion collisions

Longitudinally expanding
non-Abelian plasmas

Inflationary cosmology

Relativistic scalar systems

Ultracold atoms

Nonrelativistic scalar systems

FIGURE 1.2: Illustration of different physics disciplines where highly populated systems far from thermal equilibrium may be encountered. The upper descriptions denote to which disciplines the figures are related, while the lower labels name the underlying quantum systems. The images are from (left to right): ALICE collaboration, CERN; NASA/WMAP Science Team; Vienna University of Technology.

Heavy-ion collisions

A major motivation for the studies of universal behavior far from equilibrium are experiments with colliding heavy nuclei in the ultrarelativistic high energy limit. Such experiments are currently carried out at the “Large Hadron Collider” (LHC) at CERN and at the “Relativistic Heavy Ion Collider” (RHIC) at Brookhaven National Lab. One important goal of such ultrarelativistic heavy-ion collision experiments is to study properties of the strong interaction under similar extreme conditions as are expected in early stages of the Big Bang. The strong interaction is described by the theory of Quantum Chromodynamics (QCD) and is one of the four fundamental forces of the standard model of particle physics. The theory involves matter fields, the quarks, and exchange bosons of the interaction, the gluons, all of which have a color charge. Quarks and gluons are coupled by the gauge coupling α_s . Different from photons, which are the exchange bosons of the electromagnetic interaction, gluons are also self-interacting due to their color charge. An important property of QCD is asymptotic freedom. It constitutes that the gauge coupling α_s decreases with increasing energies, which leads to a weakly interacting theory at high energies [25, 26].

At high enough temperatures, quarks and gluons are therefore expected to form the quark gluon plasma (QGP), a plasma of deconfined quarks and gluons. In contrast, the coupling constant becomes large at low energies and quarks and gluons are confined to hadrons, such as protons, neutrons or pions, for a sufficiently small quark chemical potential. While for the weakly coupled asymptotically free theory perturbative techniques can be used for theoretical calculations [27, 28], the strongly coupled system at low energies requires non-perturbative

methods. In particular, the physically important transition between the confined and deconfined phases of QCD is a difficult theoretical problem. However, at vanishing quark chemical potential, it is amenable to Lattice Quantum Chromodynamics, where QCD is simulated in large scale numerical studies on a lattice [29]. Using these techniques, it has been established that QCD possesses a cross-over transition between the QGP and the hadronic phase around the temperature scale of 150 – 170 MeV [30].

For collider experiments of LHC and RHIC, even higher temperatures have been estimated with 200 – 300 MeV, which correspond to extreme conditions of about 10^{12} K. Therefore, a QGP is expected to be formed shortly after the collision, which subsequently undergoes the (cross-over) transition to the hadronic phase before it can be detected. Experimental observations have indeed provided strong evidence for the existence of the quark gluon plasma phase (see e.g. [31–33]). Hydrodynamic flow studies were able to describe such experimental measurements. They indicated that the emergent matter created in the collisions quickly thermalizes on time scales of only few fm/c and subsequently acts like a nearly ideal fluid [34–38]. To understand these properties from first principles, it is important to study the nonequilibrium evolution prior to the formation of the equilibrated QGP. This has been a long-standing theoretical challenge [39].

In theoretical descriptions of the initial stages, one usually changes coordinates to take account for the high velocities of the colliding nuclei, which results in an effectively longitudinally expanding metric. Since the gauge coupling $\alpha_s \approx 0.3$ at typical LHC energies is neither very small nor very large, the nonequilibrium evolution is investigated in two limiting cases. Strong coupling thermalization of a supersymmetric Yang-Mills theory is studied based on a gauge/gravity duality conjecture [40–44] and indicates quick thermalization.

In the weak coupling limit, large gluon fields with typical momentum Q are expected to be formed in the early stages of a collision and become the dominating constituents of the far-from-equilibrium matter [45–59]. These initial ‘Glasma’ fields are unstable and lead to a rapid growth of fluctuations via plasma instabilities [60–66]. As a consequence, a highly occupied non-Abelian plasma emerges. Because of its large occupation numbers $f \sim 1/\alpha_s(Q) \gg 1$ of its single-particle distribution function, the plasma can be strongly correlated even for small gauge coupling $\alpha_s(Q) \ll 1$.

With these far-from-equilibrium initial conditions, we demonstrated the existence of a non-thermal fixed point in longitudinally expanding non-Abelian plasmas using classical-statistical lattice simulations [14]. Its scaling properties allowed us to distinguish between kinetic thermalization scenarios in the literature [39, 67–72]. Our results favored the ‘bottom-up’ thermalization scenario of Ref. [67], where elastic and inelastic scattering processes are responsible for the dynamics.

This nonthermal fixed point emerging in heavy-ion collisions in the high-energy limit is a promising starting point to find universality classes between heavy-ion collisions and other

systems. In particular, universality provides new insights on the dynamics in heavy-ion collisions and opens new theoretical and experimental possibilities, as mentioned above.

Inflationary cosmology & ultracold atoms

Similar over-occupied systems can also be found in inflationary cosmology and in ultracold atomic gases.

Inflation was suggested to model an early stage of our Universe after the Big Bang [73, 74]. It solves the horizon and the flatness problems which were deduced from the cosmic microwave background (CMB) and in other cosmological observations [75–77]. These problems constitute that the early universe must be approximately homogeneous, isotropic and flat, which is achieved by an exponential expansion of the universe during the inflation epoch. This stage is usually modeled by a classical homogeneous scalar field $\phi(t)$ that is called the inflaton. Since the universe becomes very dilute due to its expansion, most of its energy density is contained in the inflaton field at the end of the inflation stage. In the subsequent reheating process of the universe, the classical inflaton decays into elementary particles, which eventually come to a state of thermal equilibrium due to their interactions [74].

In a significant range of parameters of many models for reheating, one encounters an early stage called preheating. There the inflaton decays into its scalar fluctuations and into other bosonic and fermionic particles [20, 78–86]. While different mechanisms describing this stage are considered in the literature [78–81], they often involve instabilities that lead to an exponential growth of long wavelength fluctuations. This also implies a rapid energy transport from the classical inflaton field to particle excitations. The situation is very similar to the decay of the initial ‘Glasma’ fields in heavy-ion collisions discussed above. Similar to that case, the instabilities lead to the emergence of a highly populated system with typical occupancies $f \sim 1/\lambda \gg 1$.

This over-occupied scalar system approaches a nonthermal fixed point [8, 21]. Its distribution exhibits a rich structure of different scaling regions [7, 87, 88]. As will be discussed in detail later in this work, it involves a dual cascade: there, energy is transferred to higher momenta driving the thermalization process while particles are pumped to lower momenta, occupying the zero momentum mode and thus leading to Bose-Einstein condensation far from equilibrium [89].

A similar situation may be prepared in table-top experiments using atomic gases at extremely low energies. These ultracold quantum gases can be largely isolated in experimental setups, such that they follow a unitary time evolution. They are known to exhibit universal properties near unitarity in the presence of a large s-wave scattering length a [90]. As for heavy-ion

collisions and cosmology, we are interested in a different form of universality that occurs far from equilibrium and is associated with nonthermal fixed points [10, 22–24, 89, 91–93].

More specifically, we consider a nonrelativistic atomic gas of interacting bosons with density n and scattering length a . With these quantities, we can define the dimensionless ‘diluteness parameter’ $\zeta = \sqrt{na^3}$ and a characteristic ‘coherence length’ whose inverse is given by the momentum scale $Q = \sqrt{16\pi an}$. In the dilute regime $\zeta \ll 1$, the system can exhibit an unusually large mode occupancy $f(Q) \sim 1/\zeta \gg 1$. The average particle density $n = \int d^3p/(2\pi)^3 f(p) \sim Q^3/\zeta$ becomes parametrically large, reflecting the underlying nonequilibrium distribution $f(p)$ of modes.

This is the analogous situation of an over-occupied system in heavy-ion collisions and inflationary cosmology with $f(Q) \gg 1$, which we discussed above. In the subsequent far-from-equilibrium evolution, the system approaches a nonthermal fixed point that can be described in terms of scaling exponents and scaling functions [7, 9, 10, 22, 89, 92]. Similarly to relativistic scalars, Bose condensation occurs out of equilibrium also for these nonrelativistic systems, as a consequence of a particle transport to lower momenta [89, 92, 94–96]. It is interesting to study whether these similarities between the relativistic and nonrelativistic scalar systems can be made quantitative. Clearly, there are important differences and one has to specify which properties can be universal.

Content of this work

As we discussed above, a strong over-occupation of modes $f \gg 1$ can be found in a variety of nonequilibrium systems in extreme conditions, some of which we illustrated in Fig. 1.2. Here the question arises whether relativistic scalar systems, used for instance to model the inflaton, exhibit similar scaling behavior as non-Abelian plasmas employed for heavy-ion collision studies or as nonrelativistic scalar fields used to model the dynamics of ultracold quantum gases.

One of our main objectives is to establish links between these different physics disciplines in terms of far-from-equilibrium universality classes. We study nonthermal fixed points of these systems in different geometries and compare their scaling properties. Our results open interesting theoretical and experimental perspectives, especially for heavy-ion collisions and ultracold atoms, which will be discussed in the end of this work.

We now present the outline of the thesis. Chapters of the main body start with a short presentation of the objectives and an outline of their sections and conclude with a summary.

The theoretical background for our studies is presented in Chapter 2. There we give an introduction to the considered scalar and gauge field theories in static and longitudinally

expanding backgrounds, to some principles of nonequilibrium quantum field theory and to our computational methods used in this work.

Nonthermal fixed points are introduced in Chapter 3. They are discussed at the example of scalar and gauge theories in Minkowski space-time using classical-statistical methods numerically and kinetic techniques analytically. This chapter provides a systematic overview of nonthermal fixed points in non-expanding scalar and gauge theories and includes recent literature results. It also provides an important starting point to extensions that will be discussed in the remaining chapters.

In Chapter 4 we study the dynamics of Bose-Einstein condensation in relativistic and non-relativistic scalar systems. We will find a broad universality class involving these systems whose scaling properties will be described by a vertex-resummed kinetic theory. This new universality class directly connects inflationary cosmology with ultracold Bose gases.

We extend our discussion of nonthermal fixed points to longitudinally expanding media in Chapter 5, where the expansion is reminiscent of the geometry apparent in heavy-ion collisions. We will find a new universality class that includes non-Abelian plasmas and scalar systems over a broad momentum region, providing a link between heavy-ion collisions and the inflaton in a special geometry. We also further analyze the nonthermal fixed point of longitudinally expanding non-Abelian plasmas and discuss, including recent literature, the emergent picture of the thermalization process in heavy-ion collisions at weak couplings.

In Chapter 6 we study the nonthermal fixed point of longitudinally expanding scalar systems in more detail. We further analyze the scaling properties in the universal scaling regime of non-Abelian plasmas and we delineate two further scaling regions. One of them is located at low momenta and leads to the formation of a Bose-Einstein condensate. Its scaling properties are very similar to those in non-expanding systems of Chapter 4, and can be understood in terms of the same vertex-resummed kinetic theory.

Moreover, we will argue in Chapter 6 that the important role of the infrared dynamics ensures that key features of our results for scalar and gauge theories cannot be reproduced consistently in conventional kinetic theory frameworks, which has consequences for our understanding of initial stages in heavy-ion collisions. These studies also extend the universality obtained between inflationary cosmology and ultracold Bose gases to expanding systems, and link these disciplines to heavy-ion collisions.

The thesis concludes with Chapter 7 where we discuss our results and give an outlook to possible future studies.

In the Appendices we provide details on some of our studies as well as further supplementary material.

Chapter 2

Theoretical background

While in the main part of this work, we discuss the nonequilibrium space-time evolution of different many-body systems, this chapter provides the theoretical background for our studies. Here we introduce the quantum field theories that are considered in this work (Sec. 2.1), we discuss important ingredients of a nonequilibrium evolution and how these are connected to the underlying quantum field theory (Sec. 2.2) and we describe the numerical method of classical-statistical simulations that is employed in this work (Sec. 2.3). Some technical parts are moved to Apps. A and B to simplify the presentation.

2.1 Considered field theories

In this section, we introduce relativistic and nonrelativistic scalar field theories as well as non-Abelian gauge theories. Their connections to physics disciplines have been pointed out in the introduction (Chapter 1).

We consider relativistic $O(N)$ -symmetric scalar and non-Abelian gauge theories in (non-expanding) Minkowski as well as in a longitudinally expanding space-time. The latter is well suited to discuss heavy-ion collisions. Taking account of the high velocities of the colliding nuclei, physics is described in terms of proper time τ and rapidity η . In these coordinates, the metric tensor becomes longitudinally expanding. To consider both metric tensors, we use a general time-dependent metric tensor $g_{\mu\nu}$ for our equations. On the other hand, we consider nonrelativistic scalar theory only with the Minkowski metric.

We start with discussing the metric tensor in Sec. 2.1.1 and we define the field theories by specifying their classical actions S afterwards. Further details on these theories can be found in the literature, as for instance in [27, 97].

2.1.1 Coordinates and longitudinal expansion

The metric tensor in (non-expanding) Minkowski space-time is given by

$$g_{\mu\nu}^{\text{Mink}} = \text{diag}(1, -1, -1, -1). \quad (2.1)$$

In the context of heavy-ion collisions, one performs coordinate transformation from time t and spatial coordinate z to Bjorken space-time coordinates

$$\tau = \sqrt{t^2 - z^2}, \quad \eta = \text{atanh}\left(\frac{z}{t}\right), \quad (2.2)$$

with the (longitudinal) proper time τ , longitudinal (spatial) rapidity η and transverse coordinates $\mathbf{x}_T = (x^1, x^2)$. Since a coordinate transformation implies the transformation of all Lorentz vectors and tensors [98], also the space-time metric needs to be transformed. In Bjorken coordinates, the metric takes the form

$$g_{\mu\nu}^{\text{Bjork}}(\tau) = \text{diag}(1, -1, -1, -\tau^2), \quad (2.3)$$

which characterizes one dimensional expansion in the longitudinal direction. To account for both coordinate systems, we use a general diagonal time-dependent metric $g_{\mu\nu}(x^0)$ with $g_{00} = 1$ in the following and we imply $x^0 \mapsto t$, $x^3 \mapsto z$ for the Minkowski and $x^0 \mapsto \tau$, $x^3 \mapsto \eta$ for the Bjorken case. The inverse of the metric tensor $g^{\mu\nu}$ is defined such that it satisfies

$$g^{\mu\gamma} g_{\gamma\nu} = \delta_{\nu}^{\mu}, \quad (2.4)$$

where δ_{ν}^{μ} is the usual Kronecker delta function with $\delta_{\nu}^{\mu} = 1$ for $\mu = \nu$ and 0 otherwise. The inverse of the Bjorken metric then reads

$$g_{\text{Bjork}}^{\mu\nu}(\tau) = \text{diag}\left(1, -1, -1, -\frac{1}{\tau^2}\right). \quad (2.5)$$

The metric determinant is denoted by $g(x^0) = \det(g_{\mu\nu}(x^0))$. It corresponds to $\sqrt{-g(x^0)} = 1$ for the non-expanding and $\sqrt{-g(x^0)} = \tau$ for the expanding cases.

The longitudinally expanding system describes the same physics as the original one in Minkowski space-time. The coordinate transformation to Bjorken coordinates merely changes the frame for our studies. Bjorken coordinates are beneficial if we want to describe ultra-relativistic heavy-ion collisions because in the limit of high velocities of the colliding nuclei, approximate longitudinal boost invariance implies η independence. The initial state can then be formulated at fixed proper time $\tau = \tau_0$. Moreover, in the limit of large nuclei, the system can be approximated as being homogeneous in transverse directions.¹ Therefore, a system homogeneous in

¹Physical initial conditions in heavy-ion collisions incorporate a nontrivial spatial structure of the colliding nuclei in the transverse plane as well as an impact parameter that characterizes the non-centrality of the collision.

\mathbf{x}_T and η can be considered to describe central collisions of large nuclei at mid-rapidity in the limit of high velocities. A non-expanding homogeneous system implies independence of the spatial coordinate \mathbf{x} . Such a description can be used for the (early) universe on sufficiently large length scales and for experiments with ultracold atoms where uniform potentials can be used to form a homogeneous state [99]. In this work we only discuss homogeneous systems, where Bjorken or Minkowski coordinates allow a suitable description of the dynamics.

2.1.2 Relativistic scalar field theory

We consider a massless N -component scalar field theory with real-valued scalar fields $\varphi_a(\mathbf{x}, x^0)$ and a quartic interaction with coupling λ . It is defined by the classical action

$$S_{\text{scalar}}[\varphi] = \int d^4x \sqrt{-g(x^0)} \left(\frac{1}{2} g^{\mu\nu}(x^0) (\partial_\mu \varphi_a) (\partial_\nu \varphi_a) - \frac{\lambda}{24N} (\varphi_a \varphi_a)^2 \right), \quad (2.6)$$

where summation over the $a = 1, 2, \dots, N$ scalar field components is implied. The classical equation of motion $\delta S_{\text{scalar}} / \delta \varphi_a(\mathbf{x}, x^0) = 0$ then reads

$$\left(\frac{1}{\sqrt{-g(x^0)}} \partial_0 \sqrt{-g(x^0)} \partial_0 - \sum_{i=1}^3 (-g^{ii}(x^0)) \partial_i^2 + \frac{\lambda}{6N} \varphi_b \varphi_b \right) \varphi_a = 0, \quad (2.7)$$

with an explicit summation over index i . For the static case, the two terms involving the metric reduce to the usual kinetic expression $\partial_\mu \partial^\mu \varphi_a(\mathbf{x}, t) = (\partial_t^2 - \boldsymbol{\partial}^2) \varphi_a(\mathbf{x}, t)$. For the longitudinally expanding system one finds instead $(\partial_\tau^2 + \tau^{-1} \partial_\tau - \boldsymbol{\partial}_{\mathbf{T}}^2 - \tau^{-2} \partial_\eta^2) \varphi_a(\mathbf{x}_T, \eta, \tau)$. The first difference to the evolution in Minkowski space-time is the term $\tau^{-1} \partial_\tau \varphi_a$ that is a dissipative term and that dilutes the system with the expansion rate $\sim \tau^{-1}$. The second difference is the term $-\tau^{-2} \partial_\eta^2 \varphi_a$ that leads to a red shift of longitudinal momenta. Alternatively, one can formulate the classical Hamilton equations of motion

$$\begin{aligned} \partial_0 \pi_a &= \sqrt{-g(x^0)} \left(\sum_{i=1}^3 (-g^{ii}(x^0)) \partial_i^2 - \frac{\lambda}{6N} \varphi_b \varphi_b \right) \varphi_a \\ \partial_0 \varphi_a &= \frac{\pi_a}{\sqrt{-g(x^0)}}, \end{aligned} \quad (2.8)$$

with the canonical momentum field $\pi_a(\mathbf{x}, x^0) = \delta S_{\text{scalar}} / \delta (\partial_0 \varphi_a(\mathbf{x}, x^0))$.

The traceless (Hilbert) stress-energy tensor (also known as the energy-momentum tensor) is defined via a functional derivative with respect to the metric tensor

$$T_{\mu\nu}(\mathbf{x}, x^0) = \frac{2}{\sqrt{-g}} \frac{\delta S_{\text{scalar}}}{\delta g^{\mu\nu}} = (\partial_\mu \varphi_a) (\partial_\nu \varphi_a) - g_{\mu\nu}(x^0) \mathcal{L}_{\text{scalar}}, \quad (2.9)$$

Such modifications lead to elliptic flow and other collective phenomena. While ab initio gauge simulations exist incorporating these effects [37, 38], we simplify the initial conditions and assume homogeneity in the transverse plane. This assumption corresponds to central collisions in the limit of large nuclei.

where the scalar Lagrangian density $\mathcal{L}_{\text{scalar}}$ is the kernel of the classical action $S_{\text{scalar}} = \int d^4x (-g(x^0))^{1/2} \mathcal{L}_{\text{scalar}}(\mathbf{x}, x^0)$.

2.1.3 Nonrelativistic scalar field theory

The (classical) action defining the single-component nonrelativistic scalar field theory takes the form [100]

$$S_{\text{nonrel}}[\psi, \psi^*] = \int d^4x \left[\frac{i}{2} (\psi^*(\mathbf{x}, t) \partial_t \psi(\mathbf{x}, t) - \psi(\mathbf{x}, t) \partial_t \psi^*(\mathbf{x}, t)) - \frac{1}{2m} (\nabla \psi^*(\mathbf{x}, t)) (\nabla \psi(\mathbf{x}, t)) - \frac{g}{2} (\psi(\mathbf{x}, t) \psi^*(\mathbf{x}, t))^2 \right], \quad (2.10)$$

for a nonrelativistic complex Bose field ψ . The coupling g is not dimensionless and is determined from the mass m and scattering length a as $g = 4\pi a/m$. We have employed the Minkowski metric for the action (2.10) since we only consider nonrelativistic systems in a static background. The classical evolution is given by the Gross-Pitaevskii equation

$$i\partial_t \psi(\mathbf{x}, t) = \left(-\frac{\nabla^2}{2m} + g|\psi(\mathbf{x}, t)|^2 \right) \psi(\mathbf{x}, t). \quad (2.11)$$

The total number of particles in a nonrelativistic theory, given by $N_{\text{total}} = \int d^3x |\psi(\mathbf{x}, t)|^2$, is strictly conserved, as well as the total energy density.

2.1.4 Non-Abelian gauge theory

Let us now proceed with non-Abelian $SU(N_c)$ -symmetric gauge field theories. These consist of fermionic matter fields that are coupled to gauge bosons. For instance, in Quantum Chromodynamics (QCD) each matter field carries one of the $N_c = 3$ color charges. Similarly, a gauge (gluonic) field carries an adjoint color charge $a = 1, \dots, N_c^2 - 1$, which constitutes that the pure gauge part of the theory is self-interacting. Since these gluons are bosonic, they can become highly occupied, as we noted in the introduction. In particular, their single particle distribution $f_g \propto d^3N/d^3p d^3x$ can be very large $f_g \gg 1$ in far-from-equilibrium situations. In contrast, quarks are fermions and due to the Pauli exclusion principle, they can only have small occupancies $f_\psi \leq 1$. Therefore, at early times of heavy-ion collisions where one finds large gluonic fields, quarks are often neglected in theoretical descriptions [67] since their effects on the dynamics of gluons are small [101]. Therefore, we only consider the pure gauge sector of a non-Abelian gauge theory, which is also known as the Yang-Mills sector.

We discuss here non-Abelian gauge theories for a general N_c . While QCD implies $N_c = 3$ as we noted above, we employ the $SU(2)$ gauge group in our numerical simulations, which is numerically less expensive. This approximation is motivated by studies of far-from-equilibrium

phenomena using classical-statistical lattice simulations [102] and simulations in the hard thermal loop (HTL) framework [103]. No qualitative differences of the results between different gauge groups have been found in these studies. This is confirmed within kinetic descriptions of non-Abelian plasmas, where in the limit of high occupation numbers and weak couplings, the number N_c can be entirely scaled out of the kinetic equation [104].

After these remarks, we present important properties of gauge theories. Gauge bosons can be described in terms of bosonic gauge fields $A_\mu(x)$ with $x = (\mathbf{x}, x^0)$ that transform as covariant four-vectors under Lorentz transformations. Under the coordinate transformation Bjorken coordinates in Eq. (2.2), gauge are transformed as

$$\begin{aligned} A_\tau(x) &= \cosh(\eta)A_t(x) + \sinh(\eta)A_z(x), \\ A_\eta(x) &= \tau\sinh(\eta)A_t(x) + \tau\cosh(\eta)A_z(x). \end{aligned} \quad (2.12)$$

To account for both coordinate systems, we will use gauge fields A_μ with $A_0 \mapsto A_t$, $A_3 \mapsto A_z$ for the static and $A_0 \mapsto A_\tau$, $A_3 \mapsto A_\eta$ for the Bjorken expanding case. Non-Abelian gauge fields are defined as elements of the $su(N_c)$ algebra. They can be decomposed as

$$A_\mu(x) = A_\mu^a(x) t^a, \quad (2.13)$$

where $A_\mu^a(x)$ are real-valued fields in adjoint representation with color components $a = 1, \dots, N_c^2 - 1$. The traceless Hermitian $t^a \in su(N_c)$ are the generators of the $SU(N_c)$ group and satisfy the Lie bracket relation and normalization condition

$$\left[t^a, t^b \right] = i f^{abc} t^c, \quad \text{tr} \left(t^a t^b \right) = \frac{1}{2} \delta^{ab}. \quad (2.14)$$

In fundamental representation, the generators t^a are $N_c \times N_c$ matrices and the first equation of (2.14) becomes a commutation relation. The structure constants f^{abc} are real and totally anti-symmetric color tensors. For $N_c = 3$ the Gell-Mann matrices λ_a are a common choice for the generators $t^a = \lambda^a/2$. Similarly, for $N_c = 2$ components one usually employs the Pauli-matrices σ_a for the generators $t^a = \sigma^a/2$ together with $f^{abc} = \epsilon^{abc}$ that is the totally anti-symmetric Levi-Civita symbol with the convention $\epsilon^{123} = 1$.

In gauge theories, fields can be characterized by their transformation properties under a (local) gauge transformation $G(x) \in SU(N_c)$. Matter fields in the fundamental representation of the $SU(N_c)$ group $\psi(x) = (\psi_i)(x)$ have components $i = 1, \dots, N_c$ and transform as

$$\psi(x) \mapsto G(x)\psi(x), \quad (2.15)$$

where the gauge transformation becomes a $N_c \times N_c$ matrix $G(x) = (G_{ij})(x)$. In contrast, gauge fields transform differently

$$A_\mu(x) \mapsto G(x)A_\mu(x)G^\dagger(x) - \frac{i}{g}(\partial_\mu G(x))G^\dagger(x), \quad (2.16)$$

where g is the gauge coupling. We will also use the coupling $\alpha_s = g^2/(4\pi)$ of the strong interaction in the following.

A crucial concept in gauge theories is gauge-invariance. All physical observables $O(x)$ are required to transform such that they are gauge-invariant under the trace over gauge components $\text{tr}(O(x))$. Regarding the transformation properties of gauge fields in Eq. (2.16), one thus finds that gauge fields $A_\mu(x)$ are not directly observable. Instead, one considers the (anti-symmetric) field strength tensor

$$\begin{aligned} F_{\mu\nu} &= \partial_\mu A_\nu - \partial_\nu A_\mu - ig[A_\mu, A_\nu] \\ F_{\mu\nu}^a &= \partial_\mu A_\nu^a - \partial_\nu A_\mu^a + g f^{abc} A_\mu^b A_\nu^c, \end{aligned} \quad (2.17)$$

where we used Eq. (2.14) for the second line. One can easily check that the field strength tensor transforms as

$$F_{\mu\nu}(x) \mapsto G(x)F_{\mu\nu}(x)G^\dagger(x), \quad (2.18)$$

and is thus a physical observable. In analogy to Quantum Electrodynamics (QED), where the last term in Eq. (2.17) is missing due to the Abelian nature of the electromagnetic gauge fields, the components of the field strength tensor are called chromo-electric and chromo-magnetic fields

$$E_a^j(x) = -\sqrt{-g(x^0)} F_a^{0j}(x), \quad B_a^j(x) = -\sqrt{-g(x^0)} \frac{1}{2} \epsilon^{jkl} F_{kl}^a(x), \quad (2.19)$$

with $F_a^{\mu\nu} = g^{\mu\alpha} g^{\nu\beta} F_{\alpha\beta}^a$. With this tensor, we can write a gauge-invariant classical action for the pure gauge (Yang-Mills) sector of gauge theories

$$S_{\text{YM}}[A] = -\frac{1}{2} \int d^4x \sqrt{-g} \text{tr}(F^{\mu\nu} F_{\mu\nu}) = -\frac{1}{4} \int d^4x \sqrt{-g} F_a^{\mu\nu} F_{\mu\nu}^a. \quad (2.20)$$

Because of the non-linear gauge term in the field strength tensor (2.17), the Yang-Mills action defines a self-interacting theory for the $N_c^2 - 1$ gauge fields.

The (classical) equations of motion follow from $\delta S_{\text{YM}}[A]/\delta A_\mu^a(x) = 0$ and read

$$D_\mu^{ab}(x) \sqrt{-g(x^0)} F_b^{\mu\nu}(x) = 0. \quad (2.21)$$

Here we have introduced the covariant derivative

$$D_\mu(x) = \partial_\mu - ig A_\mu(x). \quad (2.22)$$

In the adjoint representation, the generators are $(t^a)_{\text{adj}}^{bc} = -if^{abc}$ and the covariant derivative of Eq. (2.21) can be thus written as $D_\mu^{ab}(x) = \delta^{ab} \partial_\mu - g f^{abc} A_\mu^c(x)$. The covariant derivative extends the usual spatial derivative to additionally preserve gauge transformation properties. To illustrate this, let us again consider a matter field $\psi(x)$ that transforms in fundamental representation according to Eq. (2.15). Then its covariant derivative transforms in the same representation according to

$$D_\mu(x)\psi(x) \mapsto G(x)D_\mu(x)\psi(x), \quad (2.23)$$

as can be checked directly.

For the numerical simulations of classical gauge fields in real-time, it turns out to be of advantage to partially fix the gauge. We will employ the temporal gauge condition (called Fock-Schwinger or axial gauge in the expanding case) $A_0 = 0$, which leads to the effective action

$$S_{\text{YM,eff}}[A] = \int d^4x \sqrt{-g(x^0)} \left(-\frac{1}{2} g^{jk}(x^0) (\partial_0 A_j^a) (\partial_0 A_k^a) - \frac{1}{4} F_a^{jk} F_{jk}^a \right), \quad (2.24)$$

with summation over spatial indexes $j, k = 1, 2, 3$. With the conjugate momentum fields identified as the chromo-electric fields $E_a^j(\mathbf{x}, x^0) = \delta S_{\text{YM,eff}} / \delta (\partial_0 A_j^a(\mathbf{x}, x^0))$ of Eq. (2.19), the Hamiltonian reads

$$H_{\text{YM,eff}}[A, E] = \int d^3x \left(-\frac{1}{2\sqrt{-g(x^0)}} g^{jk}(x^0) E_a^j E_a^k + \frac{1}{4} F_a^{jk} F_{jk}^a \right). \quad (2.25)$$

This leads to the classical Hamilton equations of motion

$$\begin{aligned} \partial_0 E_a^j(x) &= -\frac{\delta H_{\text{YM,eff}}}{\delta A_j^a(x)} = \sqrt{-g(x^0)} D_k^{ab}(x) F_b^{kj}(x) \\ \partial_0 A_j^a(x) &= \frac{\delta H_{\text{YM,eff}}}{\delta E_a^j(x)} = -g_{jk}(x^0) \frac{E_a^k(x)}{\sqrt{-g(x^0)}}. \end{aligned} \quad (2.26)$$

These are equivalent to the classical equations $\delta S_{\text{YM}} / \delta A_j^a = 0$ in (2.21) for $A_0 = 0$. Since the original equations of motion also involved the Gauss law $\delta S_{\text{YM}} / \delta A_0^a = 0$, we have to take this equation

$$D_j^{ab}(x) E_b^j(x) = 0 \quad (2.27)$$

as an additional constraint at each space-time point. The Gauss law constraint has to be satisfied at initial time. Since it is preserved by the equations of motion (2.26), the constraint

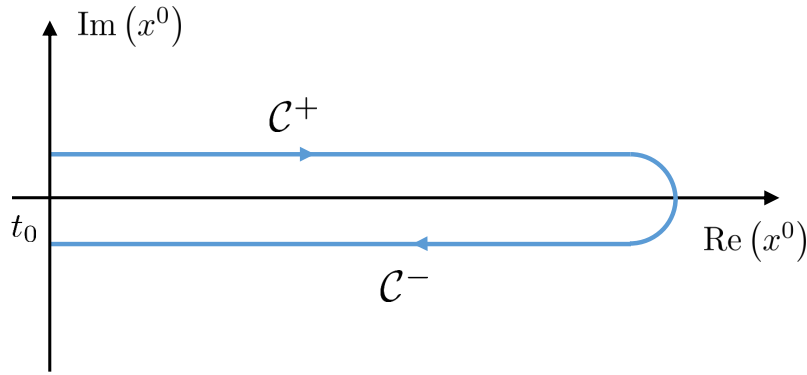


FIGURE 2.1: Illustration of the closed time path inherent to quantum theory.

is also fixed at subsequent times.

In analogy to scalars in Eq. (2.9), the traceless energy-momentum tensor for Yang-Mills theory can be computed to

$$T_{\mu\nu}(\mathbf{x}, x^0) = -g^{\alpha\beta} F_{\mu\alpha}^a F_{\nu\beta}^a + \frac{1}{4} g_{\mu\nu} F_{\alpha\beta}^a F_a^{\alpha\beta}. \quad (2.28)$$

2.2 Nonequilibrium quantum field theory

Introductions to nonequilibrium quantum field theory can be found for instance in Refs. [97, 105, 106]. Based on these references, we give a brief introduction where we discuss important concepts of the underlying framework in this section. To simplify the discussion, we use a scalar field theory. For non-Abelian gauge theories, most of the concepts can be similarly applied and we refer to Ref. [106] for further details.

2.2.1 Quantum field theory on a closed time path

In the Schrödinger picture of quantum theory, a system with the Hamilton operator $H(t)$ can be fully described by the time evolution of its density operator $\rho_D(t)$ that follows the Liouville-von-Neumann equation

$$\partial_t \rho_D(t) = -i [H(t), \rho_D(t)]. \quad (2.29)$$

Its solution can be written as

$$\rho_D(t) = U(t, t_0) \rho_0 U(t_0, t), \quad (2.30)$$

with the unitary time-evolution operator $U(t, t') = T \exp \left(-i \int_{t'}^t dt'' H(t'') \right)$.² The initial density matrix $\rho_0 \equiv \rho_D(t_0)$ is normalized to $\text{Tr}(\rho_0) = 1$, which also holds at later times due to the unitary evolution. In this picture, the evolution of the expectation value of an observable O can be computed as

$$\begin{aligned} \langle O \rangle(t) &= \text{Tr}(\rho_D(t) O) \\ &= \text{Tr}(\rho_0 U(t_0, t) O U(t, t_0)) . \end{aligned} \quad (2.31)$$

Equivalently, the system can be studied in the Heisenberg picture with time dependent Heisenberg operators $O(t) = U(t_0, t) O U(t, t_0)$ and the initial density matrix. The second line of Eq. (2.31) shows that the real-time evolution of the expectation value can be described by a closed time path that starts and ends at t_0 , which is also illustrated in Fig. 2.1. This time path is called the Schwinger-Keldysh time contour \mathcal{C} [107, 108]. It proceeds from t_0 until t in real time forming the positive direction branch \mathcal{C}^+ . Subsequently, it goes into the reverse direction back to t_0 , which indicates the negative direction branch \mathcal{C}^- , closing the time contour.

These concepts can be extended to quantum field theory, where one can define the generating functional

$$Z[J, R; \rho_0] = \text{Tr} \left(\rho_0 \text{T}_{\mathcal{C}} e^{i \left(\int_{x, \mathcal{C}} J_a(x) \Phi_a(x) + \frac{1}{2} \int_{xy, \mathcal{C}} R_{ab}(x, y) \Phi_a(x) \Phi_b(y) \right)} \right) , \quad (2.32)$$

with $Z[J, R = 0; \rho_0] = 1$ due to the normalization of ρ_0 . We included here external sources J, R multiplied by scalar field operators $\Phi_a(x)$ and integrated over d spatial dimensions and over the closed time path $\int_{x, \mathcal{C}} = \int_{\mathcal{C}} dx^0 \sqrt{-g(x^0)} \int d^d x$. The time ordering operator $\text{T}_{\mathcal{C}}$ orders all operators to its right along the time contour, with usual time ordering along the positive branch \mathcal{C}^+ , reversed ordering along \mathcal{C}^- , and with any time on \mathcal{C}^- considered later than any time on \mathcal{C}^+ . The time ordering becomes essential when we consider n-point correlation functions. For instance, with $\langle \cdot \rangle \equiv \text{Tr}(\rho_0 \cdot)$, the connected 1- and 2-point functions are defined as

$$\begin{aligned} \phi_a(x) &= \langle \Phi_a(x) \rangle = \frac{1}{i \sqrt{-g(x^0)}} \left. \frac{\delta Z}{\delta J_a(x)} \right|_{J, R=0} , \\ G_{ab}(x, y) + \phi_a(x) \phi_b(y) &= \langle \text{T}_{\mathcal{C}} \Phi_a(x) \Phi_b(y) \rangle \\ &= \frac{1}{i \sqrt{-g(x^0)} i \sqrt{-g(y^0)}} \left. \frac{\delta^2 Z}{\delta J_a(x) \delta J_b(y)} \right|_{J, R=0} . \end{aligned} \quad (2.33)$$

The function $\phi_a(x)$ is the macroscopic field (also called coherent field or, sometimes, condensate) while $G_{ab}(x, y)$ is the propagator. The latter can be further decomposed into the

²The time ordering operator T is defined such that for two operators $A(t_1)$ and $B(t_2)$ formulated at times $t_1 > t_2$, the time-ordering of their product is $T A(t_1) B(t_2) = T B(t_2) A(t_1) = A(t_1) B(t_2)$.

real-valued statistical and spectral correlation functions

$$F_{ab}(x, y) = \frac{1}{2} \langle \{\Phi_a(x), \Phi_b(y)\} \rangle - \phi_a(x) \phi_b(y), \quad \rho_{ab}(x, y) = i \langle [\Phi_a(x), \Phi_b(y)] \rangle, \quad (2.34)$$

according to

$$G_{ab}(x, y) = F_{ab}(x, y) - \frac{i}{2} \rho_{ab}(x, y) \operatorname{sgn}_{\mathcal{C}}(x^0 - y^0). \quad (2.35)$$

Since $F_{ab}(x, y)$ and $\rho_{ab}(x, y)$ are not time-ordered correlation functions, their time arguments do not need to be distinguished between the \mathcal{C}^+ and \mathcal{C}^- time branches. Moreover, the statistical function is symmetric $F_{ab}(x, y) = F_{ba}(y, x)$ and the spectral function is anti-symmetric $\rho_{ab}(x, y) = -\rho_{ba}(y, x)$. In Eq. (2.35) we used the signum function $\operatorname{sgn}_{\mathcal{C}}(x^0 - y^0)$ that equals $= 1$ when x^0 is later on the closed time path than y^0 and $= -1$ when it is earlier.³

The spectral function ρ determines the structure of excitations of the system, very similar to the Källén-Lehmann spectral representation of the (full) propagator in vacuum quantum field theory [109–111]. In contrast, the statistical function F provides the information about how often states are occupied in the quantum system. This can be visualized by the decomposition⁴

$$F(p^0, \mathbf{p}, t) = \left(f(p^0, \mathbf{p}, t) + \frac{1}{2} \right) \tilde{\rho}(p^0, \mathbf{p}, t), \quad (2.36)$$

where we have introduced the real-valued spectral function $\tilde{\rho}(p^0, \mathbf{p}, t) = -i\rho(p^0, \mathbf{p}, t)$ in Fourier space. Out of equilibrium, there are exactly two independent two-point correlation functions, which may be chosen as F and $\tilde{\rho}$. However, in thermal equilibrium, they are no longer independent, and related by the Kubo-Martin-Schwinger (KMS) condition [112, 113] (also known as the fluctuation-dissipation relation), where $f(p^0, \mathbf{p}, t) \mapsto f_{\text{BE}}(p^0) = (e^{p^0/T} - 1)^{-1}$ is the Bose-Einstein distribution with temperature T . We can thus interpret $f(p^0, \mathbf{p}, t)$ as a generalized (off-shell) occupation number that is able to describe thermalization.

The generating functional in Eq. (2.32) can also be used to derive the equations of motion for the correlation functions. Let us first identify the eigenstates and eigenvectors of the field operators at initial time $\Phi^\pm(t_0)$ on the branches \mathcal{C}^\pm

$$\Phi^\pm(t_0) |\varphi^\pm\rangle = \varphi_0^\pm(\mathbf{x}) |\varphi^\pm\rangle. \quad (2.37)$$

³Since the spectral function is odd in its arguments, it vanishes at $x^0 = y^0$ and we do not need to define the signum function there.

⁴The correlation functions $F = F_{aa}/N$ and $\rho = \rho_{aa}/N$ have been written in Wigner coordinates $t = (x^0 + y^0)/2$, $s^0 = x^0 - y^0$, $\mathbf{X} = (\mathbf{x} + \mathbf{y})/2$ and $\mathbf{s} = \mathbf{x} - \mathbf{y}$, and have been subsequently Fourier transformed with respect to the relative coordinates s^0 and \mathbf{s} . Since we consider spatially homogeneous systems, the correlation functions do not depend on \mathbf{X} . We therefore write $F(p^0, \mathbf{p}, t, \mathbf{X}) \mapsto F(p^0, \mathbf{p}, t)$ and $-i\rho(p^0, \mathbf{p}, t, \mathbf{X}) \mapsto -i\rho(p^0, \mathbf{p}, t)$.

With this, it is possible to separate the initial conditions from the rest of the evolution [97] by expressing the generating functional Z as a path integral

$$Z[J, R; \rho_0] = \underbrace{\int [d\varphi_0^+] [d\varphi_0^-] \langle \varphi^+ | \rho_0 | \varphi^- \rangle}_{\text{initial conditions}} \times \underbrace{\int_{\varphi_0^+}^{\varphi_0^-} \mathcal{D}'\varphi e^{i(S_{\mathcal{C}}[\varphi] + \int_{x,C} J_a(x)\varphi_a(x) + \frac{1}{2} \int_{xy,C} R_{ab}(x,y)\varphi_a(x)\varphi_b(y))}}_{\text{quantum dynamics}}, \quad (2.38)$$

with integration measure $\int [d\varphi_0^\pm] = \int \prod_{a=1}^N \prod_{\mathbf{x}} d\varphi_{a,0}^\pm(\mathbf{x})$ for the initial conditions. The integration measure of the residual path integral $\int_{\varphi_0^+}^{\varphi_0^-} \mathcal{D}'\varphi$ excludes the end points of the time contour \mathcal{C} and is further restricted by the requirements $\varphi(t = t_0^\pm) = \varphi_0^\pm$ for the fields at initial time of both branches. One observes in Eq. (2.38) that the initial density operator ρ_0 only enters the initial conditions while the subsequent evolution is governed by the classical action $S_{\mathcal{C}}[\varphi]$. Note that all integrals involve the closed time path, which characterizes the quantum nature of the dynamics.

In analogy to quantum field theory in vacuum or in equilibrium, we can define the nonequilibrium generating functional for connected correlation functions⁵

$$W[J, R] = -i \ln Z[J, R]. \quad (2.39)$$

From derivatives with respect to the sources, we obtain the correlation functions introduced in Eq. (2.33)

$$\frac{\delta W[J, R]}{\delta J_a(x)} = \phi_a(x), \quad \frac{\delta W[J, R]}{\delta R_{ab}(x, y)} = \frac{1}{2} (G_{ab}(x, y) + \phi_a(x)\phi_b(y)). \quad (2.40)$$

Since the functional W depends on the sources instead of the correlation functions, we can use Eq. (2.40) to perform a Legendre transform with respect to the sources

$$\Gamma[\phi, G] = W[J, R] - \int_x \frac{\delta W[J, R]}{\delta J_a(x)} J_a(x) - \int_{xy} \frac{\delta W[J, R]}{\delta R_{ab}(x, y)} R_{ab}(x, y). \quad (2.41)$$

This functional is called the two-particle irreducible (2PI) effective action. As the original generating functional, it encodes the complete information about the system. It leads to the quantum equations of motion of the coherent field and the propagator

$$\begin{aligned} \frac{\delta \Gamma}{\delta \phi_a(x)} &= -J_a(x) - \int_{y,C} R_{ab}(x, y)\varphi_b(y), \\ \frac{\delta \Gamma}{\delta G_{ab}(x, y)} &= -\frac{1}{2} R_{ab}(x, y). \end{aligned} \quad (2.42)$$

⁵The dependence on the initial density operator ρ_0 can be absorbed in the sources for Gaussian initial conditions [97].

To understand its importance, we state that the 2PI effective action can be brought into the form [97, 106]

$$\Gamma[\phi, G] = S_{\mathcal{C}}[\phi] + \frac{i}{2} \text{Tr}_{\mathcal{C}} \ln G^{-1} + \frac{i}{2} \text{Tr}_{\mathcal{C}} G_0^{-1}[\phi] G + \Gamma_2[\phi, G] + \text{const}, \quad (2.43)$$

with the classical inverse propagator $iG_{0,ab}^{-1}(x, y)[\phi] = \delta S_{\mathcal{C}}[\phi] / \delta \phi_a(x) \delta \phi_b(y)$. The residual term $\Gamma_2[\phi, G]$ can be expanded in an infinite series of two-particle irreducible (2PI) Feynman diagrams, where every line corresponds to the full propagator G while vertices are taken from the classical action. The 2PI property means that the diagrams are not allowed to become disconnected after cutting two propagator lines. This constraint considerably reduces the number of possible diagrams that $\Gamma_2[\phi, G]$ involves at each order of a loop expansion. The 2PI quantum equations of motion (2.42) are self-consistent equations that can be brought into an explicit form, i.e. formulated as coupled integro-differential equations for the correlation functions ϕ , F and ρ [97, 106]. With the expansion (2.43), approximations for the equations typically follow from choosing a truncation of the $\Gamma_2[\phi, G]$ functional, by taking only a subset of possible Feynman diagrams, for instance.

Typically one employs perturbative truncations as in a loop expansion or non-perturbative truncations where an infinite subset of Feynman diagrams is taken into account. An example for the latter is the $1/N$ expansion to next-to-leading order [114]. The classical-statistical approximation that is discussed in Sec. 2.3.1 can also be considered as a non-perturbative truncation of the effective action. However, in that case, one usually employs the framework of classical-statistical field theory in explicit lattice simulations instead of the 2PI equations for the correlation functions.

2.2.2 Distribution function in homogeneous systems

Here we reconsider the correlation functions of Eqs. (2.33) and (2.34) and use them to define the single-particle distribution function in Fourier space. First we note that for homogeneous systems, the expectation values of the Heisenberg field operator $\Phi_a(\mathbf{x}, x^0)$ and its canonical momentum operator $\Pi_a(\mathbf{x}, x^0) = \sqrt{-g(x^0)} \partial_0 \Phi_a(\mathbf{x}, x^0)$ become

$$\phi_a(x^0) = \langle \Phi_a(\mathbf{x}, x^0) \rangle \quad \pi_a(x^0) = \langle \Pi_a(\mathbf{x}, x^0) \rangle. \quad (2.44)$$

The statistical operator in (2.34) then reduces to

$$F_{ab}(\mathbf{x} - \mathbf{x}', x^0, x^{0'}) = \frac{1}{2} \langle \{ \Phi_a(\mathbf{x}, x^0), \Phi_b(\mathbf{x}', x^{0'}) \} \rangle - \phi_a(x^0) \phi_b(x^{0'}). \quad (2.45)$$

The distribution function can be defined using the spatial Fourier transform⁶ of the equal time statistical correlation function and its derivatives

$$\begin{aligned}
F(\tilde{\mathbf{p}}, x^0) &\equiv \frac{1}{N} \sum_{a=1}^N F_{aa}(\tilde{\mathbf{p}}, x^0, x^0) \\
\ddot{F}(\tilde{\mathbf{p}}, x^0) &\equiv \sqrt{-g(x^0)} \sqrt{-g(x^{0'})} \partial_0 \partial_{0'} F(\tilde{\mathbf{p}}, x^0, x^{0'}) \Big|_{x^0=x^{0'}} \\
\dot{F}(\tilde{\mathbf{p}}, x^0) &\equiv \frac{1}{2} \left(\sqrt{-g(x^0)} \partial_0 + \sqrt{-g(x^{0'})} \partial_{0'} \right) F(\tilde{\mathbf{p}}, x^0, x^{0'}) \Big|_{x^0=x^{0'}}
\end{aligned} \tag{2.46}$$

according to [106]

$$f_{\text{def 1}}(\mathbf{p}, x^0) + \frac{1}{2} = \sqrt{F(\tilde{\mathbf{p}}, x^0) \ddot{F}(\tilde{\mathbf{p}}, x^0) - \dot{F}^2(\tilde{\mathbf{p}}, x^0)}. \tag{2.47}$$

This definition is employed in our numerical simulations for relativistic scalars, and we will often drop the subscript ‘def 1’. Similarly, we can define an effective dispersion relation by

$$\omega(\mathbf{p}, x^0) = \sqrt{\frac{\ddot{F}(\tilde{\mathbf{p}}, x^0)}{(-g(x^0)) F(\tilde{\mathbf{p}}, x^0)}}. \tag{2.48}$$

For the longitudinally expanding case, the longitudinal momentum variable is identified as $p_z \equiv \nu/\tau$. This choice of variable is motivated by the form of the longitudinal kinetic term ($\tau^{-2} \partial_\eta^2 \varphi_a$) in the (classical) field equation (2.7). The definitions in Eqs. (2.47) and (2.48) are motivated by quasiparticle definitions in free theory, and we note that the distribution $f(\mathbf{p}, x^0)$ has also been shown to thermalize to a Bose-Einstein distribution in the interacting case with a spectral function rather peaked around its quasiparticle dispersion relation $\omega(\mathbf{p}, x^0)$ [111].

In fact, the definition of the occupation number (2.47) is based on effective creation and annihilation operators in the interacting theory. Following Refs. [115, 116] for our geometries, we may also define the distribution function in the convenient way

$$\begin{aligned}
f_{\text{def 2}}(\mathbf{p}, x^0) &= \frac{1}{V N} \sum_b \langle a_{b, \tilde{\mathbf{p}}}^\dagger(x^0) a_{b, \tilde{\mathbf{p}}}(x^0) \rangle \\
&= \frac{1}{2V N} \sum_b \langle \{a_{b, \tilde{\mathbf{p}}}^\dagger(x^0), a_{b, \tilde{\mathbf{p}}}(x^0)\} \rangle - \frac{1}{2},
\end{aligned} \tag{2.49}$$

⁶More specifically, the Fourier transformation is part of a Wigner transformation with spatial central coordinates $\mathbf{X} = (\mathbf{x} + \mathbf{x}')/2$ and relative coordinate $\mathbf{s} = \mathbf{x} - \mathbf{x}'$ given by

$$F_{ab}(\tilde{\mathbf{p}}, x^0, x^{0'}) = \frac{d^3 X}{V} \int d^3 s F_{ab}(\mathbf{x}, \mathbf{x}', x^0, x^{0'}) e^{-i\tilde{\mathbf{p}}\mathbf{s}},$$

where we have considered a final volume V of the system and where we have introduced the conjugate momenta $\tilde{\mathbf{p}}$ of the spatial coordinates. In Minkowski space, these are the same as the usual momenta \mathbf{p} . For the expanding case, transverse momenta are the same $\tilde{\mathbf{p}}_T = \mathbf{p}_T$ while the rapidity wave number $\tilde{p}_z \equiv \nu$ is the conjugate momentum variable to η .

where V is the spatial volume of the considered system, and we already anticipated the usual commutation relations in the second line. The annihilation operator can be defined as

$$a_{b,\tilde{\mathbf{p}}}(x^0) = i\sqrt{-g(x^0)} \int d^3x \left(\xi_{\tilde{\mathbf{p}}}^*(x^0) \overleftrightarrow{\partial}_0 (\Phi_b(\mathbf{x}, x^0) - \phi_b(x^0)) \right) e^{-i\tilde{\mathbf{p}}\mathbf{x}}, \quad (2.50)$$

with $a \overleftrightarrow{\partial}_0 b = a \partial_0 b - b \partial_0 a$, and correspondingly the creation operator is defined as $a_{b,\tilde{\mathbf{p}}}^\dagger(x^0) = (a_{b,\tilde{\mathbf{p}}}(x^0))^\dagger$. The mode functions $\xi_{\tilde{\mathbf{p}}}(x^0)$ have to satisfy $(\partial_0 \xi_{\tilde{\mathbf{p}}}(x^0))^* = \partial_0 \xi_{\tilde{\mathbf{p}}}^*(x^0)$ as well as the normalization condition

$$\xi_{\tilde{\mathbf{p}}}(x^0) \overleftrightarrow{\partial}_0 \xi_{\tilde{\mathbf{p}}}^*(x^0) = \frac{i}{\sqrt{-g(x^0)}}. \quad (2.51)$$

As a consequence of this condition and of the equal-time canonical commutation relations

$$\begin{aligned} [\Phi(\mathbf{x}, x^0), \Pi(\mathbf{x}', x^0)] &= i\delta(\mathbf{x} - \mathbf{x}'), \\ [\Phi(\mathbf{x}, x^0), \Phi(\mathbf{x}', x^0)] &= [\Pi(\mathbf{x}, x^0), \Pi(\mathbf{x}', x^0)] = 0, \end{aligned} \quad (2.52)$$

the creation and annihilation operators indeed satisfy the usual commutation relations

$$\begin{aligned} [a_{a,\tilde{\mathbf{p}}}(x^0), a_{b,\tilde{\mathbf{p}}'}^\dagger(x^0)] &= (2\pi)^3 \delta_{ab} \delta(\tilde{\mathbf{p}} - \tilde{\mathbf{p}}'), \\ [a_{a,\tilde{\mathbf{p}}}(x^0), a_{b,\tilde{\mathbf{p}}'}(x^0)] &= [a_{a,\tilde{\mathbf{p}}}^\dagger(x^0), a_{b,\tilde{\mathbf{p}}'}^\dagger(x^0)] = 0. \end{aligned} \quad (2.53)$$

The definition of these operators in Eq. (2.50) is equivalent to the mode expansion of the scalar field operator and its canonical momentum operator

$$\begin{aligned} \Phi_b(\mathbf{x}) &= \phi_b + \int \frac{d^3\tilde{\mathbf{p}}}{(2\pi)^3} \left(a_{b,\tilde{\mathbf{p}}} \xi_{\tilde{\mathbf{p}}} e^{i\tilde{\mathbf{p}}\mathbf{x}} + a_{b,\tilde{\mathbf{p}}}^\dagger \xi_{\tilde{\mathbf{p}}}^* e^{-i\tilde{\mathbf{p}}\mathbf{x}} \right), \\ \Pi_b(\mathbf{x}) &= \pi_b + \sqrt{-g} \int \frac{d^3\tilde{\mathbf{p}}}{(2\pi)^3} \left(a_{b,\tilde{\mathbf{p}}} \partial_0 \xi_{\tilde{\mathbf{p}}} e^{i\tilde{\mathbf{p}}\mathbf{x}} + a_{b,\tilde{\mathbf{p}}}^\dagger \partial_0 \xi_{\tilde{\mathbf{p}}}^* e^{-i\tilde{\mathbf{p}}\mathbf{x}} \right), \end{aligned} \quad (2.54)$$

where each of the terms depends on time x^0 . Assuming that the anomalous occupation numbers $\langle \{a_{b,\tilde{\mathbf{p}}}(x^0), a_{b,\tilde{\mathbf{p}}'}(x^0)\} \rangle / (2NV)$ and $\langle \{a_{b,\tilde{\mathbf{p}}}^\dagger(x^0), a_{b,\tilde{\mathbf{p}}'}^\dagger(x^0)\} \rangle / (2NV)$ vanish identically, the mode decomposition in Eq. (2.54) leads for the statistical correlation function to

$$\begin{aligned} F(\tilde{\mathbf{p}}) &= \left(f_{\text{def } 2}(\tilde{\mathbf{p}}) + \frac{1}{2} \right) 2|\xi_{\tilde{\mathbf{p}}}|^2, \quad \ddot{F}(\tilde{\mathbf{p}}) = \left(f_{\text{def } 2}(\tilde{\mathbf{p}}) + \frac{1}{2} \right) 2|\sqrt{-g} \partial_0 \xi_{\tilde{\mathbf{p}}}|^2, \\ \dot{F}(\tilde{\mathbf{p}}) &= \left(f_{\text{def } 2}(\tilde{\mathbf{p}}) + \frac{1}{2} \right) \sqrt{-g} (\xi_{\tilde{\mathbf{p}}}^* \partial_0 \xi_{\tilde{\mathbf{p}}} + \xi_{\tilde{\mathbf{p}}} \partial_0 \xi_{\tilde{\mathbf{p}}}^*), \end{aligned} \quad (2.55)$$

where we used point symmetry under $\mathbf{p} \mapsto -\mathbf{p}$. Using these expressions and Eq. (2.51) in the definition of the distribution function (2.47), one obtains the equivalence

$$f(\mathbf{p}, x^0) \equiv f_{\text{def } 1}(\mathbf{p}, x^0) = f_{\text{def } 2}(\mathbf{p}, x^0) \quad (2.56)$$

for both definitions in (2.47) and (2.49). We emphasize that this equivalence is based on the assumption of vanishing anomalous expectation values, as we pointed out in this derivation. Therefore, this may be considered as a condition for a reasonable interpretation of the system in terms of quasiparticles.

We show in App. A that for a quasi-free non-expanding system or a longitudinally expanding system at sufficiently late times, the mode functions can be expressed as

$|\xi_{\tilde{\mathbf{p}}}|^2 = 1/(2\omega(\mathbf{p})\sqrt{-g(x^0)})$, $|\sqrt{-g}\partial_0\xi_{\tilde{\mathbf{p}}}|^2 = \sqrt{-g(x^0)}\omega(\mathbf{p})/2$ and $(\xi^*\partial_0\xi + \xi\partial_0\xi^*) = 0$. Inserting these expressions into Eqs. (2.55) leads to

$$F(\tilde{\mathbf{p}}) = \frac{f(\mathbf{p}, x^0) + 1/2}{\sqrt{-g(x^0)}\omega(\mathbf{p})}, \quad \dot{F}(\tilde{\mathbf{p}}) = \sqrt{-g(x^0)}\omega(\mathbf{p})(f(\mathbf{p}, x^0) + 1/2), \quad \ddot{F}(\tilde{\mathbf{p}}) = 0, \quad (2.57)$$

which is consistent with the definition of the dispersion relation in Eq. (2.48).

Moreover, we have introduced in Sec. 2.2.1 a generalized distribution function $f(p^0, \mathbf{p}, x^0)$ that results from the relation in Eq. (2.36) of the correlation functions F and $\tilde{\rho}$. For a free spectral function

$$\tilde{\rho}_{\text{free}}(p^0, \mathbf{p}, x^0) = 2\pi \operatorname{sgn}(p^0) \delta((p^0)^2 - \omega^2(\mathbf{p})), \quad (2.58)$$

one has a Delta-peak at the on-shell condition $p^0 = \omega(\mathbf{p})$. Integrating Eq. (2.36) with the free spectral function along $2\int_0^\infty dp^0$ and using the point symmetry of the statistical correlator, one arrives at the equal time relation

$$F(\tilde{\mathbf{p}}, x^0, x^0) = \frac{f(p^0 = \omega(\mathbf{p}), \mathbf{p}, x^0) + 1/2}{\omega(\mathbf{p})}, \quad (2.59)$$

which is the same relation as in Eq. (2.57) if one identifies $f(\omega(\mathbf{p}), \mathbf{p}, x^0) \mapsto f(\mathbf{p}, x^0)$. This motivates a third definition for the distribution function [117, 118]

$$f_{\text{def 3}}(\mathbf{p}, x^0) + \frac{1}{2} = \int_0^\infty \frac{dp^0}{2\pi} 2p^0 F(p^0, \mathbf{p}, x^0). \quad (2.60)$$

We have now discussed three definitions of the distribution function (2.47), (2.49) and (2.60). They are equivalent if a quasi-free spectral function is assumed (2.58). The definitions are also applicable for a general spectral function, however, then the interpretation in terms of quasiparticles may be problematic. Our second definition (2.49) has been frequently used in the literature, as for instance in Refs. [8, 119]. The third definition (2.60) has been mostly used in the derivation of transport or kinetic equations from nonequilibrium quantum evolution equations [117, 118] and it is less practicable in lattice computations.

Instead, we will use our primary definition (2.47) for scalars that has the important advantages that we do not need to know the specific form of the mode functions ξ or of the spectral

function $\tilde{\rho}$ to describe the distribution. Since we employ classical-statistical lattice simulations numerically, we provide the corresponding definitions in Sec. 2.3.3.

For gauge theories, we also define a distribution function in App. B directly in the classical-statistical approximation that is used for our numerics. This requires to fix the gauge at read-out time, which we discuss in that appendix. We use a variation of the second definition (2.49) to define the corresponding distribution function for gauge theories.

2.2.3 Initial conditions

We employ Gaussian initial conditions, where we have to specify the one- and two-point correlation functions (2.44), (2.34). Moreover, we choose the statistical correlation functions at initial time such that they satisfy the quasi-free relations of Eq. (2.55). Therefore, we only have to initialize the coherent field and its derivative $\phi_a(\tau_0)$, $\dot{\phi}_a(\tau_0)$ as well as the single particle distribution $f(p_T, p_z, \tau_0)$ at the starting time τ_0 .⁷ We will write our initial conditions for the longitudinally expanding cases while the corresponding initial conditions for the non-expanding theories are simply deduced by substituting $\sqrt{p_T^2 + p_z^2} \mapsto p$ and $\tau \mapsto t$.

The first set of initial conditions is chosen to exhibit a large characteristic occupancy with

$$f(p_T, p_z, \tau_0) = \frac{n_0}{\lambda} \Theta\left(Q - \sqrt{p_T^2 + (\xi_0 p_z)^2}\right), \quad (2.61)$$

and vanishing coherent field $\phi_a(\tau_0) = \partial_\tau \phi_a(\tau_0) = 0$. Here the parameters describe the initial occupancy n_0 , initial anisotropy ξ_0 and the characteristic momentum scale Q of the distribution at initial time. In a static background, we choose an isotropic distribution $\xi_0 = 1$, and hence $f(p, t_0) = (n_0/\lambda) \Theta(Q - p)$. For gauge theories, we choose the same initial conditions with the substitution $\lambda \mapsto 2g^2$. We will refer to these initial conditions as ‘over-occupation’ initial conditions. As we discussed in the introduction (Sec. 1), such a state can be found in a variety of nonequilibrium disciplines including heavy-ion collisions, inflationary cosmology and ultracold atoms.

Our second set of initial conditions is characterized by a large coherent field,

$$\phi_a(\tau_0) = \sigma_0 \sqrt{\frac{6N}{\lambda}} \delta_{a,1}, \quad \partial_\tau \phi_a(\tau_0) = 0, \quad (2.62)$$

and vanishing occupancy $f(p_T, p_z, \tau_0) = 0$. The amplitude parameter σ_0 is the only dimensionful scale in such a state. These initial conditions will be called coherent field initial conditions.

⁷The initial conditions for the spectral function

$$\rho_{ab}(x, y)|_{x^0=y^0} = 0, \quad \sqrt{-g(x^0)} \partial_{x^0} \rho_{ab}(x, y)|_{x^0=y^0} = \delta_{ab} \delta(\mathbf{x} - \mathbf{y})$$

follow directly from the Heisenberg field commutation relations (2.52) and do not need to be specified separately.

The latter conditions lead to instabilities and thus to an exponential growth of occupation numbers within a resonant momentum region. Eventually, an over-occupied system emerges while the coherent field decays. Therefore a systems with over-occupation initial conditions can be considered as starting at a later time subsequent to coherent field initial conditions. We will discuss this transition in Secs. 3.2.2 and 5.2.4 in more detail.

Note that these sets of initial conditions describe large occupation numbers (large fluctuations) or a large coherent field, respectively, since we consider only weak couplings $\lambda \ll 1$. Therefore, both sets of initial conditions admit a rigorous description of the dynamics in terms of classical-statistical field theory to leading order in the coupling λ [11–13, 20, 82, 88, 100]. Since we are interested in the weak coupling limit, with $\lambda \rightarrow 0^+$ but λf finite for typical momenta, the mapping from a quantum to a classical system is valid at all simulation times. We will discuss this classical-statistical approximation in more detail in Sec. 2.3.1.

In particular, we will omit the ‘quantum-1/2’ in Eqs. (2.47) and (2.55) for over-occupation initial conditions. At weak couplings, this classical approximation does not change the subsequent evolution of the system to good accuracy while it prevents spurious Rayleigh-Jeans divergences [120]. For coherent field initial conditions, the quantum vacuum should not be omitted if one intends to describe the instabilities at early times. Instead, we employ an intermediate cutoff such that the quantum vacuum involves the whole primary resonance band. We only show simulation results that do not change under variation of this intermediate cutoff. In practice, it is sufficient to capture this primary resonance band since secondary instabilities quickly emerge from nonlinear interactions with the primary instabilities. Therefore, they do not require the quantum vacuum as an initial ‘seed’ to grow [87, 121].

2.3 Classical-statistical lattice simulations

In this section we discuss classical-statistical lattice simulations that will be used throughout this thesis to achieve numerical results. This technique is commonly used in the literature (see e.g. [97]) and we provide some important aspects here.

In Sec. 2.3.1 we discuss the range of validity of the classical-statistical approximation. We describe the lattice algorithm and the numerical setup in Sec. 2.3.2. Specific setup details for $O(N)$ -symmetric relativistic and nonrelativistic scalar field theories are provided in Secs. 2.3.3 and 2.3.4, respectively. Setup details for simulations in non-Abelian gauge theory are moved to App. B to ease the presentation in this section.

We note that all equations in Sec. 2.3.3 and App. B are provided for a general diagonal time-dependent metric $g_{\mu\nu}(x^0)$ to account for both the Minkowski and Bjorken metric, and the same equations can thus be used for a more general space-time. Moreover, the presentation in App. B is valid for Yang-Mills theories with $N_c \geq 2$ of the underlying gauge group $SU(N_c)$. For our numerical simulations, we use the $SU(2)$ gauge theory, where powerful optimizations exist that considerably reduce the required computational resources as compared to the cases with larger N_c [15, 122].

2.3.1 Classical-statistical approximation

We will now discuss the classical-statistical field theory approximation of full quantum dynamics and state its range of validity. This was studied in Refs. [11, 13, 100] for relativistic and nonrelativistic scalar field theories from a two-particle irreducible (2PI) approach and from a kinetic framework. Similarly, the classical approximation in thermal equilibrium was investigated in Ref. [123]. We will mostly discuss scalar field theory based on Ref. [97]. In gauge theories, one has a very similar ‘classicality’ condition that states when the classical-statistical approximation can provide accurate results. The arguments are also similar to those in scalar field theory and we refer to Ref. [124] for further details.

We start with the generating functional $Z[J, R; \rho_0]$ of Eq. (2.38). It involves the integration over the closed time path \mathcal{C} with the positive and negative time branches \mathcal{C}^\pm . We denote fields on each of the branches as φ^\pm and we rewrite the classical action over this time path as

$$S_{\mathcal{C}}[\varphi] = S[\varphi^+] - S[\varphi^-], \quad (2.63)$$

where $S = S_{\text{scalar}}$ is the classical action given by Eq. (2.6) with only the forward time path. A similar decomposition can be made for the source terms entering the generating functional

in Eq. (2.38). Next we introduce the scalar fields

$$\varphi = \frac{\varphi^+ + \varphi^-}{2}, \quad \tilde{\varphi} = \varphi^+ - \varphi^-, \quad (2.64)$$

which lead to the action

$$S[\varphi, \tilde{\varphi}] = S_0[\varphi, \tilde{\varphi}] + S_{\text{int,cl}}[\varphi, \tilde{\varphi}] + S_{\text{int,qu}}[\varphi, \tilde{\varphi}]. \quad (2.65)$$

The different parts of the action read

$$\begin{aligned} S_0[\varphi, \tilde{\varphi}] &= \int_{t_0} d^4x \partial^\mu \tilde{\varphi}_a(x) \partial_\mu \varphi_a(x) \\ S_{\text{int,cl}}[\varphi, \tilde{\varphi}] &= \int_{t_0} d^4x \frac{-\lambda}{6N} \tilde{\varphi}_a(x) \varphi_a(x) \varphi_b(x) \varphi_b(x) \\ S_{\text{int,qu}}[\varphi, \tilde{\varphi}] &= \int_{t_0} d^4x \frac{-\lambda}{24N} \tilde{\varphi}_a(x) \tilde{\varphi}_a(x) \tilde{\varphi}_b(x) \varphi_b(x), \end{aligned} \quad (2.66)$$

where we chose the Minkowski metric for brevity but the proceeding arguments can be similarly employed for a more general metric. The integration $\int_{t_0} d^4x$ proceeds on a single forward time branch starting from $x^0 = t_0$. From integration by parts we get

$$S_0[\varphi, \tilde{\varphi}] = - \int d^3x \pi_{0,a}(\mathbf{x}) \tilde{\varphi}_{0,a}(\mathbf{x}) + \int_{t_0} d^4x \tilde{\varphi}_a(x) (-\partial^\mu \partial_\mu) \varphi_a(x). \quad (2.67)$$

We can now define a classical action $S_{\text{cl}}[\varphi, \tilde{\varphi}]$

$$\begin{aligned} S_{\text{cl}}[\varphi, \tilde{\varphi}] &= \int_{t_0} d^4x \tilde{\varphi}_a(x) \left(-\partial^\mu \partial_\mu \varphi_a(x) - \frac{\lambda}{6N} \varphi_a(x) \varphi_b(x) \varphi_b(x) \right) \\ &= \int_{t_0} d^4x \tilde{\varphi}_a(x) \frac{\delta S[\varphi]}{\delta \varphi_a(x)}, \\ &= \int d^3x \pi_{0,a}(\mathbf{x}) \tilde{\varphi}_{0,a}(\mathbf{x}) + S_0[\varphi, \tilde{\varphi}] + S_{\text{int,cl}}[\varphi, \tilde{\varphi}] \end{aligned} \quad (2.68)$$

where $S[\varphi]$ is the classical action of Eq. (2.6). Let us also consider the integration over the initial conditions in the generating functional (2.38)

$$\begin{aligned} \int [d\varphi_0^+] [d\varphi_0^-] \langle \varphi^+ | \rho_0 | \varphi^- \rangle &= \int [d\varphi_0] [d\tilde{\varphi}_0] \langle \varphi_0 + \tilde{\varphi}_0/2 | \rho_0 | \varphi_0 - \tilde{\varphi}_0/2 \rangle \\ &= \int [d\varphi_0] [d\tilde{\varphi}_0] [d\pi_0] W[\varphi_0, \pi_0] e^{i \int d^3x \pi_{0,a}(\mathbf{x}) \tilde{\varphi}_{0,a}(\mathbf{x})}, \end{aligned} \quad (2.69)$$

where we have introduced the (Wigner) distribution functional $W[\varphi_0, \pi_0]$ of fields at initial time t_0 , which is the Fourier transform of the original initial density. With these ingredients, the generating functional (2.38) reads

$$Z[J, R; \rho_0] = \int [d\varphi_0] [d\pi_0] W[\varphi_0, \pi_0] \int \mathcal{D}'\varphi \mathcal{D}\tilde{\varphi} e^{i \int_{t_0} d^4x \tilde{\varphi}_a(x) \frac{\delta S[\varphi]}{\delta \varphi_a(x)} + S_{\text{int,qu}}[\varphi, \tilde{\varphi}] + \text{sources}}, \quad (2.70)$$

with source terms⁸

$$\text{sources} = i \int_{t_0} d^4x \left(\varphi_a(x) \tilde{J}_a(x) + \tilde{\varphi}_a(x) J_a(x) \right) + \text{bilinear source terms}. \quad (2.71)$$

One observes that if the quantum vertex $S_{\text{int,qu}}[\varphi, \tilde{\varphi}]$ were absent, one could analytically integrate

$$\int \mathcal{D}\tilde{\varphi} e^{i \int_{t_0} d^4x \tilde{\varphi}_a(x) \frac{\delta S[\varphi]}{\delta \varphi_a(x)}} = \delta \left[\frac{\delta S[\varphi]}{\delta \varphi} \right], \quad (2.72)$$

which yields a Delta-functional with the classical equation of motion $\delta S/\delta \varphi = 0$ in Eq. (2.7). Leaving the quantum vertex out is essentially the classical approximation. Up to a Jacobian that plays the role of an irrelevant normalization constant [97], one can rewrite the Delta functional to $\delta[\varphi - \varphi^{\text{cl}}]$. This leads to the classical generating functional

$$Z^{\text{cl}} = \int [d\varphi_0] [d\pi_0] W[\varphi_0, \pi_0]_{|\varphi=\varphi^{\text{cl}}}. \quad (2.73)$$

Then one can compute the classical-statistical average of an observable $O[\varphi, \pi]$ as a phase-space average over field trajectories given by solutions of the classical field equation

$$\langle O[\varphi, \pi] \rangle_{\text{cl}} = \int [d\varphi_0] [d\pi_0] W[\varphi_0, \pi_0] O[\varphi^{\text{cl}}(\varphi_0, \pi_0), \pi^{\text{cl}}(\varphi_0, \pi_0)]. \quad (2.74)$$

Finally we want to understand the range of validity of this approximation. The classical and quantum vertices of Eq. (2.66) are illustrated in Fig. 2.2 a). While the full quantum theory has both vertices, the quantum vertex is absent in the classical-statistical approximation, which implies that also some Feynman diagrams are missing. Since the vertices mainly differ in their types of legs, we need to obtain the correlation functions connecting these legs. They can be obtained by functional derivatives of the generating functional for connected correlation functions $W[J, R] = -i \ln Z[J, R]$ with respect to the sources in Eq. (2.71)

$$\begin{aligned} F_{ab}(x, y) &= \left. \frac{\delta^2 iW[J, R]}{\delta i\tilde{J}_a(x) \delta i\tilde{J}_b(y)} \right|_{J=\tilde{J}=0}, & -iG_{ab}^R(x, y) &= \left. \frac{\delta^2 iW[J, R]}{\delta i\tilde{J}_a(x) \delta iJ_b(y)} \right|_{J=\tilde{J}=0}, \\ -iG_{ab}^A(x, y) &= \left. \frac{\delta^2 iW[J, R]}{\delta iJ_a(x) \delta i\tilde{J}_b(y)} \right|_{J=\tilde{J}=0}, & \tilde{F}_{ab}(x, y) &= \left. \frac{\delta^2 iW[J, R]}{\delta iJ_a(x) \delta iJ_b(y)} \right|_{J=\tilde{J}=0} = 0. \end{aligned} \quad (2.75)$$

Here $F_{ab}(x, y)$ is the statistical correlation function of Eq. (2.34), the anomalous propagator $\tilde{F}_{ab}(x, y)$ is zero for vanishing sources, $G_{ab}^R(x, y) = \theta(x^0 - y^0) \rho_{ab}(x, y)$ is the retarded propagator, $G_{ab}^A(x, y) = G_{ba}^R(y, x)$ is the advanced propagator and $\rho_{ab}(x, y) = G_{ab}^R(x, y) - G_{ab}^A(x, y)$

⁸While source terms are important for computations of correlation functions via functional derivatives, we consider only closed systems with vanishing external sources in this work. Therefore, we neglect them in the following presentation for simplicity but include the sources when taking functional derivatives with respect to them.

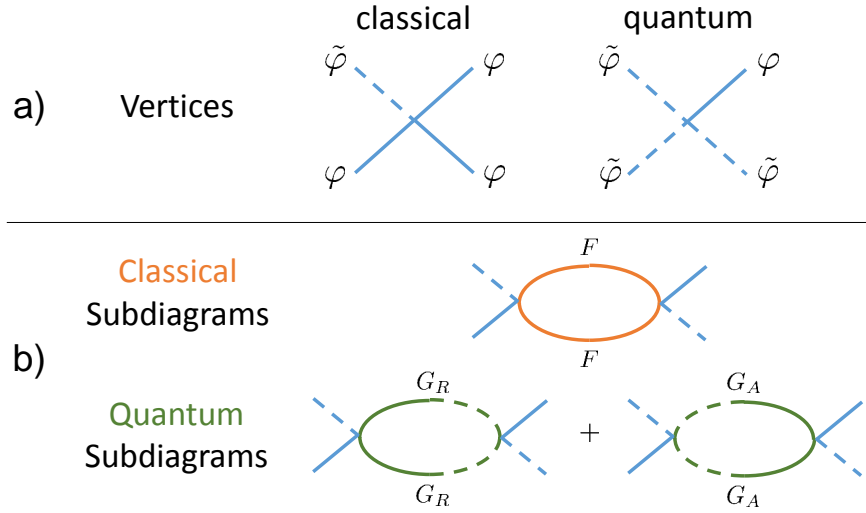


FIGURE 2.2: **a)** Illustration of the classical and quantum vertices $S_{\text{int,cl}}$ and $S_{\text{int,qu}}$ as defined in Eq. (2.66). **b)** Possible sub-diagrams (of Feynman diagrams) with full propagators and identical external legs. The classical-statistical approximation only involves the classical sub-diagram while the quantum sub-diagrams are missing.

is the spectral function of Eq. (2.34). Hence, F connects to φ legs while G^R and G^A connect a φ leg with a $\tilde{\varphi}$ leg.

Some typical sub-diagrams that involve two vertices are shown in Fig. 2.2 b) together with the connecting correlation functions. These are all existing one-loop sub-diagrams with these external legs and they all have to be summed over when entering a Feynman diagram. The quantum diagrams involve one quantum vertex and are therefore absent in the classical approximation. Hence, one condition for the validity of the classical approximation is $F^2(x, y) \gg (G^R)^2(x, y) + (G^A)^2(x, y)$, with $F^2(x, y) = F_{ab}(x, y)F_{ab}(x, y)$. Because of $G_{ab}^R(x, y)G_{ab}^A(x, y) = 0$, this ‘classicality’ condition can be stated as

$$F^2(x, y) \gg \rho^2(x, y). \quad (2.76)$$

We can restate this condition also for the distribution function as defined in Eq. (2.60) from the statistical propagator in Fourier space $F(p^0, \mathbf{p}, x^0)$. As we showed, this definition is equivalent to the other definitions of the distribution function of Sec. 2.2.2 for a quasi-free spectral function (2.58). We find from the ‘classicality’ condition (2.76) with an isotropy assumption $F_{ab} \approx F \delta_{ab}$ and $\rho_{ab} \approx \rho \delta_{ab}$ the corresponding condition for the distribution function

$$f(\mathbf{p}, x^0) \gg \frac{1}{2}. \quad (2.77)$$

The classical-statistical approximation is only valid at weak couplings $\lambda \ll 1$ since otherwise occupancies become quickly of order unity, violating the ‘classicality’ condition [120]. This condition has been verified in detail by comparing quantum to classical-statistical results in the context of scalar quantum field dynamics [7, 11, 88, 100] and coupled to fermions [85, 86].

2.3.2 Numerical algorithm and lattice setup

In classical-statistical simulations, one discretizes the fields $\varphi_a(\mathbf{x}, x^0)$ and their conjugate momentum fields $\pi_a(\mathbf{x}, x^0)$ on a spatial lattice, and similarly for gauge fields (see App. B for more details). The algorithm we use proceeds along the following steps:

1. The fields and conjugate momenta are randomly initialized at time t_0 according to the (Gaussian) Wigner distribution functional $W[\varphi_0, \pi_0]$.
2. Solve the classical equations of motion to get classical fields $\varphi_a^{\text{cl}}(\mathbf{x}, x^0)$ and $\pi_a^{\text{cl}}(\mathbf{x}, x^0)$ at later times $x^0 > t_0$.
3. Repeat steps 1 and 2 to get an ensemble of classical fields $\varphi_a^{\text{cl}}(\varphi_0, \pi_0)$, $\pi_b^{\text{cl}}(\varphi_0, \pi_0)$ distributed according to the initial field distribution $W[\varphi_0, \pi_0]$.

Observables can be determined at any time of interest by performing the classical-statistical averaging in Eq. (2.74). It can be computed by a classical-statistical ensemble average

$$\langle O[\varphi, \pi] \rangle_{\text{cl}} \approx \frac{1}{N_{\text{samp}}} \sum_{(\varphi_0, \pi_0)} O[\varphi^{\text{cl}}(\varphi_0, \pi_0), \pi^{\text{cl}}(\varphi_0, \pi_0)], \quad (2.78)$$

where N_{samp} is the number of samples in the ensemble.

Apart from the sample average, one can also use symmetries of the system for the averaging procedure. For instance, spatial homogeneity can be employed to compute the stress energy tensor by additionally averaging over the volume

$$\langle T_{\mu\nu} \rangle_{\text{cl}}(x^0) = \langle \langle T_{\mu\nu}(\mathbf{x}, x^0) \rangle_V \rangle_{\text{cl}}. \quad (2.79)$$

Similarly, we can use isotropy in momentum space to average over the directions of momenta \mathbf{p}/p . In the expanding case, we then average over transverse directions \mathbf{p}_T/p and over the sign of ν . This can be applied for the computation of correlation functions

$$\begin{aligned} F(p, t) &= \langle F(\mathbf{p}, t) \rangle_{\mathbf{p}/p} \quad \text{static} \\ F(p_T, \nu, \tau) &= \langle F(\mathbf{p}_T, \nu, t) \rangle_{\mathbf{p}_T/p_T, \text{sgn}(\nu)} \quad \text{expanding}, \end{aligned} \quad (2.80)$$

and from them for the distribution functions $f(p, t)$ or $f(p_T, p_z, \tau)$, respectively. Averaging over symmetries considerably reduces the number of samples needed to get results with high accuracy. Even single-run simulations on large lattices can yield accurate results for many observables. The reason is that the system exhibits self-averaging, where the relative variance of an observable decreases with growing volume [116], which has been previously discussed in condensed matter systems [125–129]. The concept of ergodicity is closely related to self-averaging, with the difference that observables are averaged over some extended time window

instead of the volume. If not stated otherwise, we show simulation results obtained from $N_{\text{samp}} = 1, 2$ samples on large lattices. To simplify the notation, we will drop the index cl and we will imply with $\langle \cdot \rangle$ both a classical ensemble average and an average over symmetries.

Our real-time simulations are performed on three-dimensional spatial lattices of the size $N_1 \times N_2 \times N_3$ with lattice spacings a_i , $i = 1, 2, 3$ and periodic boundary conditions. Spatial coordinates are given by $x^i = a_i n_i$ with numbers $n_i = 0, \dots, N_i - 1$. We stick to the coordinate mapping of Sec. 2.1.1 with $x^0 \mapsto t$, $x^3 \mapsto z$ for the Minkowski and $x^0 \mapsto \tau$, $x^3 \mapsto \eta$ for the Bjorken expanding case. To account for the different geometry of the latter, we distinguish between transverse and longitudinal directions $N_1 = N_2 = N_T$ with $a_1 = a_2 = a_T$ and $N_3 = N_\eta$ with $a_3 = a_\eta$, while we use cubic lattices N_s^3 with spacings $a_i = a_s$ in the static case. In addition, we parallelize our computations by splitting the lattice along the N_3 direction. We have explicitly checked that our results are insensitive to changes of the discretization parameters.

2.3.3 Scalar fields on a lattice

We provide here details of our numerical implementation of scalar field theory on a real-time lattice. Similar implementations have been used in the literature [8, 106, 119, 121].

We initialize the scalar fields at initial time t_0 (or τ_0) according to their mode expansion in analogy to the quantum case in Eq. (2.54)

$$\begin{aligned} \varphi_b(\mathbf{x}, t_0) &= \phi_b(t_0) + \int \frac{d^3 \tilde{\mathbf{p}}}{(2\pi)^3} (\alpha_{b, \tilde{\mathbf{p}}} \xi_{\tilde{\mathbf{p}}}(t_0) e^{i\tilde{\mathbf{p}}\mathbf{x}} + \alpha_{b, \tilde{\mathbf{p}}}^* \xi_{\tilde{\mathbf{p}}}^*(t_0) e^{-i\tilde{\mathbf{p}}\mathbf{x}}) \\ \pi_b(\mathbf{x}, t_0) &= \pi_b(t_0) + \sqrt{-g(t_0)} \int \frac{d^3 \tilde{\mathbf{p}}}{(2\pi)^3} (\alpha_{b, \tilde{\mathbf{p}}} \partial_0 \xi_{\tilde{\mathbf{p}}}(t_0) e^{i\tilde{\mathbf{p}}\mathbf{x}} + \alpha_{b, \tilde{\mathbf{p}}}^* \partial_0 \xi_{\tilde{\mathbf{p}}}^*(t_0) e^{-i\tilde{\mathbf{p}}\mathbf{x}}), \end{aligned} \quad (2.81)$$

where $\tilde{\mathbf{p}}$ are the conjugate momenta of the spatial coordinates (see footnote 6 in Sec. 2.2.2).⁹ As discussed in App. A, we take the initial mode functions $\xi_{\tilde{\mathbf{p}}}(t_0)$ as solutions of the free equations of motion.

The functions $\alpha_{b, \tilde{\mathbf{p}}}$ and $\alpha_{b, \tilde{\mathbf{p}}}^*$ are the classical-statistical versions of the quantum ladder operators at initial time $a_{b, \tilde{\mathbf{p}}}(t_0)$ and $a_{b, \tilde{\mathbf{p}}}^\dagger(t_0)$. Since in the classical approximation the corresponding

⁹To stay close to the continuum expressions, we will stick to the continuum notation for the integrals in the discretized theory. Since we have a finite volume and finite lattice spacings, spatial coordinates and Fourier modes are discrete, and the integrals and Delta functions are mapped to

$$\int d^3 x \mapsto a^3 \sum_{\mathbf{x}}, \quad \int \frac{d^3 \tilde{\mathbf{p}}}{(2\pi)^3} \mapsto \frac{1}{V} \sum_{\tilde{\mathbf{p}}}, \quad \delta(\mathbf{x} - \mathbf{y}) \mapsto \frac{1}{a^3} \delta_{\mathbf{x}, \mathbf{y}}, \quad (2\pi)^3 \delta(\mathbf{p} - \mathbf{q}) \mapsto V \delta_{\mathbf{p}, \mathbf{q}}, \quad (2.82)$$

with $a^3 = a_1 a_2 a_3$ and volume $V = N^3 a^3$.

functions commute, the anti-commutators of the ladder operators are mapped to simple products. We demand that these functions satisfy the relation¹⁰

$$\langle \alpha_{a,\tilde{\mathbf{p}}}^* \alpha_{b,\tilde{\mathbf{p}'}} \rangle = \left(f(\mathbf{p}, t_0) + \frac{1}{2} \right) (2\pi)^3 \delta_{ab} \delta(\tilde{\mathbf{p}} - \tilde{\mathbf{p}'}), \quad (2.83)$$

which is the classical analogy of Eq. (2.49), and additionally spatial homogeneity has been used. We also demand that the anomalous occupation numbers vanish

$$\langle \alpha_{a,\tilde{\mathbf{p}}} \alpha_{b,\tilde{\mathbf{p}'}} \rangle = \langle \alpha_{a,\tilde{\mathbf{p}}}^* \alpha_{b,\tilde{\mathbf{p}'}}^* \rangle = 0, \quad (2.84)$$

such that the definitions of the distribution function (2.47) and (2.49) become equivalent at initial time (see Eq. (2.56)) to get a reasonable quasi-particle definition. To satisfy the conditions (2.83) and (2.84), we use Gaussian distributed random numbers multiplied by a random complex phase of unitary norm. The complex phase factors allow us to implement the $\delta(\tilde{\mathbf{p}} - \tilde{\mathbf{p}'})$ conditions in Eq. (2.83) and the conditions of Eq. (2.84) correctly. The Gaussian distributed random numbers ensure that all higher order n -point correlation functions at initial time are consistent with our Gaussian initial conditions.

For our simulations, we use the leapfrog algorithm where the classical fields $\varphi_a(\mathbf{x})$ and $\pi_a(\mathbf{x})$ are alternately updated according to a discretized version of the Hamilton equations of motion in Eq. (2.8). The coupling dependence can be conveniently scaled out of the equations with $\varphi \mapsto \varphi/\sqrt{\lambda}$ and $\pi \mapsto \pi/\sqrt{\lambda}$, thus entering only the initial conditions. We discretize the second spatial derivative according to the second-order central difference scheme

$$\partial_i^2 \varphi_a(\mathbf{x}) \mapsto a_i^{-2} \left(\varphi_a(\mathbf{x} + a_i \hat{i}) + \varphi_a(\mathbf{x} - a_i \hat{i}) - 2\varphi_a(\mathbf{x}) \right), \quad (2.85)$$

with the unit step \hat{i} into the i -direction. This leads to the discrete lattice momenta¹¹ $\tilde{p}_{i,\text{latt}}^2 = 4 \sin^2(\pi n_i/N_i)/a_i^2$. For the time derivatives of the fields we employ a forward Euler-scheme

$$\partial_0 \varphi_a(\mathbf{x}, x^0) \mapsto a_0^{-1} \left(\varphi_a(\mathbf{x}, x^0 + a_0) - \varphi_a(\mathbf{x}, x^0) \right). \quad (2.86)$$

We note that the conjugate momentum fields are shifted by $a_0/2$ with respect to the scalar fields. This, together with a small time step $a_0 \ll \sqrt{-g_{ii}} a_i$ for each spatial i , ensure the stability of the leapfrog algorithm. We use an adaptive time step with up to $a_0/(\sqrt{-g_{ii}} a_i) \leq 7\%$.

¹⁰When considering over-occupation initial conditions in Eq. (2.61), we drop the quantum 1/2 as discussed in Sec. 2.2.3.

¹¹The discrete Fourier transform is given by

$$\varphi_a(\tilde{\mathbf{p}}) = a^3 \sum_{\mathbf{x}} \varphi_a(\mathbf{x}) e^{-i\mathbf{x}\tilde{\mathbf{p}}_{\text{disc}}},$$

with the discrete momenta $\tilde{p}_{i,\text{disc}} = 2\pi n_i/(a_i N_i)$.

The statistical equal-time correlation function and its derivatives (2.46) can be computed in the classical approximation as

$$\begin{aligned} F(\tilde{\mathbf{p}}, x^0) &= (NV)^{-1} \langle \varphi_a(\tilde{\mathbf{p}}, x^0) \varphi_a^*(\tilde{\mathbf{p}}, x^0) \rangle, & \ddot{F}_{ab}(\tilde{\mathbf{p}}, x^0) &= (NV)^{-1} \langle \pi_a(\tilde{\mathbf{p}}, x^0) \pi_a^*(\tilde{\mathbf{p}}, x^0) \rangle, \\ \dot{F}_{ab}(\tilde{\mathbf{p}}, x^0) &= (NV)^{-1} \text{Re} \left(\langle \varphi_a(\tilde{\mathbf{p}}, x^0) \pi_a^*(\tilde{\mathbf{p}}, x^0) \rangle \right). \end{aligned} \quad (2.87)$$

The distribution function is computed with the same formula as in Eq. (2.47) in the quantum theory.

From the classical stress-energy tensor $T_{\mu\nu}$ in Eq. (2.9), we can compute the energy density ϵ and the transverse and longitudinal pressures P_T , P_L as

$$\epsilon(x^0) = \langle T^0_0 \rangle, \quad P_T(x^0) = -\frac{1}{2} \langle T^1_1 + T^2_2 \rangle, \quad P_L(x^0) = -\langle T^3_3 \rangle. \quad (2.88)$$

2.3.4 Nonrelativistic scalars on a lattice

Following a very similar argumentation as in Sec. 2.3.1, the nonequilibrium quantum dynamics of the highly occupied system can be accurately mapped onto a classical-statistical field theory evolution also for nonrelativistic scalar theories as long as $f \gg 1$ for typical momenta [100].¹² The numerical simulations are performed as discussed in Sec. 2.3.2. The classical equation of motion (2.11) of Sec. 2.1.3 is solved on a three-dimensional grid using a split-step method, and we refer to Refs. [23, 89] for further details.

Similarly to the relativistic case, we can define a distribution function $f(\mathbf{p}, t)$ with the help of the two-point correlation function for spatially homogeneous ensembles

$$F(\mathbf{x} - \mathbf{x}', t, t') = \frac{1}{2} \langle \psi(\mathbf{x}, t) \psi^*(\mathbf{x}', t') + \psi(\mathbf{x}', t') \psi^*(\mathbf{x}, t) \rangle. \quad (2.89)$$

Evaluated at equal times $t = t'$, we can define the distribution function for non-vanishing momenta [100]

$$f(\mathbf{p}, t) = \int d^3x e^{-i\mathbf{p}\mathbf{x}} F(\mathbf{x}, t, t). \quad (2.90)$$

As for scalar and gauge theories in Minkowski space-time, we consider spatially isotropic systems, which allows us to additionally average over the direction of the momentum.

¹²This approximation is also known as the truncated Wigner method in the nonrelativistic case.

Chapter 3

Nonthermal fixed points in Minkowski space-time

In this chapter, our main goal is to introduce the concepts of scaling regions, nonthermal fixed points (NTFP) and universality classes far from equilibrium. In Sec. 3.1 we provide the corresponding definitions and put special emphasis on their relations to other scaling phenomena in physics, in particular to renormalization group fixed points and wave turbulence.

With the help of classical-statistical lattice simulations, we discuss in Sec. 3.2 the thermalization process of non-expanding systems (in Minkowski space-time) in $d = 3$ spatial dimensions at the example of N -component scalar and non-Abelian gauge theories. We mainly focus on their nonthermal fixed points, especially on scaling regions at higher momenta. For scalar systems, we also discuss subtle differences between $N = 1$ and $N \geq 2$ theories with respect to their nonthermal fixed point. However, despite these subtleties, the scaling properties of the nonthermal fixed point for scalars are qualitatively independent of the number of components. Similarly, for non-Abelian $SU(N_c)$ gauge theories, no strong dependence on N_c for scaling phenomena is expected based on kinetic arguments and lattice simulations [102, 104, 130]. Therefore, we only simulate the $N_c = 2$ theory for simplicity.

We will mostly characterize nonthermal fixed points in terms of scaling properties of the distribution function $f(p, t)$ in this work. Boltzmann (also termed kinetic) equations describe the evolution of the distribution function. They have an overlapping range of validity with classical-statistical lattice simulations for occupation numbers in the range $1 \ll f \ll 1/\lambda$ [12, 13, 106], and equivalently for gauge theories with the substitution $\lambda \mapsto \alpha_s$. For this reason, kinetic equations are especially well suited to discuss nonthermal fixed points analytically [8, 104, 131]. Therefore, we introduce in Sec. 3.3 the framework of kinetic theory. We will discuss the scaling regions of Sec. 3.2 in this framework.

The sections 3.2 and 3.3 provide a systematic overview of nonthermal fixed points in non-expanding scalar and gauge theories and incorporate recent literature results. Important parts of this chapter are summarized in Sec. 3.4.

The techniques and concepts introduced in this chapter will be also used in the remainder of this work. A profound knowledge of nonthermal fixed points and the thermalization process in non-expanding media is important for the extension to dynamics of Bose-Einstein condensation (Chapter 4) and, in particular, when contrasted to longitudinally expanding scalar and gauge systems (Chapters 5 and 6).¹

3.1 Nonthermal fixed points

The thermalization process of closed quantum systems at weak couplings may be divided into several stages. In general, the evolution starts from an initial condition and flows into the thermal equilibrium state. Depending on the initial conditions, the stages in-between as well as the thermalization time may be very different. In Fig. 1.1 of the introduction we showed two possible ways to thermal equilibrium. Starting with initial conditions close to equilibrium, the system relaxes to the thermal state. In contrast, from far-from-equilibrium initial conditions, the system may approach a nonthermal fixed point before it eventually thermalizes [7, 8], leaving the fixed point solution.² The different lines collapsing to a single one close to the nonthermal fixed point symbolize the memory loss of the initial conditions. The subsequent evolution then mostly depends on conserved quantities such as energy density. This is the stage of the nonthermal fixed point, and it is the subject of this section. The transient dynamics that lead to this stage and the final thermalization will be discussed later.

Our main observable to describe a nonthermal fixed point in this work is the single-particle distribution $f(p, t)$, introduced in Sec. 2.2.2. We will classify universality classes far from equilibrium in terms of scaling properties of this function. Close to nonthermal fixed-points, the distribution function within an inertial momentum range follows a self-similar evolution. In this universal regime the distribution is then determined by a time-*independent* scaling function f_S , an overall scaling with time described by the scaling exponent α , and the exponent β for the scaling with momentum:

$$f(p, t) = t^\alpha f_S(t^\beta p). \quad (3.1)$$

¹We have published parts of the results and discussion of non-expanding systems presented here in Refs. [15, 118, 120].

²In this work, we only consider highly correlated initial conditions as in Sec. 2.2.3 with a large coherent field or large occupation numbers $f \gg 1$ for modes up to a characteristic momentum scale Q . These allow us to describe the dynamics in terms of classical-statistical fields (see Sec. 2.3.1). Another possibility for far-from-equilibrium initial conditions are very dilute systems with $f \ll 1$. They may also lead to scaling or turbulent behavior, as for instance in Refs. [104, 132] for non-Abelian plasmas. However, they are beyond the scope of this work.

Here, the time factors can be regarded dimensionless by mapping $t \mapsto Qt$ with a typical scale Q . The scaling exponents determine the scaling behavior of typical momentum $p_{\text{typ}} \sim t^{-\beta}$ within the scaling region and of the amplitude at typical momentum $f(p_{\text{typ}}) \sim t^\alpha$.

Depending on the evolution of typical momenta, scaling regions can be classified in terms of direct and indirect cascades. A negative exponent $\beta < 0$ signals increasing typical momenta and we will use the term direct cascade for this situation. Likewise, typical momenta decrease for $\beta > 0$, marking an inverse cascade.

Another possible property of a scaling region is a conservation law. Typically in static backgrounds, a scaling region conserves one quantity such as energy density or particle number density. The quantity is then conserved between any two co-moving momenta $t^{-\beta}p_1$ and $t^{-\beta}p_2$ within the scaling region. Such a conservation law leads to a relation between the scaling exponents α and β . Using Eq. (3.1), *particle number conservation*

$$\int_{t^{-\beta}p_1}^{t^{-\beta}p_2} d^d p f(p, t) = t^{\alpha-d\beta} \int_{p_1}^{p_2} d^d q f_S(q) = \text{const}, \quad (3.2)$$

with the substitution $q = t^\beta p$ leads to the relation

$$\alpha = d\beta, \quad \text{for particle number conservation} \quad (3.3)$$

in d spatial dimensions. Similarly, *energy conservation* for ultrarelativistic systems with quasi-particle energy $\omega(p) = p$ reads $\int_{t^{-\beta}p_1}^{t^{-\beta}p_2} d^d p p f(p, t) = \text{const}$, and enforces the relation

$$\alpha = (d+1)\beta, \quad \text{for energy conservation.} \quad (3.4)$$

The relations (3.3) and (3.4) cannot be satisfied simultaneously for nontrivial scaling exponents. Therefore, a scaling region in Minkowski space-time can only exhibit one of such conservation laws. Combined with the evolution of typical momenta, a scaling region describes the transport of a conserved quantity to the infrared or to the ultraviolet.

A nonthermal fixed point may consist of several scaling regions simultaneously. Each scaling region has its own set of scaling exponents and scaling function, and is located in some separate momentum region of the distribution function. The different regions can be distinguished by comparing their sets of scaling properties (α, β) and $f_S(p)$. Often their scaling functions $f_S(p)$ are so different that the distinction becomes directly visible in the distribution function at a fixed time.

Multiple scaling behavior can emerge as a consequence of multiple conservation laws such as the self-similar transport of a different conserved quantity in one regime compared to another. Another possible reason includes a change of the underlying dynamics, for example, from a

perturbative to a non-perturbative mechanism below a characteristic momentum scale. We will give examples for such situations below.

Theories, or more specifically the scaling regions of nonthermal fixed points, can be grouped into universality classes according to their scaling properties (α, β) and $f_S(p)$. This opens intriguing theoretical and experimental perspectives of accessing and testing universal properties of one theory by use of another theory within the same universality class. We will also find examples for universality classes far from equilibrium in this work.

The critical behavior of nonthermal fixed points appears in more general correlation functions like the statistical and spectral propagators $F(p^0, \mathbf{p}, t)$ and $\rho(p^0, \mathbf{p}, t)$. They are independent correlation functions out of equilibrium³ and their scaling behavior can be parametrized as [97, 133]

$$\begin{aligned} F(p^0, \mathbf{p}, t) &= t^{\alpha+2\beta z} F_S(t^{\beta z} p^0, t^\beta \mathbf{p}), \\ \rho(p^0, \mathbf{p}, t) &= t^{(2-\eta)\beta} \rho_S(t^{\beta z} p^0, t^\beta \mathbf{p}), \end{aligned} \quad (3.5)$$

with fixed point functions $F_S(x, y)$ and $\rho_S(x, y)$. These scaling relations introduce a nonequilibrium anomalous dimension η and the dynamic scaling exponent z . The latter emerges since rotational symmetry and frequencies may scale differently because of medium effects. The exponents α and β appearing in Eq. (3.5) are the same as in the scaling relation for the distribution function $f(p, t)$ in Eq. (3.1) for large occupation numbers $f \gg 1$. This can be seen from Eq. (2.60), which relates $F(p^0, \mathbf{p}, t)$ to the distribution function. While the relations (3.5) certainly provide more information about the nonthermal fixed point and pose less restrictions to its form, a description in terms of the distribution function $f(p, t)$ appears to be sufficient for most of our applications in this work, as we will explain in the following subsection. Possibilities to measure the additional exponent η are discussed in Sec. 4.2.3.

3.1.1 Relations to critical phenomena in thermal equilibrium

The study of critical phenomena has long since entered textbook level (e.g. [3–5]). Examples for critical phenomena are second order phase transitions, such as ferromagnetic or superfluid transitions, or transitions at a critical point of a phase diagram. Critical phenomena involve a diverging correlation length $\xi \sim |T - T_c|^{-\nu}$ and a similar power law evolution in $|T - T_c|$ for other observables such as the specific heat or susceptibilities. Since temperatures have to be close to the critical temperature T_c to observe such scaling phenomena, experimental set-ups require some fine-tuning of the parameters.

³These are the propagators of Eq. (2.34) Fourier transformed according to footnote 4. Their functional independence is discussed below Eq. (2.36).

Most importantly, the scaling exponents of the power law behavior (critical behavior) of observables are universal and can be studied theoretically with the renormalization group (RG) (e.g. [3–5]). It describes how the system evolves under the change of typical length (or energy) scales. In applications to critical phenomena, the correlation length ξ becomes the natural scale of the system. As the temperature T approaches the critical temperature T_c , the correlation length increases and microscopic details of the theory become less relevant. Eventually, only macroscopic scaling properties survive. This can be seen in the RG procedure, where the system “flows” to a fixed point. The RG fixed point involves the above mentioned scaling properties in $|T - T_c|$ for observables and is characterized by its critical exponents. We note that RG methods have also been applied to real-time phenomena and nonthermal fixed points [9, 134, 135].

A nonthermal fixed point can be understood as a far-from-equilibrium generalization of RG fixed points of critical behavior in thermal equilibrium. This becomes more obvious when we use the self-similar scaling relations for correlation functions (3.5) to obtain the equivalent relations for an arbitrary scaling parameter s [97, 117]

$$\begin{aligned} F(p_0, \mathbf{p}, t) &= s^{\alpha/\beta+2z} F(s^z p_0, s\mathbf{p}, s^{-1/\beta}t), \\ \rho(p_0, \mathbf{p}, t) &= s^{2-\eta} \rho(s^z p_0, s\mathbf{p}, s^{-1/\beta}t). \end{aligned} \quad (3.6)$$

In static critical phenomena, the exponent η is the anomalous scaling dimension of the propagator G due to field renormalization. The system is governed by the diverging correlation length ξ that describes typical spatial correlations of the system. Dynamic criticality extends the static case by additionally introducing a temporal correlation scale t_{relax} that quantifies the typical relaxation time of the system to the critical point. It diverges as $t_{\text{relax}} \sim \xi^z$ in the limit when $T \rightarrow T_c$, which implies the so called critical slowing down [6]. The corresponding spectral function can be written in Fourier space as

$$\rho(p_0, \mathbf{p}) = s^{2-\eta} \rho(s^z p_0, s\mathbf{p}) \quad \text{for dynamic criticality.} \quad (3.7)$$

Since one assumes that the system is close to the critical point, there is no nontrivial dependence on the (central) time coordinate t and its relaxation to equilibrium is characterized by the dynamic critical exponent z . For the same reason, the dynamic system exhibits a fluctuation-dissipation relation (2.36) that connects the correlation functions $F(p_0, \mathbf{p}, t)$ and $\rho(p_0, \mathbf{p}, t)$ such that they do not evolve independently.

In contrast, our far-from-equilibrium situation additionally contains a nontrivial (central) time direction t . In terms of the scaling behavior in Eq. (3.6), it can be characterized by the scaling exponent β . Moreover, the fluctuation-dissipation relation is not valid any more and $F(p_0, \mathbf{p}, t)$ evolves independently from $\rho(p_0, \mathbf{p}, t)$. This implies the additional scaling exponent α . Hence,

the scaling relations (3.6) are indeed a natural extension of the dynamic critical phenomena with scaling behavior (3.7).

In the on-shell limit, the spectral function is given by its quasi-free form (2.58) and is not explicitly time-dependent. Moreover, the anomalous dimension vanishes $\eta = 0$ while the dynamic exponent z characterizes the dispersion relation $\omega(\mathbf{p}) \sim |\mathbf{p}|^z$. Although we do not assume any on-shell approximation for the spectral function, deviations should be small from these values at large momenta. This is because kinetic descriptions, which involve an on-shell approximation, can accurately describe the evolution of the system for occupancies $f \ll 1/\lambda$, as has been shown in Refs. [8, 104] for scalar and gauge theories. We are therefore primarily interested in the scaling exponents α and β . These characterize the self-similar evolution of the distribution function in Eq. (3.1). Therefore, our main observable is the distribution function, which is sufficient to measure the scaling exponents α and β . However, in particular at low momenta, the exponents η and z may have nontrivial values because the spectral function may show deviations from its quasi-free form [7, 10, 118]. We will consider possible dependencies on these exponents in Sec. 4.2.3.

There are important practical differences between static or dynamic critical phenomena and nonthermal fixed points. One difference is that, while the temperature in critical phenomena needs to be adjusted close to the critical temperature T_c , a wide range of initial conditions leads to the same nonthermal fixed point in the far-from-equilibrium situation. This self-organized criticality does not require any fine-tuning.

The RG fixed points in thermal equilibrium can be grouped into universality classes, where different microscopic theories exhibit the same macroscopic scaling behavior. This static universality is based on general properties such as the dimension of the system, its symmetries and the range of the interaction. This concept was extended to dynamical systems close to the static RG fixed points [4, 6]. Static universality classes can then be further decomposed into smaller dynamic universality classes based on additional criteria such as conservation laws.

In our far-from-equilibrium situation of nonthermal fixed points, one may similarly classify self-similar scaling regions into universality classes. Then, despite different microscopic interactions or symmetries, systems may exhibit the same scaling properties and thus may become nearly indistinguishable. Such universality classes can indeed be found for scalar and gauge theories and will be reported in the remaining chapters. A consistent classification pattern of universality classes far from equilibrium has not been found yet for nonthermal fixed points and is a current topic of research.

3.1.2 Nonthermal fixed points and wave turbulence

Wave turbulence [8, 131] describes the transport of conserved quantities such as energy density through momentum space. The flux of the conserved quantity is independent of momentum within the turbulent region. Accordingly, in momentum space power-law cascades form. This can be either a ‘direct cascade’, for transport towards higher momenta, or an ‘inverse cascade’ into the infrared. In the inertial range of momenta, where the distribution function is described as a momentum power-law, one can write

$$f(p) \sim p^{-\kappa}, \quad (3.8)$$

with a spectral exponent κ specific to the underlying turbulence mechanism.⁴

Driven systems typically have a mechanism for in- and outflow of a conserved quantity (also called source and sink) and can be maintained in the critical state describing wave turbulence. In contrast, in isolated (closed) systems as in our case, the approach to a nonthermal fixed point (the attractor) can be regarded as self-organized criticality [136], i.e. without applied sources or sinks that could lead to stationary cascades. Therefore, the scaling function $f_S(p)$ is in general more complicated. However, in many situations one also finds an approximate power law in some part of the scaling region with the same spectral exponent κ as in the corresponding driven case.

This is the reason why originally, nonthermal fixed points in closed systems were often associated with wave turbulence. Various examples are provided in the literature [7–10, 22, 89, 92, 118, 120]. Since the dynamical relations (3.3) and (3.4) may be very different in driven systems [8], this link is not entirely clear so far.

⁴One can distinguish between weak and strong wave turbulence [8, 117]. If a perturbative mechanism can be used to explain the observed power law in Eq. (3.8), such turbulent behavior is called weak turbulence. This is usually possible for not too large occupation numbers $f \ll 1/\lambda$ [8, 131]. If the underlying mechanism requires a non-perturbative framework, as typically for very high occupancies $f \gtrsim 1/\lambda$, the observed behavior is called strong turbulence [7, 117]. One such example is an infrared scaling region in scalar systems that is based on a $1/N$ resummation of Feynman diagrams [7, 10].

3.2 Thermalization process in non-expanding systems

In this section, we consider the thermalization process of non-expanding scalar and gauge theories.⁵

Employing strongly correlated far-from-equilibrium initial conditions, such as over-occupation initial conditions in Eq. (2.61), we illustrated in Fig. 1.1 that the system may approach a nonthermal fixed point. A typical thermalization process of non-expanding systems for this situation is depicted in Fig. 3.1. After a short transient evolution, the system approaches the nonthermal fixed point. There self-similar dynamics sets in as described by Eq. (3.1). While the occupation numbers decrease, typical momenta p_{typ} grow. The system exhibits classical dynamics as long as the typical occupation numbers per mode are much larger than unity,

$$f(p, t) \gg 1, \quad (3.9)$$

as discussed in Sec. 2.3.1. If occupation numbers fall below unity, quantum processes will become important. We saw this in Sec. 2.3.1 in terms of correlation function F and ρ and this can also be seen in a Boltzmann transport framework where classical scattering processes are sub-leading to quantum ones for occupation numbers smaller than unity [12, 13].

The time scale t_{Quant} for entering the quantum regime is not a universal quantity and depends in general on the properties of the initial state as well as the dynamics in the classical regime. For the considered cases of large initial fields or large initial fluctuations at weak coupling, this time scale can be parametrically estimated by evaluating the condition $f(p_{\text{typ}}, t_{\text{Quant}}) \sim 1$. This leads to

$$t_{\text{Quant}} \sim Q^{-1} \lambda^{1/\alpha}, \quad (3.10)$$

where we used the self-similar form of the distribution function (3.1) during the classical scaling regime. Therefore, the range of validity of classical-statistical techniques in time is naturally confined to weak couplings. We note here that in general the use of classical-statistical methods at large couplings requires great care since genuine quantum effects may dominate the dynamics already at rather early times. This was investigated in detail in [120, 137], where artifacts such as negative occupation numbers and a strong sensitivity to the lattice cutoff were found. This is due to the Rayleigh-Jeans divergence in the classical theory, which can be understood as a consequence of the non-renormalizability of the classical-statistical approximation [11, 13, 138, 139].

Let us discuss the evolution of typical momenta. Here we define the typical momentum of the distribution as the momentum scale p_{typ} where the energy density is dominated, i.e. where

⁵Some parts of this section have entered our publications in Refs. [15, 120].

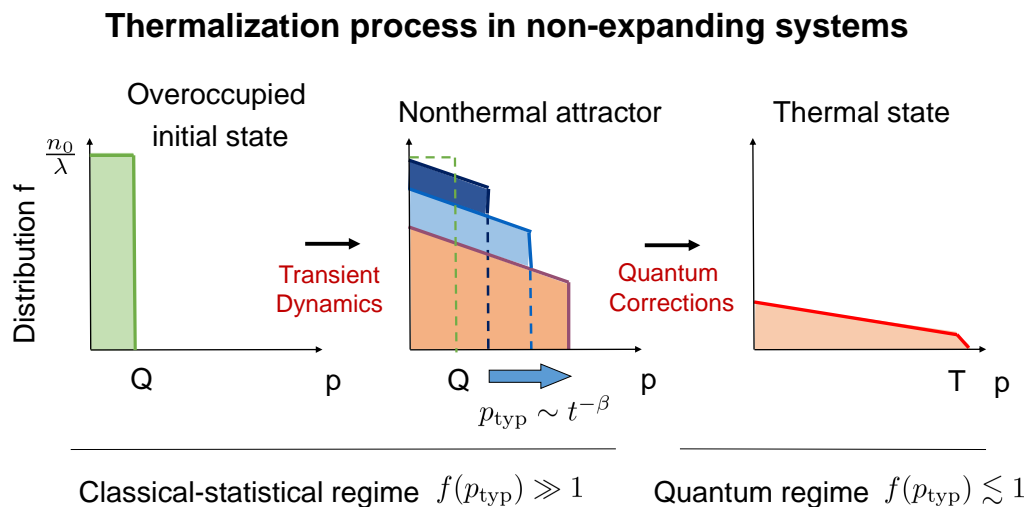


FIGURE 3.1: Illustration of a thermalization process in non-expanding systems. Starting from typical far-from-equilibrium initial conditions, the distribution function $f(p, t)$ approaches a nonthermal fixed point. When typical occupation numbers become of order unity, quantum corrections set in and drive the system to its thermal equilibrium.

$d\epsilon/dp$ has its maximum. Then we can estimate

$$\epsilon \propto \int d^3p \omega(p) f(p, t) \sim p_{\text{typ}}^4 f(p_{\text{typ}}, t) \sim \frac{n_0}{\lambda} Q^4. \quad (3.11)$$

In the last step we used energy conservation and an over-occupied initial state (2.61). The typical momentum can then be estimated as

$$p_{\text{typ}} \sim \sqrt[4]{\frac{\epsilon}{f(p_{\text{typ}}, t)}} \sim \lambda^{-1/4} Q \sqrt[4]{\frac{n_0}{f(p_{\text{typ}}, t)}}, \quad (3.12)$$

The decrease of the typical occupancy $f(p_{\text{typ}}, t)$ is thus correlated with the growth of the typical momentum. It stops growing when the quantum regime at $f \sim 1$ is reached. Since the thermal state $f^{\text{therm}}(p) = (\exp(\omega(p)/T) - 1)^{-1}$ is dominated by momenta of the temperature scale $\omega(p) \simeq p \sim T$, where one has $f^{\text{therm}}(T) \sim 1$, the temperature can be estimated with Eq. (3.12) as

$$T \sim \epsilon^{1/4} \sim \lambda^{-1/4} Q \gg Q. \quad (3.13)$$

Therefore, the typical momentum p_{typ} grows from the initial hard scale Q to the temperature scale T , and thermalization may occur parametrically on the time scale of t_{Quant} . In general, t_{Quant} can be regarded as the lower bound for the thermalization time.

Note that this simple analysis shows two more properties: We saw that the typical momentum needs to grow, which implies $\beta < 0$ in the scaling regime. This is the situation of a direct

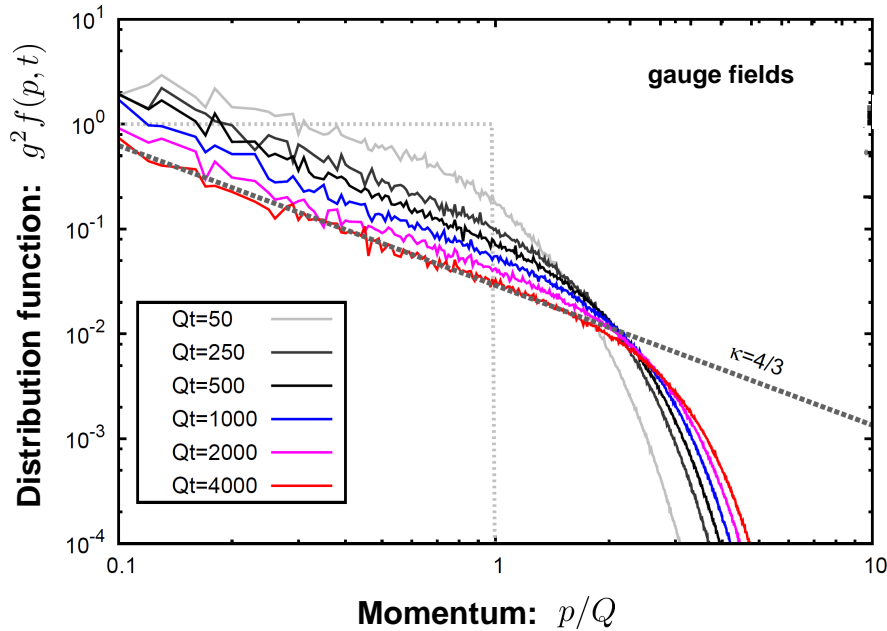


FIGURE 3.2: The distribution function of non-Abelian plasmas at different times. The initially over-occupied system (gray dashed line) quickly approaches a nonthermal fixed point and evolves in a self-similar way. The distribution can be described as an approximate $p^{-\kappa}$ power law up to a hard momentum, beyond which it decreases exponentially. Typical momenta increase, signaling a direct cascade that drives the thermalization process.

cascade. Moreover, we defined typical momenta to dominate the energy density. Because of its conservation law, one may expect that energy density is the conserved quantity transported in this cascade. Hence, for non-expanding systems, the dynamics at typical hard momenta is generally governed by a direct energy cascade.

3.2.1 Non-Abelian plasmas

Nonthermal fixed points in the thermalization process of non-Abelian plasmas in a static background were studied in Refs. [16–19] employing classical-statistical lattice simulations. Here we will use large lattices to review the results of such previous numerical studies.

We consider over-occupation initial conditions $f(p, 0) = \Theta(Q - p)/g^2$, which corresponds to initial amplitude $n_0 = 2$ in Eq. (2.61). We use a 256^3 lattice with lattice spacing $Qa = 1/4$. The evolution of the distribution function $f(p, t)$ is shown in Fig. 3.2. Starting from an over-occupied initial condition (gray dashed line), one observes how the spectrum quickly extends towards higher momenta. The spectrum at later times is well described by a power-law $p^{-\kappa}$ with $\kappa = 4/3$ for momenta $p \lesssim p_{\text{typ}}$, followed by a rapid (approximately exponential) fall-off. Note that this fall-off is part of the scaling region since we have $f(p, t) \gg 1$ for all momenta

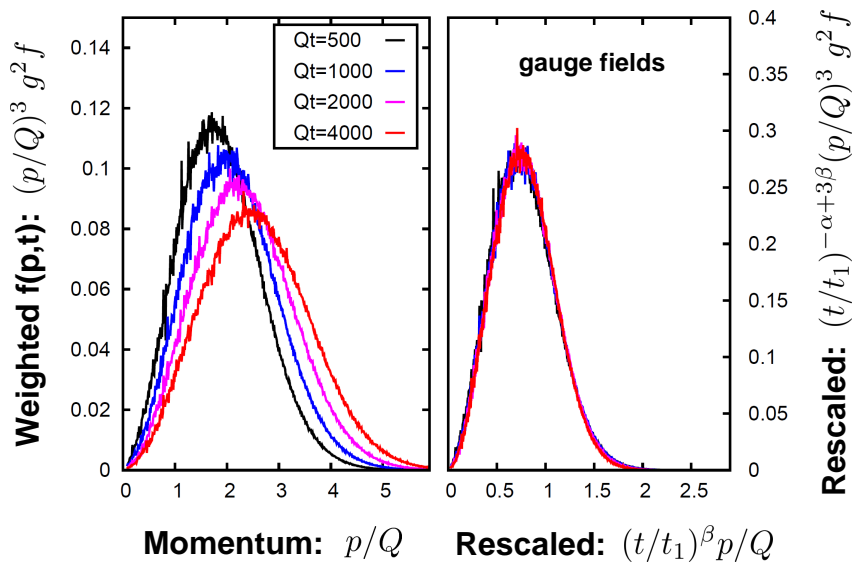


FIGURE 3.3: Shown is the weighted distribution $p^3 f$ at different times as a function of momentum. The original data is shown in the left panel while it is rescaled by powers of time on the right, with $Qt_1 = 1000$. The rescaled data collapses to a single stationary curve demonstrating self-similarity. For the scaling exponents, the values $\alpha = -4/7$ and $\beta = -1/7$ were employed.

shown in the plot for the weak coupling $g^2 = 10^{-6}$. We also note that the specific spectral exponent $\kappa = 4/3$ was associated with wave turbulence for transient times [16]. It was shown in Ref. [104] by use of a kinetic description (see Sec. 3.3.2) that it becomes $\kappa = 1$ at late times within the scaling regime.

In Fig. 3.2, one observes that the typical momenta grow with time while typical occupation numbers decrease. This is the situation of a direct cascade we discussed above and implies $\beta < 0$. We argued that for hard momenta, energy should be transported in the cascade, ultimately leading to thermalization. Energy conservation within the scaling region requires the relation $\alpha = 4\beta$ of Eq. (3.4), which has to be extracted from numerical results. Moreover, we need to show explicitly that the evolution is governed by a self-similar behavior.

To demonstrate the emergence of self-similarity in our simulations and to measure the scaling exponents, we follow Ref. [18] and study the time evolution of the single particle distribution weighted by powers of momentum. We consider the third power

$$f^{(3)}(p, t) = p^3 f(p, t), \quad (3.14)$$

which corresponds to the energy density per momentum mode $d\epsilon/dp$. The distribution $f^{(3)}(p, t)$ is shown in the left panel of Fig. 3.3 as a function of momentum at different times Qt of the

evolution. The peak of the distribution corresponds to the momentum scale p_{typ} that dominates the energy density of the system at a given time. One observes how the position of the peak moves towards higher momenta characterizing the transport of energy towards the ultraviolet as expected.

Self-similarity can be observed in the right panel of Fig. 3.3, where we show the weighted distribution $f^{(3)}(p, t)$ rescaled by powers of time. According to the self-similarity condition in Eq. (3.1) this quantity

$$t^{-\alpha+3\beta} f^{(3)}(p, t) = \tilde{p}^3 f_S(\tilde{p}) \quad (3.15)$$

yields a stationary distribution when plotted as a function of the rescaled momentum $\tilde{p} = t^\beta p$. This is indeed what we observe in the right panel of Fig. 3.3. With the choice

$$\alpha = -4/7, \quad \beta = -1/7, \quad (3.16)$$

the data obtained at different times of the evolution collapses onto a single curve. This is a manifestation of the self-similarity of the evolution. Moreover, the values of the scaling exponents match the requirements for a direct energy cascade. As we will further discuss in Sec. 3.3.2, the values for α and β can be understood from a kinetic description of non-Abelian plasmas in terms of elastic $2 \leftrightarrow 2$ and inelastic effective $2 \leftrightarrow 3$ scatterings.

According to Eq. (3.10), quantum fluctuations become important at

$$t_{\text{Quant}} \sim Q^{-1} \alpha_s^{-7/4}, \quad (3.17)$$

for a weak gauge coupling $\alpha_s = g^2/4\pi$. Then the system leaves the classical attractor and approaches thermal equilibrium [130].

We add two important remarks. Firstly, for early transient times of the evolution, non-Abelian plasmas have been observed to exhibit self-similar dynamics with different scaling properties than described above [17]. Instead of the spectral exponent $\kappa = 4/3$ in the scaling function $f_S(p) \sim p^{-\kappa}$, the exponent $\kappa = 3/2$ was measured. This exponent was explained in terms of wave turbulence in the presence of a condensate, with $2 \leftrightarrow (1 + \text{soft})$ scatterings dominating the dynamics, where ‘soft’ is associated with the condensate. Although we consider a closed system instead, in a recent study [101] the exponents $\alpha = -4/5$ and $\beta = -1/5$ were measured, which also can be understood from $2 \leftrightarrow (1 + \text{soft})$ scattering processes. This hints to the creation of a transient condensate that decays shortly afterwards. However, these values of the exponents are found only at early times and the system subsequently approaches the values given in Eq. (3.16).

Secondly, we have discussed the evolution of the distribution function only at hard momenta so far. From this we can also estimate the evolution of the Debye screening mass at leading

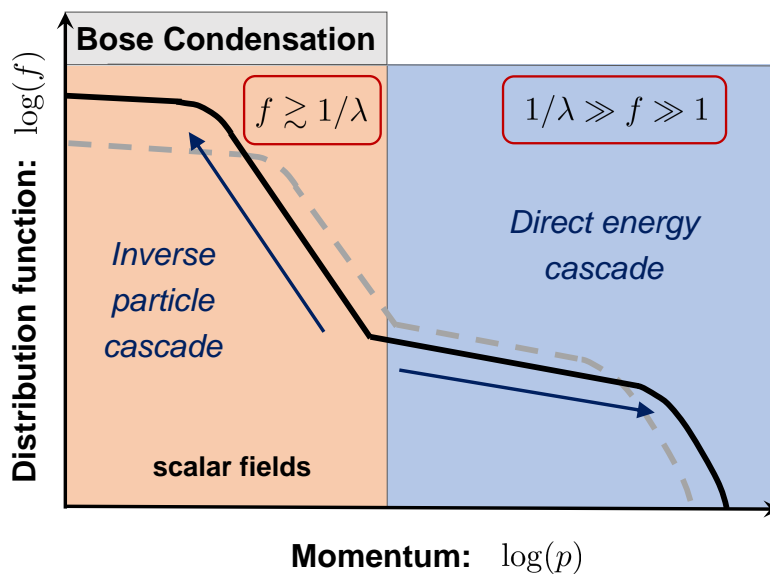


FIGURE 3.4: The distribution function f at different times of the scalar nonthermal fixed point. Dynamics are governed by a dual cascade with a direct energy cascade at hard momenta for $f \lesssim 1/\lambda$ and an inverse particle cascade at low momenta for $f \gtrsim 1/\lambda$. The gray dashed curve corresponds to an earlier time. Arrows indicate the cascade directions.

order perturbation theory [70]

$$m_D^2 = 4g^2 N_c \int \frac{d^3p}{(2\pi)^3} \frac{f(p, t)}{p} \sim t^{\alpha-2\beta} \sim t^{-2/7}. \quad (3.18)$$

This dynamically decreasing screening mass is a typical electric scale located at low momenta of the theory. Gauge-invariant quantities can be used to investigate the evolution of even softer scales. In Ref. [140] the authors recently computed spatial Wilson loops $W(t, A)$ with the enclosed area A and, assuming an area law for large distances $\langle \text{Tr}W(t, A) \rangle \propto \exp(-\sigma A)$, extracted the spatial string tension σ from it. This scale $\sqrt{\sigma}$ is of the order of the inverse magnetic screening length and constitutes a soft scale of the plasma below the screening mass. It was measured to scale as

$$\sigma \sim t^{-2/3}, \quad (3.19)$$

and was associated with the sphaleron transition rate, which is a topological quantity. This leads to the three characteristic scales $\sqrt{\sigma} \ll m_D \ll p_{\text{typ}}$ that are known so far. The dynamics of non-Abelian plasmas at low momenta is a current topic of research.

3.2.2 Relativistic scalars: scaling, cosmological context & basin of attraction

In relativistic scalar theories, the attractor of the nonthermal fixed point reveals a rich structure. Different from non-Abelian theories, the definition of the occupation numbers in scalar systems can be extended to low momenta [106] since no gauge-dependencies exist. This allows us to study infrared dynamics directly from the distribution function.

The fixed-point distribution is illustrated in Fig. 3.4 for a non-expanding $\mathcal{O}(N)$ -symmetric scalar field theory. Additionally to the direct energy cascade that drives the thermalization process [8, 21], it involves an inverse particle cascade [7, 9, 117]. The latter transports particle to soft momenta and thus occupies the zero mode of the system, leading to Bose-Einstein condensation far-from-equilibrium [89]. Hence, the scalar attractor can be described by a dual cascade.

We will discuss the infrared region in Chapter 4 in detail. Here we review the scaling region at hard momenta for not too large occupation numbers $f \ll 1/\lambda$. As shown in Ref. [8] using a very similar rescaling method as in Fig. 3.3 and Eq. (3.15), the distribution function indeed exhibits self-similarity (3.1) with the scaling exponents

$$\alpha = -4/5, \quad \beta = -1/5. \quad (3.20)$$

These values confirm that physics is governed by a direct energy cascade. The exponents can be associated with $2 \leftrightarrow (1 + \text{soft})$ scattering processes, where the soft particle is taken from the condensate [8]. We will review this in Sec. 3.3.1.

The stationary function $f_S(p)$ can be described by a power-law $p^{-\kappa}$ with $\kappa = 3/2$ for momenta $p \lesssim p_{\text{typ}}$, followed by a rapid exponential fall-off. Since in a double-logarithmic figure power laws appear as straight lines, this is also illustrated in Fig. 3.4. The spectral exponent $3/2$ is also found for wave turbulence in driven systems, where it can be associated to a $2 \leftrightarrow (1 + \text{soft})$ scattering process [8, 131]. This is why the authors of Ref. [8] called this thermalization scenario turbulent thermalization.

The thermalization process in a cosmological context

Turbulent thermalization was developed to describe the reheating process of the scalar inflaton field after cosmological inflation.⁶ According to this specific reheating scenario, the energy density at early times after inflation is stored in the large coherent field $\phi(t)$ for small self-coupling λ . These are exactly our coherent field initial conditions introduced in Eq. (2.62)

⁶Compare to Chapter 1, where we very briefly discussed inflationary cosmology.

of Sec. 2.2.3. In order to compare systems with different initial conditions, we define the characteristic energy scale

$$Q_\epsilon = \sqrt[4]{\lambda \epsilon / N}, \quad (3.21)$$

and note that for the considered initial conditions of Sec. 2.2.3, this scale is independent of the coupling constant.

The evolution equations for this reheating scenario are commonly formulated in conformal time and field variables [78, 121]. At sufficiently early times, the evolution equations in these new variables take the approximate form of equations of motion in a static background. As long as fluctuations are small, the coherent field follows its classical evolution equation

$$\left(\partial_t^2 + \frac{\lambda}{6N} \phi^2(t) \right) \phi(t) = 0, \quad (3.22)$$

where we assumed the massless case for simplicity and chose $\phi_a(t) = \phi(t)\delta_{a,1}$. Since this leads to $\phi(t)$ being a rapidly oscillating Jacobian elliptic function, we can also consider the behavior of the envelope of the maximum field amplitude $\bar{\phi}(t)$ as a function of time. For the subsequent evolution one can identify three characteristic periods in time, which are parametrically given as follows.

1. *Instability* for $0 \ll t \ll Q_\epsilon^{-1} \log(\lambda^{-1})$: In this resonant regime, the field $\phi(t)$ is a periodically oscillating function with frequency characterized by the initial rescaled field amplitude $\sigma_0 = \sqrt{\lambda/(6N)} \phi(t_0)$ and leads to the phenomenon of parametric resonance [79, 81]. In this instability mechanism, the initial amplitude also determines the initial resonance band in momenta for which an exponential growth of $f(p, t)$ can be observed [81].⁷ The rapid growth of fluctuations leads to strong non-linearities which broaden the resonance band and produce enhanced growth rates [87]. The instability regime ends when fluctuations are of order $f \sim 1/\lambda$, which occurs at $t \sim Q_\epsilon^{-1} \log(\lambda^{-1})$. At this time, the coherent field has considerably decayed into fluctuations and, as a consequence, a wide range of growing modes lead to a prethermalization of the equation of state at the end of this early stage [141–143], while the distribution function itself is still far from equilibrium.

2. *Nonthermal fixed-point* for $Q_\epsilon^{-1} \log(\lambda^{-1}) \ll t \ll Q_\epsilon^{-1} \lambda^{-5/4}$: In this regime, the distribution function becomes self-similar [8]. Elastic scattering processes dominate and a dual cascade forms in distinct momentum ranges: A direct energy cascade towards the ultraviolet modes [8] and an inverse particle cascade towards the infrared develop [7], as we have discussed above. This scaling regime ends when typical momenta are of order unity. According to Eq. (3.10)

⁷The resonance band is different for scalar theories with $N = 1$ and $N > 1$ components. While for $N = 1$ modes in a narrow resonance band around $p \approx 1.27\sigma_0$ are unstable, for $N > 1$ all modes between $0 \leq p \leq \sigma_0/\sqrt{2}$ are enhanced. However, both cases lead to nonlinearities and scaling behavior.

this occurs for

$$t_{\text{Quant}} \sim Q_\epsilon^{-1} \lambda^{-5/4}. \quad (3.23)$$

3. *Thermalization* for $t \gg Q_\epsilon^{-1} \lambda^{-5/4}$: In this regime elastic and inelastic processes lead to a Bose-Einstein distribution. This regime is beyond the range of validity of classical-statistical simulations. At sufficiently late times the classical evolution will always end up showing a classical thermal distribution with a temperature parameter T_Λ depending on the Rayleigh-Jeans cutoff Λ . The inability of the classical approach to describe this late-time thermalization stage has been studied in detail in the literature [11, 106].

The characteristic time scales are given as weak coupling parametric estimates for our purposes. In addition, some of the prefactors can be significantly different from one. For instance, the time scale for the end of the instability regime is more accurately given by $t \simeq (2\gamma_0)^{-1} \log(\lambda^{-1})$, where $\gamma_0 \simeq 0.033 Q_\epsilon$ for the single component scalar field theory [81] is the largest growth rate of the primary instabilities.

Basin of attraction for scalar nonthermal fixed point

As we argued above, both types of initial conditions of Sec. 2.2.3 lead to the same nonthermal attractor. We show this in Fig. 3.5 for the distribution function λf at the example of a single-component scalar field theory for three different initial conditions. Coherent field initial conditions (2.62) have a large macroscopic field $\sqrt{\lambda} \phi_0 = 2.21 Q_\epsilon$ with no initial fluctuations $f(p, 0) = 0$, while over-occupation initial conditions (2.61) were chosen with initial amplitudes $n_0 = 39$ as well as $n_0 = 7.5$. The characteristic scale Q_ϵ given by (3.21) is kept constant, thus fixing Q for given n_0 .⁸ While the single particle spectra are very different at initial time ($Q_\epsilon t = 0$), at late times the curves for all three distributions fall on top of each other. Hence, both types of initial conditions belong to the basin of attraction for this nonthermal fixed point.

A crucial property of the scaling regime is the strict independence of the scaling exponents α and β and the scaling function $f_S(p)$ from model parameters, such as the value of the coupling constant λ or the initial conditions such as the initial field value ϕ_0 . This is a powerful consequence of a fixed point and thus, of universality, which finds its manifestation in the self-similar behavior (3.1). The latter represents a reduction of the possible dependence of the dynamics on variations in time and momenta, since it states that $t^{-\alpha} f(p, t)$ only depends

⁸The simulations for the over-occupation initial conditions were performed on 256^3 lattices, while for the condensate driven initial condition we employ a 768^3 lattice. We checked that smaller lattices lead to the same observations. We use the lattice cutoff $\Lambda/Q_\epsilon = 15.3$, where we have verified that the results are insensitive to the cutoff. We employ a weak coupling $\lambda = 10^{-4}$.

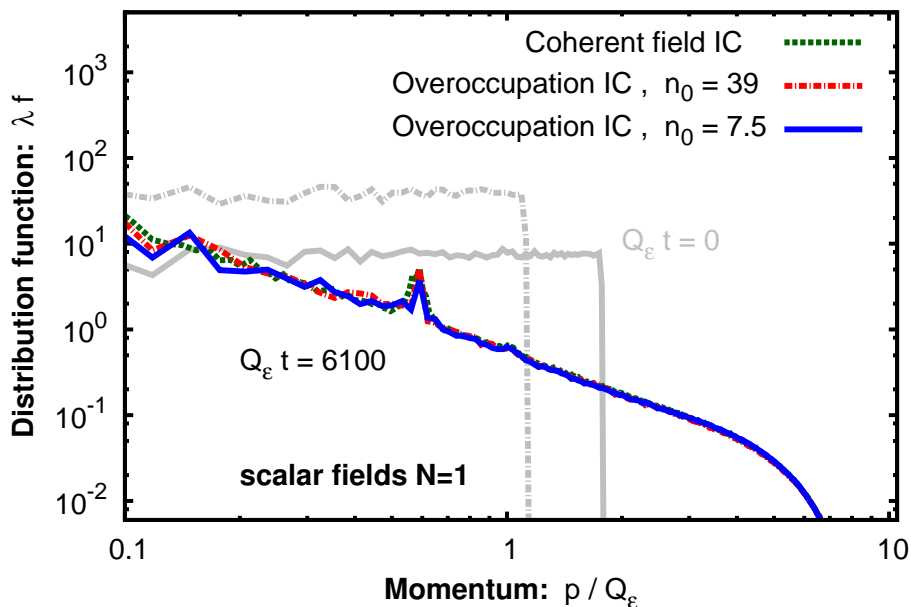


FIGURE 3.5: The distribution function λf for three different initial conditions with the same characteristic scale Q_ϵ . Gray curves show the systems at initial time while colored curves correspond to the later time $Q_\epsilon t = 6100$. One observes that the distribution function becomes independent of the initial conditions at the later time.

on the product $t^\beta p$ instead of separately depending on time and momenta. Therefore (3.1) represents a strong statement about the loss of information on the parameters of the underlying system already at this transient stage of the nonequilibrium time evolution.

3.2.3 $O(N)$ -symmetric scalar systems in more detail

The nonthermal fixed point of the $N = 1$ scalar system slightly differs from the generic attractor shown in Fig. 3.4, that is valid for all $N > 1$. Based on Ref. [144], we will review these subtle differences of the nonthermal fixed points for $N = 1$ and $N \geq 2$ scalar components.

Moreover, using large lattices, we will study the non-thermal fixed point for the $O(1)$ scalar theory.⁹ We will point out that the inverse particle cascade, which has so far only been established for $O(N)$ symmetric theories with $N \geq 2$ [7, 117, 146], also occurs for the single component theory. This finding directly complements the investigations of Refs. [8, 21], where the direct energy cascade has been studied for the single component theory while the phenomenon of a dual cascade was not considered.

The fixed point attractor in Fig. 3.4 shows the main features of the nonthermal fixed point in scalar field theories for all $N \geq 1$. While we discussed the properties of the direct energy cascade in Sec. 3.2.2, we will study the inverse particle cascade in Chapter 4. The case of

⁹Our results have been published in Ref. [120] and preliminary results have been included in [145].

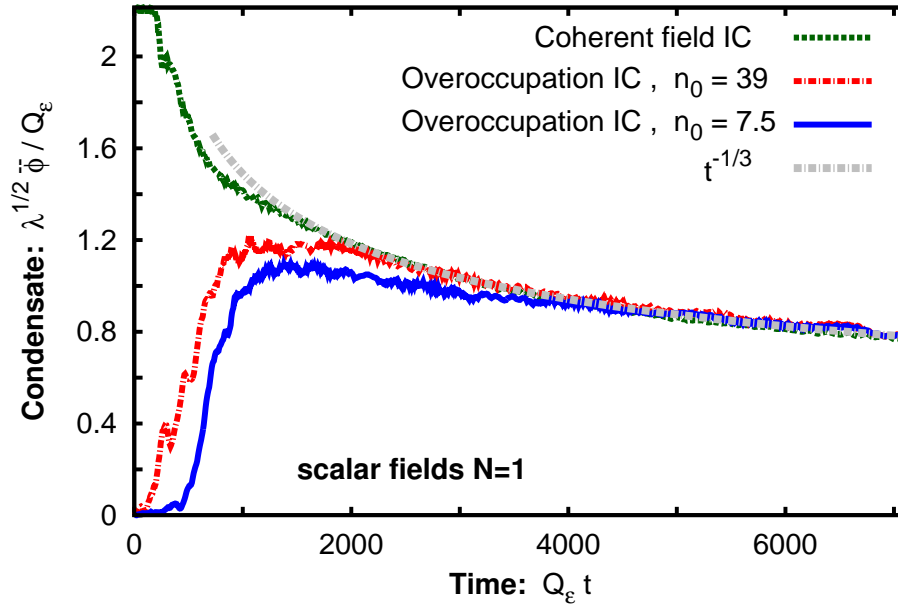


FIGURE 3.6: The condensate observable $\sqrt{\lambda} \bar{\phi}$ as a function of time for the $N = 1$ scalar theory with the initial conditions of Fig. 3.5. All curves collapse after some transient time, signaling the memory loss of details of the initial conditions. Their evolution can then be described by a $\sqrt{\lambda} \bar{\phi} \sim t^{-1/3}$ power law.

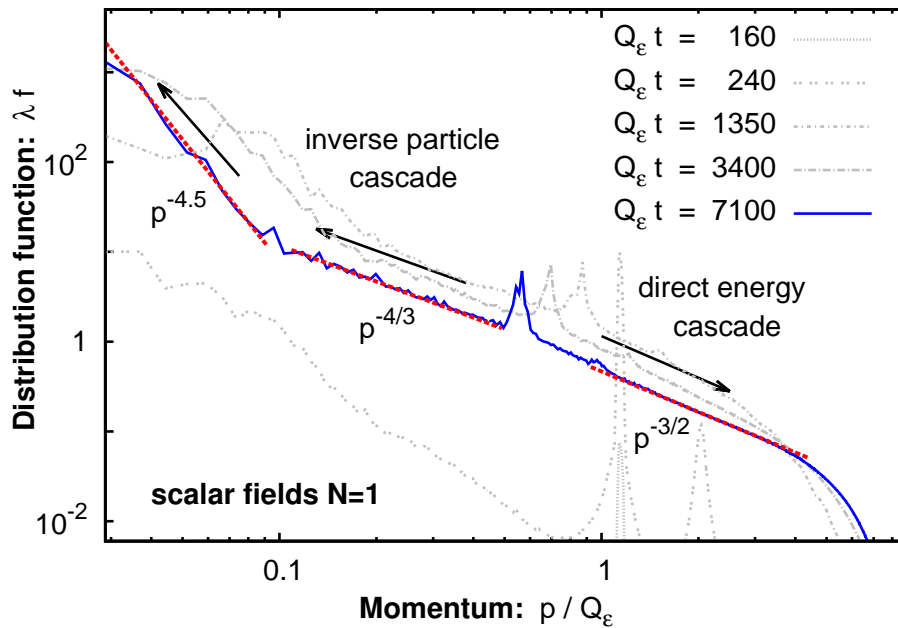


FIGURE 3.7: The distribution function λf at different times for a single-component scalar system with coherent field initial conditions. Power-laws with exponents $3/2$, $4/3$ and 4 are also shown as red dashed lines.

a single component scalar field theory ($N = 1$) is, however, special. It additionally involves more features than illustrated in the graphic.

To understand this difference, we consider the condensate that we define here as the absolute value $\phi_{\text{cond}} = \sqrt{\sum_a (\phi_{\text{cond}}^a)^2}$ of the spatially averaged fields $\phi_{\text{cond}}^a = \sum_x \varphi_a(\mathbf{x})/N_s^3$.¹⁰ Being a quickly oscillating function, we only consider its envelope $\bar{\phi}(t)$. We show its evolution in Fig. 3.6 for single-component scalar field theories for the same initial conditions and discretizations as in Fig. 3.5 above. For coherent field initial conditions, the condensate starts to decay at $t \sim Q_\epsilon^{-1} \log(\lambda^{-1})$, when the corrections from classical-statistical fluctuations change this behavior dramatically and trigger a transient rapid field decay. This happens when the size of fluctuations has grown such that their contribution to the energy density becomes comparable to that from the macroscopic field. At this stage the evolution becomes strongly non-linear and finally leads to a power-law decay of the field amplitude

$$\bar{\phi}(t) \sim t^{-\delta}, \quad (3.24)$$

with the observed exponent $\delta = 1/3$ [8] given by the gray dashed line in Fig. 3.6. When starting with over-occupation initial conditions, the condensate is formed by the inverse particle cascade, which will be studied in Chapter 4. More importantly, once the condensate is created, it starts to decay in Fig. 3.6 in the same way as for coherent field initial conditions in (3.24). Hence, this decay is not caused by a specific choice of initial conditions and is a property of the $N = 1$ scalar theory. Also note that the condensate $\bar{\phi}$ can be associated to the particle density of condensed particles n_c by the proportionality relation $n_c \propto \bar{\phi}^3$ [8], and hence, decay of $\bar{\phi}$ indeed results in a decay of $n_c \sim t^{-1}$.

In contrast, the condensate barely decays $\bar{\phi} \approx \text{const}$ for scalar theories with components $N > 1$, as was pointed out in Ref. [144]. To understand this, let us consider a local condensate that can be regarded as an inhomogeneous mean field $\phi_{\text{loc}}^a(\mathbf{x})$ without the (quasiparticle) fluctuations of the original field $\varphi_a(\mathbf{x})$. One could approximate it by local averaging $\phi_{\text{loc}}^a(\mathbf{x}) \approx \langle \varphi_a \rangle_{\Omega_{\mathbf{x}}}$ with areas of $\Omega_{\mathbf{x}}$ large enough to considerably reduce fluctuation effects while small enough to maintain the local inhomogeneities of the condensate.

The difference between $N = 1$ and $N > 1$ can now be understood by considering the evolution of the local condensate ϕ_{loc}^a and its time derivative $\dot{\phi}_{\text{loc}}^a$ at a fixed spatial point \mathbf{x} . We follow Ref. [144] for the following discussion. For $N = 1$ there is only a single field component ϕ_{loc} of the condensate and hence, the oscillations proceed in this field direction. For $N > 1$, there are more field directions and therefore, the condensate has more options to oscillate locally. These options are similar to different polarizations of a plane wave. One possibility is

¹⁰Note that this definition of the condensate only applies for single run results. Therefore, ϕ_{cond}^2 is a sum of the coherent field squared $\phi^2 = \langle \varphi \rangle^2$ and the zero mode of the statistical propagator $F(p=0)/V$. While the coherent field decays during the early instability stages of the evolution, a condensate is created in the zero mode. This condensation mechanism we will discuss in Chapter 4. For our purpose, we will not distinguish between these contributions to the condensate here.

that the field vector ϕ_{loc}^a is proportional to its derivative $\dot{\phi}_{\text{loc}}^a$ at every instant of time. This situation resembles a linearly polarized wave and is analogous to the $N = 1$ theory. Another possibility is that ϕ_{loc}^a and $\dot{\phi}_{\text{loc}}^a$ are orthogonal to each other such that the local amplitude $\bar{\phi}_{\text{loc}}$ remains approximately constant. This situation is similar to a circularly polarized plane wave. Analytical arguments [144] suggest that the circularly polarized condensate is energetically favored over a linear or, more generally, an elliptical polarization. Since circular motion carries an angular orbital momentum, the circular orbit of the local condensate carries a large local density of at least one of the conserved charges of the form $\sim \rho_{\text{loc}}^{ab} = \dot{\phi}_{\text{loc}}^a \phi_{\text{loc}}^b - \dot{\phi}_{\text{loc}}^b \phi_{\text{loc}}^a$. Because of global charge conservation, the volume average over the charges ρ_{loc}^{ab} is zero while they locally differ. Hence, the reason for the different evolution of the (global) condensate $\bar{\phi}$ is that the condensate locally carries a large conserved charge density for $N > 1$ that is absent for $N = 1$ [144, 146].

Let us now study the evolution of the distribution function of a single-component scalar system. We use coherent field initial conditions with the same parameters as in Fig. 3.6. Thus we will encounter the instability dynamics described in Sec. 3.2.2 at early times as well as direct consequences of the condensate decay. We show our results for the evolution of the distribution function¹¹ in Fig. 3.7. At early times $Q_\epsilon t = 160$ and 240 one observes the resonance behavior of the instability stage for $N = 1$. The resonance peak occurs first around $p_*/Q_\epsilon \approx 1.1$ and its location is proportional to the amplitude of the condensate at early times, $p_* = 0.52\sqrt{\lambda}\phi_0$ [81].

A major difference to $N > 1$ cases is that a ‘bump’ remains also at later times during the nonthermal fixed-point stage of the evolution approximately at the same location as the previous resonance peak. Its location is also proportional to the condensate $\bar{\phi}$ and is thus shifted to softer momenta as the condensate decays [8]. The ‘bump’ serves as a source for energy and particles, leading to momentum-scale invariant energy and particle fluxes towards the ultraviolet and the infrared, respectively, which manifests itself in different momentum power laws to the left and to the right of the still visible ‘bump’ in Fig. 3.7. Remarkable, it is this very situation of wave turbulence that we mentioned in Sec. 3.1.2, however, now in an isolated system far from equilibrium. In this case, wave turbulence is a consequence of the additional ‘bump’ acting like a source in the system.

On the double logarithmic plot the power-laws are well described by straight lines with different slopes, corresponding to different values of the spectral power law exponent κ of Eq. (3.8) in distinct momentum ranges. The spectrum at $Q_\epsilon t = 7100$ is compared to three power laws with the exponents

$$\kappa_S = 4.5, \quad \kappa_M = \frac{4}{3}, \quad \kappa_H = \frac{3}{2}. \quad (3.25)$$

¹¹In order to display the whole inverse particle cascade, we used rather large lattices up to 768^3 . Moreover, to cover the entire range of momenta shown in Fig. 3.7, we actually combined the data from two simulations with different lattice cutoffs $\Lambda/Q_\epsilon = 10.2$ and $\Lambda/Q_\epsilon = 15.3$. In the overlapping momentum regions the two simulations agree to very good accuracy. We emphasize that this is only done for presentational purposes.

The hard scale exponent $\kappa_H = 3/2$ describes the energy cascade towards higher momenta and results from effective $2 \leftrightarrow (1 + \text{soft})$ processes involving the condensate [8, 21]. The inverse particle cascade towards lower momentum modes shows two distinct momentum regimes depending on the size of the occupation numbers $f(p)$ in each regime. For $\lambda f(p) \lesssim \mathcal{O}(1)$ the weak wave turbulence exponent $\kappa_M = 4/3$ describes the transport of particles [8]. This is another difference of the $N = 1$ theory since this turbulent region between the ‘bump’ and the steep power law at low momenta is absent in theories with $N > 1$ since this ‘bump’ is also absent there. In the non-perturbative regime of ultrasoft momenta where $\lambda f(p) \gtrsim \mathcal{O}(1)$, the steep power law with exponent $\kappa_S = 4.5$ is part of a more general stationary function $f_S(p)$ that flattens considerably towards the deep infrared, as we will discuss in Sec. 4.1. This region is common to all $N \geq 1$ theories and has been depicted above in Fig. 3.7.

We emphasize that the entire inverse particle cascade, which is described by κ_M and the scaling function $f_S(p)$ in the non-perturbative regime, can be understood in terms of elastic processes only. We note that while the perturbative region with κ_M can be understood in wave turbulence from the leading $2 \leftrightarrow 2$ scattering collisions term, the dynamics in the enhanced region is a consequence of an emergent effective scattering matrix element for $2 \leftrightarrow 2$ processes, which can be described in terms of a momentum dependent effective coupling $\lambda_{\text{eff}}(p)$ [7, 89, 117]. This vertex-resummation is based on a systematic large- N expansion to next to leading order of the 2PI effective action for the N -component scalar quantum field theory. Therefore, it is remarkable that one finds this predicted region also for the single-component field theory.

We finally note that in Ref. [144] the emergence of the ‘bump’ and the condensate decay of the $N = 1$ theory are studied analytically. It is argued that number changing $4 \rightarrow 2$ processes, where the incoming particles are soft and the outgoing ones are at larger momenta, may be the main reason for this decay. Parametric estimates show that the condensate is expected to decay to particles at the location of the ‘bump’ in the distribution. This is different for $N > 1$ where the $4 \rightarrow 2$ processes cannot consist of 4 soft incoming particles because of charge conservation. Instead, one of the incoming particles has to be from the remaining spectrum. This has two consequences. The condensate decay rate is strongly suppressed compared to the $N = 1$ case. Moreover, the scattering region for outgoing particles is not bound to a narrow momentum range any more, which explains the absence of the ‘bump’ for $N > 1$.

3.3 Nonthermal fixed points from kinetic theory

In this section we choose an analytic approach to nonthermal fixed points in non-expanding media based on kinetic descriptions. These have an overlapping range of validity with classical-statistical simulations for $1 \ll f \ll 1/\lambda$, and similar for gauge theories with the substitution $\lambda \mapsto \alpha_s$ [12, 13, 104]. In Refs. [8, 131, 147] perturbative kinetic theory has been successfully applied to explain the self-similar evolution close to nonthermal fixed points as well as in the context of wave turbulence. This review gives further insight into the above discussion of nonthermal fixed points in scalar and gauge theories. It also sets the stage for non-perturbative extensions of the kinetic framework for scalar field theory in Sec. 4.2 that account for large occupancies that typically occur at low momenta.

In a kinetic framework, the dynamics is formulated in terms of the single-particle distribution function $f(\mathbf{p}, t)$. The latter obeys for spatially homogeneous systems the kinetic (or Boltzmann) equation

$$\frac{\partial f(\mathbf{p}, t)}{\partial t} = C[f](\mathbf{p}, t), \quad (3.26)$$

with a generic ‘collision integral’ $C[f](\mathbf{p}, t)$ that depends on the theory and the approximation employed. In general, it is a sum over all possible collisions of quasiparticles with in- or outgoing momentum \mathbf{p} that are allowed by the underlying theory. Hence, the kinetic equation (3.26) is a rate equation for the distribution function that counts gain and loss of quasiparticles with momentum \mathbf{p} . Isotropy further allows to simplify Eq. (3.26) by averaging over the direction of the external momentum \mathbf{p} .

Nonthermal fixed points can be characterized by the self-similar evolution of Eq. (3.1). This form, merely involving the scaling exponents α and β as well as the scaling function $f_S(p)$, strongly reduces the possible dependence of the distribution function $f(p, t)$ on variations in time and momenta. The self-similar form in Eq. (3.1) can be rewritten as

$$f(\mathbf{p}, t) = s^{\alpha/\beta} f(s\mathbf{p}, s^{-1/\beta}t), \quad (3.27)$$

where s is an arbitrary scaling parameter. For $s = t^\beta$ and $f_S(p) \equiv f(p, 1)$ one indeed recovers the scaling form in Eq. (3.1). This leads to the scaling behavior of the collision integral with exponent μ

$$C[f](\mathbf{p}, t) = s^{-\mu} C[f](s\mathbf{p}, s^{-1/\beta}t) = t^{-\beta\mu} C[f_S](t^\beta \mathbf{p}, 1). \quad (3.28)$$

This exponent is a function of the scaling exponents α and β , of the spatial dimensionality d , and it depends on the type of scattering processes that dominate the dynamics in the considered scaling region. The self-similar evolution implies for the left hand side of the

kinetic equation (3.26)

$$\frac{\partial}{\partial t} \left[t^\alpha f_S(t^\beta \mathbf{p}) \right] = t^{\alpha-1} [\alpha + \beta \mathbf{q} \cdot \nabla_{\mathbf{q}}] f_S(\mathbf{q})|_{\mathbf{q}=t^\beta \mathbf{p}}. \quad (3.29)$$

Comparing both sides of the kinetic equation, one arrives at a scaling relation for the temporal exponents

$$\alpha - 1 = -\beta\mu, \quad (3.30)$$

and an equation that determines the fixed point distribution $f_S(p)$

$$[\alpha + \beta \mathbf{p} \cdot \nabla_{\mathbf{p}}] f_S(\mathbf{p}) = C[f_S](\mathbf{p}, 1). \quad (3.31)$$

Further relations can be obtained by imposing energy conservation or particle number conservation. As demonstrated in Sec. 3.1, these lead to

$$\begin{aligned} \alpha &= \beta d && \text{if particle number,} \\ \alpha &= (\beta + z)d && \text{if energy density} \end{aligned} \quad (3.32)$$

is conserved in momentum space within the scaling region. Here we generalized the dispersion relation to scale as $\omega(\mathbf{p}) = s^{-z}\omega(s\mathbf{p})$, where for instance $z \approx 1$ for relativistic theories above the mass scale.

The collision integral of an $n \leftrightarrow m$ scattering process can be decomposed into

$$C^{n \leftrightarrow m}[f](\mathbf{p}) = \int d\Omega_d^{n \leftrightarrow m} |M^{n \leftrightarrow m}|^2 F^{n \leftrightarrow m}[f]. \quad (3.33)$$

Here $\int d\Omega_d^{n \leftrightarrow m}$ is the integration measure of an $n \leftrightarrow m$ scattering process in d spatial dimensions, $|M^{n \leftrightarrow m}|^2$ is the matrix element of the specific interaction and $F^{n \leftrightarrow m}[f]$ involves the gain minus loss structure that contains the distribution function and accounts for the in- and outgoing quasiparticles. The details of the underlying field theory enter the matrix elements $|M^{n \leftrightarrow m}|^2$. The latter can be derived from nonequilibrium quantum evolution equations in the two-particle irreducible (2PI) framework [117, 148] or they can be computed directly in perturbation theory [12, 149].

In the following, we specify the type of interactions we will consider for scalar and gauge theories. We will concentrate on solving the scaling relation (3.30) for the different conservation laws and we will comment on relations to wave turbulence at suitable places.

3.3.1 Scalar systems

For relativistic scalar systems, the leading interactions in perturbation theory are elastic scattering processes $2 \leftrightarrow 2$ and $2 \leftrightarrow (1 + \text{soft})$, where the soft particle belongs to the condensate [8, 13, 106]. For $2 \leftrightarrow 2$ scatterings, the integration measure reads

$$\int d\Omega_d^{2\leftrightarrow 2}(\{\mathbf{p}_i\}) = \int \frac{d^d p_2}{(2\pi)^d} \frac{d^d p_d}{(2\pi)^d} \frac{d^d p_4}{(2\pi)^d} (2\pi) \frac{\delta(\omega_1 + \omega_2 - \omega_3 - \omega_4)}{2\omega_1 2\omega_2 2\omega_3 2\omega_4} \times (2\pi)^d \delta^{(d)}(\mathbf{p}_1 + \mathbf{p}_2 - \mathbf{p}_3 - \mathbf{p}_4), \quad (3.34)$$

with the abbreviation $\omega_i \equiv \omega(\mathbf{p}_i) = \sqrt{m^2 + p_i^2}$ and with $\mathbf{p} \equiv \mathbf{p}_1$. The matrix element for elastic scatterings of scalar particles is at leading order in perturbation theory just a constant given by

$$|M_{\text{scalar}}^{2\leftrightarrow 2}|^2 = \lambda^2 \frac{N+2}{6N^2}. \quad (3.35)$$

In particular, note that it is independent of the distribution function or momenta. The function $F^{2\leftrightarrow 2}[f]$ that involves the distribution function reads

$$F^{2\leftrightarrow 2}[f](\{\mathbf{p}_i\}) = (1+f_1)(1+f_2)f_3f_4 - f_1f_2(1+f_3)(1+f_4) \underset{f \gg 1}{\approx} (f_1+f_2)f_3f_4 - f_1f_2(f_3+f_4). \quad (3.36)$$

It incorporates the information that \mathbf{p}_1 and \mathbf{p}_2 are incoming and \mathbf{p}_3 and \mathbf{p}_4 are outgoing quasi-particles, and the factors $(1+f_i)$ stem from Bose enhancement. In the last line of Eq. (3.36) we used that $f \gg 1$ for typical momenta. The collision integral with this approximation describes the dynamics of a classical field theory [12, 13]. On the other hand, our perturbative approach requires $f \ll 1/\lambda$ since otherwise for $\lambda f \sim 1$ an infinite number of collision processes becomes of the same order and perturbation theory breaks down. Hence, one may use the above kinetic equation in the regime $1/\lambda \gg f \gg 1$ to describe the dynamics of the quantum field theory.

We will now consider the scaling behavior in Eq. (3.27) in this overlapping region for hard momenta $p \gg m$. Plugging this scaling ansatz into the above equations yields the scaling relations

$$\int d\Omega_d^{2\leftrightarrow 2}(\{\mathbf{p}_i\}) = s^{-3d+4+(d+1)} \int d\Omega_d^{2\leftrightarrow 2}(\{s\mathbf{p}_i\}), \quad F^{2\leftrightarrow 2}[f](\{\mathbf{p}_i\}) = s^{3\alpha/\beta} F^{2\leftrightarrow 2}[f](\{s\mathbf{p}_i\}), \quad (3.37)$$

which lead to

$$\mu^{2\leftrightarrow 2} = 2d - 5 - 3\alpha/\beta. \quad (3.38)$$

Together with the conservation laws in Eq. (3.32), the scaling exponents read

$$\begin{aligned} \text{rel. } 2 \leftrightarrow 2 \text{ particle transport: } \alpha &= -\frac{d}{5}, \quad \beta = -\frac{1}{5}, \\ \text{rel. } 2 \leftrightarrow 2 \text{ energy transport: } \alpha &= -\frac{d+1}{7}, \quad \beta = -\frac{1}{7}. \end{aligned} \quad (3.39)$$

The $2 \leftrightarrow (1 + \text{soft})$ collision integral can be deduced from the $2 \leftrightarrow 2$ scatterings by replacing the distribution at internal \mathbf{p}_k momenta $f(\mathbf{p}_k, t) \mapsto f(\mathbf{p}_k, t) + n_c(2\pi)^d \delta^{(d)}(\mathbf{p}_k)$, which includes the condensate n_c . While the collisions without a condensate are the original $2 \leftrightarrow 2$ scatterings and the collisions with more than two condensate particles are phase space suppressed, the collisions with exactly one condensate factor form the $2 \leftrightarrow (1 + \text{soft})$ collision integral. One can then separate the equation into two, by grouping parts that are proportional to $\delta^{(d)}(\mathbf{p})$ into a separate equation than the residual parts. The resulting equations can for instance be found in Ref. [8]. For instance, this procedure reduces the number of factors of the distribution function in the functional $F^{2 \leftrightarrow 2}$ of Eq. (3.36). In the classical approximation, one has three factors which is reduced to only two in $F^{2 \leftrightarrow (1 + \text{soft})}$, which has important consequences on the scaling behavior. For our discussion of scaling properties, we only state how the integration measure and of the function F scale:

$$\begin{aligned} \int d\Omega_d^{2 \leftrightarrow (1 + \text{soft})}(\{\mathbf{p}_i\}) &= s^{-2d+3+(d+1)} \int d\Omega_d^{2 \leftrightarrow (1 + \text{soft})}(\{s\mathbf{p}_i\}), \\ F^{2 \leftrightarrow (1 + \text{soft})}[f](\{\mathbf{p}_i\}) &= s^{2\alpha/\beta} F^{2 \leftrightarrow (1 + \text{soft})}[f](\{s\mathbf{p}_i\}), \end{aligned} \quad (3.40)$$

which leads to

$$\mu^{2 \leftrightarrow (1 + \text{soft})} = d - 4 - 2\alpha/\beta. \quad (3.41)$$

Together with the conservation laws in Eq. (3.32), the scaling exponents read

$$\begin{aligned} \text{rel. } 2 \leftrightarrow (1 + \text{soft}) \text{ particle transport: } \alpha &= -\frac{d}{4}, \quad \beta = -\frac{1}{4}, \\ \text{rel. } 2 \leftrightarrow (1 + \text{soft}) \text{ energy transport: } \alpha &= -\frac{d+1}{5}, \quad \beta = -\frac{1}{5}. \end{aligned} \quad (3.42)$$

For the direct energy cascade in scalar systems discussed in Sec. 3.2.2 we noted the values $\alpha = -4/5$ and $\beta = -1/5$. Thus, they can be explained by $2 \leftrightarrow (1 + \text{soft})$ scattering processes.

The values for α and β in both types of elastic scatterings in Eqs. (3.39) and (3.42) are negative for both conservation laws. This is a general property of $n \leftrightarrow m$ scattering processes with constant matrix elements [118]. This indicates that a self-similar solution of the form given by Eq. (3.27) only allows for transport of conserved quantities from lower to higher momenta, i.e. it only allows a direct cascade. In particular, if we want to have an inverse cascade within this perturbative kinetic theory, we need to change our scaling ansatz (3.27). On the other

hand, the perturbative description is not valid for large occupancies $f \gtrsim 1/\lambda$ that typically occur at low momenta. We will discuss these issues in Sec. 4.2 where we will introduce the vertex-resummed kinetic theory that extends the perturbative kinetic framework and is also valid for high occupancies.

3.3.2 Non-Abelian plasmas

The kinetic evolution of non-Abelian plasmas with an over-occupied initial distribution has been studied in Refs. [70, 72, 104, 130, 150]. The elastic $2 \leftrightarrow 2$ scattering processes are the leading contribution in a naive power counting of the coupling. However, near-collinear splittings in inelastic $n \leftrightarrow n+1$ collisions strongly enhance the corresponding collision integrals and become of the same order as elastic processes. Resummation of the leading near-collinear contributions results in an effective inelastic $2 \leftrightarrow 3$ scattering process, which has been developed in Ref. [149]. Hence, this (AMY) effective kinetic theory involves both elastic and inelastic processes and describes a consistent effective kinetic framework for non-Abelian gauge theories. Since a linear dispersion relation is assumed this effective kinetic theory is only valid for momenta above the Debye mass of Eq. (3.18), i.e. $p \gtrsim m_D$. Moreover, the collision integrals rely on a perturbative derivation in the coupling. Therefore, its range of validity is also limited to weak couplings $\alpha_s \ll 1$ and occupation numbers satisfying $f < 1/\alpha_s$. This kinetic framework also involves screening effects that we will comment on below. For non-expanding plasmas, this framework has been used numerically by Refs. [104, 130]. To further simplify the discussion, we will concentrate on elastic processes.

The collision integral for elastic scatterings can be written in the generic form in Eq. (3.33). The integration measure $\int d\Omega_d^{2\leftrightarrow 2}$ and the operator $F^{2\leftrightarrow 2}[f]$ are given by Eqs. (3.34) and (3.36), respectively, where we use again the classical approximation $f \gg 1$. The dispersion relation in the non-Abelian case is massless $p^0 = \omega(\mathbf{p}) = p$. For non-Abelian $SU(N_c)$ gauge theories, the scattering matrix element at leading order is given by [149]

$$|M_{\text{gauge}}^{2\leftrightarrow 2}(\{\mathbf{p}_i\})|^2 = 64\pi^2\alpha_s^2 N_c^2 \left(3 - \frac{tu}{s^2} - \frac{su}{t^2} - \frac{ts}{u^2} \right), \quad (3.43)$$

where $s = (p_1^\mu + p_2^\mu)^2$, $t = (p_1^\mu - p_3^\mu)^2$ and $u = (p_1^\mu - p_4^\mu)^2$ are the Mandelstam variables with $(p^\mu)^2 = (p^0)^2 - p^2$. The matrix element diverges in the limit $t = (p_1^\mu - p_3^\mu)^2 \rightarrow 0$ for collisions with small or collinear momentum transfer. To avoid these divergences, it is necessary to consider screening effects. These are included in the (AMY) effective kinetic framework, and the elastic scattering matrix element is regulated by the Debye mass m_D given by Eq. (3.18).

With these modifications in mind, we can consider two types of collisions, large angle scatterings that do not lead to the above mentioned divergences, and small angle processes that need

to be regularized. As we will discuss shortly, in both situations one obtains the same scaling exponents α and β in the self-similar scaling regime.

Let us start with large-angle scatterings. Since the matrix element (3.43) is dimensionless and the only dimensionful quantity it involves are momenta \mathbf{p}_i , it is straight forward to check that it does not change under rescalings with s . Hence, the collision integral has the same scaling exponent μ as for elastic collisions in scalar systems (3.38). We thus recover the same scaling exponents as in Eq. (3.39) for scalars. Energy density conservation for typical hard momenta finally implies

$$\alpha = -\frac{d+1}{7}, \quad \beta = -\frac{1}{7}. \quad (3.44)$$

To discuss the scaling behavior for small angle scatterings, we use the small-angle approximation of the collision integral, which will be useful for the upcoming discussion of scaling phenomena in longitudinally expanding plasmas in Sec. 5.3.3. Kinetic equations employing a small-angle approximation have been derived in Refs. [67, 151] for non-Abelian gauge theories in the context of heavy-ion collisions. The approximation mainly consists of a Taylor expansion of the collision integral to leading non-vanishing order in the transferred momentum $q = |\mathbf{p}_3 - \mathbf{p}_1|$. With the expanded expressions for the Mandelstam variables $s = 2 p_1 p_2 (1 - (\mathbf{p}_1 \mathbf{p}_2)/(p_1 p_2))$, $t \simeq -q^2 (1 - (\mathbf{p}_1 \mathbf{q})/(p_1 q) + \mathcal{O}(q^2/p_1^2))$ and $u \simeq -2 p_1 p_2 (1 - \cos\theta_{12} + \mathcal{O}(q/p_i))$, the t -channel of the matrix element $|M_{\text{gauge}}^{2\leftrightarrow 2}|^2/(64\pi^2\alpha_s^2 N_c^2)$ in Eq. (3.43) becomes

$$-\frac{su}{t^2} \simeq 4 \frac{p_1^2 p_2^2}{q^4} \left(\frac{(1 - (\mathbf{p}_1 \mathbf{p}_2)/(p_1 p_2))^2}{(1 - (\mathbf{p}_1 \mathbf{q})/(p_1 q))^2} + \mathcal{O}\left(\frac{q}{p_i}\right) \right). \quad (3.45)$$

Small momentum transfer thus strongly enhances the matrix element, which justifies the small-angle expansion. In the small-angle approximation, the elastic collision integral becomes a total divergence $C_{\text{small-angle}}^{2\leftrightarrow 2} \simeq -\nabla_{\mathbf{p}} \mathbf{j}$, where \mathbf{j} can be interpreted as the particle flux in momentum space. For non-Abelian gauge theories, the approximated collision integral reads [150]

$$C_{\text{small-angle}}^{2\leftrightarrow 2} = \nabla_{\mathbf{p}} (\hat{q} \nabla_{\mathbf{p}} f + \eta_{-1} \mathbf{p}/p f(1+f)). \quad (3.46)$$

The Boltzmann equation has become a Fokker-Planck equation in momentum space with the (diffusion and drift) parameters

$$\hat{q} = 4\pi\alpha_s^2 N_c^2 L \int \frac{d^d q}{(2\pi)^d} f(\mathbf{q})(1+f(\mathbf{q})), \quad \eta_{-1} = 4\pi\alpha_s^2 N_c^2 L \int \frac{d^d q}{(2\pi)^d} 2 \frac{f(\mathbf{q})}{q}, \quad (3.47)$$

where $L = \int dq/q$ is regularized at low momenta by the screening mass and at high momenta by some typical momentum. With the classical approximation $f \gg 1$, the collision integral

thus scales as

$$C_{\text{small-angle}}^{2 \leftrightarrow 2}[f](\mathbf{p}, t) = s^{-(d-2-3\alpha/\beta)} C[f](s\mathbf{p}, s^{-1/\beta}t), \quad (3.48)$$

which leads to the scaling exponent

$$\mu_{\text{small-angle}}^{2 \leftrightarrow 2} = d - 2 - 3\alpha/\beta. \quad (3.49)$$

For the considered case of $d = 3$ spatial dimensions, this is the same scaling behavior as for elastic collisions in scalar systems (3.38) and implies the same scaling exponents as for large-angle scatterings in Eq. (3.44).

The effective kinetic theory has been used in Ref. [104] to describe the self-similar dynamics of an over-occupied non-Abelian plasma. The authors showed both analytically and numerically using the effective kinetic theory that non-Abelian plasmas indeed exhibit self-similar scaling behavior at the fixed point with the exponents of Eq. (3.44) for $d = 3$ dimensions. They also showed that these scaling exponents are consistent with a self-similar evolution with both elastic $2 \leftrightarrow 2$ and effective inelastic $2 \leftrightarrow 3$ processes. Moreover, these are the same scaling exponents as obtained in classical lattice simulations that we reviewed in Sec. 3.2.1. Indeed, it was demonstrated in Ref. [104] that the distribution function obtained from kinetic theory matches the distribution extracted from classical lattice simulations.

The scaling function $f_S(p)$ can also be explained using a perturbative treatment. As we have already noted in Sec. 3.2.1, one observes a power law $p^{-\kappa}$ for momenta $p \lesssim p_{\text{typ}}$, with an exponential decrease for higher momenta. The spectral exponents $\kappa = 4/3$ and $\kappa = 3/2$ observed in Refs. [16, 17] were explained by elastic $2 \leftrightarrow 2$ and $2 \leftrightarrow (1 + \text{soft})$ processes, respectively, using corresponding 2PI processes. The scaling function at late times was obtained in Ref. [104] using the effective kinetic framework discussed above. It was shown that the spectral exponent becomes $\kappa = 1$ eventually, which turns out to be a consequence of the combination of $2 \leftrightarrow 2$ and effective inelastic $2 \leftrightarrow 3$ processes.

3.4 Summary

We have seen in this chapter that nonthermal fixed points in Minkowski space-time involve scaling regions that are described by a self-similar evolution $f(p, t) = t^\alpha f_S(t^\beta p)$. The scaling exponents α and β and the scaling function $f_S(x)$ determine the scaling region. Each scaling regime can only contain one conserved quantity locally, which is usually either particle or energy conservation. Moreover, nonthermal fixed points can be understood as extensions of renormalization group fixed points of critical behavior in thermal equilibrium to our far-from-equilibrium situations.

We have also discussed the thermalization process in weakly coupled non-expanding systems. Starting from over-occupied initial conditions (or from strong classical fields), the system approaches a nonthermal fixed point, losing the memory about details of the initial conditions. This stage is governed by classical dynamics for large enough occupancies $f \gg 1$. As soon as occupation numbers become of order unity $f \sim 1$, quantum corrections to the dynamics become important and the system leaves the nonthermal attractor. At this point, typical momenta have reached the temperature scale $p_{\text{typ}} \sim T$ and the system enters its final thermalization stage, where correlations of the system approach their thermal form.

We have given an overview of nonthermal fixed points in isolated non-Abelian gauge and scalar systems, both numerically with classical-statistical simulations and analytically with kinetic equations. The non-Abelian plasma exhibits a scaling region with scaling exponents $\alpha = -4/7$ and $\beta = -1/7$, which characterizes a direct energy cascade to higher momenta and drives the thermalization process. Its scaling function follows a power law $f_S(p) \sim p^{-\kappa}$ up to a typical hard momentum and falls off rapidly afterwards. The value for κ is $4/3$ at early times and changes to 1 at late times. The dynamics is governed by elastic $2 \leftrightarrow 2$ and effective inelastic $2 \leftrightarrow 3$ scattering processes.

The nonthermal fixed point of the $O(N)$ -symmetric scalar field theory exhibits a dual cascade, one at low momenta with large occupation numbers $f \gtrsim 1/\lambda$ and the other one at higher momenta with lower occupation numbers $f \ll 1/\lambda$. The highly occupied region involves an inverse particle cascade from higher to lower momenta and will be studied in the next chapter. The scaling region at larger momenta describes a direct energy cascade from lower to higher momenta with scaling exponents $\alpha = -4/5$ and $\beta = -1/5$. The functional form is $f_S(p) \sim p^{-\kappa}$ with $\kappa \approx 3/2$ and a subsequent rapid decrease at very hard momenta. The dynamics is mainly governed by $2 \leftrightarrow (1 + \text{soft})$ scattering processes involving the condensate.

A subtle difference exists between scalar systems with $N = 1$ and $N \geq 2$ components. For the latter, a local condensate in the system carries an approximately conserved charge that is similar to the spin in circularly polarized light. This protects the condensate from a rapid decay. However, in single-component scalar systems, such a conserved charge is absent. As a

consequence, the condensate decays as a power law in time into a narrow momentum region, which appears as a ‘bump’ in the distribution function. Acting as a source for particles and energy, it becomes the separating point for the two branches of the dual cascade. In particular, an additional power law region $f(p) \sim p^{-\kappa}$ with $\kappa = 4/3$ emerges for not too large occupation numbers $f \lesssim 1/\lambda$ above the soft momenta where occupancies become large $f \sim 1/\lambda$ and below the location of the ‘bump’. This new region can be understood as part of the inverse particle cascade at lower momenta. The complete particle cascade of the $N = 1$ scalar field theory thus consists of this part with occupancies $f \lesssim 1/\lambda$ and of the highly occupied sector at even lower momenta with larger occupancies $f \gtrsim 1/\lambda$.

Chapter 4

Universality class of condensation dynamics

We study in this chapter the far-from-equilibrium infrared dynamics of scalar field theories close to their nonthermal fixed point. In the previous chapter, we have already discussed general properties of nonthermal fixed points and we have illustrated the nonthermal fixed point of scalar systems in Fig. 3.4. The dynamics is governed by a dual cascade, with a direct energy cascade at hard momenta for $f \lesssim 1/\lambda$ [8, 21] and an inverse particle cascade for the highly over-occupied region at low momenta with $f \gtrsim 1/\lambda$ [7, 9, 117]. While the energy cascade and the thermalization dynamics were covered in Sec. 3.2.2, we concentrate here on the self-similar scaling region at low momenta which describes the dynamics of Bose-Einstein condensation via an inverse particle cascade [89].

Our results are compared to nonrelativistic scalar systems that are used to model ultracold Bose gases. There, the nonthermal fixed point has a similar dual cascade structure as for the relativistic case illustrated in Fig. 3.4. However, the scaling properties of the direct energy cascade at hard momenta do not agree with the relativistic case [8]. Another difference is that the nonrelativistic system conserves the total particle number density whereas in the relativistic theory number-changing processes are possible. On the other hand, a similar inverse particle cascade was found in nonrelativistic theories as in the relativistic case [10, 22–24, 89, 91–93], also describing Bose condensation out of equilibrium [89, 92, 94–96].

We study this low momentum scaling region with two different methods, as illustrated in Fig. 4.1. For high occupancies of typical modes $f \gg 1$, classical-statistical simulations are applicable and allow us to measure the scaling properties of the infrared region for scalar theories. In Sec. 4.1 we will find the same scaling properties within our numerical uncertainties for different numbers of field components N in the relativistic theory and we will be able to

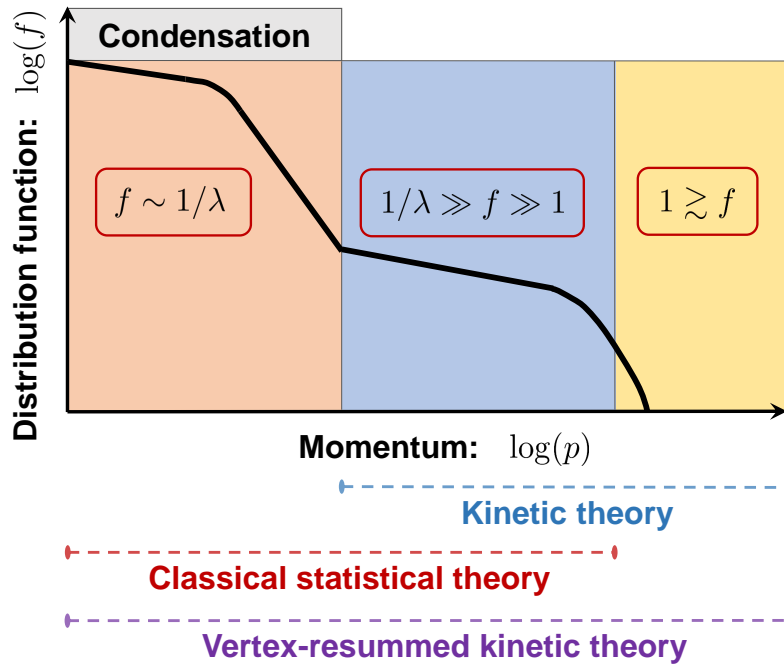


FIGURE 4.1: Schematic scaling form of the scalar occupation number distribution f as a function of momentum. Classical-statistical field theory is valid for $f \gg 1$. Kinetic theory is restricted to $f \ll 1/\lambda$. In scalar field theory, a ‘vertex-resummed’ kinetic description from a $1/N$ -expansion at NLO can additionally describe the IR momentum range, as will be shown in this chapter.

describe Bose-Einstein condensation quantitatively. Moreover, we will find that also nonrelativistic scalar systems share the same scaling properties. This will allow us to define a broad universality class at low momentum modes.

We give an analytical explanation in terms of scatterings of quasiparticle in Sec. 4.2. Since the large occupancies at low momenta lead to strongly nonlinear dynamics, this regime is not well described by standard kinetic theory where the soft momentum region is approximated by an additional single zero mode. Such a perturbative kinetic description leads to a finite condensation time t_{cond} and to a self-similar evolution in the time difference $t_{\text{cond}} - t$ [152, 153], which will be discussed in Sec. 4.2.1. The reason why it is not able to describe our simulation results lies in the fact that the perturbative approximation relies on occupancies being small compared to $1/\lambda$, which is not fulfilled in the infrared for our over-occupied systems. This limitation is illustrated in Fig. 4.1. One also observes there that the (perturbative) kinetic theory has an important overlap with classical-statistical simulations for $1/\lambda \gg f \gg 1$, which we used in Sec. 3.3.1 to analyze nonthermal fixed points analytically.

Instead, we use a vertex-resummed kinetic theory in Sec. 4.2.2, which is based on an expansion in the number of field components N to next-to-leading order [114, 154] and is expected to describe the infrared region with large occupancies $f \gtrsim 1/\lambda$ correctly (see Fig. 4.1). The approach incorporates important vertex corrections [7, 89] and extends well-established kinetic

descriptions [8, 131, 147] to the non-perturbative regime of over-occupied modes. A more general transport equation that also incorporates off-shell processes is discussed at the end of Sec. 4.2.2. While this framework reduces to the vertex-resummed kinetic theory in the on-shell limit, it can be used to study dependencies on the anomalous dimension η introduced in Sec. 3.1.

Main results of this chapter are summarized in Sec. 4.3.¹

4.1 Universality from lattice simulations

As we have discussed in Sec. 3.2.2, the different cascades of the nonthermal fixed point of scalar systems in Fig. 3.4 exhibit a self-similar evolution of the form $f(p, t) = t^\alpha f_S(t^\beta p)$ (Eq. 3.1) in a given scaling regime. In the following, all quantities are considered to be dimensionless by use of some suitable momentum scale, which is specified below.

The scaling properties can be different for scaling regimes in different momentum regions. For instance, we already discussed in Sec. 3.1 that one finds $\beta < 0$ indicating a direct cascade at large momenta while in the infrared, the inverse cascade requires a different sign, i.e. $\beta > 0$. Similarly, the scaling exponent α and the scaling function $f_S(p)$ may differ in different scaling regions. Interestingly, two theories can share the same universal properties in one scaling region while they may differ significantly in another scaling region. For relativistic and nonrelativistic scalar systems, the scaling regions at large momenta differ [8]. Despite this difference, we will find the same scaling behavior at low momenta for relativistic and nonrelativistic theories in this section.

In the following we will compute the exponents α , β and the scaling function f_S of the self-similar distribution (3.1) in the infrared regime using classical-statistical simulations. We will start with $\mathcal{O}(N)$ symmetric relativistic scalar fields.

4.1.1 Self-similar dynamics from classical-statistical simulations

We start our evolution with over-occupation initial conditions (2.61) with initial amplitude $n_0 = 125$, such that the initial distribution reads $f(p, 0) = 125/\lambda \Theta(Q - p)$. All quantities shown will be made dimensionless by appropriate powers of the typical scale $Q_\epsilon = \sqrt[4]{\lambda\epsilon/N}$ that was introduced in Eq. (3.21). For the considered over-occupation initial condition, one has $\epsilon \sim NQ^4/\lambda$ such that Q_ϵ becomes independent of the coupling and the number of field components. Specifically, the scale Q in the initial conditions can be related to Q_ϵ by $Q \approx 0.8 Q_\epsilon$. Because

¹We have published most results of this chapter in Ref. [118]. Since this project was done in close collaboration with Asier Piñeiro Orioli, some of the following content may also enter his upcoming doctoral thesis.

of our choice of the initial conditions, we always plot rescaled functions $f(p, t) \mapsto \lambda f(p, t)$ such that this combination also becomes independent of the coupling.

As we discussed in Sec. 2.3.2, we use large lattices to improve numerical statistics. For the $N = 2$ component theory, computations were made on a large 768^3 lattice with lattice spacing $Q_\epsilon a_s = 0.9$ and we additionally averaged over five realizations. For $N = 4$ we employed a 512^3 lattice with spacing $Q_\epsilon a_s = 1.8$ and averaged over 18 – 50 realizations. We checked that for $N = 2$ all shown results are insensitive to the lattice spacing and the volume. For the relevant infrared quantities this is to good accuracy also the case for the coarser lattices employed for $N = 4$.

We study the evolution of the distribution function for the relativistic $N = 2$ component theory in Fig. 4.2 close to the nonthermal fixed point. There we concentrate on the low-momentum part of the distribution and analyze its infrared scaling properties. We show in the figure the evolution of the rescaled distribution function $(t/t_{\text{ref}})^{-\alpha} f(p, t)$ as a function of the rescaled momentum $(t/t_{\text{ref}})^\beta p$, where the reference time $Q_\epsilon t_{\text{ref}} = 600$ is the earliest time shown. In the inset, the original (unscaled) distribution $f(p, t)$ is shown for comparison at different times together with the initial distribution. With the appropriate choice of the scaling exponents α and β , all the curves at different times lie remarkably well on top of each other after rescaling. This is a clear sign of the self-similar dynamics (3.1) near a nonthermal fixed point. The scaling exponents obtained are

$$\alpha = 1.51 \pm 0.13, \quad \beta = 0.51 \pm 0.04, \quad (4.1)$$

where the error bars are due to statistical averaging and fitting errors, which is further described in App. C.1. The distribution function for the relativistic theory in Fig. 4.2 turns out to be well described by the fit (gray dashed line)

$$f_S(p) \simeq \frac{a}{(p/b)^{\kappa_<} + (p/b)^{\kappa_>}}, \quad (4.2)$$

with spectral exponents $\kappa_< \simeq 0.5$ and $\kappa_> \simeq 4.5$. We note that the value for $\kappa_>$ is rather close to those obtained for stationary turbulence in nonrelativistic systems [10]. The parameters a and b can be understood as normalizations of the distribution function f and its momentum p . A scaling function $f_S(p)$ is universal up to such non-universal normalizations that contain system-dependent aspects.

The observed values for the scaling exponents (4.1) satisfy remarkably well the relation

$$\alpha \approx 3\beta, \quad (4.3)$$

in $d = 3$ spatial dimensions, which implies particle number density conservation as we discussed in Sec. 3.1. Notice that since we consider here a relativistic theory, particle number

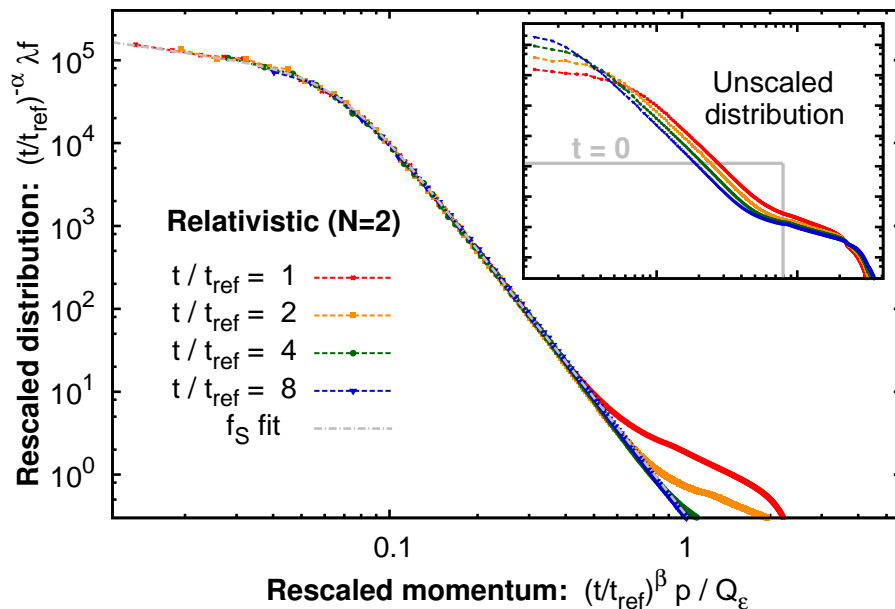


FIGURE 4.2: Rescaled distribution function of the relativistic two-component theory as a function of the rescaled momentum for different times. We have chosen the reference time $Q_\epsilon t_{\text{ref}} = 600$. The gray dashed line illustrates the scaling function of Eq. (4.2). The inset shows the original distribution without rescaling.

conservation within a momentum region is not necessarily expected. Together with the positive value of $\beta > 0$, we conclude that particle number is being transported towards low momenta, thus confirming an inverse particle cascade.

In order to check for a possible dependence of the infrared scaling properties on the number of field components, we also perform lattice simulations for $N = 4$. Fig. 4.3 shows $(t/t_{\text{ref}})^{-\alpha} f(p, t)$ as a function of $(t/t_{\text{ref}})^\beta p$. The curves corresponding to different times lie again on top of each other after the rescaling, signaling a self-similar evolution with scaling function (gray dashed line) given by Eq. (4.2). We extract the exponents as above using the analysis of App. C.1

$$\alpha = 1.65 \pm 0.09, \quad \beta = 0.59 \pm 0.03. \quad (4.4)$$

To estimate systematic errors, we investigate how the values for the exponents α and β depend on the reference time t_{ref} at which we start our self-similarity analysis. To this end, we perform our self-similarity analysis of App. C.1 for different reference times t_{ref} . Similar to our plots 4.2 and 4.3, this analysis proceeds by rescaling the distribution function at several later times in the range from t_{ref} up to $4 - 5 t_{\text{ref}}$ and comparing the rescaled curves to the distribution at the reference time. In Fig. 4.4, we show the extracted values for α and β as a function of the reference time for $N = 4$. One finds that the exponents α and β approach the values 1.5 and 0.5 as time evolves. For the relativistic two-component system as well, the exponents α and β are found to start from larger values at early reference times than the ones given in Eq. (4.1),

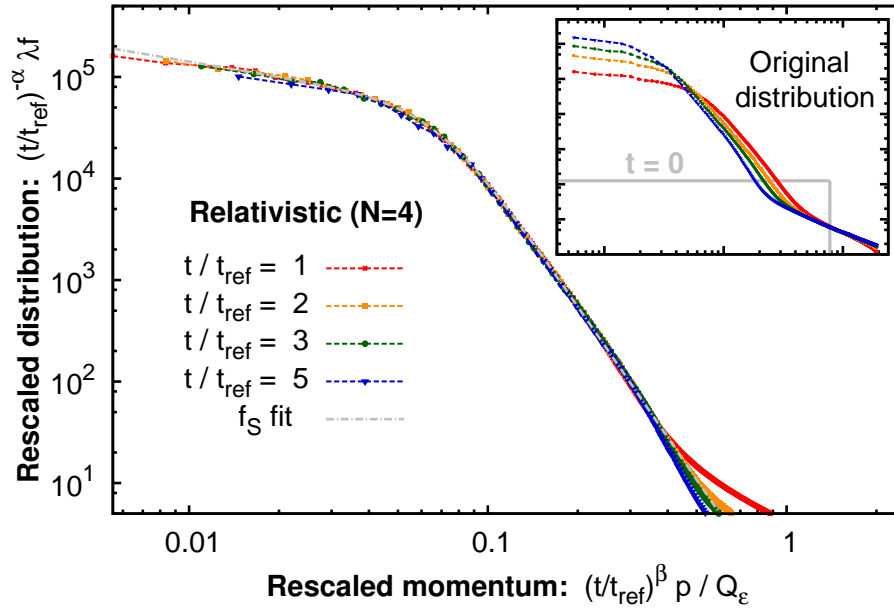


FIGURE 4.3: Rescaled distribution function of the relativistic four-component theory as a function of the rescaled momentum for different times. We have chosen the reference time $Q_{\epsilon} t_{\text{ref}} = 800$. The gray dashed line illustrates the scaling function of Eq. (4.2). The inset shows the original distribution without rescaling.

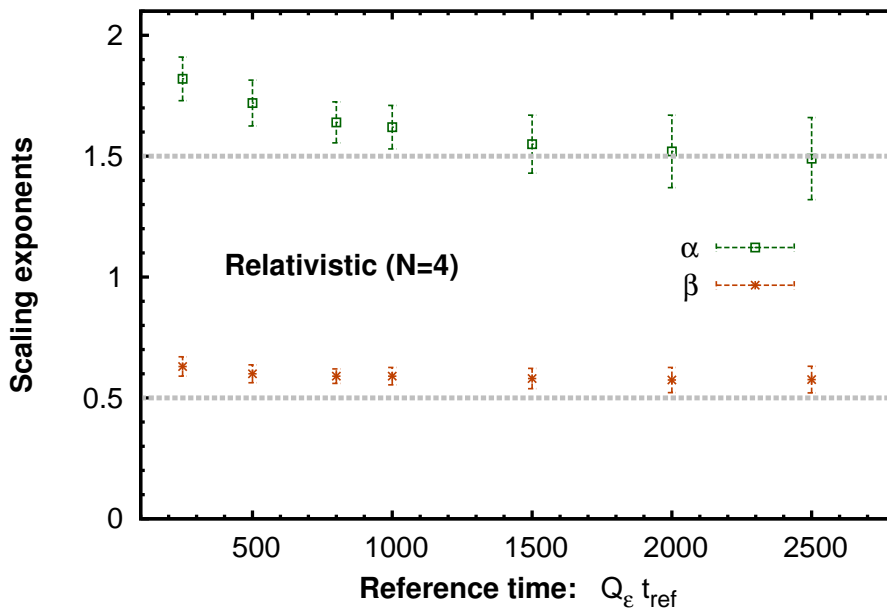


FIGURE 4.4: The exponents α and β with statistical error bars for the relativistic $N = 4$ component field theory extracted at different reference times t_{ref} .

and then decrease to the latter.

These values for the scaling exponents, together with the scaling form of the distribution function compare well to those for the relativistic $N = 2$ component system. Within statistical errors we find no indication for a strong dependence of the corresponding universality class on the number of field components N . The scaling exponents of the infrared region are approximately

$$\alpha \approx 1.5, \quad \beta \approx 0.5, \quad (4.5)$$

while the scaling function follows the form of Eq. (4.2). However, small discrepancies in α , β and f_S are still possible. These could occur in the presence of a non-vanishing anomalous dimension η , which we discuss in Sec. 4.2.3 in more detail.

A recent study [144] confirmed our observation that the scaling function $f_S(p)$ given by Eq. (4.2) is the same for a different number of field components.² This approximate N -independence of the fixed point distribution $f_S(p)$ is observed for relativistic scalar theories with $N = 1, 2, 3, 4, 8$ field components. This is truly remarkable since, as pointed out there, different N imply different condensate and topological structures in the lattice configurations, which, in a dissipative setup, can lead to different N -specific forms for the distribution function. However, such a difference is not observed in our numerical simulations. Our results thus indicate that the infrared scaling region is part of a universality class for a different number of field components N . In Sec. 4.2.2 we will find a description for the observed universal scaling behavior in terms of a vertex-resummed kinetic theory.

4.1.2 Universality with nonrelativistic Bose gases

We now compare our previous results obtained for relativistic scalar systems to nonrelativistic scalars describing ultracold quantum gases.

We employ over-occupation initial conditions similar to Eq. (2.61) where we initialize the distribution function as $f(p, t = 0) = 50/(2mgQ) \Theta(Q - p)$ and consider no condensate initially. For the plots we typically average over 10 realizations on a lattice with 512^3 points and a lattice spacing a_s such that $Qa_s = 1$, where we checked insensitivity of our infrared results to cutoff changes. We always plot dimensionless quantities obtained by the rescalings $f(p, t) \mapsto f(p, t) 2mgQ$, $t \mapsto t Q^2/(2m)$ and $\mathbf{p} \mapsto \mathbf{p}/Q$. This reflects the classical-statistical nature of the dynamics in the highly occupied regime. It has the important consequence that if we measure time in units of $2m/Q^2$ and momentum in units of Q then the combination $f(p, t) 2mgQ$ does not depend on the values of m , g and Q [97].

²There is only a small difference in the deep infrared spectral exponent $\kappa_{<}$. While we observe $\kappa_{<} \simeq 0.5$, Ref. [144] reports of a flat distribution in the deep infrared with $\kappa_{<} \simeq 0$.

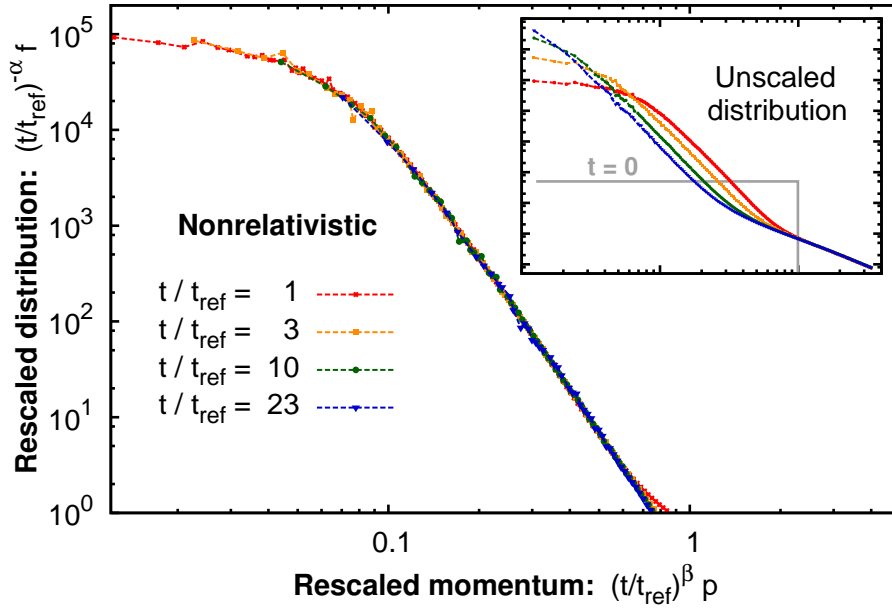


FIGURE 4.5: Rescaled distribution function of the nonrelativistic theory as a function of the rescaled momentum for different times. We have chosen the reference time $t_{\text{ref}} Q^2/(2m) = 300$. The inset shows the original distribution without rescaling.

In Fig. 4.5 we show the evolution of the distribution function for the nonrelativistic system. As in the relativistic case, we plot $(t/t_{\text{ref}})^{-\alpha} f(p, t)$ against $(t/t_{\text{ref}})^{\beta} p$, where the reference time $t_{\text{ref}} Q^2/(2m) = 300$ is the earliest time shown, to study self-similarity. We show the original distribution without rescaling in the inset. After rescaling with appropriately chosen exponents, all curves lie on top of each other in the infrared to remarkable accuracy. The exponents employed are

$$\alpha = 1.66 \pm 0.12, \quad \beta = 0.55 \pm 0.03, \quad (4.6)$$

and the errors bars were estimated as above (see App. C.1 for details). The values in Eq. (4.6) agree within errors with the exponents of the relativistic systems in (4.1) and (4.4). To study systematic error dependencies, we performed a similar scaling analysis as for the relativistic $N = 4$ theory of Fig. 4.4. We again find monotonically decreasing exponents α and β towards the values of Eq. (4.5). We note, however, that our runs last not long enough for the values of the scaling exponents to come as close to these values as for the relativistic systems.

Remarkably, not only the scaling exponents but also the numerically computed fixed point distribution $f_S(\xi)$ of Eq. (4.2) agrees for relativistic and nonrelativistic theories in the infrared scaling regime. This is shown in Fig. 4.6, where we plot the normalized distribution f_S/a as a function of the rescaled variable ξ/b for both relativistic (with $N = 2$ and $N = 4$) and nonrelativistic theories. The normalizations a and b of Eq. (4.2) can be extracted according to

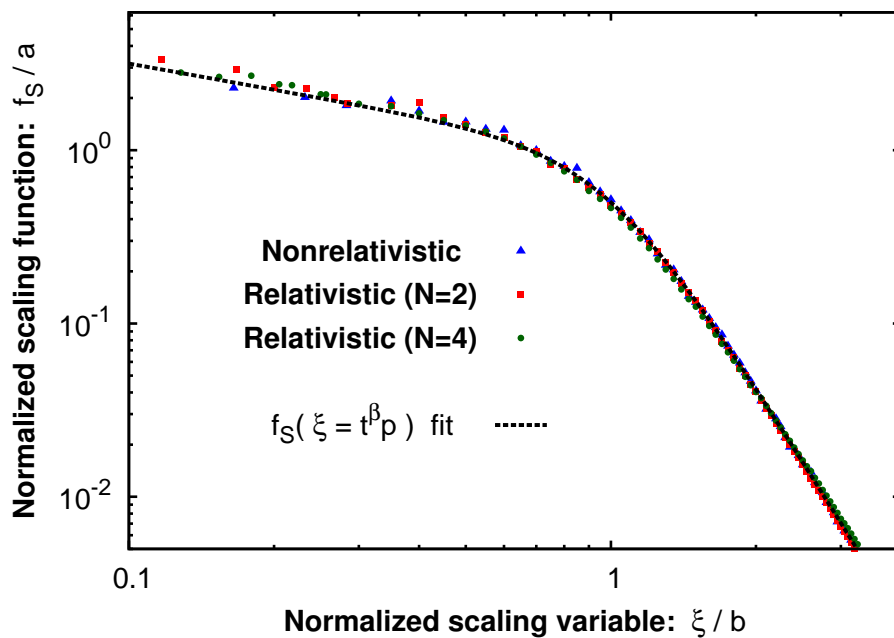


FIGURE 4.6: The scaling function $f_S(\xi \equiv t^\beta p) = t^{-\alpha} f(p, t)$, normalized by system-dependent constants a and b , exhibits accurate agreement between the nonrelativistic (triangles) and relativistic $O(2)$ (squares) and $O(4)$ (circles) simulation results. The curves are shown for times $t Q^2/(2m) = 300$, $Q_\epsilon t = 500$ and $Q_\epsilon t = 800$, respectively.

$f_S(\xi = b) = a/2$ and $df_S(\xi = b)/d\xi = -a(\kappa_> + \kappa_<)/(4b)$.³ The lattice results for nonrelativistic and relativistic theories agree and can indeed be well described by the fit function in Eq. (4.2) (dashed line). This demonstrates that these theories indeed belong to the same universality class at low momenta.

4.1.3 Generation of a mass gap

To understand the appearance of nonrelativistic dynamics in the relativistic theory, we analyze the effective dispersion relation $\omega(p, t)$ that we defined in Eq. (2.48) in terms of statistical correlation functions $F(\mathbf{p}, t)$. The dispersion relation is shown in Fig. 4.7 at three different times. Although the underlying theory is massless, it can be clearly observed that for low

³Alternatively to the fixed point form in Eq. (4.2), other non-universal normalizations could be defined via $f_S(\xi = B) = A$ and $df_S(\xi = B)/d\xi = -2A/B$ such that A characterizes the amplitude of the scaling function at $\xi = B$, where the occupation number receives its dominant contribution. This would lead to the equivalent scaling function we chose in Ref. [118]

$$f_S(\xi) = \frac{A(\kappa_> - \kappa_<)}{(\kappa_> - 2)(\xi/B)^{\kappa_<} + (2 - \kappa_<)(\xi/B)^{\kappa_>}}, \quad (4.7)$$

with the same universal spectral exponents $\kappa_>$ and $\kappa_<$ as in (4.2). The two sets of normalizations can be related to each other by

$$a = A(\kappa_> - \kappa_<) \frac{(2 - \kappa_<)^{\kappa_</(\kappa_> - \kappa_<)}}{(\kappa_> - 2)^{\kappa_>/(\kappa_> - \kappa_<)}} , \quad b = B \left(\frac{\kappa_> - 2}{2 - \kappa_<} \right)^{1/(\kappa_> - \kappa_<)} . \quad (4.8)$$

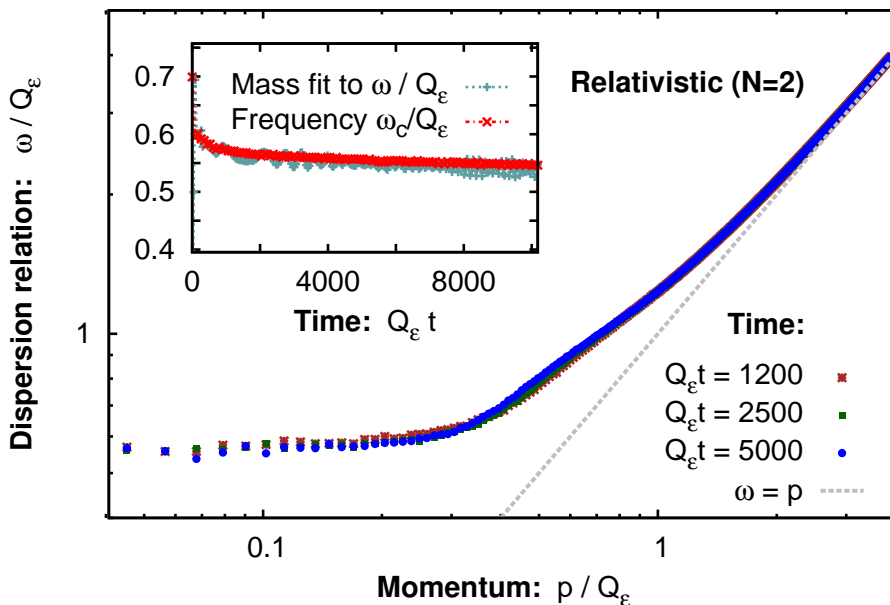


FIGURE 4.7: Dispersion relation for the relativistic $N = 2$ component theory at different times for the same parameters as for Fig. 4.2. In the inset, the time evolution of the mass gap at zero momentum is shown, which is obtained from a $\sqrt{m^2 + p^2}$ fit to ω_p at low momenta (+ symbol) and by measuring the oscillation frequency ω_c of the unequal-time correlation function (x symbol).

momenta the system generates a mass gap, whereas at large momenta we recover a linear dispersion. The appearance of an effective mass-like contribution can already be understood from the mean-field approximation, where the term $\sim (\lambda/6) \int d^3q/(2\pi)^3 f(\mathbf{q}, t)/\omega(\mathbf{q}, t)$ generates a mass-like correction for the over-occupied systems.

To extract the mass gap from our lattice simulations, we fit a $\sqrt{m^2(t) + p^2}$ function to the $\omega(p, t)$ results. The time evolution of the effective mass $m(t)$ is shown in the inset of Fig. 4.7. We find that after a quick initial evolution this dispersion relation enters a quasi-stationary regime, which implies that the mass stays approximately constant. In addition, we also analyze the oscillation frequency ω_c of the unequal-time correlation function $F(\mathbf{p}, t, 0)$ for $|\mathbf{p}| = 0$. Since the oscillation frequency of the zero-momentum mode corresponds to the renormalized mass of the theory, this provides an independent estimate of the mass gap that does not rely on the definition (2.48) of a dispersion relation. Indeed we find $\omega_c \simeq m(t)$ to very good accuracy as shown in the inset of Fig. 4.7.

In the presence of a mass gap m , low momentum modes with $p \lesssim m$ are expected to behave nonrelativistically. From Fig. 4.7 we can estimate the mass to be $m \simeq 0.55 Q_\epsilon \simeq 0.69 Q$ for the whole period of the self-similar evolution. We find that this mass scale lies to good approximation between the scaling regions for the inverse particle cascade at lower momenta and the direct energy cascade at higher momenta. This can be observed, for instance, from

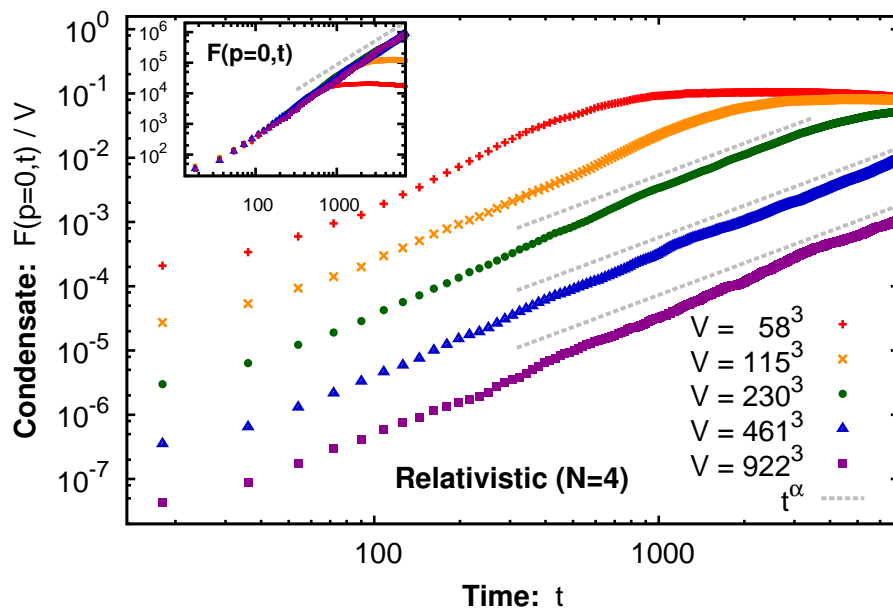


FIGURE 4.8: Evolution of the zero-momentum correlation divided by volume $F(\mathbf{p} = \mathbf{0}, t)/V$ for the relativistic $N = 4$ component theory for different volumes. In the inset the same curves are shown for the correlation function $F(\mathbf{p} = \mathbf{0}, t)$.

the inset of Fig. 4.2, where the initial scale Q marked by the distribution at $t = 0$ can be used as a reference.

The emergence of a mass gap in the relativistic theory explains why the dynamics in the infrared regime is governed by nonrelativistic physics. Of course, in general the presence of a mass gap does not necessarily imply the universal scaling behavior between both theories. However, it may be seen as a necessary condition for a relativistic theory to belong to the same far-from-equilibrium universality class as the Gross-Pitaevskii field theory.

4.1.4 Condensate formation

Our over-occupation initial conditions (2.61) have a vanishing condensate at initial time. However, the inverse particle cascade continuously populates the zero mode, which leads to the formation of a condensate far from equilibrium [8, 89]. Close to the nonthermal fixed point, condensate formation follows a power law evolution, as we show in the following.

To quantify Bose-Einstein condensation, we consider the (equal-time) correlation function $F(\mathbf{p}, t)$ of Eq. (2.46). Following Ref. [89], we decompose this function into a quasiparticle and a condensate part

$$\frac{f(p, t)}{\omega(p, t)} + (2\pi)^3 \delta^{(3)}(\mathbf{p}) \phi_0^2(t) = F(\mathbf{p}, t), \quad (4.9)$$

with a vanishing condensate initially $\phi_0^2(t=0) = 0$. Note that Eq. (4.9) extends our former relation (2.57), for high occupancies, by including the zero mode.⁴ To analyze our simulation results for $t > 0$, we follow Ref. [89] and note that for a finite volume V the zero mode at $\mathbf{p} = 0$ in Eq. (4.9) scales with $(2\pi)^3 \delta^{(3)}(\mathbf{0}) \mapsto V$ proportional to volume. Therefore, we can identify the condensate term by its scaling behavior as the volume is changed. Stated differently, if we divide the correlation function $F(\mathbf{p}, t)$ by volume, only correlations which scale with the system size are not suppressed at large volumes and late enough times. Then the zero mode $F(\mathbf{p} = 0, t)/V$ is related to the volume-independent part at late times.

We show this quantity during the self-similar regime for the $N = 4$ component theory in Fig. 4.8 for different volumes, ranging from $VQ_\epsilon^3 = 58^3$ to the largest volume $\sim 922^3$. All dimensional quantities have been rescaled by a suitable power of Q_ϵ . One observes that initially, the curves are separated by a volume factor since there is no condensate. However, after a transient regime the zero-momentum correlation becomes volume independent. The curves corresponding to different volumes converge towards the same value, thus signaling the formation of a condensate ϕ_0^2 filling the entire volume.

To understand the volume dependence during condensation, we show in the inset of Fig. 4.8 the zero mode $F(\mathbf{p} = 0, t)$ without dividing by volume. One observes that all curves lie on top of each other and follow the same evolution before the condensate is eventually created. This follows from the relation in Eq. (4.9). As long as the condensate is being filled, the zero mode evolves as a quasiparticle according to $F(\mathbf{p} = 0, t) \simeq f(p = 0, t)/m$. When the condensate has become large, the growth stops. The zero mode now mainly consists of the condensate part $F(\mathbf{p} = 0, t)/V \simeq \phi_0^2(t)$.

The zero-momentum correlation grows as a power-law in time, as can be observed from the straight (gray dashed) lines in the double logarithmic plot of Fig. 4.8 and its inset. The power-law growth is rather well described by the scaling exponent α found in Eq. (4.4) from the self-similar evolution of the distribution function. This can be understood from Eq. 4.9, where at zero momentum

$$F(\mathbf{p} = 0, t) \simeq \frac{f(p = 0, t)}{m} \sim t^\alpha. \quad (4.10)$$

We emphasize that the observed power-law is restricted to the formation of the condensate during the self-similar regime, where we find the scaling exponent α to govern the dynamics. In particular, we do not discuss the evolution at late times outside the regime of the classical attractor where total particle number changing processes in the relativistic theory can lead to important differences as compared to the number conserving nonrelativistic system [89].

⁴The relation (2.57) that connects $F(\mathbf{p}, t)$, $\omega(p, t)$ and $f(p, t)$ is a consequence of the equivalence between the definitions (2.47) and (2.49) for the distribution function as well as of the assumption of a quasi-free dispersion relation. We have explicitly checked that our data satisfy the relation (2.57) to high accuracy even at low momenta.

The power law growth of the zero mode is an important result of our numerical simulations. Its immediate consequence is that the time needed for a Bose-Einstein condensate to form, the condensation time t_{cond} , diverges with the system size. This can be already observed qualitatively in Fig. 4.8, where the condensate is formed in large volumes at later times. To be more quantitative, we can use the scaling exponent α to estimate this condensation time. Taking the value of the zero-momentum correlator $F(\mathbf{p} = 0, t)/V$ at the initial time t_{start} of the self-similar regime as $f(p = 0, t_{\text{start}})/V$ and its final value at the time t_{cond} as $\phi_0^2(t_{\text{cond}})$, we can estimate from $F(\mathbf{p} = 0, t)/V \sim t^\alpha$ the condensation time as

$$\begin{aligned} t_{\text{cond}} &\simeq t_{\text{start}} \left(\frac{\phi_0^2(t_{\text{cond}})}{f(p = 0, t_{\text{start}})} \right)^{1/\alpha} V^{1/\alpha} \\ &\sim V^{1/\alpha}. \end{aligned} \quad (4.11)$$

Hence, condensation time diverges as a power law of the volume. We emphasize that this is due to the self-similar evolution of the system in Eq. (3.1). In particular, this differs from predictions in perturbative kinetic theory where a finite condensation time is found [152, 153]. This will be discussed in the following section. We also note that Bose-Einstein condensation can be observed in nonrelativistic systems as well [89, 92–96]. There we find the same scaling properties as in Eqs. (4.10) and (4.11) in Ref. [118].

4.2 Universality from resummed kinetic approaches

The increase of condensation time with volume (4.11) as well as the self-similar evolution at low momenta with scaling exponents (3.1) are crucial observations to understand the mechanism for Bose-Einstein condensation. This section is devoted to finding a microscopic explanation for these phenomena.

In Refs. [152, 153] perturbative kinetic theory (see Sec. 3.3.1) was used to describe the infrared and condensation dynamics, which we will review in Sec. 4.2.1. This framework predicts a finite condensation time t_{cond} even in the infinite volume limit and involves a different self-similar scaling behavior from Eq. (3.1), where self-similarity proceeds in the time difference $t_{\text{cond}} - t$. For the over-occupied initial conditions that are employed in this chapter, these properties are not consistent with our numerical observations in Sec. 4.1. The reason for its failure lies in the fact that at low momenta, occupation numbers become non-perturbatively large $f \gtrsim 1/\lambda$ and perturbation theory breaks down. Hence, we need to employ an alternative description.

Remarkably, the over-occupied regime can still be described in terms of a generalized kinetic theory by taking into account vertex corrections, which we discuss in Sec. 4.2.2. This vertex-resummed theory will be further extended in Sec. 4.2.3 to also allow for off-shell processes and an anomalous scaling dimension η that we introduced in Sec. 3.1.

4.2.1 Condensation in a perturbative kinetic theory

We briefly summarize here main results of Refs. [152, 153]. There Bose-Einstein condensation is studied for a relativistic scalar theory within the (perturbative) kinetic framework that we discussed in Sec. 3.3.1. For the period of condensate formation only elastic $2 \leftrightarrow 2$ scattering processes are considered and the system is initialized with an over-occupied distribution with $f \gg 1$ for momenta below a typical scale. At low momenta and sufficiently late times, the distribution function exhibits self-similar behavior of the form

$$f(p, t) = B^{-\kappa}(t) f_S(p/B(t)). \quad (4.12)$$

where the function $B(t)$ decreases with time. The distribution function is constant up to a typical infrared momentum scale p_{IR} and follows an approximate time-independent power law $f(p, t) \sim p^{-\kappa}$ for larger momenta. The growth of the zero mode $f(0, t)$ can be analytically computed if the self-similar behavior of Eq. (4.12) is plugged into the kinetic equation. One then obtains

$$f(0, t) \sim (t_{\text{cond}} - t)^{-\kappa/(2(\kappa-2))}, \quad (4.13)$$

with a spectral exponent $\kappa > 2$. Therefore, as time approaches the finite condensation time $t \rightarrow t_{\text{cond}}$, the zero mode diverges $f(0, t) \rightarrow \infty$, signaling the formation of the condensate. Note that the condensation time is finite although one involves an infinite volume of the system for these kinetic considerations. Moreover, numerical simulations of the kinetic equation provide $\kappa \approx 2.48$. The authors noted that their result is close to $\kappa = 7/3$, which corresponds to a constant flux of particles in momentum space towards the condensate.

Hence, the underlying mechanism of this perturbative kinetic framework is an inverse particle cascade that populates the zero mode until a condensate is formed. While we also observe an inverse particle cascade in our lattice simulations of Sec. 4.1, the details are very different from this kinetic scenario. In our case, condensation time diverges with volume while it is finite at infinite volume in the kinetic case. The self-similar evolution of this scenario is also different from our results, where we observe self-similarity in the time t instead of the time difference $t_{\text{cond}} - t$. Moreover, we observe for large momenta within the infrared scaling region a much steeper power law $p^{-\kappa_{>}}$ with the exponent $\kappa_{>} \approx 4.5$ than what is found in the perturbative kinetic theory.

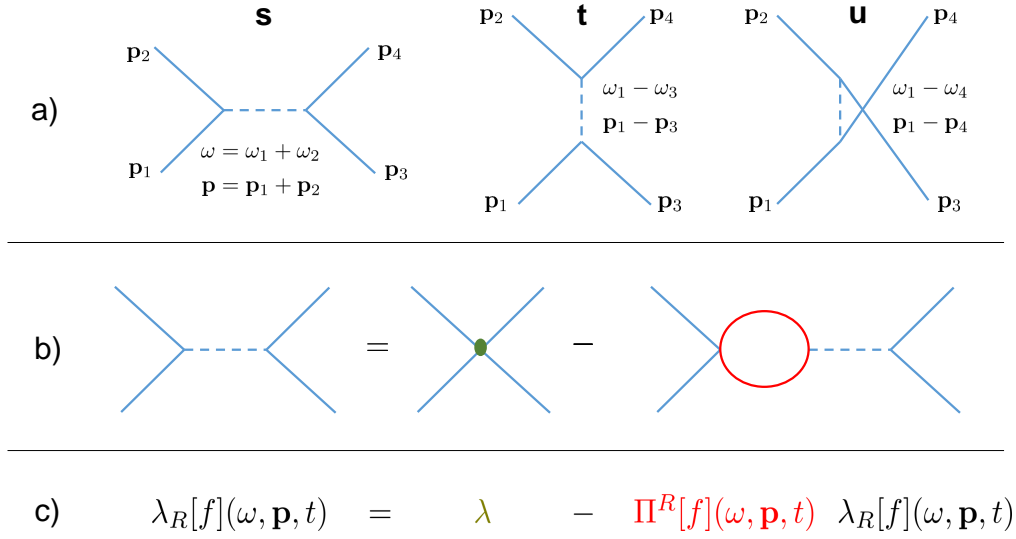


FIGURE 4.9: Effective coupling: **a)** Illustration of the different scattering channels. The vertex correction at NLO may be viewed as an effective interaction, which involves the exchange of an intermediate particle. **b)** The effective coupling can be understood as a resummation of ‘one-loop’ diagrams, which is diagrammatically illustrated. **c)** Self-consistent equation for the effective coupling λ_R corresponding to the diagrammatic illustration.

4.2.2 Vertex-resummed kinetic theory and scaling properties

As noted above, the large occupancies at low momenta require taking into account vertex corrections. For nonrelativistic and relativistic N -component field theories, important vertex corrections can be systematically computed from an expansion in the number of field components N to next-to-leading order (NLO) [7, 10, 114, 117, 154]. Already at NLO, these corrections resum scattering events up to an infinite order. This allows us to describe even the highly over-occupied regime at low momenta.

Since we want to describe condensate formation for relativistic scalars within the vertex-resummed kinetic theory, it is sufficient to consider the corresponding elastic collision integral $C_{\text{NLO}}^{2\leftrightarrow 2}[f](\mathbf{p})$. It has the same structure as the leading order elastic collision integral of Eq. (3.33) and also involves the same integration measure $\int d\Omega_d^{2\leftrightarrow 2}$ and operator $F^{2\leftrightarrow 2}[f]$ given by Eqs. (3.34) and (3.36), respectively. The only difference to the perturbative matrix element of Eq. (3.35) consists in a substitution of the coupling constant to an effective coupling

$$\lambda^2 \mapsto \lambda_{\text{eff}}^2[f](\{\mathbf{p}_i\}, t). \quad (4.14)$$

The latter depends on incoming momenta \mathbf{p}_1 and \mathbf{p}_2 and outgoing momenta \mathbf{p}_3 and \mathbf{p}_4 as well as on the distribution function $f(p, t)$, which makes it implicitly time dependent. Hence, the effective coupling λ_{eff}^2 enters the matrix element at next-to-leading order in the $1/N$ expansion

as

$$|M_{\text{NLO}}^{2\leftrightarrow 2}|^2[f](\{\mathbf{p}_i\}, t) = \frac{\lambda_{\text{eff}}^2[f](\{\mathbf{p}_i\}, t)}{6N}. \quad (4.15)$$

The effective coupling can be decomposed in scattering events in the s -, t - and u -channels that are incorporated in the resummed coupling λ_R of a single collision as

$$\lambda_{\text{eff}}^2[f](\{\mathbf{p}_i\}, t) \equiv \frac{1}{3} [|\lambda_R|^2[f](\omega_1 + \omega_2, \mathbf{p}_1 + \mathbf{p}_2, t) + |\lambda_R|^2[f](\omega_1 - \omega_3, \mathbf{p}_1 - \mathbf{p}_3, t) + |\lambda_R|^2[f](\omega_1 - \omega_4, \mathbf{p}_1 - \mathbf{p}_4, t)], \quad (4.16)$$

where we assume an on-shell dispersion relation with $\omega_i \equiv \omega(\mathbf{p}_i) = \sqrt{m^2 + \mathbf{p}_i^2}$. The coupling λ_R can be written as [117]

$$\lambda_R[f](\omega, \mathbf{p}, t) = \frac{\lambda}{1 + \Pi^R[f](\omega, \mathbf{p}, t)}, \quad (4.17)$$

with the on-shell expression for the retarded ‘one-loop’ self-energy of the relativistic theory

$$\begin{aligned} \Pi^R[f](\omega, \mathbf{p}, t) &= \lim_{\epsilon \rightarrow 0^+} \frac{\lambda}{12} \int \frac{d^d q}{(2\pi)^d} \frac{f(\mathbf{q}, t)}{\omega_{\mathbf{p}+\mathbf{q}} \omega_{\mathbf{q}}} \\ &\times \left[\frac{1}{\omega_{\mathbf{p}+\mathbf{q}} + \omega_{\mathbf{q}} - \omega - i\epsilon} + \frac{1}{\omega_{\mathbf{p}+\mathbf{q}} - \omega_{\mathbf{q}} - \omega - i\epsilon} \right. \\ &\left. + \frac{1}{\omega_{\mathbf{p}+\mathbf{q}} - \omega_{\mathbf{q}} + \omega + i\epsilon} + \frac{1}{\omega_{\mathbf{p}+\mathbf{q}} + \omega_{\mathbf{q}} + \omega + i\epsilon} \right]. \end{aligned} \quad (4.18)$$

The different scattering channels of Eq. (4.16) are depicted in the a)-panel of Fig. 4.9. Each elastic interaction can be regarded as involving the exchange of an effective intermediate particle whose four-momentum corresponds to the respective channel [114]. In essence, the effective coupling results from a resummation of diagrams [97, 117, 118]. The corresponding self-consistent equation is depicted diagrammatically in the b)-panel and mathematically in the c)-panel of Fig. 4.9. Indeed, the resummed effective coupling λ_R given by Eq. (4.17) is the solution of this self-consistent equation. We note that all of the above equations for the vertex-resummed kinetic theory correspond to the on-shell limit of more general evolution equations in Refs. [117, 155], which involve corresponding resummations. Such generalized evolution equations will be discussed in Sec. 4.2.3.

For sufficiently high momenta, the distribution function becomes $\lambda f \ll 1$ and thus the retarded self-energy becomes small $|\Pi^R[f]| \ll 1$. In this case, the resummation for the effective coupling λ_R in Fig. 4.9 can be interpreted as a geometric series summing over an infinite number of elastic scattering processes. In particular, the leading term corresponds to the coupling constant λ while higher order terms are suppressed by powers of the coupling constant. One then recovers the perturbative kinetic expressions with $\lambda_{\text{eff}}^2[f](\{\mathbf{p}_i\}, t) \rightarrow \lambda^2$.

However, we emphasize that the resummation depicted in Fig. 4.9 b) and c) is more general than a mere perturbative summation of diagrams. This self-consistent procedure leads to the effective coupling λ_R in Eq. (4.17) that is also valid for large self-energies $|\Pi^R[f]| \gg 1$ and, correspondingly, for large occupation numbers $f \gtrsim 1/\lambda$. Therefore, the resulting vertex-resummed kinetic theory is a non-perturbative kinetic method that also includes vertex corrections for large occupancies. Especially at low momenta, this changes the situation dramatically. The effective coupling of a single collision becomes $\lambda_R[f](\omega, \mathbf{p}, t) \simeq \lambda/\Pi^R[f](\omega, \mathbf{p}, t)$, which is the main difference to the perturbative condensation scenario in Sec. 4.2.1.

Before studying scaling properties of the infrared region within the vertex-resummed kinetic theory, we have to consider the form of the dispersion relation $\omega(\mathbf{p})$. As we have observed numerically in lattice simulations in Sec. 4.1.3, a medium-generated mass gap exists even if the mass parameter of the underlying microscopic theory is set to zero. The infrared scaling region is bound by the mass from above $p \leq m$ such that the infrared modes behave effectively nonrelativistically. We can therefore obtain the relevant integration measure in the infrared $\int d\Omega_{d,\text{IR}}^{2\leftrightarrow 2}$ from the general relativistic case (3.34), by expanding the dispersion relation $\omega_{\mathbf{p}} = \sqrt{p^2 + m^2} \simeq m + p^2/2m$. This leads to $\delta(\omega_{\mathbf{p}_1} + \omega_{\mathbf{p}_2} - \omega_{\mathbf{p}_3} - \omega_{\mathbf{p}_4}) \simeq \delta((p_1^2 + p_2^2 - p_3^2 - p_4^2)/(2m))$ and $2\omega_{\mathbf{p}_1} 2\omega_{\mathbf{p}_2} 2\omega_{\mathbf{p}_3} 2\omega_{\mathbf{p}_4} \simeq 16m^4$ to lowest non-vanishing order. Although the mass is approximately constant in the non-expanding case for $N > 1$ scalar theories (see Sec. 4.1.3), we keep the discussion general by considering a possible time-dependence of the effective mass $m \mapsto m(t) \sim t^{-\sigma}$. This will be particularly useful for our upcoming discussion of longitudinally expanding scalars in Chapter 6.

Let us now discuss the scaling properties that follow from the vertex-resummed kinetic theory at low momenta. To obtain these, we have to study how the collision integral changes under the rescaling of momentum and time

$$\mathbf{p} \rightarrow s \mathbf{p}, \quad t \rightarrow s^{-1/\beta} t. \quad (4.19)$$

This type of rescaling is consistent with the scaling form of the distribution function in Eq. (3.27). According to Eq. (3.33), the collision integral can be decomposed into three parts, and we first investigate each part separately. For the integration measure, we have

$$\int d\Omega_{d,\text{IR}}^{2\leftrightarrow 2}(\{\mathbf{p}_i\}, t) = s^{-3d+4\sigma/\beta+d+(2-\sigma/\beta)} \int d\Omega_{d,\text{IR}}^{2\leftrightarrow 2}(\{s\mathbf{p}_i\}, s^{-1/\beta} t). \quad (4.20)$$

With the scaling ansatz for the distribution function in Eq. (3.27), the function $F^{2\leftrightarrow 2}[f]$ scales as in Eq. (3.37). Our last ingredient to obtain the scaling properties of the full collision integral $C_{\text{NLO}}^{2\leftrightarrow 2}[f](\mathbf{p})$ is the scaling behavior of the effective coupling. To this end, we need to understand how the retarded self-energy $\Pi^R[f](\omega, \mathbf{p}, t)$ of Eq. (4.18) changes under the rescaling prescription in Eq. (4.19). In particular, we need to study how the sum in rectangular brackets

in Eq. (4.18), consisting of terms of the form

$$\frac{1}{\omega_{\mathbf{p}+\mathbf{q}} \pm \omega_{\mathbf{q}} \pm (\omega + i\epsilon)}, \quad (4.21)$$

scales after we expand $\omega_{\mathbf{p}}$. Apparently, these terms become large if the leading mass contributions cancel, in which case they scale as $\sim m(t)/p^2 = s^{2-\sigma/\beta} m(s^{-1/\beta}t)/(sp)^2$. The scaling behavior of the retarded self-energy follows from this as⁵

$$\Pi^R[f](\omega, \mathbf{p}, t) \simeq s^{\alpha/\beta+\sigma/\beta-(d-2)} \Pi^R[f](\omega_s, s\mathbf{p}, s^{-1/\beta}t). \quad (4.22)$$

For $|\Pi^R| \gg 1$ and thus $\lambda_R \simeq \lambda/\Pi^R$ at low momenta, the effective coupling of Eq. (4.16) scales as

$$\lambda_{\text{eff}}^2[f](\{\mathbf{p}_i\}, t) \simeq s^{-2(\alpha/\beta+\sigma/\beta-(d-2))} \lambda_{\text{eff}}^2[f](\{s\mathbf{p}_i\}, s^{-1/\beta}t). \quad (4.23)$$

With the determined scaling behavior of the integration measure (4.20), the effective coupling (4.23) and the function $F^{2\leftrightarrow 2}$ (3.37), we can finally obtain the scaling behavior of the vertex-resummed collision integral

$$C_{\text{NLO,IR}}^{2\leftrightarrow 2}[f](\mathbf{p}, t) \simeq s^{-2+\alpha/\beta+\sigma/\beta} C_{\text{NLO}}^{2\leftrightarrow 2}[f](s\mathbf{p}, s^{-1/\beta}t). \quad (4.24)$$

Rescaling the kinetic equation $\partial_t f = C[f]$ with the above prescription and comparing both of its sides, one obtains an equation for the scaling function $f_S(p)$ (see Eq. (3.31)) and the relation $\alpha - 1 = -\beta\mu$ for the temporal scaling exponents (see Eq. (3.30)). The scaling exponent of the collision integral μ (3.28) can be extracted from Eq. (4.24) and reads

$$\mu_{\text{NLO,IR}}^{2\leftrightarrow 2} = 2 - \alpha/\beta - \sigma/\beta. \quad (4.25)$$

This leads to the scaling exponent $\beta = (1 + \sigma)/2$. For the non-expanding theory with $N > 1$ scalar components, the mass is approximately constant. Therefore taking $\sigma = 0$ and assuming particle number conservation, we compute the scaling exponents of

$$\text{resummed particle transport in massive systems:} \quad \alpha = \frac{d}{2}, \quad \beta = \frac{1}{2}. \quad (4.26)$$

For $d = 3$ spatial dimensions, these are the same values as observed in our lattice simulations of Sec. 4.1.1. Hence, the vertex-resummed kinetic theory predicts the values of Eq. (4.26) for all numbers of components⁶ $N > 1$. The scaling exponents of the $N = 1$ scalar theory

⁵Since only sums or differences $\omega = \omega(\mathbf{p}) \pm \omega(\mathbf{q})$ enter the self-energy in the definition of the effective coupling (4.16), the frequency ω has to be suitably rescaled as $\omega_s = \omega(s\mathbf{p}) \pm \omega(s\mathbf{q})$.

⁶This can be seen as follows. Using $m^2 \sim \int d^3p f/\omega$ to estimate the effective mass, one finds that it is dominated by soft momenta because of the strong enhancement of the infrared scaling region. Inelastic $4 \rightarrow 2$ scattering processes with only soft incoming particles are highly suppressed because of charge conservation for $N > 1$ scalar components [144], similar to what we discussed in Sec. 3.2.3. Therefore, the effective mass is approximately constant for $N > 1$.

receive small corrections due to the time-dependence of the effective mass. As we discussed in Sec. 3.2.3, the effective mass decreases with exponent $\sigma = 1/3$. The vertex-resummed kinetic theory thus predicts the slightly different values $\alpha = 2$ and $\beta = 2/3$ for the scaling exponents for $N = 1$.

Such differences are absent when considering the scaling function $f_S(p)$ within the vertex-resummed kinetic framework. As noted above, the scaling function has to satisfy the time-independent equation (3.31) with the resummed collision integral $C_{\text{NLO}}^{2\leftrightarrow 2}[f_S]$. The number of components N only appears as an overall factor in the collision integral. It can be scaled out entirely by rescaling the distribution function $f_S(p)/\sqrt{N} \mapsto f_S(p)$, and thus it does not affect the functional form of $f_S(p)$. We therefore conclude that, apart from the small corrections for the scaling exponents for $N = 1$, the vertex-resummed kinetic theory predicts the same scaling exponents and the same scaling function independent of the number of scalar components N . Indeed, we observed in our lattice simulations of Sec. 4.1.1 the same scaling function $f_S(p)$ given by Eq. (4.2) and, within numerical uncertainties, the same scaling exponents as in Eq. (4.26) for $N = 2$ and $N = 4$ scalar theories. The N -independence of the scaling function is further confirmed in Ref. [144] for scalar theories with $N = 1, 2, 3, 4, 8$ field components. Hence, the same scaling properties are obtained in lattice simulations even for small N , which can be understood within the vertex-resummed kinetic framework. This is quite surprising given the fact that the vertex-resummed kinetic theory is derived from a $1/N$ expansion to NLO. Nevertheless, it provides a microscopic explanation for the observed universality.

In Sec. 4.1.2 we showed with lattice simulations that nonrelativistic Bose gases share the same scaling properties as obtained in relativistic systems, to good numerical accuracy. A similar vertex-resummed kinetic theory can be formulated for nonrelativistic scalar fields, as we will show in Sec. 4.2.3. The corresponding integration measure reads

$$\int d\Omega_{d,\text{nr}}^{2\leftrightarrow 2}(\{\mathbf{p}_i\}) = \int \frac{d^d p_2}{(2\pi)^d} \frac{d^d p_3}{(2\pi)^d} \frac{d^d p_4}{(2\pi)^d} (2\pi)^{d+1} \delta(\omega_1 + \omega_2 - \omega_3 - \omega_4) \delta^{(d)}(\mathbf{p}_1 + \mathbf{p}_2 - \mathbf{p}_3 - \mathbf{p}_4), \quad (4.27)$$

with the dispersion relation $\omega_{\mathbf{p}} = \mathbf{p}^2/(2m)$. The vertex-resummed matrix element of the nonrelativistic theory can be written as

$$|M_{\text{NLO,nr}}^{2\leftrightarrow 2}|^2[f](\mathbf{p}_1, \mathbf{p}_3, t) \sim |g_{\text{eff}}|^2[f](\mathbf{p}_1, \mathbf{p}_3, t), \quad (4.28)$$

and corresponds therefore to the t - and, after switching the integration variables p_3 and p_4 , to the u -channel interactions of Fig. 4.9 a). In complete analogy to the relativistic case in Eq. (4.17), the effective coupling is given by

$$g_{\text{eff}}[f](\mathbf{p}_1, \mathbf{p}_3, t) = \frac{g}{1 + \Pi_{\text{nr}}^R[f](\omega_1 - \omega_3, \mathbf{p}_1 - \mathbf{p}_3, t)} \quad (4.29)$$

with the nonrelativistic ‘one-loop’ retarded self-energy

$$\Pi_{\text{nr}}^R[f](\omega, \mathbf{p}, t) = \lim_{\epsilon \rightarrow 0^+} 2g \int \frac{d^d q}{(2\pi)^d} f(\mathbf{p} - \mathbf{q}, t) \left[\frac{1}{\omega_{\mathbf{q}} - \omega_{\mathbf{p}-\mathbf{q}} - \omega - i\epsilon} + \frac{1}{\omega_{\mathbf{q}} - \omega_{\mathbf{p}-\mathbf{q}} + \omega + i\epsilon} \right]. \quad (4.30)$$

Using the scaling behavior of the distribution function in Eq. (3.27), one obtains the same scaling relations for $\int d\Omega_{d,\text{nr}}^{2\leftrightarrow 2}$, $F^{2\leftrightarrow 2}[f]$, Π_{nr}^R and $|M_{\text{NLO},\text{nr}}^{2\leftrightarrow 2}|^2$ as discussed above for the relativistic theory with a constant mass. Consequently, it leads to the same scaling exponents as in the relativistic case in Eq. (4.26). We thus find in the over-occupied infrared regime the same scaling exponents within the vertex-resummed descriptions for both nonrelativistic and relativistic N -component scalar field theories. This is an important analytical result of our discussion. The quantitative agreement of the scaling exponents $\alpha = 3/2$ and $\beta = 1/2$ for $d = 3$ with the full simulation results of section 4.1 is remarkable.

Because of the positive values of α and β and their relation $\alpha = d\beta$, the underlying mechanism for Bose-Einstein condensation in the resummed kinetic theory can be understood as an inverse particle cascade to lower momenta. It considerably differs from the perturbative mechanism of Sec. 4.2.1 because it involves a self-similar behavior in time t instead of self-similarity in the difference $t_{\text{cond}} - t$. In particular, the mechanism of the resummed theory does not imply a finite condensation time.

For comparison, we repeat our scaling analysis for the vertex-resummed relativistic kinetic equation in the absence of any mass gap. To this end, we use $\omega_{\mathbf{p}} = p$ and proceed as above to find scaling relations for α and β . With

$$C_{\text{NLO},m=0}^{2\leftrightarrow 2}[f](\mathbf{p}, t) = s^{\alpha/\beta-1} C_{\text{NLO},m=0}^{2\leftrightarrow 2}[f](s\mathbf{p}, s^{-1/\beta}t), \quad (4.31)$$

we find for the

$$\text{resummed particle transport with } m = 0: \quad \alpha = d, \quad \beta = 1. \quad (4.32)$$

These estimates indicate that the simulation results of Sec. 4.1.1 for the relativistic theory cannot be interpreted in terms of a massless scaling region in the infrared, which is further supported by the presence of a mass gap found in Sec. 4.1.3.

4.2.3 Anomalous scaling beyond vertex-resummed kinetic theory

The vertex-resummed kinetic theory considered above is an on-shell approximation of a more general transport equation. The latter is discussed in this subsection for the nonrelativistic theory and it is used to derive the corresponding scaling exponents. We will also outline how

the vertex-resummed kinetic theories discussed above can be obtained from such transport equations.

The transport equation is formulated with statistical and spectral correlation functions F and $\tilde{\rho} = -i\rho$ of the nonrelativistic theory that are defined as

$$\begin{aligned} F_{ab}(x, y) &= \frac{1}{2} \left\langle \left\{ \Psi_a(x), \Psi_a^\dagger(y) \right\} \right\rangle - \langle \Psi_a(x) \rangle \langle \Psi_b^\dagger(y) \rangle, \\ \tilde{\rho}_{ab}(x, y) &= \left\langle \left[\Psi_a(x), \Psi_a^\dagger(y) \right] \right\rangle, \end{aligned} \quad (4.33)$$

with the abbreviated notation $x = (\mathbf{x}, x^0)$. Here, Ψ and Ψ^\dagger are the Heisenberg field operators of the complex scalar fields ψ and ψ^* with the classical action given by Eq. (2.10) of Sec. 2.1.3. The index notation $a, b = 1, 2$ in Eq. (4.33) employs

$$\Psi_1 \equiv \Psi, \quad \Psi_2 \equiv \Psi^\dagger, \quad (4.34)$$

in order to have a compact notation for the different two-point functions that can be built from two complex fields. The correlation functions in Eq. (4.33) are defined in complete analogy to the relativistic theory in Eq. (2.34).

The quantum evolution equations for the correlation functions F and $\rho = i\tilde{\rho}$ for Gaussian initial conditions can be derived within the 2PI effective action framework, as we noted at the end of Sec. 2.2.1, and their evolution equations at NLO in the 2PI $1/N$ expansion are known [10, 114, 154]. Additionally, one can employ a gradient expansion to lowest order [148] and Fourier transform the correlation functions (as in footnote 4 of Sec. 2.2.1) to $(F_p)_{ab} \equiv F_{ab}(p^0, \mathbf{p}, t)$ and $(\tilde{\rho}_p)_{ab} \equiv \tilde{\rho}_{ab}(p^0, \mathbf{p}, t)$. The resulting transport equation reads [118, 155]

$$\begin{aligned} \frac{\partial}{\partial t} \text{Tr}[F_1] &= - \frac{2}{(2\pi)^{2d+2}} \int d^{d+1}p_2 d^{d+1}p_3 d^{d+1}p_4 \delta^{(d+1)}(p_1^\mu + p_2^\mu - p_3^\mu - p_4^\mu) |g_{\text{eff}}|^2[F](p_1^\mu - p_3^\mu, t) \\ &\times \left\{ 2 \text{Tr}[\sigma^3 F_1 F_3] \text{Tr}[F_2 \tilde{\rho}_4] + \text{Tr}[\sigma^3 F_1 \tilde{\rho}_3] \text{Tr}[F_2 F_4] - \text{Tr}[\sigma^3 \tilde{\rho}_1 F_3] \text{Tr}[F_2 F_4] \right\}, \end{aligned} \quad (4.35)$$

in a compact four vector $p^\mu = (p^0, \mathbf{p})$ and matrix notation in (a, b) -index space with $\text{Tr}[F_p] \equiv F_{aa}(p^\mu, t)$ and $\sigma^3 = \text{diag}(1, -1)$ denotes the third Pauli matrix.⁷ The time- and momentum-dependent effective coupling corresponding to Eq. (4.29) reads

$$g_{\text{eff}}[F](p^0, \mathbf{p}, t) = \frac{g}{1 + \Pi_{\text{nr}}^R[F](p^0, \mathbf{p}, t)} \quad (4.36)$$

with the retarded self-energy

$$\Pi_{\text{nr}}^R[F](p^0, \mathbf{p}, t) = 2g \int \frac{d^{d+1}q}{(2\pi)^{d+1}} F_{ab}(q^\mu - p^\mu, t) G_{ba}^R(q^\mu, t). \quad (4.37)$$

⁷The corresponding transport equation for the spectral function is $\partial_t \tilde{\rho}_{ab}(p^0, \mathbf{p}, t) = 0$ to leading order gradient expansion, which implies time-independence of $\tilde{\rho}$.

The retarded propagator G_{ab}^R is related to the spectral function by

$$G_{ab}^R(p^0, \mathbf{p}, t) = \int \frac{d\omega}{2\pi} \frac{\tilde{\rho}(\omega, \mathbf{p}, t)}{\omega - p^0 - i\epsilon}, \quad (4.38)$$

with the implied limit $\epsilon \rightarrow 0^+$.

Before discussing the scaling properties of the generalized transport equation (4.35), we explain how the vertex-resummed kinetic theory discussed in the previous subsection can be derived from it. In analogy to the relativistic case in Eq. (2.36), one defines a generalized (off-shell) occupation number $f(p^0, \mathbf{p}, t)$ by

$$F_{ab}(p^0, \mathbf{p}, t) = \left(f(p^0, \mathbf{p}, t) + \frac{1}{2} \right) \tilde{\rho}_{ab}(p^0, \mathbf{p}, t), \quad (4.39)$$

with $-f(-p^\mu, t) = f(p^\mu, t) + 1$. Most importantly, one assumes a free-field form of the spectral function [155]

$$\tilde{\rho}(p^0, \mathbf{p}) = 2\pi \begin{pmatrix} \delta(p^0 - \omega_{\mathbf{p}}) & 0 \\ 0 & -\delta(p^0 + \omega_{\mathbf{p}}) \end{pmatrix}, \quad (4.40)$$

where $\omega_{\mathbf{p}} = \mathbf{p}^2/2m$. Plugging Eqs. (4.39) and (4.40) into the evolution equation (4.35), and defining the distribution function as

$$f(\mathbf{p}, t) + \frac{1}{2} = \frac{1}{2} \int \frac{dp^0}{2\pi} F_{aa}(p^0, \mathbf{p}, t), \quad (4.41)$$

one obtains the vertex-resummed kinetic theory for nonrelativistic scalars that we discussed above. Since we are only interested in the over-occupied regime $f(\mathbf{p}, t) \gg 1$, we additionally drop the 1/2 for our scaling analysis.

In the relativistic case, the derivation proceeds in complete analogy to the nonrelativistic theory. The corresponding evolution equations for F are derived in Ref. [117]. The vertex-resummed kinetic equation follows from the definition of the generalized occupation number in Eq. (2.36), an on-shell assumption for the spectral function in Eq. (2.58) and the definition of the (on-shell) distribution function in Eq. (2.60).

To study the scaling properties of the transport equation (4.35), we make the scaling ansatz for correlation functions

$$\begin{aligned} F_{ab}(p^0, \mathbf{p}, t) &= t^{\alpha+\beta z} F_{S,ab}(t^\beta z p^0, t^\beta \mathbf{p}) \\ \rho_{ab}(p^0, \mathbf{p}, t) &= t^{(2-\eta)\beta} \rho_{S,ab}(t^\beta z p^0, t^\beta \mathbf{p}). \end{aligned} \quad (4.42)$$

This scaling form is similar to Eq. (3.5) of Sec. 3.1 in the relativistic theory and involves a nonequilibrium anomalous dimension η and dynamic scaling exponent z . Plugging Eq. (4.42)

into the effective coupling, one obtains

$$|g_{\text{eff}}|^2[F](p^0, \mathbf{p}, t) = t^{-2[\alpha + \beta(2 - \eta - d)]} |g_{\text{eff}}|^2[F_S](t^{z\beta} p^0, t^\beta \mathbf{p}). \quad (4.43)$$

Integrating Eq. (4.35) with $\int dp^0/(4\pi)$, the transport equation can be brought into a kinetic form $\partial_t f(\mathbf{p}, t) = C[F](\mathbf{p}, t)$ with the right hand side scaling as

$$C[F](\mathbf{p}, t) = t^{\alpha - \beta(2 - \eta)} C[F_S](t^\beta \mathbf{p}). \quad (4.44)$$

By analogy with our discussion in Sec. 3.3 on kinetic theory, one obtains a relation for the temporal exponents $\alpha - 1 = \alpha - \beta(2 - \eta)$ and the fixed point equation $[\alpha + \beta \mathbf{p} \cdot \nabla_{\mathbf{p}}] f_S(\mathbf{p}) = C[F_S](\mathbf{p})$. While the prior relation already determines the exponent β , we additionally assume particle number conservation $n = \int d^{d+1}p/(2\pi)^{d+1} F_{aa}/2 = \text{const.}$ This leads to the same relation as for the vertex-resummed kinetic theory $\alpha = d\beta$. In summary, we find for the

$$\text{generalized particle transport (nonrelativistic):} \quad \alpha = \frac{d}{2 - \eta}, \quad \beta = \frac{1}{2 - \eta}. \quad (4.45)$$

These values do not assume an on-shell approximation of the spectral function as in the vertex-resummed kinetic theory. Interestingly, the dynamic exponent z cancels in the calculation while the values involve the anomalous dimension η , which generalizes the values in Eq. (4.26). However, since the latter accurately describes our lattice results obtained in Sec. 4.1 for different theories, we find, within our numerical errors, no strong indication for a deviation from the canonical value $\eta = 0$. Nevertheless, the analytical results in Eq. (4.45) can be used in future studies to investigate if η takes a (small) non-vanishing value and if this value depends on the underlying theory.

4.3 Summary

In this chapter, we have studied the scaling region of scalar systems at low momenta that is responsible for Bose-Einstein condensation far from equilibrium. We have found in our lattice simulations that the scaling properties of both nonrelativistic and relativistic $O(N)$ -symmetric scalar systems for different numbers of components N agree to good accuracy. This indicates that the corresponding scaling regions of the different scalar theories are part of a broad universality class.

We have also obtained the scaling properties of the region. The values of the scaling exponents are $\alpha \approx 3/2$ and $\beta \approx 1/2$, which confirms the interpretation of an inverse particle cascade. Its scaling function can be written as $f_S(p) \simeq a/((x/b)^{\kappa_<} + (x/b)^{\kappa_>})$, with spectral exponents $\kappa_< \simeq 1/2$ and $\kappa_> \simeq 4.5$. Interestingly, the value of $\kappa_>$ is rather close to the value obtained for stationary turbulence in nonrelativistic systems.

The universality can be partially attributed to the observation that a medium generated effective mass emerges in relativistic scalars. All momenta within the scaling region are below this mass, which is approximately constant for $N \geq 2$ component scalar systems.

We have also studied condensate formation. The zero mode can be understood as an extension of the scaling region at low momenta and grows with the same scaling exponent α , until the growth stops, signaling the formation of the condensate. The formation time of the Bose-Einstein condensate diverges with volume $t_{\text{cond}} \sim V^{1/\alpha}$. In contrast, previous studies in perturbative kinetic theory predicted a finite condensation time even for an infinite volume.

As discussed in the beginning of this chapter, an analytical study of this scaling region needs to account for its high occupation numbers. Therefore, we employed the vertex-resummed kinetic theory. By use of scaling arguments, we were able to reproduce the values of the scaling exponents α and β . Moreover, the vertex-resummed kinetic theory predicts that these values, as the functional form of $f_S(p)$, are independent of the number of scalar components N and are the same for the nonrelativistic theory. Our lattice simulations are consistent with these results. The good agreement of the analytical results from the vertex-resummed kinetic theory with lattice data is quite surprising given the fact that this effective kinetic theory is based on a $1/N$ expansion to next-to-leading order.

The vertex-resummed kinetic theory can be extended to also involving off-shell processes in the dynamics. These more general transport equations lead to the values $\alpha = d/(2 - \eta)$ and $\beta = 1/(2 - \eta)$, with a possible anomalous dimension η . These results allow to measure η in future studies. Our numerical results indicate a small $\eta \approx 0$ within our numerical precision.

Chapter 5

Universality class and thermalization in expanding systems

In this chapter, we present a novel universality class of non-Abelian plasmas and superfluid scalar systems far from equilibrium. Together with the studies in the following chapter, our results provide a direct link between heavy-ion collisions and ultracold Bose gases. Since symmetries and underlying scattering processes for scalar and gauge theories show profound differences, the observation of universal dynamics in this case is highly nontrivial. To put our studies in the context of heavy-ion collision experiments, in both cases we investigate longitudinally expanding systems in three spatial dimensions.

Apart from the new universality class, we analyze the nonthermal fixed point of non-Abelian plasmas in more detail than we have found previously [14]. We also discuss its consequences on the equilibration mechanisms of heavy-ion collisions at weak couplings. Including recent literature, this leads to a consistent picture of thermalization that we also present. We note that a detailed analysis of the entire nonthermal fixed point in scalar systems and its different scaling regions is moved to Chapter 6.

This chapter involves the following content. We first adjust our concepts concerning non-thermal fixed points to longitudinally expanding systems (Sec. 5.1). We then report of the novel universality class for longitudinally expanding systems (Sec. 5.2). In Sec. 5.3 we further analyze the nonthermal fixed point of expanding non-Abelian plasmas and discuss its consequences on the thermalization process in heavy-ion collisions at weak couplings. We conclude this chapter with a summary of our results in Sec. 5.4.¹

¹We have published some parts presented in this chapter in Refs. [2, 14, 15]. Some preliminary results of this and the following chapter have been included in [145].

5.1 Nonthermal fixed points in expanding media

The space-time evolution of systems in the context of heavy-ion collisions is naturally formulated in Bjorken coordinates, as we noted in Sec. 2.1.1. The metric tensor in the new coordinates describes a longitudinally expanding space-time. The general picture of a thermalization process in Fig. 1.1 is also valid for longitudinally expanding systems, and we extend the concept of nonthermal fixed points to expanding media in this section.

For the following presentation, we classify dynamic universality classes in terms of scaling properties of a time-dependent distribution function. For longitudinally expanding systems, the distribution function depends on proper time τ , on transverse momentum p_T , and on longitudinal momentum that we define as $p_z = \nu/\tau$ with the rapidity wave number ν (see Sec. 2.1.1 and footnote 6). In the scaling regime the distribution is then determined by a time-independent scaling function f_S , an overall scaling with time described by the scaling exponent α , and two exponents β and γ for the scaling with transverse and longitudinal momentum

$$f(p_T, p_z, \tau) = \tau^\alpha f_S \left(\tau^\beta p_T, \tau^\gamma p_z \right). \quad (5.1)$$

These scaling exponents determine the scaling behavior of typical momenta $p_{T,\text{typ}} \sim \tau^{-\beta}$ and $p_{z,\text{typ}} \sim \tau^{-\gamma}$ and of the amplitude at typical momenta $f(p_{T,\text{typ}}, p_{z,\text{typ}}) \sim \tau^\alpha$. As in the non-expanding case, systems belonging to the same universality class have the same values for α , β and γ as well as the same form of $f_S(p_T, p_z)$ in a given inertial range of momenta. A nonthermal fixed point may consist of several scaling regions each of which has its own set of scaling exponents and scaling function, and is located in some separate momentum region of the distribution function.

A major complication to the static case is that, as a consequence of longitudinal expansion, energy density has a non-trivial evolution that can be described by Bjorken's law

$$\partial_\tau \epsilon = - \frac{\epsilon + P_L}{\tau}. \quad (5.2)$$

The evolution of the energy density hence depends on the expansion rate $1/\tau$ as well as the evolution of the longitudinal pressure P_L . Therefore it is in general not possible to determine the final temperature of the system without further assumptions about the evolution, which makes the thermalization process more complicated than in the static case.

Moreover, the one-dimensional expansion of the system also leads to a red shift of longitudinal momentum modes. Interactions naturally compete with this process but it is a non-trivial question whether they are sufficiently strong to maintain a close-to-isotropic system at all times of the evolution, or if the system becomes anisotropic. In the latter case, the dynamical equation of state $P_L(\tau)/\epsilon(\tau)$ of the system becomes small and the energy density approaches the scaling behavior $\epsilon \sim \tau^{-1}$ that is independent of P_L . This scaling behavior is a direct

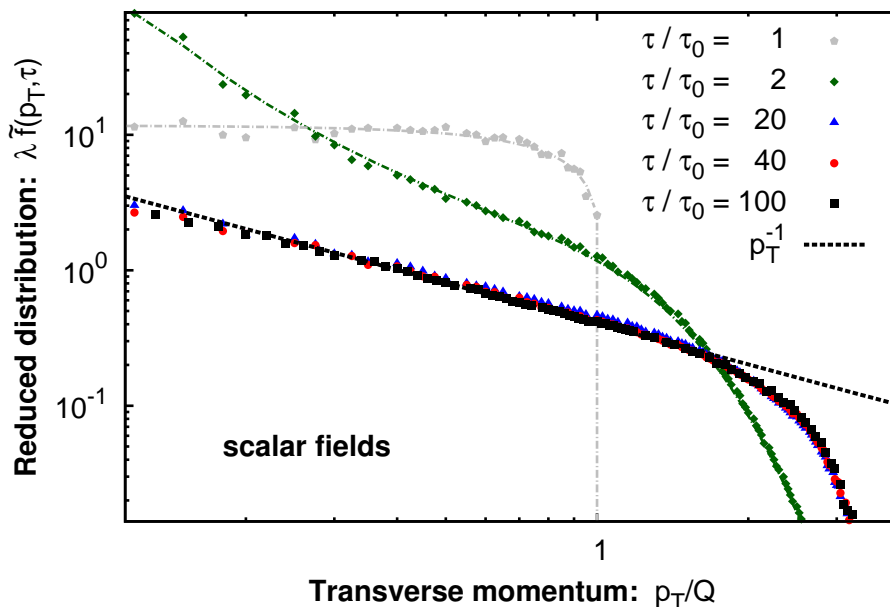


FIGURE 5.1: The scalar reduced distribution quickly approaches a time-independent form, with $\lambda \tilde{f}(p_T, \tau) \sim 1/p_T$ for $p_T \lesssim Q$.

consequence of the dilution of the system due to the expansion that expresses itself in the expansion rate $1/\tau$ in Eq. (5.2). Similarly, particle number density decreases due to the dilution of the system as $n \sim \tau^{-1}$. When discussing conservation laws, we therefore rescale the conserved quantity by time, such that energy or particle number density conservation read $\tau \epsilon \sim \text{const}$ and $\tau n \sim \text{const}$.

It is not clear a priori whether the dynamics of expanding systems may exhibit the scaling features associated with a non-thermal fixed point. This is in particular because of the competition of interactions with the red shift of longitudinal momentum modes, and the dilution of the system. Therefore the central questions concerning the evolution of expanding systems are:

- 1) How efficient are interactions as compared to the expansion? How does the anisotropy of the system evolve?
- 2) Do expanding systems approach nonthermal fixed points? What are their scaling properties?
- 3) Does a common universality class exist that involves different field theories?

We will address these questions using the machinery of real-time classical-statistical lattice simulations that we introduced in Sec. 2.3 and App. B.

5.2 Universality class in expanding systems: From non-Abelian plasmas to superfluid scalars

In the following, we address the questions raised in the previous section. In particular, we will find that expanding scalar and gauge systems approach nonthermal fixed points which lie in the same universality class. Before discussing the details of the scaling regions, we reduce the distribution and study the conservation laws.

5.2.1 Reduced distribution and conservation laws

To consider general properties of expanding highly correlated systems at weak couplings, we reduce the distribution function by integrating over longitudinal momenta

$$\tilde{f}(p_T, \tau) = \frac{\tau}{\tau_0} \int \frac{dp_z}{2\pi Q} f(p_T, p_z, \tau). \quad (5.3)$$

In the definition of the reduced distribution we additionally multiply with time, which counteracts the dilution from the expansion. The longitudinal reduction considerably simplifies the distribution. For this quantity, we do not need to deal with the competition of interactions with the red shift of longitudinal momentum modes or with the evolution of the anisotropy of the system. Therefore, the reduced distribution is a suitable quantity for a first general approach to expanding systems.

If not stated otherwise, we employ over-occupation initial conditions (2.61) for both scalar and gauge fields, with initial parameters $n_0 = 35$, $\xi_0 = 1$ and $Q\tau_0 = 10^3$ for a scalar theory with $N = 4$ components, and with $n_0 = \xi_0 = 1$ and $Q\tau_0 = 10^2$ for an $SU(2)$ gauge theory. For the scalar theory we employ up to $192^2 \times 768$ lattices with spacings $Qa_T = 0.5 - 1.1$ and $Q\tau_0 a_\eta = 0.04 - 0.075$ in transverse and longitudinal directions. For gauge fields we use transverse and longitudinal lattice sizes $N_T = 256 - 512$ and $N_\eta = 1024 - 4096$ with lattice spacings $Qa_T = 0.5 - 1$ and $a_\eta = (0.625 - 2.5) \cdot 10^{-3}$. Simulation results with other initial conditions of the scalar theory are postponed to Chapter 6. For non-Abelian plasmas, we have varied initial conditions and parametrization in Refs. [14, 15] and we will show some of the results in Sec. 5.3 and App. D.

The reduced distribution for scalar systems is plotted as a function of transverse momentum at different times in Fig. 5.1. One observes that it quickly reaches an approximately time-independent form. With the scaling ansatz (5.1) follows $\tilde{f}(p_T, \tau) \sim \tau^{\alpha-\gamma+1} \int dp_z f_S(\tau^\beta p_T, p_z)$ such that time independence implies the scaling relations

$$\alpha - \gamma + 1 = 0 \quad , \quad \beta = 0. \quad (5.4)$$

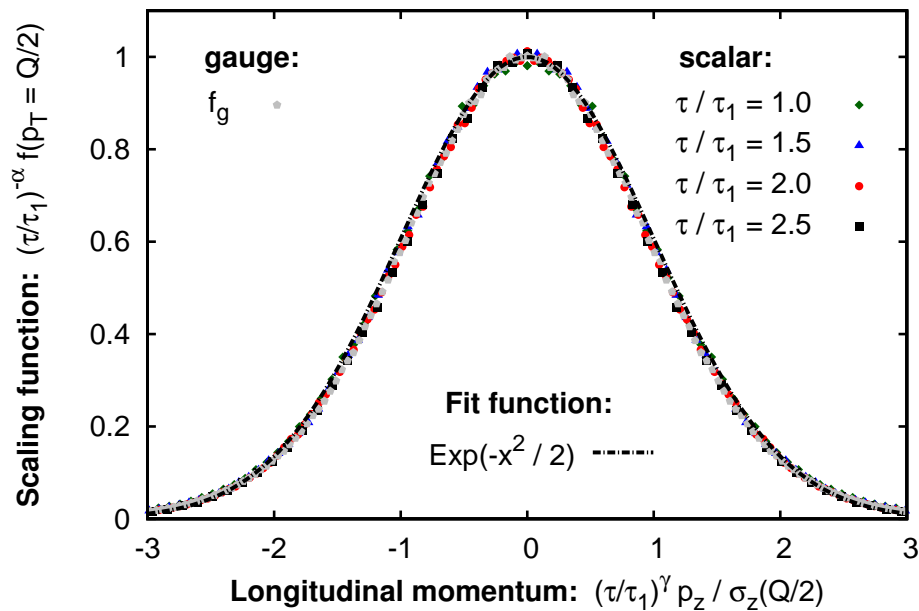


FIGURE 5.2: The normalized fixed point distribution ($\tau_1 = 40 \tau_0$) for the scalar theory compared to the gauge theory.

We have explicitly verified that the same relations hold in the scalar field theory case also for $N = 2$ components. Remarkably, the very same relations have been observed in Ref. [14] for non-Abelian gauge theory.

In order to clarify the physics that determines the universality class, we note that Fig. 5.1 also exhibits a rather accurate power law $\tilde{f}(p_T, \tau) \sim 1/p_T$ for $p_T \lesssim Q$. Hence the particle number per transverse momentum mode $\tau dn/dp_T \sim p_T \tilde{f}$ is uniformly distributed over transverse momenta and constant as a function of time. Since the longitudinal momenta are red-shifted due to the expansion, one finds $p_z \ll p_T$ for typical momentum modes. Accordingly, the energy distribution per transverse mode $\tau d\epsilon/dp_T \sim p_T^2 \tilde{f}$ is also independent of time. Thus there is effectively neither a particle nor an energy flux in transverse momentum, which is implied by $\beta = 0$ in Eq. (5.4).

The existence of a scaling solution where both energy and particle number are conserved within the momentum range of the scaling region is remarkable when contrasted to the discussion in isotropic systems without longitudinal expansion of Sec. 3.1. There is no single scaling solution conserving both energy and particle number in the non-expanding case. Instead only one conservation law constrains the scaling solution.

The fact that for longitudinally expanding systems both conservation laws are effective in the same momentum regime works in favor of a large universality class encompassing rather different systems. For instance, the exponent $\beta = 0$ is entirely fixed by enforcing both conservation laws without further knowledge about the underlying dynamics. Consequently, one may expect the same exponent to appear in a larger class of isolated systems, which are dominated

by number conserving processes and undergo a longitudinal expansion. In contrast, one of the scaling exponents α or γ and the scaling function f_S are not fixed by conservation laws. The observation that theories with different symmetry groups and number of field components can exhibit the same universal aspects is intriguing.

5.2.2 Details of the universal scaling region

The conservation laws at each transverse momentum mode reported in the previous subsection indicate that modes are redistributed along the longitudinal direction. Fig. 5.2 shows our results for the scalar theory for intermediate momenta $p_T \sim Q/2$, where the rescaled distribution as a function of the rescaled longitudinal momentum is given for different times. According to Eq. (5.1) this fixed point distribution should be independent of time. Indeed we find that all data collapses onto a single curve using the scaling exponents

$$\alpha = -2/3, \quad \beta = 0, \quad \gamma = 1/3, \quad (5.5)$$

to few percent accuracy² in accordance with the scaling relation (5.4). The same exponents as in Eq. (5.5) were found to characterize non-Abelian plasmas [14]. Note that a freely streaming system suffers under the longitudinal red shift $p_{z,\text{typ}}^{\text{free}} \sim \tau^{-1}$ while the occupancy and typical transverse momenta do not change without interactions. Hence, free streaming implies the exponents $\alpha_{\text{free}} = 0$, $\beta_{\text{free}} = 0$ and $\gamma_{\text{free}} = 1$. Our observed values in Eq. (5.5) thus clearly indicate the importance of interactions counteracting the red shift. However, they are not efficient enough to maintain a constant anisotropy since $\beta \neq \gamma$, such that the typical anisotropy $p_{T,\text{typ}}/p_{z,\text{typ}} \sim \tau^{\gamma-\beta}$ of the system increases with time. In Fig. 5.2, we also give our results for the normalized fixed point distribution of the non-Abelian gauge theory. The Gaussian shaped curve with width squared $\sigma_z^2(p_T) = \int dp_z p_z^2 f(p_T, p_z, \tau_1) / \int dp_z f(p_T, p_z, \tau_1)$ for the scalar theory is seen to accurately agree with the corresponding gauge theory case. Since also the scaling exponents agree in both theories, we encounter a new universal regime.

To further analyze this universality, we study the transverse momentum distribution. Fig. 5.3 shows the scalar and gauge distribution function at vanishing longitudinal momentum for different times. The data in the top panel is shown for an $N = 4$ scalar system but we find similar results also for $N = 2$. At intermediate momenta one finds a $\sim 1/p_T$ behavior. The longitudinal distribution in Fig. 5.2 was shown at $p_T \sim Q/2$ located within this scaling region. Hence, this power law is a property of the scaling region. In the bottom panel of Fig. 5.3, we show the corresponding results for the gauge theory distribution function. Again we see a $\sim 1/p_T$ behavior, for non-Abelian plasmas even in nearly the entire momentum range. Hence, this power law is a characteristic feature of the scaling region. We have verified that the scaling behavior of Eq. (5.1), with the exponents in Eq. (5.5) up to systematic errors, is realized in the

²We will discuss the error bars in Sec. 6.1.3 in detail.

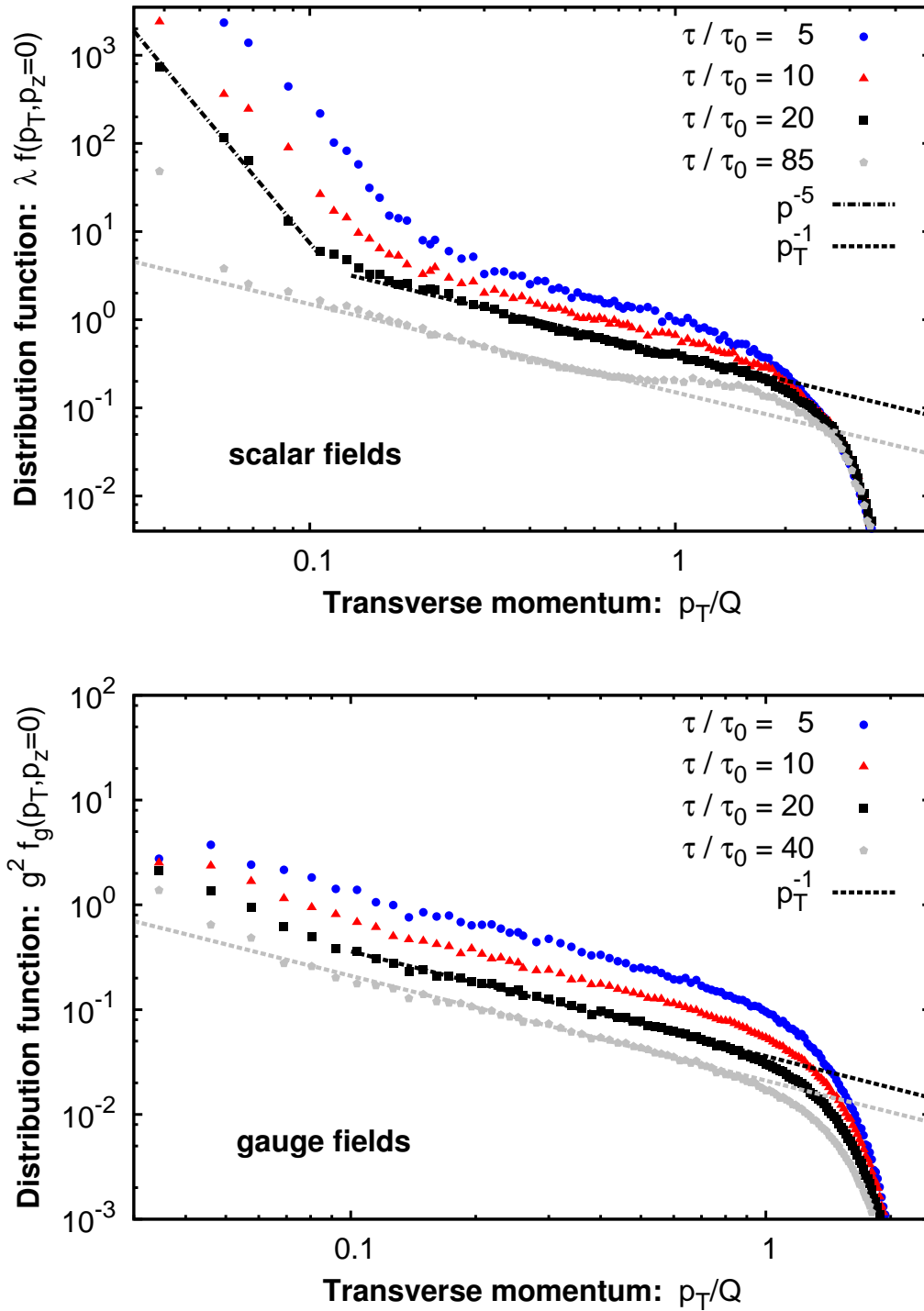


FIGURE 5.3: (**top**) The distribution function for the scalar theory at $p_z = 0$ for different times up to $\tau/\tau_0 = 85$. (**bottom**) The gauge theory distribution function at $p_z = 0$ for different times up to $\tau/\tau_0 = 40$, with $g^2 \equiv 4\pi\alpha_s$.

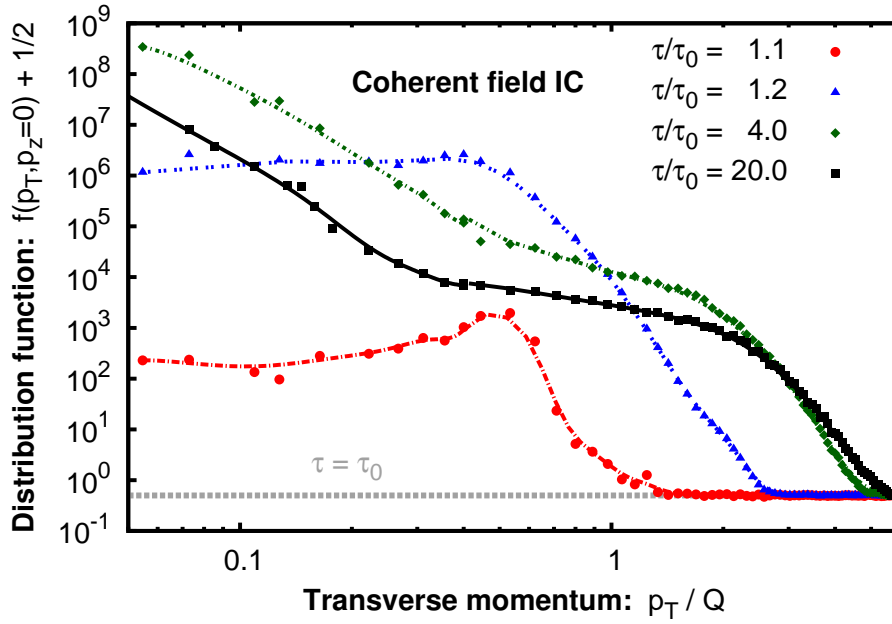


FIGURE 5.4: Snapshots of the scalar distribution at vanishing longitudinal momentum at different times for the coherent field initial conditions in Eq. 2.62, with coupling constant $\lambda = 10^{-4}$. Starting with the pure vacuum (gray) distribution, fluctuations are built up via the parametric resonance mechanism (red circles) and lead to an over-occupied system (blue triangles). The latter approaches the nonthermal fixed point (green rhombi and black squares) that was observed with over-occupation initial conditions above.

entire momentum region described by the $1/p_T$ power law for both the scalar and the gauge field theory.

These results are a striking manifestation of universality. Indeed, since the scaling exponents α , β and γ in Eq. (5.5) as well as the scaling function f_S agree for both theories, these scaling regions of expanding scalar and gauge theories lie in the same universality class. This is the first example for a far-from-equilibrium universality class for scalar and gauge systems.

5.2.3 Scaling regions in expanding scalar and gauge theories

In the upper panel of Fig. 5.3, apart from the $\sim 1/p_T$ behavior at intermediate momenta, one observes a distinct infrared regime for scalar systems below the momentum scale where the occupation number becomes of order $\sim 1/\lambda$. While this infrared regime limits from below the $1/p_T$ behavior at intermediate momenta, the figure shows that the bound shifts towards lower momenta at later times. The inertial momentum range satisfying the $1/p_T$ power law increases with time on a logarithmic scale, confirming it to be a robust property of the far from equilibrium scalar dynamics.

The infrared region in scalar systems is isotropic and can be well described by a power law $\sim p^{-\kappa_>}$ with a large exponent $\kappa_> \approx 4.5 - 5$. We conclude that the very high occupancies at low-momenta enhance scattering rates to overcome the rate of longitudinal expansion. The situation is very similar to non-expanding systems, where a nonthermal infrared fixed point was observed previously for scalar field theories [7, 9, 10, 22, 89, 92, 120], within an inverse particle cascade that leads to Bose-Einstein condensation. As we discussed in Chapter 4 and Ref. [118], this scaling region even incorporates a universality classes connecting superfluid relativistic scalar systems and nonrelativistic Bose gases. We will analyze this infrared region in expanding scalars in detail in Sec. 6.1. We will show there that it indeed describes an inverse particle cascade that triggers Bose-Einstein condensation, in a very similar way as we discussed for non-expanding scalar systems.

As noted above, the gauge distribution shown in the lower panel of Fig. 5.3 also exhibits a $\sim 1/p_T$ behavior. A relative enhancement is observed in the deep infrared, which is however far weaker than the corresponding behavior in the scalar theory; it remains to be seen whether this enhancement becomes stronger at later times. Regardless, the concept of a gauge dependent number distribution is problematic at low momenta and further studies in this regime should concentrate on gauge invariant correlation functions. Such an analysis would also be important in view of the idea of a strong infrared enhancement for over-populated gauge fields [72], where the formation of a Bose condensate is debated.

We finally discuss the distribution functions at higher transverse momenta. For the scalar system one observes from Fig. 5.3 that at the latest available times of $\tau/\tau_0 \sim 85$ a flat distribution for $p_T \gtrsim Q$ emerges. The distribution function in this inertial range still exhibits self-similar behavior (5.1) with the relations (5.4) albeit with a different scaling function f_S and a different longitudinal scaling behavior characterized by the exponent $\gamma = 1/2$. The systematics of this regime of hard transverse momenta will be discussed in more detail in Sec. 6.1. In contrast, the gauge theory, for the shorter times explored, shows no such additional scaling regime at hard momenta.

5.2.4 Basin of attraction

The non-thermal fixed point observed for scalar field theories is not only approached with over-occupation initial conditions. Similar to our discussion in non-expanding scalars in Sec. 3.2.2, also coherent-field initial conditions (2.62) belong to its basin of attraction. These initial conditions lead to a parametric resonance instability at early times in the static case [78, 81, 87] as well as in the expanding scalar field theory [121, 156] despite the longitudinal expansion. In Fig. 5.4, we show the space-time evolution of an expanding scalars system with coherent-field initial conditions at the example of the transverse momentum distribution $f(p_T, p_z = 0, \tau)$. The resonance leads to instabilities and rapid particle production at early times (red circles).

An over-occupation of momentum modes up to a characteristic momentum scale $Q \equiv \sigma_0$ of Eq. (2.62) is built up on a short time scale (blue triangles) while the coherent field decays. As discussed in Ref. [121], the end of the instability regime is given by

$$\tau_{\text{instab}}/\tau_0 \simeq \left(1 + \frac{1}{3Q\tau_0\gamma_0} \log \lambda^{-1}\right)^{3/2}, \quad (5.6)$$

with $\gamma_0 \simeq 0.15$. At the end of this stage, we identify an over-occupied system with a similar form as given by over-occupation initial conditions in Eq. (2.61). Hence starting with an over-occupied single particle distribution may be regarded as an already time evolved system with coherent field initial conditions. At later times (green rhombi and black squares), the system approaches the same nonthermal fixed point. Therefore, both types of initial conditions lie in the basin of attraction of the nonthermal fixed point in expanding scalars.

5.3 Non-Abelian plasmas and thermalization in more detail

In this section, we study the non-thermal fixed point of non-Abelian plasmas in more detail. We explicitly show its scaling properties as in Ref. [14] and provide an additional error analysis for the scaling exponents in Sec. 5.3.1. As we will discuss in Sec. 5.3.2, our simulation results allowed us to distinguish between different thermalization scenarios in the literature [39, 67–69, 71, 72]. The observed scaling exponents are consistent with the thermalization scenario of Ref. [67] that is based on elastic and inelastic scatterings only. In Sec. 5.3.3 we will review how the scaling exponents can be derived from such a kinetic description by use of a self-similar distribution function. Over the last years, our studies considerably contributed to a consistent understanding of the thermalization process of expanding non-Abelian plasmas in the high-energy (weak coupling) limit that we will discuss in Sec. 5.3.4.

5.3.1 Self-similar evolution and scaling exponents

The self-similarity of non-Abelian plasmas can be demonstrated by investigating the scaling properties of the rescaled single particle distribution in analogy to the scalar case in Sec. 5.2.2. In the right panel of Fig. 5.5 we show the rescaled gluon distribution as a function of rescaled longitudinal momenta $(Q\tau)^\gamma p_z$. This longitudinal distribution is shown for modes with transverse momenta $p_T \simeq Q$ and the same initial conditions as used throughout Sec. 5.2. The left panel of Fig. 5.5 shows the original data for comparison. Indeed, the rescaled data for different times in the range from $\tau/\tau_0 = 7.5$ to 40 is seen to collapse onto a single curve to high accuracy, which is a manifestation of self-similarity in the evolution of the non-Abelian system.

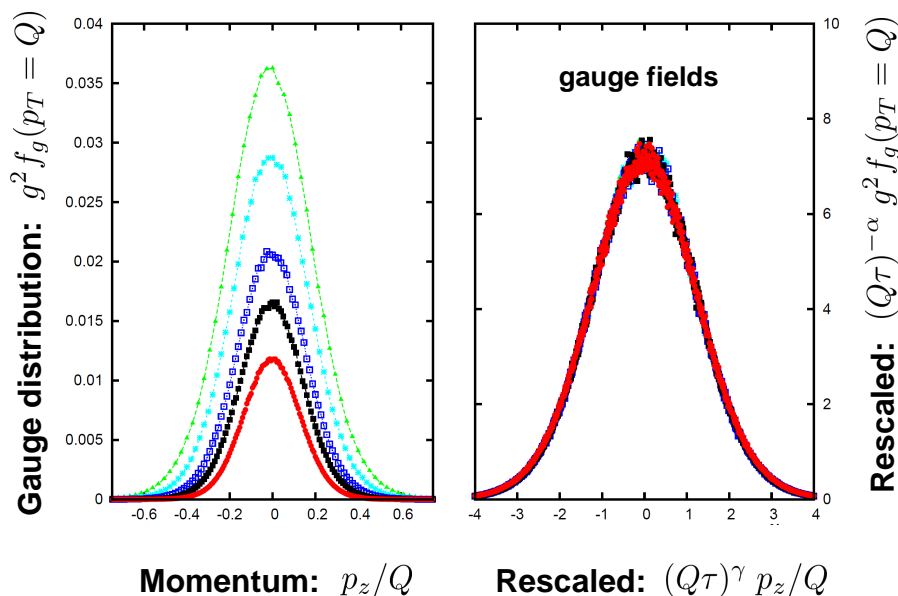


FIGURE 5.5: **(left)** Gluon distribution as a function of longitudinal momentum p_z at different times $\tau/\tau_0 = 7.5, 10, 15, 20, 30$ (top to bottom) of the evolution. **(right)** The same data after rescaling the distribution function and the longitudinal momentum with powers of τ . The rescaled data for different times all collapses onto a single curve, signaling a self-similar evolution.

To keep our presentation short, we move a detailed discussion about the extraction of scaling exponents in non-Abelian plasmas and their systematic errors to App. D while we summarize only key aspects of our analysis here. We find that the scaling exponents that are inferred from the self-similar behavior are affected by large systematic errors.³ The systematic errors mainly result from two ingredients:

- 1) The universal values of scaling exponents are defined at the nonthermal fixed point. Since we can only simulate up to finite times, the measured exponents can differ from their final values. We have seen a similar situation for the infrared scaling regime in non-expanding scalar theories in Fig. 4.4.
- 2) According to Bjorken's law (5.2), finite anisotropy $P_L/\epsilon > 0$ leads to deviations from $\epsilon \sim \tau^{-1}$ and eventually affects all of the scaling exponents.

For instance, for longitudinally expanding systems, the relations in Eq. (5.4) should hold close to the nonthermal fixed point. However, we find from the self-similar evolution of the data set in Fig. 5.5 that the best fitting values are $\alpha_{\text{selfsim}} - 3\beta_{\text{selfsim}} - \gamma_{\text{selfsim}} = -1.05 \pm 0.04$ instead of -1 , $\beta_{\text{selfsim}} = -0.02 \pm 0.02$ instead of zero and $\gamma_{\text{selfsim}} \approx 0.285 \pm 0.025$. To reduce

³For our scalar simulations, the exponents suffer less from systematic effects. While they are well described by the values in Eq. (5.5), we will provide their error estimates in a separate study in Sec. 6.1.3.

systematic errors, we consider the gauge-invariant hard scales Λ_T and Λ_L that are defined in Eq. (D.3) of App. D.1, and were introduced in Refs. [15, 157]. Their perturbative expressions can be stated in terms of the distribution function as

$$\begin{aligned}\Lambda_T^2(\tau) &\simeq \frac{\int d^2p_T dp_z 2p_T^2 \omega_p f(p_T, p_z, \tau)}{\int d^2p_T dp_z \omega_p f(p_T, p_z, \tau)}, \\ \Lambda_L^2(\tau) &\simeq \frac{\int d^2p_T dp_z 4p_z^2 \omega_p f(p_T, p_z, \tau)}{\int d^2p_T dp_z \omega_p f(p_T, p_z, \tau)}, \\ \epsilon(\tau) &\sim \int d^2p_T dp_z \omega_p f(p_T, p_z, \tau),\end{aligned}\tag{5.7}$$

where we have also included the energy density ϵ and used for the relativistic quasi-particle energy $\omega_p \simeq p_T$ in the anisotropic limit $p_T \gg p_z$. Since the hard scales and the energy density receive their dominating contributions from roughly the same hard modes, the hard scales can be interpreted as our typical hard momenta (see below Eq. (5.1)), $\Lambda_T = p_{T,\text{typ}}$ and $\Lambda_L = p_{z,\text{typ}}$. These perturbative expressions in (5.7) scale as

$$\epsilon \sim \tau^{\alpha-3\beta-\gamma}, \quad \Lambda_T^2 \sim \tau^{-2\beta}, \quad \Lambda_L^2 \sim \tau^{-2\gamma}.\tag{5.8}$$

Comparing different initial conditions and discretizations, we indeed find in App. D that their scaling exponents approach the values given by Eq. (5.5). While the combined exponent $\alpha - 3\beta - \gamma$ and the transverse exponent β monotonically approach their expected final values -1 and 0 , respectively, the scaling exponent of the longitudinal scale is measured to be

$$2\gamma = 0.67 \pm 0.07 \text{ (stat.)},\tag{5.9}$$

after a transient evolution. All of these values are consistent with the values in Eq. (5.5) obtained for scalar fields. This is a strong evidence for universal behavior between two different field theories.

5.3.2 Distinguishing between thermalization scenarios

By extracting the scaling exponents (α, β, γ) with two different methods in the previous subsection, we can estimate the systematic uncertainties of our analysis. Concerning the scaling exponents β and $\alpha - 3\beta - \gamma$ the results of the different methods show very good agreement. Their scaling corrections due to finite time and finite anisotropy effects decrease monotonically in time, as the gauge invariant analysis shows. For the considered range of times, these systematic errors are on the order of 0.06 for β and 0.05 for the scaling exponent $\alpha - 3\beta - \gamma$ of the energy density. Based on the strictly monotonic behavior we can safely extrapolate the values of β and $\alpha - 3\beta - \gamma$ to the highly anisotropic scaling limit, where

$$\beta \nearrow 0, \quad \alpha - 3\beta - \gamma \nearrow -1.\tag{5.10}$$

This result is in agreement with our numerical results from scalar theory in Eq. (5.4). Moreover, most weak coupling thermalization scenarios also assume these relations for their classical evolution regime.

The scaling exponent γ can be used to distinguish between different weak coupling thermalization scenarios. The ‘bottom-up’ scenario (BMSS) [67] is entirely based on elastic $2 \leftrightarrow 2$ and inelastic $2 \leftrightarrow 3$ scatterings. It considers the Debye scale m_D of Eq. (3.18) as the typical scale for small longitudinal momentum transfer, leading to the exponent $\gamma = 1/3$ for the classical high-occupancy regime. In contrast, the one loop self-energy for anisotropic momentum distributions has been suggested to lead to plasma instabilities even during the evolution of highly occupied non-Abelian plasmas [158, 159]. The additional influence of plasma instabilities has been considered in the scenarios (BD) [68] and (KM) [71]. There plasma instabilities create an overpopulation of unstable soft modes $p_T \lesssim m_D$, such that the interaction of hard excitations with the highly populated soft modes becomes the dominant process. Differing in the expected range of longitudinal unstable modes, they lead to $\gamma = 1/4$ for the (BD) and $\gamma = 1/8$ for the (KM) scenarios. In the different thermalization scenario (BGLMV) [72], it is instead argued that the combination of high occupancy and elastic scattering can generate a transient Bose-Einstein condensate. The latter then leads to a system with fixed (P_L/P_T) anisotropy, which implies $\gamma = \beta$.

While the result of our self-similar scaling analysis points to values of $\gamma \simeq 0.28$, between the values $\gamma = 1/3$ in the ‘bottom-up’ scenario and $\gamma = 1/4$ in the instability modified (BD) scenario by Boedeker, our gauge invariant analysis result $\gamma \simeq 0.33$ of Eq. (5.9) shows a clear preference for the ‘bottom-up’ scenario [67]. We believe that the deviation between the two methods can be attributed to scaling corrections at finite anisotropy and finite times. However, an important difference between the methods is that for the gauge-invariant analysis we were able to get a time differentiated measurement of the exponents. Moreover, we compared the results for different initial conditions and discretization parameters (Fig. D.1 of App. D), reducing systematic dependencies on the initial conditions. Therefore, we think that the gauge invariant measurement is more rigorous. Within these uncertainties of our simulations, our numerical results can be described most accurately by the ‘bottom-up’ scenario.

5.3.3 Kinetic analysis for non-Abelian plasmas

As we have seen, the ‘bottom-up’ thermalization scenario correctly captures the universal scaling properties of expanding non-Abelian plasmas. This finds a simple a posteriori explanation in terms of a kinetic description that we already discussed in Sec. 3.3.2 for non-expanding gauge theory. The kinetic equation in longitudinally expanding systems reads [71, 151]

$$\left[\partial_\tau - \frac{p_z}{\tau} \partial_{p_z} \right] f(p_T, p_z, \tau) = C[f](p_T, p_z; \tau), \quad (5.11)$$

for the single particle distribution $f(p_T, p_z, \tau)$ with a collision integrals $C[f](p_T, p_z; \tau)$ characterizing scattering processes. The difference to the kinetic equation in isotropic non-expanding systems (3.26) lies in an additional term on the left hand side $-p_z/\tau \partial_{p_z} f$ that incorporates the longitudinal red shift and dilution of the longitudinally expanding medium.

In the high occupancy classical regime of the bottom-up scenario, the interaction of hard quasi-particle excitations is dominated by elastic scatterings $2 \leftrightarrow 2$ which are consistent with the observed particle and energy density conservation (5.4). Inelastic $2 \leftrightarrow 3$ interactions also occur but they primarily affect the soft sector as long as the typical occupancies of the hard excitations are large ($f(p_{T,\text{typ}}, p_{z,\text{typ}}) \gg 1$), and plasma instabilities were not considered in that work. For elastic $2 \leftrightarrow 2$ scattering, the collision integral involves the matrix element of Eq. (3.43) where small-angle scatterings are strongly enhanced (see Sec. 3.3.2). Hence, the effect of elastic collisions is to broaden the longitudinal momentum distribution by multiple incoherent small-angle scatterings, which is the key to understanding the observed scaling properties of non-Abelian plasmas.

The elastic collision integral in the small angle approximation $C_{\text{small-angle}}^{2 \leftrightarrow 2}$ was introduced in Eq. (3.46) for non-expanding gauge theory. Here we discuss a system with typically large anisotropies $p_z \ll p_T$ due to the longitudinal expansion, which can be formulated in terms of our hard scales $\Lambda_L \ll \Lambda_T$ of Eq. (5.7). This allows us to estimate the leading contributions to the collision integral parametrically. Estimating the derivatives as $\Lambda_T \partial_{p_T} f \sim f$ and $\Lambda_T \partial_{p_z} f \sim f \Lambda_T/\Lambda_L \gg f$, one can further simplify Eq. (3.46). The leading contribution to $C_{\text{small-angle}}^{2 \leftrightarrow 2}$ is of the order $(\Lambda_T/\Lambda_L)^2 \gg 1$ and leads to the Fokker-Planck form

$$C_{\text{small-angle}}^{2 \leftrightarrow 2}[f](p_T, p_z; \tau) \simeq \hat{q} \partial_{p_z}^2 f(p_T, p_z, \tau) + \mathcal{O}(1). \quad (5.12)$$

The momentum diffusion parameter (3.47) is approximated as

$$\hat{q} \simeq 4\pi\alpha_s^2 N_c^2 L \int \frac{d^2 p_T dp_z}{(2\pi)^3} f^2(p_T, p_z, \tau) \quad (5.13)$$

for high occupancies. Hence, the kinetic process resulting from Eq. (5.12) can be interpreted as a random walk of excitations in momentum space, where quasiparticles receive small kicks in longitudinal direction. Although this approximation may not capture all details, it is expected to describe the relevant physics necessary to determine the scaling exponents. Indeed, the Gaussian shaped fixed point distribution of Figs. 5.2 and 5.5 can be regarded as a natural consequence of the Fokker-Planck type kinetic equation.

While the original work by Baier, Mueller, Schiff and Son [67] (BMSS) determines the basic properties of the kinetic evolution from self-consistency arguments, the self-similar behavior observed from numerical simulations indicates that the framework of scaling regimes [8] can be applied. We continue this analysis by plugging the self-similar distribution (5.1) into the

Boltzmann equation (5.11). Comparing both sides leads to the time-independent condition

$$\alpha f_S(p_T, p_z) + \beta p_T \partial_{p_T} f_S(p_T, p_z) + (\gamma - 1) p_z \partial_{p_z} f_S(p_T, p_z) = C_{\text{small-angle}}^{2 \leftrightarrow 2} [f_S](p_T, p_z), \quad (5.14)$$

and to the relation for temporal exponents

$$\alpha - 1 = -\beta \mu. \quad (5.15)$$

Here we used the scaling behavior (3.28) of the collision integral for which one extracts $\mu = -3\alpha/\beta + 2 - \gamma/\beta$. This leads to the scaling relation

$$2\alpha - 2\beta + \gamma + 1 = 0. \quad (5.16)$$

Since elastic scattering processes are particle number and energy conserving, further scaling relations are obtained from conservation laws of the kinetic equation. Particle number conservation $\tau \int d^3p f = \text{const}$ can be extracted from the kinetic equation (5.11) by integration over all momenta and multiplication by τ . The self-similar behavior in Eq. (5.1) leads to the scaling relation $\alpha - 2\beta - \gamma + 1 = 0$. Similarly, approximating the mode energy of hard excitations as $\omega_p \simeq p_T$ in the anisotropic scaling limit, energy conservation $\tau \int d^3p p_t f = \text{const}$ yields the final scaling condition $\alpha - 3\beta - \gamma + 1 = 0$. These two equations combined yield the relations

$$\alpha - \gamma + 1 = 0 \quad , \quad \beta = 0. \quad (5.17)$$

that we have found numerically above in Eq. (5.4).

Remarkably, the above scaling relations are independent of many of the details of the underlying field theory such as the number of colors, the coupling constant as well as the initial conditions. Instead, they only depend on the dominant type of kinetic interactions (such as $2 \leftrightarrow 2$ scattering processes), the conserved quantities of the system and the number of dimensions. More specifically, the dynamics of small-angle elastic scattering, along with the conservation laws of quasi-particle number and energy provide the three equations to determine the scaling exponents. These are straightforwardly extracted to be

$$\alpha = -2/3, \quad \beta = 0, \quad \gamma = 1/3, \quad (5.18)$$

and agree with our numerical results.

In summary, the observed scaling behavior in gauge theories can be derived from elastic scatterings with a small-angle approximation. However, it is also conceivable that there are processes besides small angle elastic scattering which lead to the same scaling behavior.

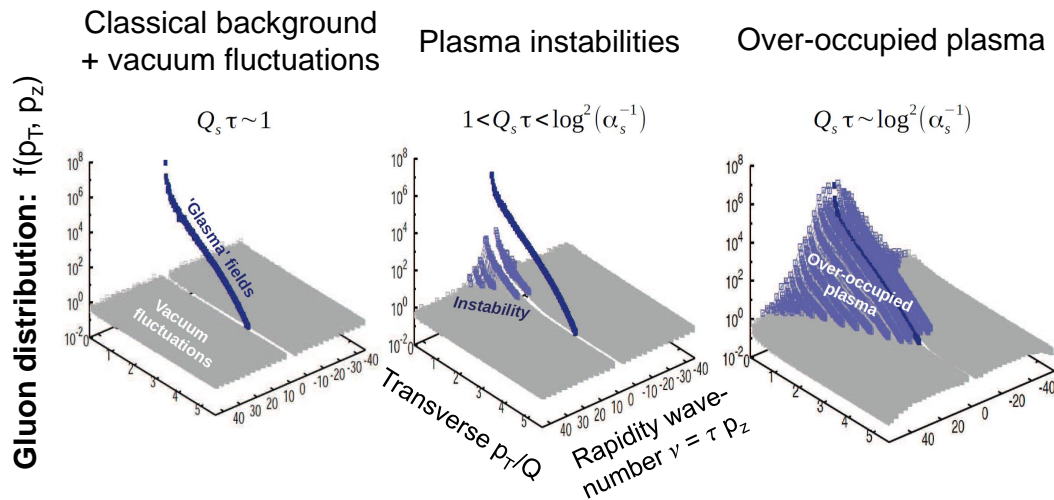


FIGURE 5.6: The distribution function for expanding non-Abelian plasmas at different times as function of transverse momentum p_T and rapidity wave number $\nu = \tau p_z$. Starting from vacuum fluctuations around the classical ‘Glasma’ fields, fluctuations grow due to plasma instabilities and lead to an over-occupied plasma. Figure is taken from Ref. [66].

5.3.4 A consistent picture of thermalization at weak couplings

So far, we discussed a first principles study of the dynamics of a highly occupied non-Abelian plasma using large scale numerical simulations and kinetic theory. The discovery of a non-thermal fixed point in this temporal regime that showed preference for the ‘bottom-up’ thermalization scenario [67] was unanticipated. This is because a consistent kinetic description of expanding non-Abelian plasmas would suggest that plasma instabilities [158–162] should qualitatively modify the evolution even at late times [68, 70, 71, 158, 163]. However, our classical-statistical simulations indicate that plasma instabilities play no significant role beyond the very early stages. While a microscopic understanding of the absence of late time instabilities remains an open question, this observation has been incorporated in kinetic descriptions of the thermalization process, as for instance in Ref. [164].

Therefore, our results provide a link between early stages of the evolution and the thermalization scenarios that were proposed in the literature. As has been confirmed numerically [66, 130, 164], it is now possible to formulate a consistent picture of thermalization at

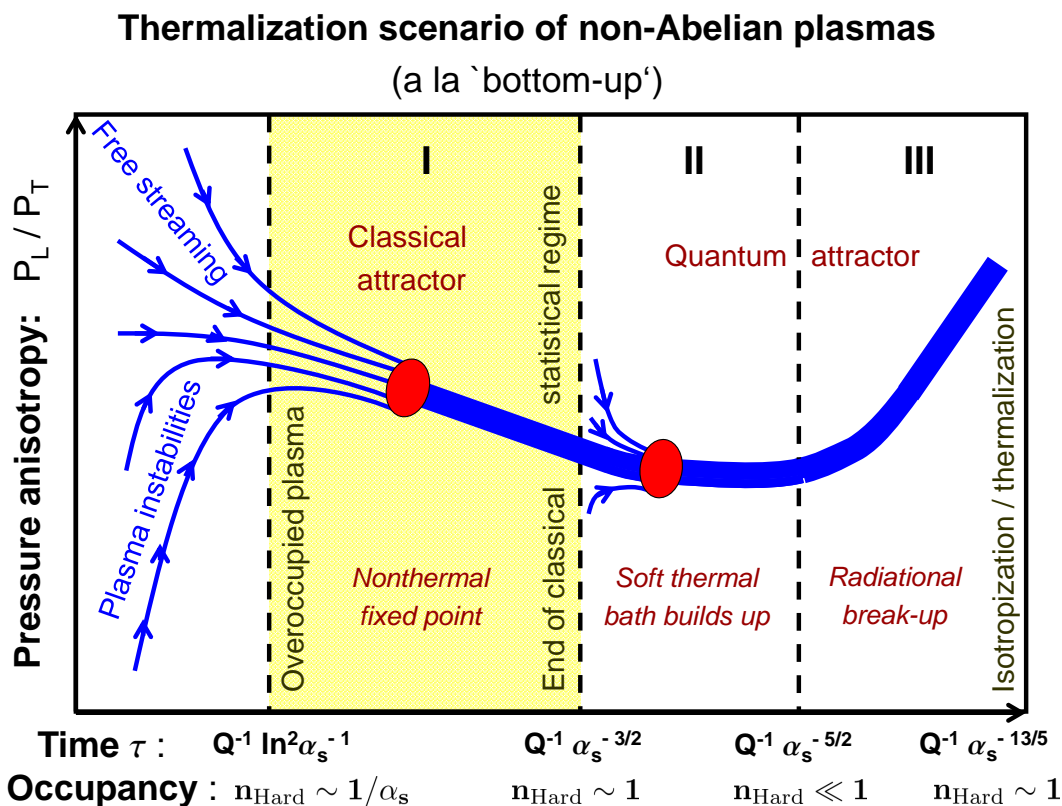


FIGURE 5.7: Schematic illustration of the thermalization process for the example of the bulk anisotropy P_L/P_T . The time evolution in the shaded yellow regime corresponds to the observed non-thermal fixed point, where its attraction property is symbolized by the red ellipse. The curves in the time regimes I - III reflect the evolution in the three thermalization stages of the bottom-up scenario [67]. We show typical time scales and typical occupancies $n_{\text{Hard}} = f(p_T = Q, p_z = 0)$ at the bottom of the figure.

weak couplings, starting from the initial Glasma fields shortly after the collision, up to the onset of hydrodynamics at late times.

In the following, we provide an overview of the thermalization process at weak couplings (see also Ref. [165, 166]). In the weak coupling limit, the colliding nuclei may be described as Color Glass Condensates (CGC) in an effective field theory description of high energy QCD [47, 167–169]. The dynamics of the nonequilibrium ‘‘Glasma’’ created in such a collision is that of highly occupied boost invariant classical gluon fields with typical momentum Q [48–59]. Since the characteristic occupancies $\sim 1/\alpha_s(Q)$ are large, the gauge fields are strongly correlated even for small gauge coupling.

Small quantum fluctuations [170] break the boost invariance and lead to (Weibel) plasma instabilities with exponential growth $\exp(\sqrt{Q\tau})$ [60–65]. The fluctuations become of the order of the Glasma field on time scales

$$Q\tau_{\text{instab}} \sim \log^2(\alpha_s^{-1}), \quad (5.19)$$

and lead to an over-occupied non-Abelian plasma [66]. This evolution is shown in Fig. 5.6.

The subsequent time evolution of the over-occupied system follows the ‘bottom-up’ picture of thermalization [67], which is illustrated schematically in Fig. 5.7 at the example of the bulk anisotropy of the plasma. Following the regime dominated by plasma instabilities (or free streaming for some other initial conditions), an effective memory loss is observed already at rather early times of the evolution and leads to the classical nonthermal fixed point for different initial conditions [14, 15]. The plasma, albeit strongly interacting at all times, becomes increasingly anisotropic in the classical-statistical regime of high occupancies. This first stage of the ‘bottom-up’ scenario ends at $\tau_{\text{Quant}} \sim Q^{-1} \alpha_s^{-3/2}$ when typical occupation numbers of hard modes $n_{\text{Hard}} = f(p_T = Q, p_z = 0)$ become of order unity since then the classical approximation breaks down.

The second and the third stages of the ‘bottom-up’ scenario are governed by wave turbulence in the low occupancy regime of hard excitations $n_{\text{Hard}} \lesssim 1$ [67, 130, 132, 164, 171]. In stage II, the anisotropy freezes while the system becomes more dilute due to inelastic processes with democratic branching. There, a hard excitation split into two daughters of comparable energy. This process leads to a turbulent cascade to lower momenta, occupying the soft sector with particles. Due to frequent interactions among the soft particles, a thermal bath forms at $\tau_{\text{Bath}} \sim Q^{-1} \alpha_s^{-5/2}$, which coincides with the time when the number of soft particles is of the same order as the number of hard particles. In stage III, the dilute and anisotropic plasma approaches thermal equilibrium through a radiational break-up of hard particles that lose their energy to the thermal bath. At late times, the relaxation of the transverse and longitudinal pressures towards their equilibrium values can be described accurately by viscous hydrodynamics [164]. For physical couplings $\alpha_s \approx 0.3$, the onset of hydrodynamics has been observed to emerge at $\tau_{\text{Hydro}} \sim 1 \text{ fm}/c$ for the scale $Q = 2 \text{ GeV}$ [164].

This weak-coupling thermalization picture is the counterpart of the holographic thermalization process of strongly coupled supersymmetric Yang-Mills theory within the AdS/CFT framework [41–44, 172–175], where the gauge-string duality is used to study the process. It generally leads to a fast thermalization of the plasma and is even robust in the presence of large anisotropy [41, 172, 173].

5.4 Summary

In this chapter, we studied nonthermal fixed points in longitudinally expanding systems. We first extended our concepts of scaling regions to expanding media, where the distribution function evolves in a self-similar way $f(p_T, p_z, \tau) = \tau^\alpha f_S(\tau^\beta p_T, \tau^\gamma p_z)$.

Using large scale numerical simulations, we reported of nonthermal fixed points in expanding scalar and gauge theories. Both systems exhibit an anisotropic scaling region at sufficiently high momenta where the occupation numbers satisfy $f \lesssim 1/\lambda$ and $f \lesssim 1/\alpha_s$, respectively. There, particle number per transverse momentum mode $\tau dn/dp_T$ as well as energy density per transverse mode $\tau d\epsilon/dp_T$ are both conserved at each transverse momentum simultaneously, implying the relations $\alpha - \gamma + 1 = 0$ and $\beta = 0$ for the scaling exponents. This is different from the static case, where only one of these conservation laws can be satisfied within a scaling region. In particular, in expanding systems, there is effectively neither a particle nor an energy flux in transverse momentum in such scaling regions.

A detailed analysis of the scaling properties in this region revealed the scaling exponents $\alpha = -2/3$, $\beta = 0$ and $\gamma = 1/3$ for both systems. Moreover, we obtained in both cases the functional form $f_S(p_T, p_z) \sim p_T^{-1} \exp(-p_z^2/\sigma_z^2)$ within the scaling region. For scalar fields, we observed that also initial conditions with an initially large coherent field lead to the same attractor. Moreover, the scaling region increases in momentum space on a logarithmic scale, which shows the robustness of this universal regime. These observations provide strong evidence of a novel far-from-equilibrium universality class encompassing longitudinally expanding scalar fields and gauge fields over a characteristic inertial range of transverse momenta.

We showed how the observed scaling behavior in gauge theories can be derived from elastic scatterings with a small-angle approximation. The corresponding kinetic process can be interpreted as a random walk of excitations in momentum space, where quasiparticles receive small kicks in longitudinal direction. In contrast, a similar explanation in terms of scattering processes does not exist so far for the scaling region in scalar systems. Since the underlying interaction processes are very different for gauge and scalar fields, our findings hint to an even more general principle behind this universality.

Our numerical results of non-Abelian gauge theory suggest that plasma instabilities play no important role beyond early times. A microscopic understanding of the absence of such instabilities remains an open question. We also discussed the current understanding of the thermalization process in weakly coupled non-Abelian plasmas, which are relevant for heavy-ion collisions in the limit of high energies and weak couplings. Our results have been incorporated in recent kinetic descriptions that confirm the ‘bottom-up’ thermalization picture.

Because of large anisotropies due to the expansion, the thermalization process is more complicated than a typical equilibration process in non-expanding systems that is depicted in

Fig. 3.1 of Chapter 3. Since during the nonthermal fixed point stage anisotropies increase, the system is highly anisotropic when characteristic occupancies become of order unity $f \sim 1$. Therefore, subsequent thermalization stages are required that isotropize the system before it can eventually approach thermal equilibrium. The current status of the thermalization picture in heavy-ion collisions in the limit of high energies provides a consistent description from the initial ‘Glasma’ fields shortly after the collision up to the onset of hydrodynamics.

Chapter 6

Nonthermal fixed point in expanding scalars

In the previous chapter, we reported on a new universality class for longitudinally expanding systems, encompassing strongly correlated non-Abelian plasmas and N -component self-interacting scalar field theories. In this chapter we significantly expand on our previous work and study the scalar attractor in detail. We extract the scaling properties in the universal scaling regime with appropriate error estimates and delineate two further self-similar regimes.

The first new self-similar regime occurs in the deep infrared (IR) region of very high occupancies $f \gtrsim 1/\lambda$, where the nonequilibrium dynamics leads to the formation of a Bose-Einstein condensate. We have studied this regime in Chapter 4 (and [118]) for non-expanding scalar systems, and find that also in the expanding case, one has an inverse particle cascade that leads to Bose-Einstein condensation. A perturbative kinetic treatment of the high-occupancy regime is limited to occupation numbers $f \ll 1/\lambda$ because it involves a perturbative series in λf . Instead, we will apply the vertex-resummed kinetic theory of Refs. [7, 89, 114, 154] to describe the high-occupancy regime at low momenta. We showed in Sec. 4.2 that this framework can be successfully used to explain scaling properties in an over-occupied momentum region. The other novel scaling regime emerges at high momenta at late times. We will study its scaling properties for different initial conditions and obtain its scaling exponents and scaling function.

In conventional kinetic approaches, our reported universality class between scalar and gauge theories leads to the parametric estimate $P_L/P_T \sim \tau^{-2/3}$ for the pressure anisotropy. However, we will see that the evolution of this quantity in our numerical simulations deviates significantly from this scaling behavior. Our results therefore challenge conventional kinetic frameworks. They suggest that modifications are needed at low momenta also in non-Abelian gauge theory to account for the high occupancies, similar to the vertex-resummed kinetic theory in scalar systems.

We have discussed the range of validity of the classical-statistical approximation in Sec. 2.3.1. One finds that the approximation accurately describes the full quantum system as long as typical occupation numbers are large $f \gg 1$. In Ref. [176] it has been argued recently that there is potentially a caveat to the underlying arguments when the system is highly anisotropic. We have studied the range of validity of the classical-statistical approximation in our longitudinally expanding systems at the example of the pressure anisotropy P_L/P_T . Since this discussion requires the knowledge of the universal scaling regime of scalar and gauge theories that we discussed in Chapter 5, we did not include the discussion in Sec. 2.3.1. Instead, our arguments are provided in App. E, and we summarize here the results. We find that the classical regime ends at $\tau_{\text{Quant}} \sim Q^{-1} \lambda^{-3/2}$. This is the same time limit as for non-Abelian plasmas, as was illustrated in Fig. 5.7 of the previous chapter. Most importantly, it also coincides with the time scale when typical occupation numbers become of the order unity, which signals the break-down of the classical approximation also in the non-expanding case, as discussed in Secs. 2.3.1 and 3.2. Therefore, the anisotropy of the system does not pose more constraints on the range of validity of our classical approximation to the dynamics. We also note that beyond the break-down time scale τ_{Quant} of the approximation, the evolution of the system is expected to change qualitatively since genuine quantum corrections become important. While for non-Abelian gauge theories there has been a lot of recent progress in understanding the dynamics of the quantum regime in more detail [130, 164], a similar analysis for the scalar theory is presently not available, and is beyond the scope of this work.

We start this chapter in Sec. 6.1 with a detailed analysis of the different scaling regions in the scalar attractor. In Sec. 6.2 we discuss their implications on the pressure ratio P_L/P_T . We conclude the chapter in Sec. 6.3 with a summary of our results.¹

6.1 The scaling regions of the nonthermal fixed point

Within the classical-statistical simulations of the expanding scalar theory in Sec. 5.2 (or in [2]), we identified three distinct scaling regimes: i) An inverse particle cascade at very soft momenta with large occupancies $f \gtrsim 1/\lambda$, ii) an intermediate range of momenta extending dynamically up to momenta close to the hard momentum scale Q of the system, and iii) a hard momentum regime for momenta $p_T \gtrsim Q$. In the following, we will expand on the discussion of the longitudinally expanding scalar theory in Sec. 5.2 and present detailed results uncovering the properties of the three inertial regimes.

The nonthermal fixed point structure is insensitive to the details of the initial conditions. Therefore, we will first investigate the time evolution for a single initial condition and then verify that the scaling results are insensitive to the initial conditions (summarized in Table 6.1)

¹We have published the presented results of this chapter in Ref. [177].

further below for parts of the attractor. Unless stated otherwise, we consider a four component (i.e. $O(4)$ -symmetric) scalar theory with over-occupation initial conditions, as in Eq. (2.61), with an initially isotropic system ($\xi_0 = 1$) and with the occupancy parameter $n_0 = 35$ at the initial time $Q\tau_0 = 10^3$. All quantities in this paper are normalized by appropriate dimensional scales. If not written explicitly, we imply $\tau \mapsto \tau/\tau_0$ and $p_i \mapsto p_i/Q$ in our equations and figures, which also holds for the scaling behavior introduced in Eq. (5.1).

Our results for the transverse momentum dependence of the spectrum at different proper times in the evolution are summarized in Fig. 6.1, which shows snapshots of the single particle distribution $f(p_T, p_z = 0, \tau)$ for vanishing longitudinal momenta. One observes the emergence of three distinct scaling regimes, at small, intermediate and high transverse momenta. We reported in Sec. 5.2 that the low momentum behavior – indicated as i) – is characterized by a strong infrared enhancement with an approximate power law $p_T^{-\kappa_>}$ power law dependence with a large exponent $\kappa_> \approx 4.5 - 5$ while the intermediate momentum regime – indicated as ii) – features an approximate p_T^{-1} power law shown by the gray and black dashed lines.

The momentum ranges for the scaling regimes i) and ii) are seen to shift dynamically towards lower momenta as a function of time as indicated by the purple dashed lines in Fig. 6.1. At late times, an additional scaling window emerges at momenta $p_T \gtrsim Q$. This novel regime was unanticipated and we shall discuss it shortly. In this regime – indicated as iii) – the single particle distribution becomes approximately independent of the transverse momentum up to very high momenta where the spectrum shows a rapid fall off.

Configuration				Lattice parameters			
ξ_0	n_0	$Q\tau_0$	N	N_T	N_η	Qa_T	$a_\eta/10^{-5}$
0.5	5	1000	4	128	768	1	5
1	4.5	1000	4	128	768	1	5
1	5	1000	4	128 – 256	512 – 4096	0.5 – 1	2.5 – 5
1	6	1000	4	128	768	1	5
1	7.5	1000	4	128	768	1	5
1	15	1000	4	192	768	0.67	5
1	35	1000	4	96 – 384	384 – 768	0.25 – 2.5	4 – 10
1	80	1000	4	128	768	0.4	5
2	15	1000	4	128	768	0.85	5
4	15	1000	4	128	1024	1	5
1	35	100	4	192	1024	0.75	25
1	5	1000	2	192	768	0.5	5
Coherent IC		1000	4	192; 256	256 – 768	0.2 – 0.9	6 – 20

TABLE 6.1: Discretization parameters for different initial conditions. Unless stated otherwise, these parameters are employed for all classical-statistical lattice simulations. In the following, the configurations of the last three lines are referred to as “ $Q\tau_0 = 100$ ”, “ $O(2)$ scalars” and “Coherent field IC” (c.f. Eq. (2.62)), respectively.

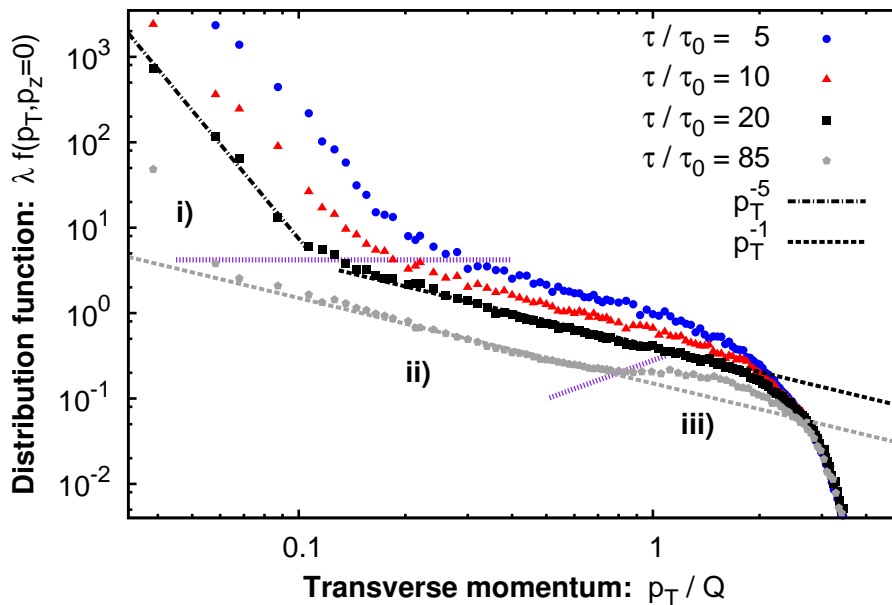


FIGURE 6.1: Dependence of the single particle distribution on the transverse momentum (for vanishing longitudinal momentum $p_z = 0$) at various times. One observes the emergence of three distinct scaling regimes labeled as i), ii) and iii) and separated by purple dashed lines. Each regime corresponds to the inertial range of momenta for a scaling region as discussed in detail below. The black and gray dashed lines are power laws compared to the regimes i) and ii).

Each of the three momentum regions corresponds to a different self-similar evolution of the single particle distribution with the scaling behavior in Eq. (5.1) and a different set of scaling exponents (α, β, γ) and scaling function $f_S(p_T, p_z)$. As discussed in Sec. 5.1, the exponents determine the evolution of typical occupancy, transverse and longitudinal momenta, respectively. We will extract the scaling quantities of each scaling region in subsequent sections.

6.1.1 Infrared cascade and Bose-Einstein condensation

We will first present a detailed analysis of the inertial range at low momenta, marked by i) in Fig. 6.1 with an approximate p_T^{-5} power law in the transverse momentum spectrum. In the study of scalar field theories with static geometry, such a low momentum region is associated with an inverse particle number cascade of an effectively massive theory and leads to the formation of a Bose-Einstein condensate [89, 118].

We can similarly investigate the presence of a dynamically generated Bose-Einstein condensate in the longitudinally expanding system by studying the finite volume scaling of correlation functions of the scalar field. In an approach similar to that considered for the non-expanding theory in Sec. 4.1.4, we examine the properties of the statistical correlation function $F_0(\tau) \equiv F(p_T = 0, \nu = 0, \tau)$ of Eq. (2.45). While the fluctuations at finite momenta are essential

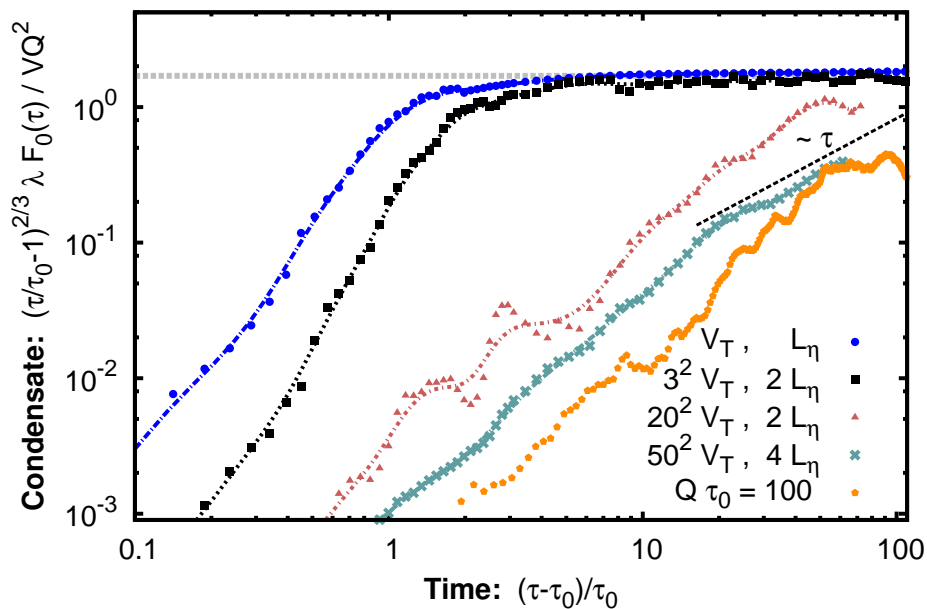


FIGURE 6.2: Time evolution of the condensate observable with over-occupation initial conditions, plotted for different volumes $V \equiv V_T L_\eta$. The lattice spacings for the smallest volume are $Qa_T = 0.75$ and $a_\eta = 5 \cdot 10^{-5}$ on a $64^2 \times 384$ grid. At sufficiently late times, the results become independent of the volume, signaling the formation of a condensate. The condensation time increases with volume. For large volumes, the condensate growth follows power laws that are marked by a dashed black line. A similar late-time behavior is found for other initial parameters, as for an earlier initial time $Q\tau_0 = 100$.

for the formation of the condensate via an inverse particle cascade, a volume independent correlation function at zero momentum $F_0(\tau)/(V_T L_\eta) = \phi_0^2(\tau)$ signals the existence of a Bose-Einstein condensate. Our results for this condensate observable are shown in Fig. 6.2, where we compare the time evolution for different volumes. Starting from over-occupation initial conditions, one observes a rapid rise of the zero momentum mode at early times. Eventually the condensate observable becomes volume independent thereby signaling the formation of a condensate. In our case, the rescaled zero mode $(\tau - \tau_0)^{2/3} F_0$ then becomes constant in time (as marked by the constant gray dashed line). Once formed, the condensate thus decreases as $\phi_0^2(\tau) \sim \tau^{-2/3}$ at late times.

The condensation time τ_c can be viewed as the onset time of volume independent evolution. While for smaller volumes the condensate is created during the simulation time, for larger volumes its formation is not completed. Nevertheless from the ordering of the curves one observes that the condensation time increases with volume. While conventional kinetic descriptions provide a finite condensation time even for infinite volumes [152, 153], the fact that the condensation time diverges with increasing volume is expected from causality and is observed in our lattice simulations.

We note that for the longitudinally expanding system causality also forbids the formation of a Bose-Einstein condensate if the rapidity range is too large. This is because at any given time τ , two points which are separated by a larger rapidity range than $\Delta\eta_c = 2\ln(\tau_c/\tau_0)$ in the longitudinal direction are not causally connected. Nevertheless one may still observe the emergence of long range correlations for a system with sufficiently small rapidity extent $\Delta\eta \leq \Delta\eta_c$ and all our considerations are only valid in the rapidity range where we do observe condensation.

As can be seen in Fig. 6.2 for larger volumes, the zero mode $\tau^{2/3}F_0(\tau)/V$ follows an approximate power law behavior at late time during the formation of the condensate. We expect from analytic considerations that will be detailed in Sec. 6.1.2 that the power law exponent approaches unity at late times. This leads to an increasing condensation time with volume $\tau_c \sim V$, as we will discuss in detail in Sec. 6.1.2. Indeed the results of Fig. 6.2 seem to support this behavior although with sizable discrepancies at earlier times and for smaller volumes.² A similar power law evolution can also be observed in simulations with different initial parameters and sufficiently large volume, as seen for the system with the earlier initial time $Q\tau_0 = 100$ for comparison.

For non-expanding systems, both relativistic and nonrelativistic lattice simulations also indicate that the condensation behavior follows a power law $F_0 \sim t^{3/2}$ (Sec. 4.1.4), where the time variable t is used in such systems. This leads to increasing condensation time with volume, as $t_c \sim V^{2/3}$. Both phenomena can be understood as a consequence of the inverse particle cascade from the low momentum region that populates the zero mode. The similarity to non-expanding systems goes further. There we found that both nonrelativistic and relativistic scalar field theories exhibit the same scaling properties at low momenta. This is attributed to the existence of a medium and condensate generated effective mass in the relativistic system.

We have also checked the existence of a dynamically generated mass for the longitudinally expanding case. We use the definition of Eq. (2.48) to estimate the effective dispersion relation $\omega(p_T, p_z, \tau)$ in the medium. We find that up to statistical fluctuations, the dispersion relation is independent of the polar angle $\theta = \arctan(p_T/p_z)$ in the entire momentum space and only depends on the absolute momentum $|\mathbf{p}| = \sqrt{p_T^2 + p_z^2}$.

Our results for $\omega(|\mathbf{p}|, \tau)$, averaged over the angle θ , are shown in Fig. 6.3 at different times. A comparison with the fitted lines (of the same color as the data points) shows that the effective dispersion relation is well described by a relativistic quasi-particle dispersion

$$\omega(p_T, p_z, \tau) = \sqrt{m^2(\tau) + |\mathbf{p}|^2}, \quad (6.1)$$

²Discrepancies from $\Delta\tau^{2/3}F_0(\tau)/V \sim \Delta\tau$ at earlier times with $\Delta\tau = \tau - \tau_0$ are expected due to finite time effects when the system is not yet close enough to the nonthermal fixed point. Such early time effects can also be observed in the scaling behavior of other quantities as shown explicitly in Fig. 6.6. Similarly, simulations with small volumes do not exhibit the power law behavior at all because the low momentum region is not completely formed and the system is thus too far from the attractor on the time scales of condensation.

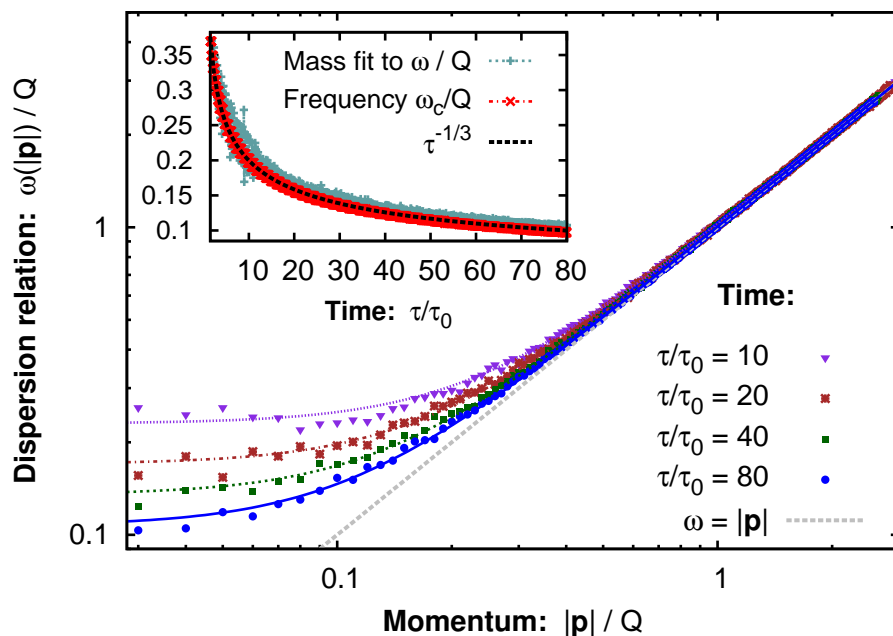


FIGURE 6.3: Effective dispersion relation at different times. Deviations from the $\omega = |\mathbf{p}|$ behavior show that a mass gap is generated for low momentum excitations. The data are fitted with fit functions $\sqrt{m^2 + |\mathbf{p}|^2}$ which are shown as lines with the same color as the data points. The time dependence of the effective mass is illustrated in the inset, extracted from the fits to the dispersion relation and by measuring the oscillation frequency of the zero momentum mode. The effective mass decreases according to a $\tau^{-1/3}$ power law.

with a time dependent effective mass $m(\tau)$.

The time dependence of $m(\tau)$ is shown in the inset of Fig. 6.3. We compare $m(\tau)$ extracted from the dispersion relation to the one extracted from the oscillation frequency $\omega_c(\tau)$ of the unequal-time correlator at zero momentum $F(p_T = 0, \nu = 0, \tau, \tau_0)$. Both measurements agree and show that the dynamically generated mass decreases as a function of time according to³

$$m(\tau) \sim \tau^{-1/3}. \quad (6.2)$$

Because of the large occupancy at low momenta (region i in Fig. 6.1) the mass is expected to be dominated by modes in the infrared scaling region. Using $m^2 \sim \int d^3p f/\omega$ to estimate the

³The scaling behavior (6.2) is only valid for scalar theories with $N > 1$ components. As we will discuss below, it results from particle number conservation $\tau n \sim \text{const}$ in the expanding medium. This is in complete analogy to the non-expanding case, where particle number conservation $n \sim \text{const}$ leads to an approximately time-independent mass [144], see also Sec. 4.1.3. For $N = 1$, however, the mass decreases as $\sim t^{-1/3}$ [8, 120], which can be understood as a consequence of inelastic processes [144]. Similarly, we find in our simulations for the expanding $N = 1$ theory a much quicker decay of the effective mass. Hence, we emphasize that the observed mass decay for the expanding $N > 1$ scalars in Eq. (6.2) is a consequence of the expanding metric and not of inelastic processes.

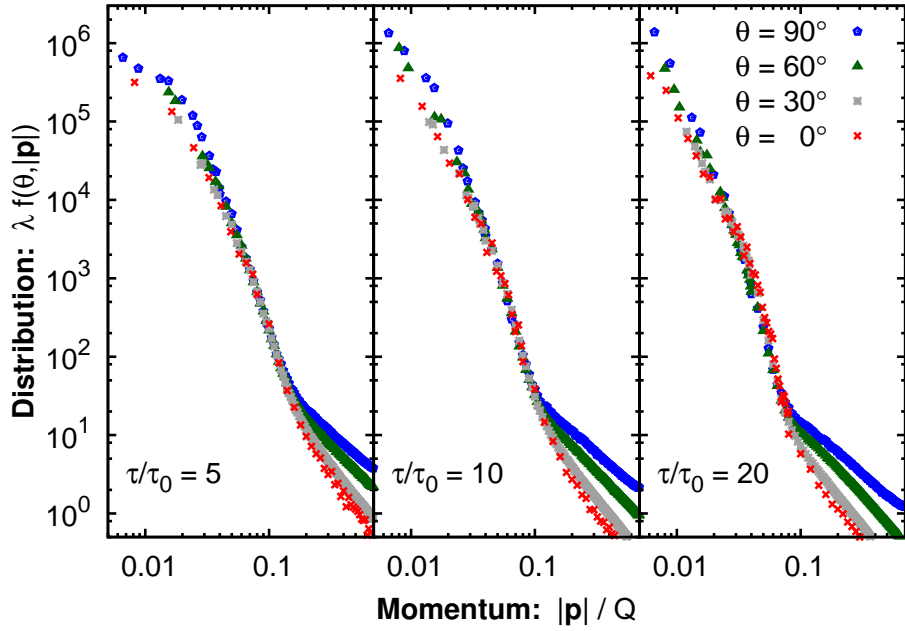


FIGURE 6.4: Distribution function for different polar angles $\theta = \arctan(p_T/p_z)$ as a function of the momentum $|\mathbf{p}| = \sqrt{p_T^2 + p_z^2}$ at different times $\tau/\tau_0 = 5, 10, 20$. While the distribution is highly anisotropic at high momenta, the infrared sector remains approximately isotropic.

evolution of the mass, one has for infrared modes

$$m^2 \sim \frac{n}{m}. \quad (6.3)$$

Particle number conservation $n \sim \tau^{-1}$ (which will be demonstrated later in this section) leads to $m \sim \tau^{-1/3}$ as observed in Eq. (6.2). To arrive at Eq. (6.3) we used $\omega(p) \approx m$ which is true for the infrared modes with $|\mathbf{p}| \lesssim m$. The contribution of the condensate to the effective mass scales in the same way. In contrast, one can estimate the contribution from the harder momentum regions ii) and iii) in Fig. 6.1 as $m_{\text{Hard}}^2 \sim \int d^3p \lambda f / \omega \sim \tau^{-1}$, which is subleading because of its faster decay in time.

We note that this is different from thermal equilibrium where the effective mass is dominated by hard momenta at the temperature scale. The difference can be understood as follows. Close to the nonthermal fixed point, the low momentum region is enhanced and its contribution to the mass decreases slower than at hard momenta, dominating at late times. In contrast, no such enhancement at low momenta exists in thermal equilibrium and all contributions to the mass are stationary.

To better understand the nature of the region at low momenta, we analyze the dependence of the single particle distribution $f(p_T, p_z, \tau)$ on the polar angle $\theta = \arctan(p_T/p_z)$. In Fig. 6.4, we show the phase-space distribution for different values of θ as a function of the absolute momentum $|\mathbf{p}| = \sqrt{p_T^2 + p_z^2}$. While the spectrum is highly anisotropic for large momenta, one

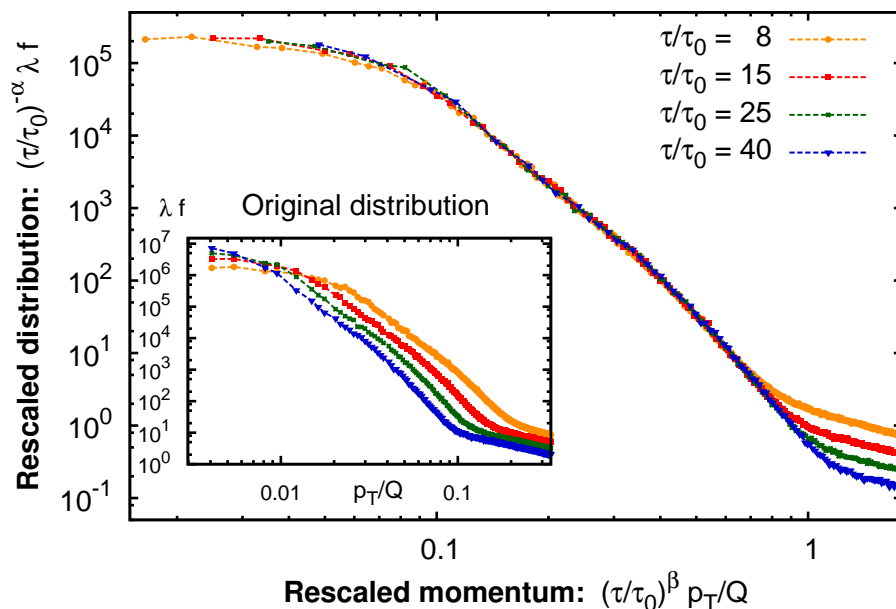


FIGURE 6.5: Rescaled transverse distribution of the expanding scalar system $\lambda f(p_T, p_z = 0, \tau)$ at low momenta as a function of the rescaled transverse momentum for different times. Spectra at different times collapse onto a single curve, demonstrating the self-similarity of the infrared cascade. For comparison, the original distributions without rescaling are shown in the inset.

observes that the strong enhancement of the infrared region is angle independent within the accuracy of the numerical simulations. An important consequence is that typical momentum scales of this region evolve isotropically $p_{T,\text{typ}} \sim p_{z,\text{typ}}$.

When comparing the values of the mass $m(\tau)$ in Fig. 6.3 with the typical momenta for the low momentum fixed point in Figs. 6.1 and 6.4, we find that the low momentum inertial range is always bounded by the effective mass $|\mathbf{p}| \lesssim m(\tau)$. Hence the dynamics of this region is governed by nonrelativistic physics with the time dependent dynamically generated mass $m(\tau)$. Moreover from Figs. 6.1 and 6.4 one observes that the low momentum region entirely involves non-perturbatively large occupation numbers with at least $\lambda f \gtrsim 5$.

We now turn to the scaling exponents α , β , γ and the scaling function $f_S(p_T, p_z)$ of Eq. (5.1) for the low momentum scaling region. Since typical transverse and longitudinal momenta evolve isotropically (Fig. 6.4), one has the relation

$$\beta = \gamma. \quad (6.4)$$

To measure the scaling properties, we change the initial amplitude to $n_0 = 125$, which allows us to access the scaling regime earlier. Since we need to be sensitive to the low momentum region, we use a large lattice with $768^2 \times 512$ lattice points and lattice spacings $Qa_T = 2$ and $a_\eta = 1.5 \times 10^{-4}$. In Fig. 6.5 we show the rescaled transverse momentum distribution

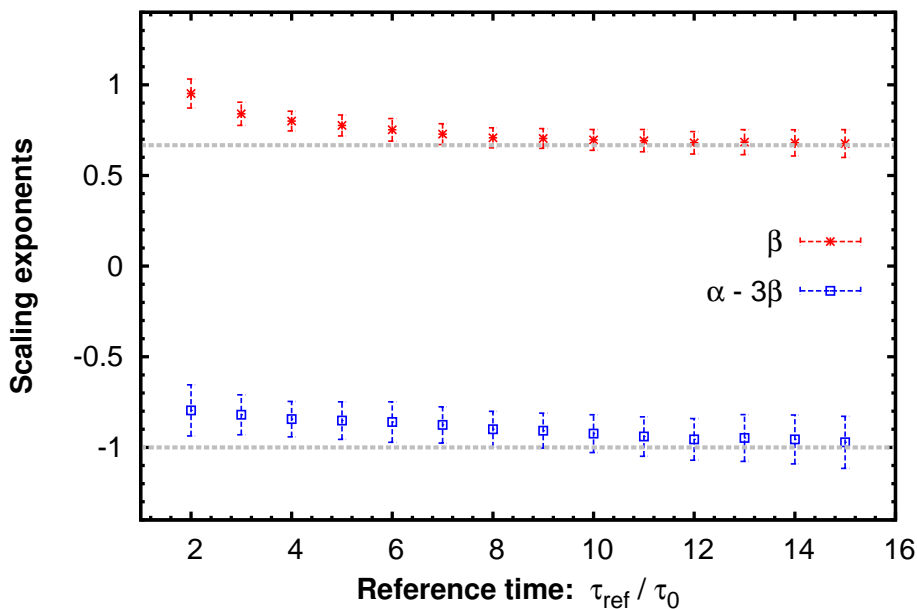


FIGURE 6.6: The exponents β and $\alpha - 3\beta$ extracted at different reference times τ_{ref} . The gray dashed lines correspond to the values $2/3$ and -1 extracted from a scaling analysis within a vertex-resummed kinetic description.

$\tau^{-\alpha} f(p_T, p_z = 0, \tau)$ as a function of the rescaled transverse momentum $\tau^\beta p_T$. The inset gives the curves at different times without rescaling for comparison. With $\alpha = 1$ and $\beta = 2/3$ the rescaled curves at different times lie remarkably well on top of each other. According to Eq. (5.1), this reveals a self-similar evolution of the distribution function f_S . If particle number is conserved, one has $\tau n = \tau N \int d^3p / (2\pi)^3 f = \text{const}$ which requires $\alpha - 3\beta = -1$ consistent with the values we used. In the inset of Fig. 6.5, the scaling region is seen to move to lower momenta. This is consistent with the positive value of the exponent $\beta > 0$ observed and can be interpreted as being due to an inverse particle cascade leading to the formation of a Bose-Einstein condensate at zero momentum.

To gain insight into the statistical and systematic errors for the exponents, we follow Sec. 4.1.1 and investigate how the values of the exponents α and β depend on the reference time τ_{ref} at which we start our self-similarity analysis. To this end, we compare the rescaled distribution function at τ_{ref} with the rescaled distribution function at different times up to $\tau/\tau_{\text{ref}} \leq 5$, and extract the best values for the exponents together with an estimate of the error (see App. C.1 for more details on the method).

In Fig. 6.6, we show the extracted values for the combination $\alpha - 3\beta$ and for β as functions of the reference time. Also shown are the values -1 and $2/3$ as gray dashed lines; the former corresponds to particle number conservation and the latter to an elastic scattering process with a resummed matrix element. (This effective elastic scattering interpretation of the numerical data will be discussed shortly in Sec. 6.1.2.) One finds that both of these quantities approach

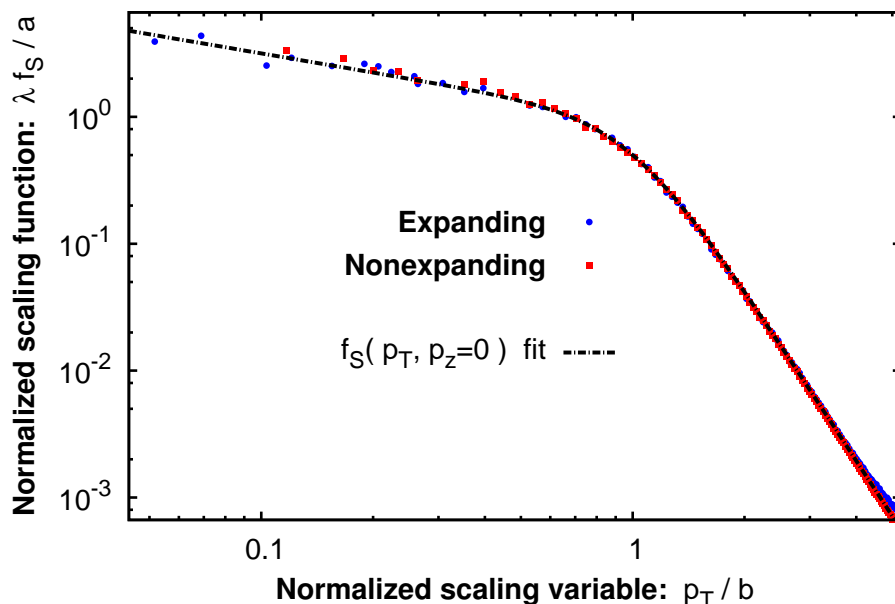


FIGURE 6.7: The normalized fixed point distribution $f(p_T, p_z = 0)$ at time $2\tau_0$. Also shown is the distribution function for a two component scalar field theory in a static box, previously shown in Fig. 4.6. Both spectra can be well described by the functional form given by Eq. (6.6) as indicated by the black dashed line.

the gray lines. We thus have

$$\alpha = 1, \quad \beta = \gamma = \frac{2}{3} \quad (6.5)$$

in the vicinity of the nonthermal fixed point with an error estimate of about 10% for β and typically 10 – 15% for $\alpha - 3\beta$, as can be determined from the error bars in Fig. 6.6.

We can also specify the functional form in the scaling region as

$$\lambda f_S(p_T, p_z) = \frac{a}{(|\mathbf{p}|/b)^{\kappa_<} + (|\mathbf{p}|/b)^{\kappa_>}}. \quad (6.6)$$

The non-universal constants a and b can be fixed by the constraints $\lambda f_S(|\mathbf{p}| = b) = a/2$ and $\lambda f'_S(|\mathbf{p}| = b) = -a(\kappa_< + \kappa_>)/(4b)$. In Fig. 6.7 we show the normalized distribution function $f(p_T, p_z = 0)$ at $\tau = 2\tau_0$ as well as the corresponding distribution function for a two component scalar field theory in a static box, discussed at length in Sec. 4.1. The scaling functions of both the static and the longitudinally expanding systems are given by Eq. (6.6). We used the values $\kappa_< = 0.5$ and $\kappa_> = 4.5$ for the scaling function in the figure but we observe that $\kappa_>$ slowly grows with time presumably approaching the value 5 that is also expected for nonrelativistic systems in wave turbulence [10, 178].

Indeed we showed in Sec. 4.1 that the infrared dynamics of a scalar field theory in a static geometry is governed by effectively nonrelativistic dynamics with a non-perturbative mechanism

that describes an inverse particle cascade. While the infrared scaling function in Eq. (6.6) can be observed in both expanding and non-expanding scalar systems, the temporal exponents $\alpha = 3/2$ and $\beta = 1/2$ for the static box in three spatial dimensions differ from the corresponding values of $\alpha = 1$ and $\beta = 2/3$ for the expanding theory. This difference stems from the different geometry; in the expanding case, one has a time dependent effective mass and particle number conservation gives $\tau n = \text{const}$ instead of $n = \text{const}$ for the fixed box. However, these differences do not alter the underlying dynamics in a fundamental way. We will show that the infrared dynamics of the expanding system is consistent with a description in terms of the same vertex-resummed kinetic theory as we used for the static case in Sec. 4.2.

6.1.2 Low momentum region from vertex-resummed kinetic theory

We will now extract the exponents α , β and γ for the inertial range at low momenta from a vertex-resummed kinetic theory and show that their values are consistent with our numerical results. We will subsequently relate these scaling exponents to the dynamics that leads to the formation of the Bose-Einstein condensate.

The kinetic equation for the distribution function f in a longitudinally expanding background is given by Eq. (5.11) that reads

$$\left(\partial_\tau - \frac{p_z}{\tau} \partial_{p_z}\right) f(p_T, p_z, \tau) = C[f](p_T, p_z, \tau). \quad (6.7)$$

The red shift term $-p_z \partial_{p_z} f / \tau$ follows from the boost invariance of the system in the longitudinal direction [14, 71, 151].

Since the occupation numbers are non-perturbatively large in the low momentum region $f \gtrsim 1/\lambda$, a perturbative approach is problematic. However for an N component scalar theory, one can employ a $1/N$ expansion of the two particle irreducible (2PI) effective action [106, 114]. To next-to-leading order (NLO) in this $1/N$ expansion, the temporal dynamics of the distribution function can be expressed as a kinetic equation with the vertex-resummed collision integral $C[f] \mapsto C_{\text{NLO}}^{2\leftrightarrow 2}[f]$ introduced in Refs. [117, 118]. We also refer to Sec. 4.2.2 for further details on the vertex-resummed collision integral.

To extract the scaling exponents of the low momentum region, we study the temporal scaling behavior of Eq. (6.7). This analysis proceeds in complete analogy to the studies in Secs. 3.3, 4.2 and 5.3.3 of previous chapters. One employs the self-similar scaling ansatz (5.1) for each side of the kinetic equation (6.7) and compares both sides. With the scaling behavior of the vertex-resummed collision integral

$$C_{\text{NLO}}^{2\leftrightarrow 2}[f](p_T, p_z, \tau) = \tau^{-\beta\mu} C_{\text{NLO}}^{2\leftrightarrow 2}[f_S](\tau^\beta p_T, \tau^\gamma p_z), \quad (6.8)$$

one obtains the time-independent condition given by Eq. (5.14) with the substitution $C_{\text{small-angle}}^{2\leftrightarrow 2}[f_S] \mapsto C_{\text{NLO}}^{2\leftrightarrow 2}[f_S]$, and a relation for temporal exponents

$$\alpha - 1 = -\beta\mu. \quad (6.9)$$

A scaling solution of the kinetic equation has to satisfy both equations simultaneously. A detailed discussion of the fixed point equation (5.14) and its solution is beyond the scope of this work. We will focus on the scaling relation Eq. (6.9) since we are primarily interested in the scaling exponents.

Therefore, we need to determine the scaling exponent of the collision integral μ . We first observe that the momentum range at low momenta is bounded by the effective mass $m(\tau)$, which motivates the approximation of the dispersion relation $\omega(p_T, p_z, \tau) \simeq m(\tau) + |\mathbf{p}|^2/2m(\tau)$. Because the leading mass term may cancel in intermediate steps, one has to determine the scaling property of the momentum $|\mathbf{p}|^2$. As our numerical results in Fig. (6.4) show, the momentum distribution in the IR is isotropic. Hence we can assume that longitudinal and transverse momenta as well as the modulus all scale equally with $\beta = \gamma$.

The precise form of the exponent μ is derived in Eq. (4.25) of Sec. 4.2.2 (with $s = \tau^\beta$) and reads

$$\mu_{\text{NLO,IR}}^{2\leftrightarrow 2} = 2 - \alpha/\beta - \sigma/\beta. \quad (6.10)$$

The reader will recall that the scaling exponent σ controls the temporal evolution of the effective mass. Using $\mu_{\text{NLO,IR}}^{2\leftrightarrow 2}$ for the scaling relation in Eq. (6.9) one obtains

$$\beta = \gamma = \frac{1 + \sigma}{2}. \quad (6.11)$$

Since our numerical results show that the mass scales with $\sigma = 1/3$, the scaling relation deduced from the effective kinetic theory results in momentum exponents that decrease with $\beta = \gamma = 2/3$. These values are consistent with the numerical results we obtained from classical-statistical simulations.

To determine the scaling exponent α from the vertex-resummed kinetic theory, we need a second condition. As for the non-expanding theory, we can use particle number conservation. Indeed, the elastic collision integral $C_{\text{NLO}}^{2\leftrightarrow 2}[f]$ vanishes when integrated over momenta. The left hand side of Eq. (6.7) can be identified with the total time derivative of the distribution function

$$\left(\partial_\tau - \frac{p_z}{\tau} \partial_{p_z} \right) f(p_T, p_z, \tau) = \frac{d}{d\tau} f \left(p_T, \frac{p_z}{\tau}, \tau \right), \quad (6.12)$$

where we identified $p_z = \nu/\tau$. Hence, integrating the kinetic equation (6.7) over p_T and ν leads to

$$0 = \frac{d}{d\tau} N \int \frac{d^2 p_T d\nu}{(2\pi)^3} f\left(p_T, \frac{\nu}{\tau}, \tau\right) = \frac{d}{d\tau} \tau n. \quad (6.13)$$

This implies $\tau n = \text{const}$ in the infrared momentum range. From the self-similar form of Eq. (5.1), one then obtains

$$\alpha = 2\beta + \gamma - 1. \quad (6.14)$$

With Eq. (6.11), this leads to

$$\alpha = \frac{1 + 3\sigma}{2}. \quad (6.15)$$

Again, plugging in $\sigma = 1/3$ we obtain $\alpha = 1$. This is again consistent with the result extracted from our classical-statistical numerical simulations. One may therefore conclude that the vertex-resummed kinetic theory obtained from the NLO $1/N$ expansion is consistent with first principles classical-statistical numerical simulations of the expanding scalar theory at low momenta.

With the scaling properties of the infrared scaling region, we are now able to further analyze the power law growth of the zero mode $F_0(\tau) \equiv F(p_T = 0, p_z = 0, \tau)$ in Fig. 6.2 for sufficiently large volumes. Similar to the non-expanding case in Eq. (4.9), the correlation function F can be decomposed into a particle and condensate part according to

$$F(p_T, \nu, \tau) = \frac{f(p_T, p_z, \tau)}{\tau \omega(p_T, p_z, \tau)} + (2\pi)^3 \delta^{(2)}(\mathbf{p_T}) \delta(\nu) \phi_0^2(\tau). \quad (6.16)$$

For finite momenta, the ‘‘particle’’ part of this expression (see Eq. (2.57)) provides an alternative definition of the distribution function. We have checked numerically that it converges to the previous definition in Eq. (2.47) with increasing accuracy in time.

When considering over-occupation initial conditions (2.61) there is no condensate initially but the inverse particle cascade populates the zero mode according to the relation

$$\tau^{2/3} F_0 \sim \frac{f(p=0, \tau)}{\omega(p=0) \tau^{1/3}} \sim \tau^{\alpha+\sigma-1/3} \sim \tau^\alpha, \quad (6.17)$$

where we have used the scaling exponent of the mass $\sigma = 1/3$. Denoting the value of the rescaled zero momentum correlator $(\tau/\tau_{\text{start}})^{2/3} F_0(\tau)/V$ at the initial time τ_{start} of the self-similar regime as $f(p=0, \tau_{\text{start}})/(\tau_{\text{start}} m(\tau_{\text{start}}) V)$ and its final value at the condensation time τ_{cond} as $\tilde{\phi}_0^2(\tau_{\text{cond}}) = (\tau_{\text{cond}}/\tau_{\text{start}})^{2/3} \phi_0^2(\tau_{\text{cond}})$, the condensation time τ_{cond} then follows

from the power law dependence of the zero mode in Eq. (6.17) as

$$\begin{aligned}\tau_{\text{cond}} &\simeq \tau_{\text{start}} \left(\frac{\tilde{\phi}_0^2(\tau_{\text{cond}}) \tau_{\text{start}} m(\tau_{\text{start}})}{f(p=0, \tau_{\text{start}})} \right)^{1/\alpha} V^{1/\alpha} \\ &\sim V^{1/\alpha}.\end{aligned}\tag{6.18}$$

This is the same relation as for the non-expanding theory in Eq. (4.11). Most importantly, it diverges with increasing volume as $\tau_{\text{cond}} \sim V$ for the expanding theory close to its attractor.

We can also estimate the number of particles in the condensate n_c beyond the onset of condensation. By use of the decomposition in Eq. (6.16) one finds

$$n_c \sim \omega(p=0) \phi_0^2 \sim \tau^{-1},\tag{6.19}$$

where in the last step we used the scaling properties of the mass and the condensate. Hence once a condensate is created, its particle number is approximately conserved and its evolution effectively decouples from the rest of the system. This is certainly not true for times prior to the formation of the condensate, where the low momentum region plays an essential role.

6.1.3 Intermediate momenta

We now turn to a more detailed analysis of the intermediate momentum sector characterized by the $\sim 1/p_T$ power law in Fig. 6.1. In contrast to the soft scaling sector, the spectrum at intermediate momenta is anisotropic; it is more efficiently described by considering the dependence on the longitudinal and transverse momenta separately. Regarding the transverse momentum dependence, we discussed in Sec. 5.2.1 that in this case, there is effectively neither a particle nor an energy flux in transverse momentum. Instead the energy and particle number densities per transverse momentum mode $\tau dn/dp_T$ and $\tau d\epsilon/dp_T$ are time independent and thus conserved at each transverse momentum separately.

Such a conservation of both energy and particle number is a general property of the anisotropic scaling regions of the longitudinally expanding scalar and gauge field theories, as observed in Sec. 5.2. In contrast, as we argued in Sec. 3.1, there is no single scaling solution conserving both energy and particle number for isotropic systems, and only one conservation law constrains the scaling solution instead. This has been observed not only for scalar and gauge theories in a static geometry [7, 8, 22] discussed in Sec. 3.2, but also within the low momentum inertial range of the expanding scalar theory studied above. There particle number conservation leads to an inverse particle cascade. We therefore should rather distinguish between conservation laws in *isotropic* and *anisotropic* scaling regions. While in the prior only one conservation law can be satisfied, the latter may conserve two quantities simultaneously.

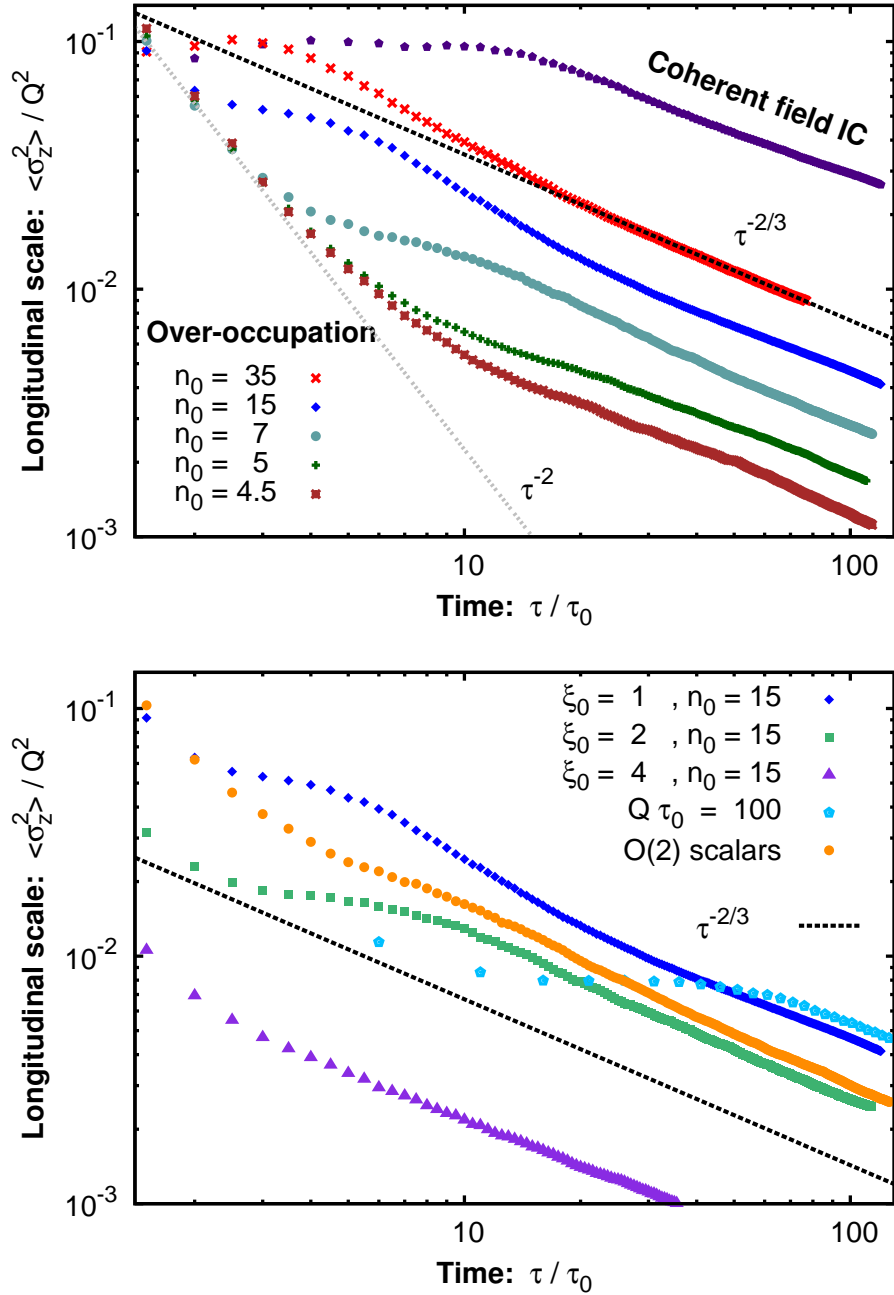


FIGURE 6.8: Time evolution of the longitudinal momentum scale $\langle \sigma_z^2 \rangle(\tau)$ for different initial conditions. **top:** After a short transient behavior, the dynamics becomes insensitive to different values of n_0 and all curves follow an approximate $\tau^{-2/3}$ power law dependence indicated by the black dashed line. Comparison to the gray dashed free streaming ($\sim \tau^{-2}$) curve shows the significance of momentum broadening. **bottom:** Three of the curves show the insensitivity of the late time behavior to variations of the initial momentum anisotropy ξ_0 . The curve labeled $Q\tau_0 = 100$ corresponds to a different initialization time and demonstrates insensitivity of late time results to the starting time. The line labeled $O(2)$ scalars shows the results for two component scalars. Since all the other curves are for $N = 4$ scalar theories, this curve demonstrates that late time results are independent of the number of degrees of freedom.

In the language of the self-similar evolution in Eq. (5.1), the conservation of energy and particle number in the anisotropic scaling regime gives rise to the scaling relations

$$\alpha - \gamma + 1 = 0, \quad \beta = 0. \quad (6.20)$$

With these constraints taken into account, the relevant dynamics in this regime is that of longitudinal momentum broadening. This phenomenon can be efficiently analyzed in terms of the characteristic longitudinal momentum scale

$$\sigma_z^2(p_T, \tau) = \frac{\int dp_z p_z^2 f(p_T, p_z, \tau)}{\int dp_z f(p_T, p_z, \tau)}. \quad (6.21)$$

In Fig. 6.8 we show the time evolution of $\langle \sigma_z^2 \rangle(\tau)$ (that is $\sigma_z^2(p_T, \tau)$ averaged over transverse momenta within the intermediate inertial range ii) for various simulation parameters. The top panel shows the behavior under variations of the initial over-occupancy n_0 , while the bottom panel corresponds to variations of the initial anisotropy ξ_0 , the initial time $Q\tau_0$ as well as the number of field components. While for different initial conditions the early time dynamics ranges from free streaming to an approximately constant behavior, one observes that the late time behavior becomes insensitive to all of these aspects. Ultimately all curves follow a universal scaling behavior in time.

According to Eq. (5.1) the scaling behavior of σ_z is characterized in terms of the scaling exponent γ ,

$$\sigma_z^2(p_T, \tau) \sim \tau^{-2\gamma}. \quad (6.22)$$

We have checked that this scaling holds for all transverse momenta within the momentum range of the scaling region. By performing a combined analysis of all data sets, we obtain an estimate of the scaling exponent

$$2\gamma = 0.66 \pm 0.05. \quad (6.23)$$

A comparison with the data in Fig. 6.8, shows that the observed scaling behavior is very well reproduced by an approximate $\tau^{-2/3}$ power law dependence.

We can also analyze the dynamics of momentum broadening on a more microscopic level by directly considering the single particle distribution at a typical transverse momentum $p_T^{\text{int.}}$ within the intermediate momentum range ii). Our results for the time evolution of the longitudinal spectrum are presented in Fig. 6.9, which shows snapshots of the distribution at $p_T^{\text{int.}} = Q/2$ for different times. The spectrum is shown as a function of the rapidity wave number $\nu = \tau p_z$ on the horizontal axis, which effectively amounts to undoing the red shift of longitudinal momenta. While for a non-interacting system the distribution becomes time independent when plotted as a function of ν , this is clearly not the case for the longitudinally expanding scalar

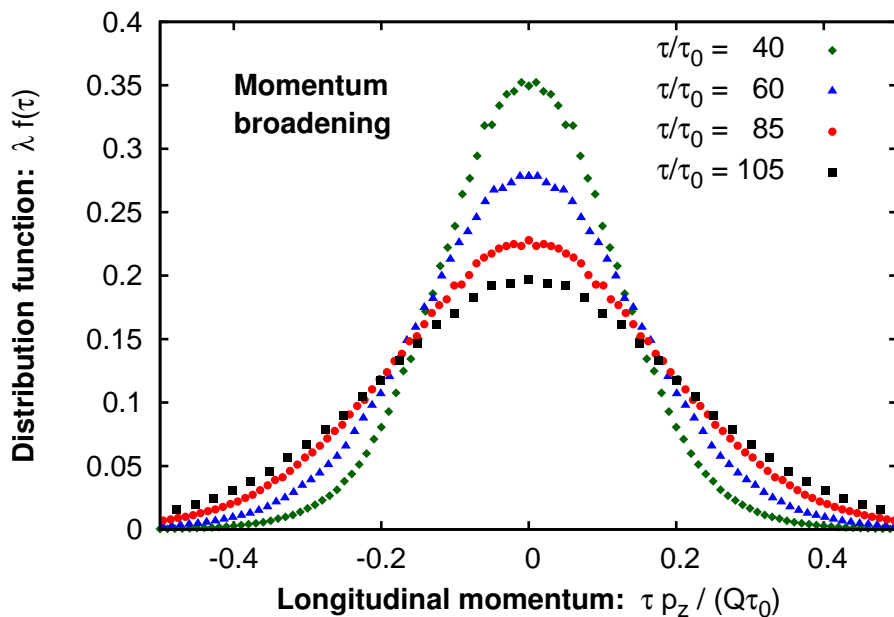


FIGURE 6.9: Dependence of the single particle distribution function on the longitudinal momentum variable $\nu = \tau p_z$ at $p_T = Q/2$ for different times of the evolution. Momentum broadening leads to a redistribution of the spectrum from lower to higher ν .

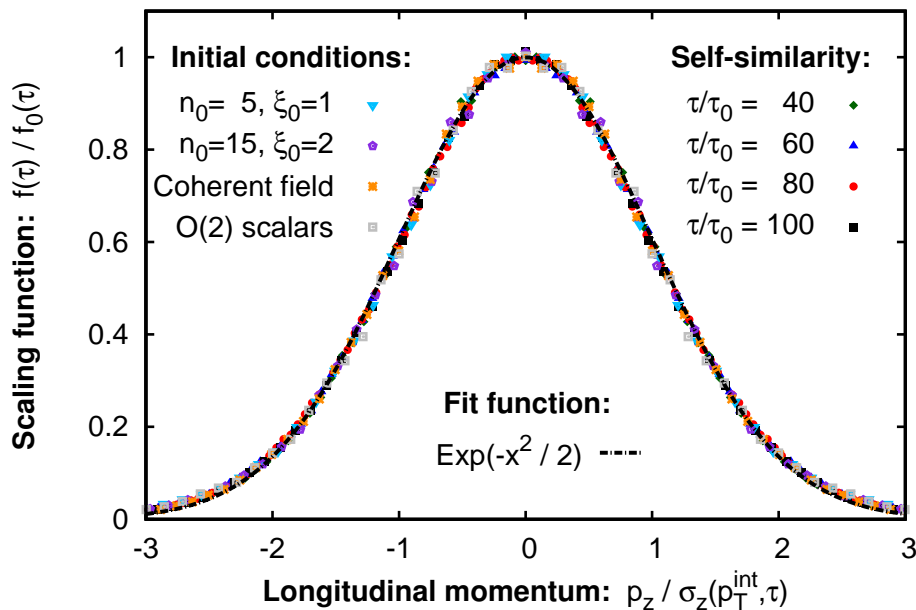


FIGURE 6.10: Normalized distribution $f_S = \tau^{-\alpha} f \sim f/f_0$ for the fixed point at typical *intermediate* transverse momenta p_T^{int} , as a function of rescaled longitudinal momenta p_z/σ_z . The rescaled spectra of Fig. 6.9 for $n_0 = 35$ and $\xi_0 = 1$ at different times collapse onto a single curve, proving the self-similarity of the evolution (right labels). As shown, the functional form of the fixed point distribution is independent of the initial conditions (left labels) and can be described by a normalized Gaussian distribution (black dashed curve).

theory. Instead, Fig. 6.9 shows a clear broadening of the longitudinal momentum distribution as a function of time along with a decreasing amplitude $f_0(\tau) = f(p_T = p_T^{\text{int}}, p_z = 0, \tau)$.

Once we take into account the decrease of the overall amplitude of the distribution according to

$$f_0(\tau) \sim \tau^\alpha \quad (6.24)$$

with $\alpha \simeq -2/3$ determined by the scaling relation in Eq. (6.20) and normalize the longitudinal momenta by the typical momentum scale $p_z/\sigma_z(p_T^{\text{int}}, \tau)$, the rescaled distribution approaches a stationary (time independent) fixed point $f_S(p_z/\sigma_z)$. This is shown in Fig. 6.10, where we present the rescaled distribution $f(p_T = p_T^{\text{int}}, p_z, \tau)/f_0(\tau)$ as a function of the rescaled longitudinal momentum $p_z/\sigma_z(p_T^{\text{int}}, \tau)$. The fact that the results at different times are indistinguishable confirms that the dynamics of momentum broadening can be accurately described by a self-similar scaling behavior as in Eq. (5.1).

The functional form of the fixed point distribution is well described by a Gaussian distribution of width σ_z , which is shown as a black dashed line. One can also verify explicitly from Fig. 6.10 that the functional form of the fixed point distribution is independent of the initial conditions as well as the number of field components. We conclude that the universal properties of the intermediate momentum regime can be summarized in terms of the scaling exponents

$$\alpha \simeq -2/3, \quad \beta \simeq 0, \quad \gamma \simeq 1/3 \quad (6.25)$$

and the scaling function

$$\lambda f_S(p_T, p_z) \simeq \frac{A}{p_T} \exp\left(-\frac{p_z^2}{2\sigma_z^2}\right), \quad (6.26)$$

with a non-universal constant A .

Remarkably, these features of the intermediate momentum regime of the expanding scalar theory are identical to those that we demonstrated previously for expanding over-occupied non-Abelian plasmas in Chapter 5 (or Refs. [14, 15]). In Sec. 5.2, we argued that this agreement provides strong proof of universality, since the underlying elementary microscopic dynamics of the two theories are very different. The results presented here significantly strengthen our previously presented arguments.

6.1.4 Hard momentum region

As noted previously, the momentum range for the intermediate scaling regime shifts towards lower momenta. At late times, an additional scaling regime emerges for hard transverse momentum modes, where the p_T spectrum in Fig. 6.1 becomes approximately independent of the

transverse momentum. Since the spectrum in this regime is highly anisotropic (with the typical longitudinal momenta much smaller than the typical transverse momenta), we will again analyze the transverse and longitudinal momentum dependence separately. Just as in the case of the intermediate momentum range, we find that there is effectively neither a particle nor an energy flux in the transverse direction. Thus as was the case in our prior discussion for the intermediate momentum range, the relevant dynamics is that of longitudinal momentum broadening and the scaling relations in Eq. (6.20) also hold for the hard momentum sector.

The momentum broadening in this novel scaling region can be efficiently described in terms of the hard longitudinal momentum scale

$$\Lambda_L^2(\tau) = \frac{\langle (\partial_\eta \partial_\mu \varphi_a(\tau, \mathbf{x}_T, \eta)) (\partial_\eta \partial^\mu \varphi_a(\tau, \mathbf{x}_T, \eta)) \rangle}{\tau^2 \langle (\partial_\mu \varphi_a(\tau, \mathbf{x}_T, \eta)) (\partial^\mu \varphi_a(\tau, \mathbf{x}_T, \eta)) \rangle}, \quad (6.27)$$

with summation over spatial indices $\mu = x^1, x^2, \eta$ implied and where $\langle \cdot \rangle$ includes a volume average. Within the quasiparticle picture (see Eq. (6.16)) and using $\omega(p_T, p_z, \tau) \simeq |\mathbf{p}|$ for hard momenta, the hard scale Λ_L^2 can be expressed as

$$\Lambda_L^2(\tau) \simeq \frac{\int d^2 p_T \int dp_z p_z^2 \omega(p_T, p_z, \tau) f(p_T, p_z, \tau)}{\int d^2 p_T \int dp_z \omega(p_T, p_z, \tau) f(p_T, p_z, \tau)}. \quad (6.28)$$

This is closely related to a transverse momentum integral of $\sigma_z^2(p_T)$. However a crucial difference is the additional weighting by the mode energy ω , which ensures that Λ_L^2 is dominated by high momentum modes.

The time evolution of the longitudinal hard scale is shown in the upper panel of Fig. 6.11. One observes that after an initial transient behavior the results for different initial conditions approach a common power law decay. By use of Eqs. (5.1) and (6.20), this scaling behavior is described by $\Lambda_L^2 \sim \tau^{-2\gamma}$ and the dynamical exponent γ can be extracted from the hard scale by taking the logarithmic derivative

$$2\gamma(\tau) = -\frac{d \log \Lambda_L^2}{d \log \tau}. \quad (6.29)$$

The resulting exponent $\gamma(\tau)$ is shown in the lower plot of Fig. 6.11 as a function of time for different initial conditions. One observes that all curves approach a constant value,

$$2\gamma = 1.05 \pm 0.1, \quad (6.30)$$

independent of the initial condition. By use of the scaling relations (6.20) we infer from this analysis the approximate values of the scaling exponents

$$\alpha \simeq -1/2, \quad \beta = 0, \quad \gamma \simeq 1/2. \quad (6.31)$$

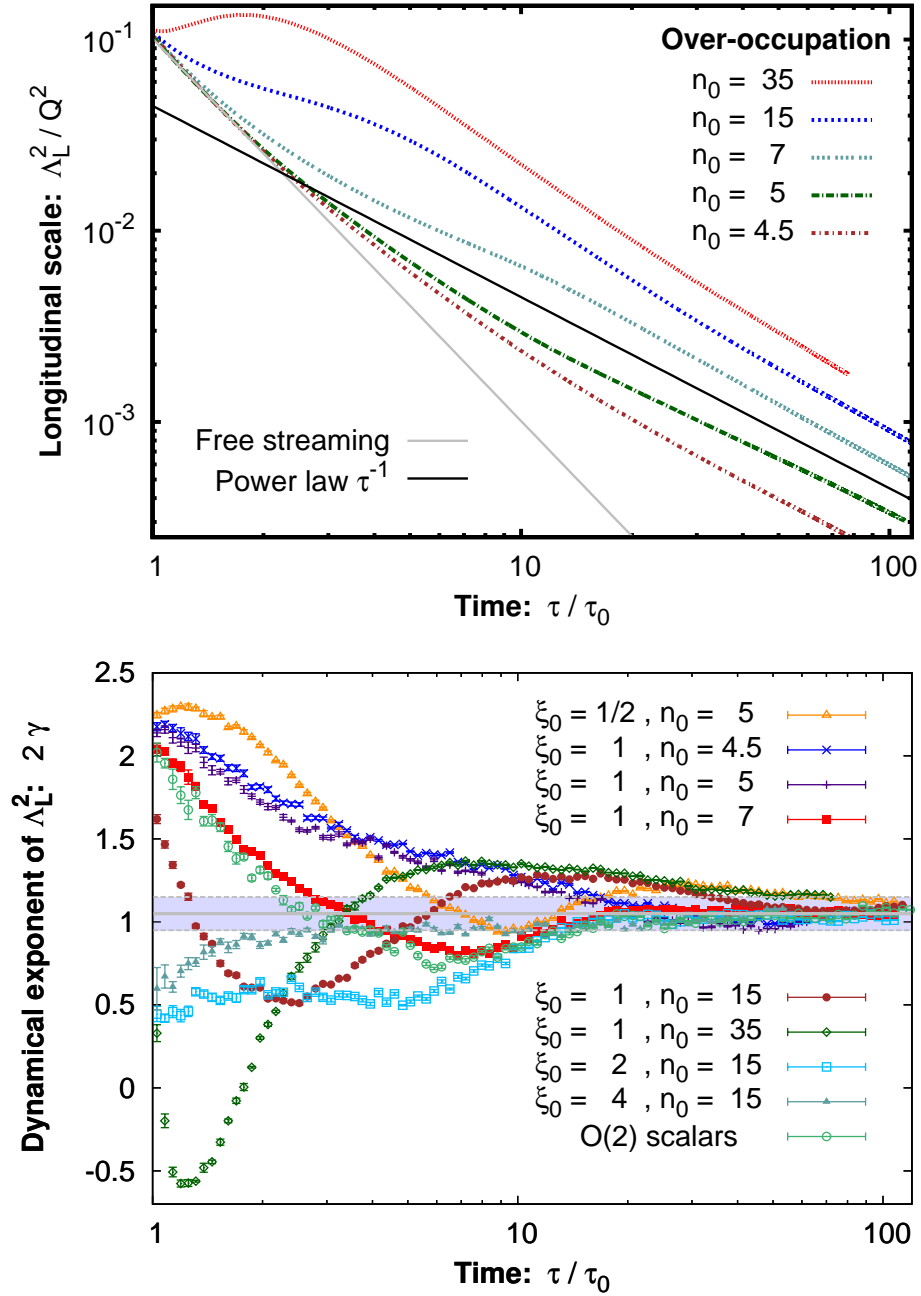


FIGURE 6.11: **top:** Time evolution of the longitudinal momentum scale at *hard* transverse momenta for different initial conditions. At late times all curves approach a common scaling behavior (black line). **bottom:** The scaling exponent 2γ is extracted from the logarithmic derivative in the lower panel. The gray lines indicate the value $2\gamma = 1.05 \pm 0.1$ obtained from an average over all shown simulations.

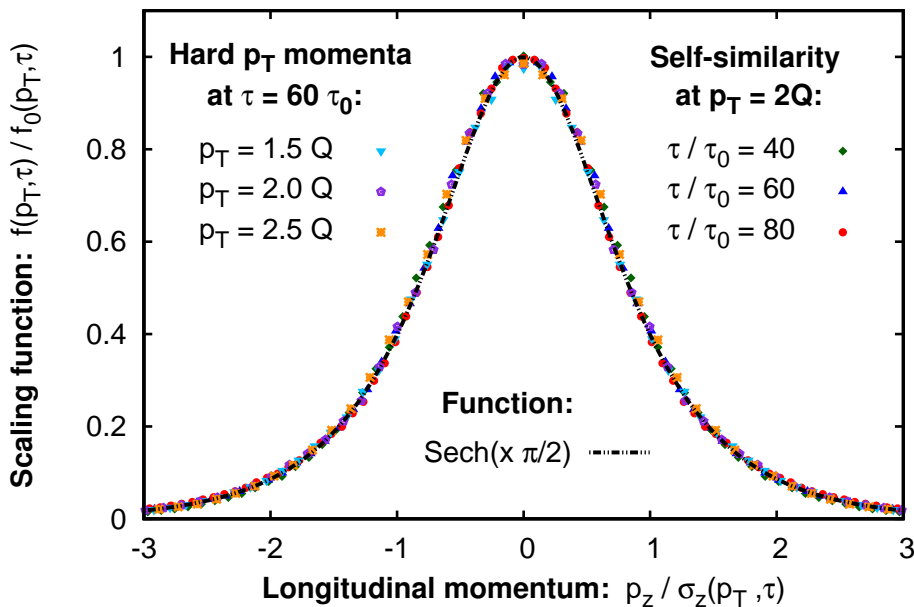


FIGURE 6.12: Normalized fixed point distribution $f_S = f/f_0$ as a function of rescaled longitudinal momenta p_z/σ_z for the fixed point at *hard* transverse momenta. The rescaled spectra at different times collapse onto a single curve, proving self-similarity of the evolution (right labels). The functional form of the fixed point distribution is the same within the momentum range of the scaling region (left labels) and can be described by a normalized hyperbolic secant function $\text{sech}(x\pi/2) = 1/\cosh(x\pi/2)$.

We note that the larger value of γ compared to the intermediate momentum sector characterizes the fact that the momentum broadening is less efficient for high momentum modes. Nevertheless the observed behavior is distinctly different from free streaming and significant momentum broadening occurs throughout the entire time. Moreover, we can understand the motion of the boundary between the intermediate and hard sectors (dashed purple line in Fig. 6.1) by comparing the decrease of the amplitude $f_0(p_T, \tau) \equiv f(p_T, p_z = 0, \tau)$ in both regions. The larger value of α in the hard region relative to the intermediate one implies a slower decrease of its amplitude. Therefore the boundary between both sectors moves to lower transverse momenta and increases the inertial range iii) of hard transverse momenta.

We have also extracted the scaling function $f_S(p_z/\sigma_z)$ following the same procedure outlined in the previous subsection. Our results are summarized in Fig. 6.12, where we show the normalized distribution function $f(p_T, p_z, \tau)/f_0(p_T, \tau)$ as a function of the normalized longitudinal momentum $p_z/\sigma_z(p_T, \tau)$. Our results at different times agree with each other and demonstrate the emergence of self-similarity with a time independent scaling function. We have also included the results for different hard transverse momenta $p_T > Q$, which show that the scaling function has the same form over the entire momentum of this scaling region. One also observes from Fig. 6.12 that the functional form of the scaling function is quite different from the Gaussian shape observed for the intermediate momentum fixed point. Compared to a Gaussian, the distribution in Fig. 6.12 features a smaller width and larger tails. This

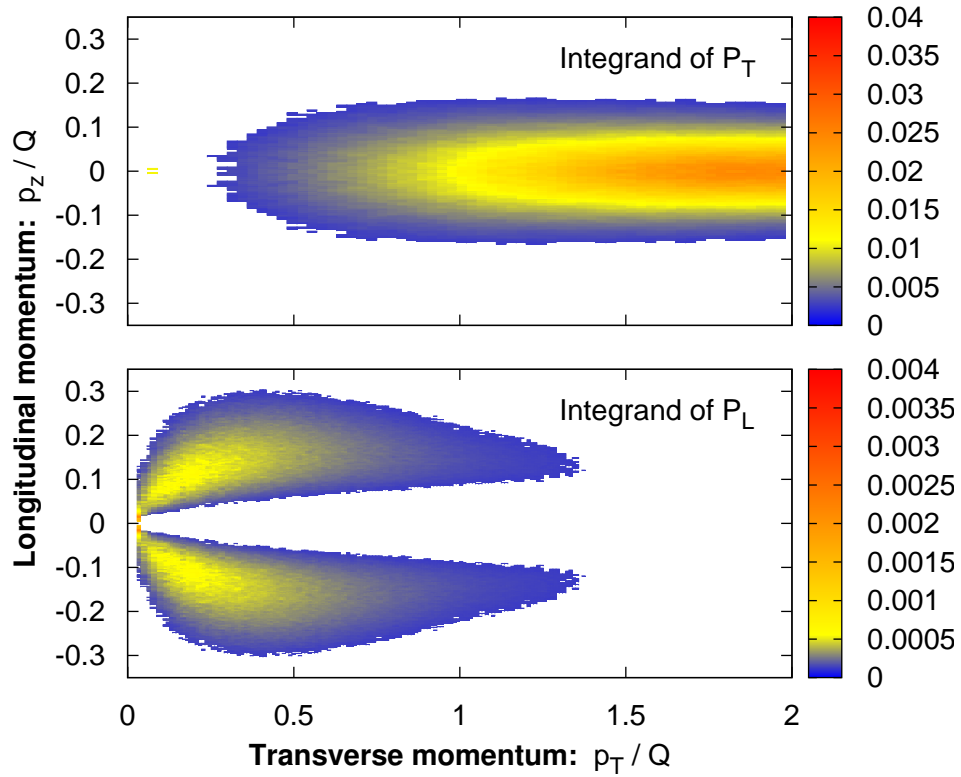


FIGURE 6.13: Contour plot of the contributions (see Eq. (6.33)) to the transverse (top) and longitudinal pressure (bottom) for initial occupancy parameter $n_0 = 35$ at time $\tau/\tau_0 = 50$. While the transverse pressure is dominated by hard excitations, one observes that the longitudinal pressure receives its dominant contributions from intermediate and soft momenta.

functional form is well described by a hyperbolic secant $\text{sech}(x \pi/2)$, which is also shown in the figure.

6.2 Implications of self-similarity for bulk anisotropy

Since the scalar field theory shows a rich dynamical structure, with different scaling behaviors observed in different momentum regimes, it is interesting to investigate how the interplay of the different sectors affects the evolution of bulk observables. We will focus on the bulk anisotropy of the system and investigate the time evolution of the ratio of the longitudinal and transverse pressures.

The components of the energy stress tensor of scalar and gauge field theories are computed as in Eq. (2.88). It is useful to consider the quasiparticle expression for the energy momentum tensor

$$T_{\mu\sigma}(\tau) \simeq N \int \frac{d^2 p_T dp_z}{(2\pi)^3} \frac{p_\mu p_\sigma f(p_T, p_z, \tau)}{\omega(p_T, p_z, \tau)}, \quad (6.32)$$

with $\mu, \sigma = x^1, x^2, \eta$ and with the rapidity wave number $p_\eta \equiv \nu = \tau p_z$. We note that for a proper treatment of the non-perturbative dynamics at low momenta, further contributions should be taken into account. While the energy density and the transverse pressure are generally dominated by the hard excitations of the system, the longitudinal pressure in particular can receive significant contributions from the soft sector. We have analyzed this behavior by performing a comparison of the integrands

$$\begin{aligned} \frac{d^2 P_T}{dp_T dp_z} &= N \frac{p_T}{(2\pi)^2} \frac{p_T^2 f(\tau, p_T, p_z)}{2 \omega(p_T, p_z, \tau)}, \\ \frac{d^2 P_L}{dp_T dp_z} &= N \frac{p_T}{(2\pi)^2} \frac{p_z^2 f(\tau, p_T, p_z)}{\omega(p_T, p_z, \tau)}. \end{aligned} \quad (6.33)$$

Our results are shown in Fig. 6.13, where we show a contour plot of both quantities. While the integrand of the transverse pressure is peaked around transverse momenta of the order of the hard scale, the longitudinal pressure receives its dominant contribution from modes with much softer transverse momenta. This points to the possibility that the quantities P_L and P_T can be dominated by modes from different momentum regions.

Let us now study the evolution of the ratio of the longitudinal pressure to the transverse pressure, P_L/P_T , whose value is a measure of the degree of bulk isotropization in the system. The time evolution of the pressure ratio P_L/P_T is shown in Fig. 6.14 (and in Fig. 6.15) as a function of time. While in all cases the bulk anisotropy of the system increases as a function of time, the quantitative behavior on the time scales observed can be different depending on the initial conditions.

For low enough initial amplitudes $n_0 \lesssim 6$ shown in Fig. 6.14, one observes an approximate $P_L/P_T \sim \tau^{-2/3}$ scaling. In this case, a strong infrared enhancement of the spectrum – corresponding to the scaling regime i) – is not fully developed during our simulations. Instead the observed behavior is consistent with the expectation that the longitudinal pressure is

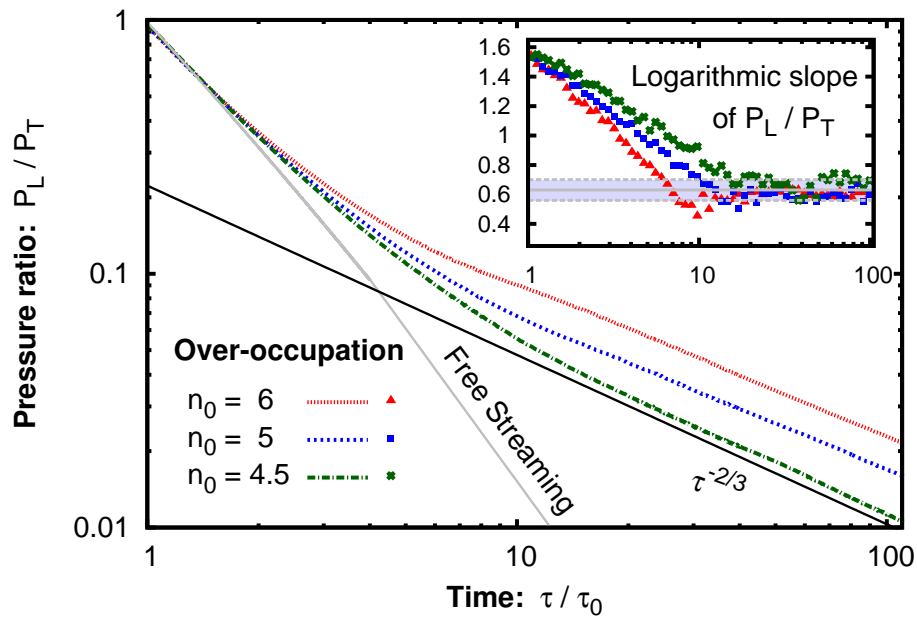


FIGURE 6.14: Ratio of the longitudinal to transverse pressure for initial conditions with small initial occupancies n_0 . The ratio P_L/P_T exhibits an approximate $\tau^{-2/3}$ scaling behavior as expected from kinetic theory. In these systems, the strongly enhanced infrared region is not fully developed during our simulations.

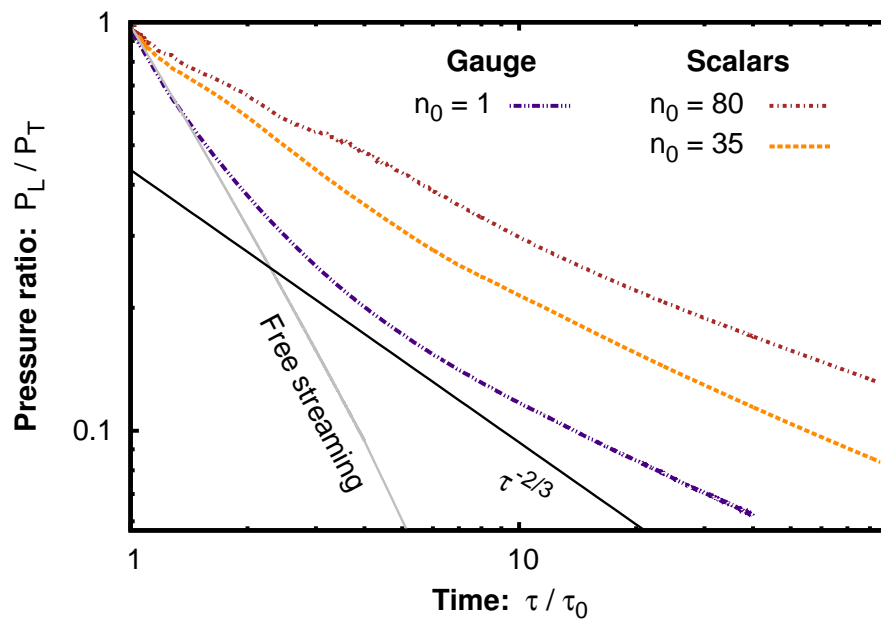


FIGURE 6.15: Comparison of the evolution of the longitudinal to transverse pressure ratio in longitudinally expanding gauge and scalar systems with large initial occupancies n_0 . While parametric estimates suggest a scaling as $P_L/P_T \sim (\tau/\tau_0)^{-2/3}$ in both cases, the observed decay of the longitudinal pressure is significantly slower due to large infrared contributions to the longitudinal pressure.

dominated by modes in the intermediate transverse momentum regime ii). Kinetic theory simulations of the expanding scalar theory [176] obtain the same result. In this kinetic framework, the soft region is approximated by a single zero mode such that the ratio P_L/P_T is also expected to be dominated by modes from region ii), which leads to this scaling behavior. There is a similar argumentation for non-Abelian plasmas. In kinetic theory, small angle scattering dominates for proper times $\tau \lesssim Q^{-1}\alpha_s^{-3/2}$, as we discussed in Sec. 5.3. Parametric estimates in the spirit of the ‘bottom-up’ scenario [67] then give a similar evolution

$$\frac{P_L}{P_T} \stackrel{\text{kinetic theory}}{\sim} (Q\tau)^{-2/3}. \quad (6.34)$$

In contrast, despite the fact that kinetic and classical-statistical descriptions seem to agree well for momenta above the screening scale [104, 164], the classical-statistical lattice simulations of non-Abelian plasmas show significant deviations from the kinetic theory scaling of Eq. (6.34). This is illustrated in Fig. 6.15, where the behavior of the gauge theory is shown for the same isotropic initial conditions and discretization as used in Sec. 5.2. The classical-statistical simulations for the scalar theory with large initial occupancy n_0 are also shown in Fig. (6.15). Similarly to gauge theory, they deviate significantly from the kinetic theory result (6.34). In these scalar simulations, the strong enhancement at soft momenta (region i given by Eq. (6.6)) is fully developed and has considerable contributions to the longitudinal pressure. In this case, the combined contributions of soft and intermediate modes lead to a slower decrease of P_L/P_T in time.

This has interesting consequences for the infrared region of non-Abelian plasmas. Since pressure is a bulk quantity, which sums over all momentum modes, an immediate conclusion from the observed discrepancy is that the infrared regime leads to significant contributions to P_L/P_T , also for non-Abelian gauge theory. This result is consistent with our earlier observation for the gauge theory case that modes with relatively small transverse momenta provide a sizable contribution to the longitudinal pressure (c.f. Ref. [15]). Therefore, the observed deviation from the evolution (6.34) hints to nontrivial dynamics at low momenta, which pose an interesting puzzle for non-Abelian plasmas and should be explored in future studies. Because of gauge ambiguities at low momenta, a direct observation of the dynamics from lattice simulations by means of the distribution function are not feasible. However, it is important to understand the dynamical mechanisms at low momenta because they may influence parts of the thermalization process in non-Abelian plasmas. Our results are also a challenge to conventional kinetic theories that we have discussed in Sec. 5.3.4. They suggest that extensions, possibly similar to the vertex-resummation in scalar theories, are required for a consistent description of non-Abelian systems.

Range	α	β	γ	$\lambda f_S(p_T, p_z)$
i)	1	2/3	2/3	$A_i ((\mathbf{p} /b)^{1/2} + (\mathbf{p} /b)^{4.5})^{-1}$
ii)	-2/3	0	1/3	$A_{ii} \exp(-p_z^2/(2\sigma_z^2))/p_T$
iii)	-1/2	0	1/2	$A_{iii} \operatorname{sech}(p_z/\sigma_z)$

TABLE 6.2: Summary of the scaling properties of the three inertial ranges observed in the longitudinally expanding scalar theory, see Sec. 6.1 for details. The parameters A_i , A_{ii} and b are non-universal constants, A_{iii} is constant for $p_T \lesssim 2Q$ and then rapidly decreases, and the longitudinal scale σ_z can depend on p_T .

6.3 Summary

In this chapter, we studied the nonthermal fixed point of a highly occupied longitudinally expanding $O(N)$ scalar theory in detail using classical-statistical simulations. The attractor features a remarkably rich structure and involves simultaneously three distinct inertial scaling regimes i) at soft, ii) at intermediate and iii) at hard transverse momenta that are shown in Fig. 6.1.

Within each inertial range of momenta, the single particle distribution exhibits a self-similar evolution characterized by a set of scaling exponents and scaling functions with $f(p_T, p_z, \tau) = \tau^\alpha f_S(\tau^\beta p_T, \tau^\gamma p_z)$. We extracted these quantities for each of the momentum sectors; these are briefly summarized in Table 6.2.

We found that the spectrum in soft regime i) evolves isotropically even though the system is longitudinally expanding. The single particle distribution is strongly enhanced and has the same functional form $f_S(p)$ as in non-expanding relativistic and nonrelativistic scalar systems that were discussed in Chapter 4. We showed that the distribution function in the infrared follows a self-similar evolution. We demonstrated that our numerical results from the classical-statistical simulations are consistent with a vertex-resummed kinetic theory that we have also used in Chapter 4 to explain the scaling properties of non-expanding scalars. Our analysis suggests that the infrared dynamics can be understood in terms of an inverse particle cascade from larger to lower momenta that leads to the formation of a Bose-Einstein condensate. We found that the condensate is formed with a power law $\tau^{2/3} F(p=0) \sim \tau^{1/\alpha}$ with the exponent $\alpha \simeq 1$ in the low momentum region for sufficiently late times and large volumes. The condensation time diverges with volume parametrically as $\tau_c \sim V$. Once the condensate is formed, it is subject to a $F(p=0) \sim \tau^{-2/3}$ power law decay. We established the presence of a dynamically generated mass, that decreases with time as $m(\tau) \sim \tau^{-1/3}$. We found that the dynamics of the soft regime i) occurs for $p_{\text{soft}} \leq m(\tau)$; this indicates that the infrared dynamics is that of a nonrelativistic system.

The generic features of these results are also found for the non-expanding system, where they form a universality class containing relativistic and nonrelativistic scalar theories. The longitudinally expanding systems differ in the values of the dynamical exponents and in the decreasing mass and condensate, all of which can be understood as a consequence of the dilution of the system due to the longitudinal expansion.

The intermediate and hard momentum regions ii) and iii) describe longitudinal energy and particle transport. We extended our analysis of the intermediate momentum regime ii) of the previous chapter that lies in the same universality class as non-Abelian plasmas. We verified the robustness of the nonthermal anisotropic fixed point by varying the initial conditions and obtained error estimates for the scaling exponents.

We discussed the emergence of a further scaling regime iii) in the expanding scalar theory, which appears for an inertial range of hard transverse momenta $p_T \gtrsim Q$. It is characterized by a flattening of the single particle transverse momentum distribution at vanishing p_z and a hyperbolic secant distribution along the longitudinal direction. The temporal evolution of the longitudinal momentum scale in this region of hard transverse momenta goes as $p_{z,\text{typ}} \sim \tau^{-1/2}$. Although this is faster than the $\sim \tau^{-1/3}$ scaling in regime ii), it is still distinctly slower than a freely streaming system with negligible self-interactions, which would imply a $\sim \tau^{-1}$ scaling behavior. Hence, also regime iii) involves nontrivial dynamics.

We studied implications of the scalar attractor on the evolution of the ratio of the longitudinal pressure to the transverse pressure P_L/P_T . Comparing this ratio between simulations of non-Abelian plasmas and scalars with large initial occupancies, we found deviations from the evolution of P_L/P_T expected from kinetic arguments. Our data suggest that these deviations result from a strong contribution of the infrared sector to the longitudinal pressure. While we have an explanation of the infrared dynamics in scalar systems by means of the vertex-resummed kinetic theory, a similar explanation in gauge theories is missing. Further studies are needed since the infrared region may modify parts of the thermalization process in non-Abelian plasmas.

Chapter 7

Conclusion and Outlook

In this work, we reported evidence of two novel far-from-equilibrium universality classes encompassing weakly-coupled non-Abelian plasmas and relativistic as well as nonrelativistic scalar systems (summarized in Fig. 7.1). We also found a remarkable system that incorporates both universality classes in different momentum regions simultaneously (illustrated by Fig. 7.2). These findings provide direct links between heavy-ion collisions, inflationary cosmology and table-top experiments with ultracold atoms and open interesting new theoretical and experimental opportunities.

More specifically, one of the universality classes is located at low momenta of nonrelativistic and $O(N)$ -symmetric relativistic scalar systems. Extending former studied in the context of wave turbulence and Bose-Einstein condensation [7, 9, 10, 22, 23, 89, 92, 117], we found that the single-particle distribution of the different theories follows a universal self-similar evolution $f(p, t) = t^\alpha f_S(t^\beta p)$. We obtained the values $\alpha \simeq 3/2$ and $\beta \simeq 1/2$ for the scaling exponents and a scaling function $f_S(p)$ that is illustrated in the right panel of Fig. 7.1. This universality between nonrelativistic and relativistic systems becomes possible because of the emergence of a mass gap due to medium and condensate effects in the (massless) relativistic theories.

To describe this infrared region of typically large occupancies $f \gtrsim 1/\lambda$, we used a vertex-resummed kinetic theory. It extends well-established kinetic descriptions by incorporating important vertex corrections that become relevant for high occupation numbers [7, 89]. The corresponding resummations follow from a systematic expansion in the number of field components N to next-to-leading order [114, 154]. With this effective kinetic description, we were able to explain the self-similar evolution with the above scaling exponents α and β . An extension of the vertex-resummed kinetic theory involves off-shell processes [7, 89]. It predicts an additional dependence of the scaling exponents on an anomalous dimension η and a dynamic exponent z [118]. While our simulations suggest small values for $\eta \approx 0$, future studies with higher numerical precision may investigate their values more accurately.

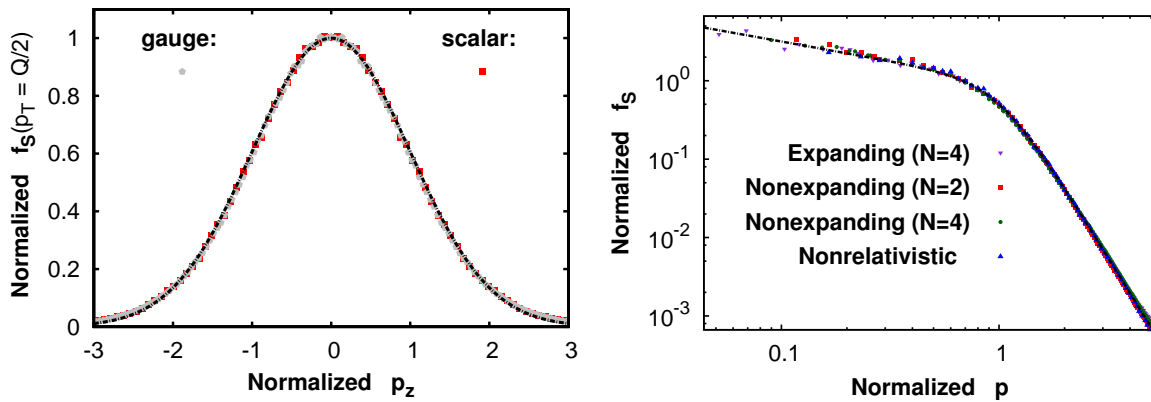


FIGURE 7.1: Shown are the fixed point distributions f_S of the two novel universality classes reported in this work: **left:** the universality class between expanding non-Abelian plasmas and scalar systems (Chapter 5); **right:** the universality class at low momenta between nonrelativistic and relativistic scalar systems in a static background (Chapter 4). For expanding scalars (Chapter 6) we found the same scaling function f_S at low momenta with similar scaling exponents, which may be regarded as an extension of this soft scaling region to longitudinally expanding systems.

The infrared scaling region describes an inverse particle cascade to lower momenta, where the Bose-Einstein condensate is built up as a power law in time with exponent α . The formation time of the condensate diverges with volume $t_{\text{cond}} \sim V^{1/\alpha}$. While previous studies in perturbative kinetic theory predicted a different condensation mechanism with a finite condensation time [152, 153], our classical-statistical simulation results can be described in terms of the resummed kinetic theory. This provides a consistent description of the infrared dynamics in scalar systems.

The universality class contains both nonrelativistic as well as relativistic scalar theories with a different number of components N , as visualized in the right panel of Fig. 7.1 at the example of the fixed point distribution. One may use this broad universality class, for instance, to learn from experiments with ultracold atoms aspects about the dynamics during the early stages of our universe [1].

The other universality class involves longitudinally expanding non-Abelian plasmas and scalar systems. This nontrivial geometry is chosen to put our studies in the context of heavy-ion collision experiments. Using large scale numerical simulations, we observed that the distribution function evolves in a self-similar way $f(p_T, p_z, \tau) = \tau^\alpha f_S(\tau^\beta p_T, \tau^\gamma p_z)$ over a wide inertial range of transverse momenta. The extracted universal scaling exponents $\alpha = -2/3$, $\beta = 0$, $\gamma = 1/3$ and scaling function $f_S(p_T, p_z)$ are the same for both theories. Different from scaling regions in Minkowski space-time, where only one quantity can be conserved locally, both energy and particle number are conserved in the anisotropic momentum region of the expanding systems simultaneously. In particular, there is effectively neither a particle nor an energy flux in transverse momentum in the expanding case.

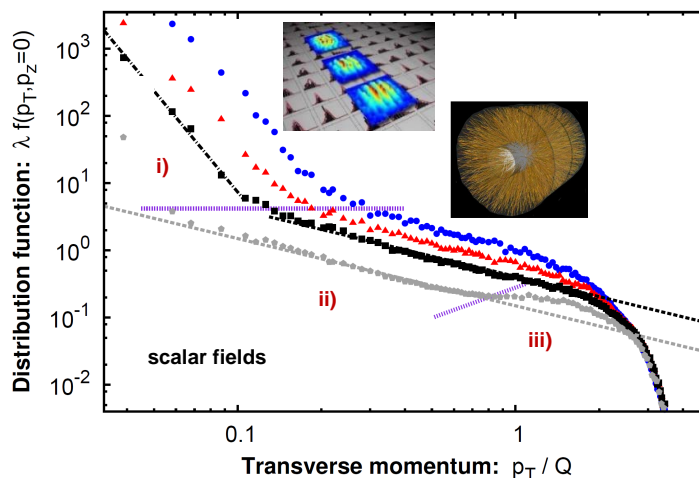


FIGURE 7.2: Using universality classes with scalar fields, a link between ultracold quantum gases and heavy-ion collisions is shown. Their universal scaling behavior can be found in the different scaling regions i) and ii), respectively, of the transverse fixed point distribution in longitudinally expanding scalar systems. This illustration is a composition of Figs. 1.2 and 6.1.

The observed universality is visualized in the left panel of Fig. 7.1 at the example of the longitudinal distribution. Since symmetries and underlying scattering processes for scalar and gauge theories show profound differences, the observation of universal dynamics in this case is highly nontrivial. Although the scaling behavior in gauge theories can be explained by elastic small-angle scatterings, the observed universality may hint to a much more general principle. Here the classification of strongly correlated quantum many-body systems in terms of nonequilibrium universality classes and associated scaling properties represents a crucial step. This provides an important direct connection between heavy-ion collisions in the limit of high energies and superfluid scalar systems.

The nonthermal fixed point of longitudinally expanding scalar systems reveals a remarkably rich structure. Apart from the universal regime with non-Abelian plasmas, we found two more scaling regions. One of them emerges at late times at hard transverse momenta $p_T \gtrsim Q$. It is characterized by a flattening of the transverse momentum distribution (at vanishing longitudinal momenta) and a hyperbolic secant distribution along the longitudinal direction, which evolves with longitudinal scaling exponent $\gamma = 1/2$. While we confirmed that this behavior corresponds to a scaling regime for a range of initial conditions, we are not aware of a known analog of this scaling in any other systems. Unfortunately, extending the gauge theory simulations to the values of τ/τ_0 where this novel regime appears in the scalar theory simulations is not feasible with present computational resources.

The other novel scaling regime in expanding scalar systems is located at low momenta and involves very high occupancies $f \gtrsim 1/\lambda$. Despite the longitudinal expansion, scatterings in

this regime are efficient enough to maintain an isotropic distribution. The scaling properties are very similar to the nonrelativistic scalars in a static background. The dynamics can also be understood in terms of an inverse particle cascade to lower momenta. This leads to the formation of a Bose-Einstein condensate for causally connected areas, with an increasing condensation time with larger volume. The vertex-resummed kinetic theory employed for non-expanding relativistic and nonrelativistic scalar systems explains the observed scaling properties also in the expanding case. Since scaling exponents slightly differ for different metric tensors, this is a powerful confirmation that important aspects of scalar systems can be correctly described by a vertex-resummed kinetic theory.

Moreover, expanding and non-expanding scalars exhibit the same scaling function. This remarkable universality is illustrated in the right panel of Fig. 7.1. The small differences of the scaling exponents can be entirely attributed to the dilution of the longitudinally expanding system. With this limitation, the universality class in scalar theories at low momenta encompasses a wide range of different systems, including $O(N)$ -symmetric relativistic scalars with different metric tensors as well as nonrelativistic Bose gases.

Hence, the nonthermal fixed point of longitudinally expanding scalars contains both universality classes simultaneously, as visualized in Fig. 7.2. This provides a strong link between heavy-ion collisions, ultracold quantum gases and inflationary cosmology in a special longitudinally expanding geometry. Such a development also opens intriguing new perspectives to experimentally access universal properties of such systems in extreme conditions with the help of quantum degenerate gases.

Apart from the emerging experimental possibilities with ultracold atoms that we noted above, our results lead to further questions and opportunities:

- The observed universality between expanding scalar and gauge theories is truly remarkable given their very different scattering matrix elements. Despite this difference, we find the same scaling behavior in both theories. Kinetic theory simulations of the expanding scalar theory [176] obtain the same scaling behavior $\sim \tau^{-2/3}$ for the pressure ratio P_L/P_T as expected from parametric estimates in the scaling region. While this confirms our lattice results of the observed scaling behavior, the agreement with the gauge theory is surprising and not evident from analytical considerations so far.
- For weakly coupled longitudinally expanding non-Abelian systems, plasma instabilities were expected to play an important role also beyond the very early stages of the thermalization process. However, our numerical results show preference to the ‘bottom-up’ thermalization scenario [67] that only involves elastic and inelastic processes. Moreover, the self-similar evolution that we observed from our lattice simulations was reproduced in Ref. [164] within the effective kinetic framework of Ref. [149]. Since this framework

neither contains a condensate nor plasma instabilities, this result confirms the interpretation of our data in terms of elastic and inelastic scatterings. However, it is still not clarified why plasma instabilities do not play an important role at late times.

- In our lattice simulations, the measured bulk anisotropy P_L/P_T shows clear deviations from its evolution according to kinetic estimates, for both scalar and gauge theories. Hence, these simulation results cannot be reproduced consistently in conventional kinetic theory frameworks. We also demonstrated the reason for that: the longitudinal pressure receives important contributions from soft modes. In scalar field theories, these contributions can be accounted for by including non-perturbative vertex-resummations to the kinetic theory, as we discussed above. Our gauge theory simulation results challenge the present kinetic framework and suggest that similar modifications as for scalar theory are needed.
- The observed deviation of P_L/P_T is very similar for highly populated scalar and gauge theories. Therefore, the soft momentum region gives a similar relative contribution to the longitudinal pressure for both theories. In scalar systems, this region is isotropic, strongly enhanced and responsible for Bose Einstein condensation. From the observed similarity of the relative contributions to P_L , our numerical results hint to an enhanced infrared region also for gauge theories. Whether this region leads to a transient Bose-Einstein condensate, which is under debate in the literature [19, 72, 104, 150, 179–182], or incorporates a nontrivial topological structure, is left to future studies.
- In this work, we found the first universality classes in far-from-equilibrium systems between gauge and relativistic as well as nonrelativistic scalar theories. Our results therefore provide a relevant foundation for future studies of self-similar scaling phenomena far from equilibrium. In particular, they show the interesting possibility of grouping scaling regions into universality classes.

Acknowledgements

At this point, I would like to express my deepest gratitude towards all the people who have supported me during the years of my doctoral studies.

Foremost, I would like to thank my doctoral advisor Jürgen Berges for giving me the opportunity to work on this exciting project. I am especially grateful for our many discussions, for his continuous support, trust, patience, encouragement and his many valuable advice in scientific as well as personal matters. I would also like to thank him for giving me the opportunity to attend numerous international workshops and conferences that were particularly useful.

I would like to thank Raju Venugopalan for our fruitful discussions, his support and encouragement and for our great collaboration. I am also very grateful for his invitation to visit BNL and his hospitality during my stay.

I also owe my gratitude to my collaborators Sören Schlichting and Asier Piñeiro Orioli for their dedicated commitment and strong support. I had the great pleasure to closely work with them and I gratefully acknowledge their contributions to this work. I particularly thank Sören and Asier for sharing their data and code on non-Abelian gauge theory and nonrelativistic scalars, respectively, with me.

I would also like to thank Larry McLerran, Dénes Sexty, Aleksi Kurkela, Jean-Paul Blaizot and Edmond Iancu for very insightful discussions.

My special thanks go to my present and former colleagues Daniil Gelfand, Roland Walz, Aleksandr Chatrchyan, Alexander Rothkopf, Valentin Kasper, Florian Hebenstreit, Naoto Tanji, Niklas Müller, Andreas Elben, Andreas Schachner, Benjamin Wallisch, Oscar Garcia Montero, Torsten Zache, Janosh Riebesell, Jan Stockemer, Letícia F. Palhares and David Mesterházy. They have provided a sensational group atmosphere, and it was a great pleasure working with them!

I also thank Andreas E., Andreas S., Alexander Mazur, Sören S., Asier P. O., Daniil G. and Valentin K. for proof-reading parts of my thesis.

I would like to thank my parents, grandparents and all my family and friends for their support and encouragement. This was essential for me, thank you!

I am very grateful to the Heidelberg University and the HGS-HIRe for FAIR for scholarships during my studies. I also thank the HGSFP for their financial support during my stay at BNL.

Finally, I deeply apologize to everyone who I might have forgotten here!

Appendix A

Mode functions and late-time asymptotics

In this Appendix we discuss explicit formulations of the mode functions that were introduced in Sec. 2.2.2. In non-expanding scalar systems with a possible dynamically generated mass $m(t)$, the mode function satisfies the free equation of motion

$$(\partial_t^2 + p^2 + m^2) \xi_{\mathbf{p}}(t) = 0. \quad (\text{A.1})$$

The mode function can be expressed as a plane wave

$$\xi_{\mathbf{p}}^{\text{non-exp}}(t) = \frac{1}{\sqrt{2\omega(p)}} e^{-i\omega(p)t}, \quad (\text{A.2})$$

with the dispersion relation $\omega(p) = \sqrt{p^2 + m^2}$, where $m(t) \approx \text{const}$ is assumed. It satisfies the normalization condition formulated in Eq. (2.51).

Similarly, a mode function has to satisfy the free equation of motion in the longitudinally expanding case

$$\left(\partial_\tau^2 + \frac{1}{\tau} \partial_\tau + p_T^2 + \frac{\nu^2}{\tau^2} + m^2(\tau) \right) \xi_{p_T, \nu}(\tau) = 0, \quad (\text{A.3})$$

where we again included a dynamically generated mass $m(\tau)$ for completeness. We can take

$$\xi_{p_T, \nu}(\tau) = \frac{\sqrt{\pi}}{2} e^{\pi\nu/2} H_{i\nu}^{(2)}(p_T \tau), \quad (\text{A.4})$$

as a mode function for a vanishing mass that satisfies all relevant conditions. Here $H_{i\nu}^{(2)}(x)$ denotes the Hankel function, which we compute numerically using the method described in Refs. [15, 157]. For vanishing transverse momentum, Eq. (A.4) is ill-defined and instead, the

mode function can be chosen as

$$\xi_{p_T=0,\nu}(\tau) = \frac{1}{\sqrt{2\nu}} \left(\frac{\tau}{\tau_0} \right)^{-i\nu}, \quad (\text{A.5})$$

which also satisfies the equation of motion (A.3) and the normalization condition (2.51). The functions (A.4) and (A.5) are used at initial time τ_0 to compute the initial field configurations in Eq. (2.81).

Let us now consider the late-time expressions at $\tau \gg \tau_0$ for the mode functions $\xi_{p_T,\nu}(\tau)$ in the expanding case. We can define a time-dependent dispersion relation

$$\tilde{\omega}(p_T, p_z, \tau) \equiv \sqrt{m^2(\tau) + p_T^2 + \nu^2/\tau^2}, \quad (\text{A.6})$$

with (time-dependent) longitudinal momentum $p_z = \nu/\tau$ and an effective mass $m(\tau)$. With this definition, we make the ansatz

$$\xi_{p_T,\nu}^{\text{late}}(\tau) = \frac{1}{\sqrt{2\tilde{\omega}(p_T, p_z, \tau)} \tau} e^{-i\Omega(p_T, p_z, \tau)} \quad (\text{A.7})$$

for mode functions at late times with the time dependent function $\Omega(p_T, p_z, \tau) = \int_{\tau_0}^{\tau} d\tau' \tilde{\omega}(p_T, p_z, \tau')$. The function in Eq. (A.7) satisfies the normalization condition of Eq. (2.51). We also need to show that Eq. (A.7) satisfies the free equation of motion (A.3). Computing the derivatives of (A.7), one obtains

$$(\partial_\tau^2 + \tau^{-1}\partial_\tau) \xi_{p_T,\nu}^{\text{late}}(\tau) = -\tilde{\omega}^2 \xi_{p_T,\nu}^{\text{late}}(\tau) + \mathcal{O}\left(\frac{\tilde{\omega}}{\tau} \xi^{\text{late}}\right). \quad (\text{A.8})$$

Hence, the ansatz in Eq. (A.7) is also an approximate solution of the free equation of motion for momenta satisfying

$$\tilde{\omega}(p_T, p_z, \tau) \tau \gg 1. \quad (\text{A.9})$$

In our case, the mass decreases with time as $m(\tau) \simeq m(\tau_{\text{start}}) (\tau/\tau_{\text{start}})^{-1/3}$, where τ_{start} is the time scale when the mass starts to follow its power law evolution. Therefore the left hand side of Eq. (A.9) grows with time as $\tilde{\omega}(p_T, p_z, \tau) \tau \geq m(\tau) \tau \simeq m(\tau_{\text{start}}) \tau_{\text{start}}^{1/3} \tau^{2/3}$. Already after a finite time one has $\tilde{\omega}(p_T, p_z, \tau) \tau \geq 1$ for all momenta, such that the condition in Eq. (A.9) is quickly reached. This confirms that Eq. (A.7) is a late-time asymptotic expression for the mode function $\xi_{p_T,\nu}(\tau)$. We note that alternatively, we get a similar form as in Eq. (A.7) by use of the tools provided in Refs. [183, 184] when starting from Eq. (A.4).

With the late-time form of the mode function in Eq. (A.7), one finds the expressions

$$|\xi_{p_T,\nu}^{\text{late}}(\tau)|^2 = \frac{1}{2\tilde{\omega}(p_T, p_z, \tau) \tau}, \quad (\text{A.10})$$

and

$$\partial_\tau \xi_{p_T, \nu}^{\text{late}}(\tau) = -i\tilde{\omega}(p_T, p_z, \tau) \xi_{p_T, \nu}^{\text{late}}(\tau), \quad (\text{A.11})$$

where we have dropped a term $\mathcal{O}(\xi/\tau)$ in the last expression. Our argumentation can be easily generalized to a more general diagonal expanding metric, which leads to the relations written in Eq. (2.57) for the statistical correlation function and its derivatives. This explains why our definition of the dispersion relation $\omega(p_T, p_z, \tau)$ in Eq. (2.48) takes the convenient form $\omega(p_T, p_z, \tau) \simeq \tilde{\omega}(p_T, p_z, \tau) = (m^2(\tau) + p_T^2 + \nu^2/\tau^2)^{1/2}$ at late times, which we confirm in Sec. 6.1.1.

Appendix B

Nonequilibrium lattice gauge theory

In gauge theories, a crucial difference to scalar fields is the concept of gauge-invariance, as we discussed in Sec. 2.1.4. Hence, gauge invariance should also be preserved in the discretized theory. For lattice QCD in vacuum or standard thermal equilibrium there are different discretization methods that differ in the level of accuracy of the lattice or temporal spacings [29, 185–187]. The technology for studying real-time, classical fields on the lattice is well known (see e.g. Ref. [188]). Here we use the Kogut-Susskind Hamiltonian formulation [186] of the Lagrangian lattice approach in temporal (or axial for longitudinally expanding systems) $A_0 = 0$ gauge [185].

Although we choose the $SU(2)$ gauge group for numerical calculations, our equations and discussions are also valid for other $SU(N_c)$ groups. Specific optimizations for the $SU(2)$ group can be found e.g. in Refs. [15, 122, 157, 189]. There the same equations of this Appendix are derived from a Lagrangian approach for $SU(2)$ theory for Minkowski and Bjorken metric, respectively. We follow a more general path here employing a (general) diagonal time-dependent metric with $g_{00} = 1$.

In the lattice framework, we consider instead of gauge fields $A_\mu^a(x)$ gauge links

$$U_j(x) = e^{ig a_j A_j^a(x) t^a}, \quad U_0(x) = \mathbb{1}. \quad (\text{B.1})$$

We used here the generators $t^a \in su(N_c)$ of Eq. (2.14), the identity matrix $\mathbb{1}$ and the shorthand notation $x = (\mathbf{x}, x^0)$. Moreover, we employed the gauge condition $A_0 = 0$ and no summation over the spatial index j is implied. A gauge link $U_j(x)$ can be understood as an approximation for the path-ordered Wilson line over a straight path $\mathcal{P} e^{ig \int_x^{x+\hat{j}} dy A_j(y)}$ connecting the neighboring lattice sites x and $x + \hat{j}$. It transforms under local gauge transformation as

$$U_j(x) \mapsto G(x) U_j(x) G^\dagger(x + \hat{j}). \quad (\text{B.2})$$

A central quantity is the plaquette

$$U_{jk}(x) = U_j(x) U_k(x + \hat{j}) U_j^\dagger(x + \hat{k}) U_k^\dagger(x), \quad (\text{B.3})$$

which is the smallest Wilson loop from lattice point x into the spatial j and k directions. While gauge links can be considered as gauge parallel transporters due to their transformation property (B.2), plaquettes transform locally as $U_{jk}(x) \mapsto G(x) U_{jk}(x) G^\dagger(x)$ and are gauge-independent under a color trace. At leading order in the lattice spacing, they can be related to the stress energy tensor

$$U_{jk}(x) \simeq e^{ig a_j a_k F_{jk}^a(x+\hat{j}/2+\hat{k}/2) t^a} \quad (\text{B.4})$$

that appears in the center of the corresponding Wilson loop.

The discretized Yang-Mills theory for a (general) diagonal time-dependent metric with $g_{00} = 1$ can be defined by the Hamiltonian

$$H_{\text{discr}}[U, E] = \sum_{\mathbf{x}} a^3 \left[-\frac{1}{2\sqrt{-g(x^0)}} \sum_{j=1}^3 \sum_a g_{jj}(x^0) E_a^j E_a^j + \frac{2N_c}{g^2} \sum_{j>0} \sum_{k>j} C_{jk} \left(1 - \frac{1}{2N_c} \text{tr} U_{jk} - \frac{1}{2N_c} \text{tr} U_{jk}^\dagger \right) \right]. \quad (\text{B.5})$$

The coefficients are chosen as

$$C_{jk} = C_{kj} = \frac{1}{a_j^2 a_k^2} \sqrt{-g(x^0)} g^{jj}(x^0) g^{kk}(x^0), \quad (\text{B.6})$$

in order to obtain the Hamiltonian in Eq. (2.25) in the continuum limit.¹ The coefficients are

$$\begin{aligned} C_{12} = C_{13} = C_{23} &= a_s^{-4} && \text{for static systems,} \\ C_{12} = \tau a_T^{-4}, \quad C_{13} = C_{23} &= \tau^{-1} a_T^{-2} a_\eta^{-2} && \text{for Bjorken expanding systems.} \end{aligned} \quad (\text{B.7})$$

¹To see that, one can expand the plaquettes in Eq. (B.4) for small lattice spacings

$$1 - \frac{1}{2N_c} \left(\text{tr} U_{jk} + \text{tr} U_{jk}^\dagger \right) \simeq \frac{g^2}{2N_c} a_j^2 a_k^2 \frac{1}{2} \sum_a F_{jk}^a F_{jk}^a.$$

With $\sum_{\mathbf{x}} a^3 \mapsto \int d^3x$ and the coefficients in Eq. (B.6) one arrives at the Hamiltonian in continuum space.

To compute the equations of motion, we define the functional (left) derivative for gauge links at equal time $x^0 = y^0$

$$\begin{aligned}\frac{\delta U_j(\mathbf{x})}{\delta A_k^a(\mathbf{y})} &= \delta_{jk} \delta_{\mathbf{x},\mathbf{y}} \frac{1}{a^3} \frac{d}{d\alpha} \left(e^{ig a_j \alpha t^a} U_j(\mathbf{x}) \right) \Big|_{\alpha=0} = ig \frac{a_k}{a^3} \delta_{jk} \delta_{\mathbf{x},\mathbf{y}} t^a U_k(\mathbf{y}) \\ \frac{\delta U_j^\dagger(\mathbf{x})}{\delta A_k^a(\mathbf{y})} &= \delta_{jk} \delta_{\mathbf{x},\mathbf{y}} \frac{1}{a^3} \frac{d}{d\alpha} \left(U_j^\dagger(\mathbf{x}) e^{-ig a_j \alpha t^a} \right) \Big|_{\alpha=0} = -ig \frac{a_k}{a^3} \delta_{jk} \delta_{\mathbf{x},\mathbf{y}} U_k(\mathbf{y}) t^a.\end{aligned}\quad (\text{B.8})$$

Together with $U_{jk}^\dagger = U_{kj}$ this leads to

$$\sum_{\mathbf{y}} a^3 \sum_{j>0} \sum_{k>j} \frac{\delta (\text{tr} U_{jk}(\mathbf{y}))}{\delta A_l^a(\mathbf{x})} = g a_l \sum_{k \neq 0, l} \text{Re} [\text{tr} (it^a [U_{lk}(\mathbf{y}) + U_{l(-k)}(\mathbf{y})])] , \quad (\text{B.9})$$

with the plaquette with negative k -direction

$$U_{j(-k)}(x) = U_j(x) U_k^\dagger(x + \hat{j} - \hat{k}) U_j^\dagger(x - \hat{k}) U_k(x - \hat{k}). \quad (\text{B.10})$$

This allows us to compute the discretized Hamilton equation $\partial_0 E = -\delta H/\delta A$

$$g \partial_0 E_a^j(x) = -a_j \sum_{k \neq 0, j} C_{jk} \text{Re} [\text{tr} (-2it^a [U_{jk}(x) + U_{j(-k)}(x)])] . \quad (\text{B.11})$$

For the update of $E_a^j(\mathbf{x}, x^0 + a_0)$ of this differential equation, we use the forward Euler scheme (2.86).

For the link update, we first get the differential equation

$$\begin{aligned}\partial_0 U_j(\mathbf{x}, x^0) &= \sum_{k, \mathbf{y}, a} a^3 (\partial_0 A_k^a(\mathbf{y}, x^0)) \frac{\delta U_j(\mathbf{x}, x^0)}{\delta A_k^a(\mathbf{y}, x^0)} \\ &= i K_j g E_a^j(\mathbf{x}, x^0) t^a U_j(\mathbf{x}, x^0),\end{aligned}\quad (\text{B.12})$$

with $K_j = -a_j g_{jj}(x^0)/\sqrt{-g(x^0)}$. Summation over the color index a is implied while no summation occurs over j , and we used Eqs. (B.8) and (2.26) for the second line. For a small time step a_0 , a discrete way of updating the gauge link is

$$U_j(\mathbf{x}, x^0 + a_0) = e^{ia_0 K_j g E_a^j(\mathbf{x}, x^0) t^a} U_j(\mathbf{x}, x^0). \quad (\text{B.13})$$

The links and (chromo-)electric fields are alternately updated according to Eqs. (B.11) and (B.13), which are the discretized versions of the classical Hamilton equations of motion in continuum (2.26). As for scalar fields, this corresponds to the leapfrog algorithm, where the electric fields are shifted by $a_0/2$ with respect to the gauge links. This, together with a small time step $a_0 \ll \sqrt{-g_{ii}} a_i$ for every spatial index i , ensure the stability of the algorithm. In practice, we also scale the coupling dependence out of the equations by mapping $E_a^j \mapsto E_a^j/g$ and $A_j^a \mapsto A_j^a/g$, such that the coupling only enters the initial conditions.

The Gauss law constraint (2.27) has also to be satisfied by the lattice fields. In its discretized form it reads

$$0 = \sum_{j>0} D_j E^j(x) = \sum_{j>0} a_j^{-1} \left(E^j(x) - U_j^\dagger(x - \hat{j}) E^j(x - \hat{j}) U_j(x - \hat{j}) \right) \quad (\text{B.14})$$

with $E^j = E_a^j t^a$. The covariant derivative appears as a discretized backward derivative with gauge links playing the role of gauge parallel transporters. Similar to the continuum theory (2.27), it can be derived from a functional derivative of the discretized Wilsonian action [122, 157, 189]. Since the Gauss law constraint is preserved by the equations of motion, it has to be satisfied by the initial conditions and its violation should be monitored during the simulation.

The lattice fields can be initialized in analogy to scalar fields (2.81) according to their mode expansion [15, 157, 190]

$$\begin{aligned} A_j^b(\mathbf{x}, t_0) &= \int \frac{d^3 \tilde{\mathbf{p}}}{(2\pi)^3} \left(\alpha_{b, \tilde{\mathbf{p}}}^{(\lambda)} \xi_{j, \tilde{\mathbf{p}}}^{(\lambda)}(t_0) e^{i\tilde{\mathbf{p}}\mathbf{x}} + \alpha_{b, \tilde{\mathbf{p}}}^{(\lambda)*} \xi_{j, \tilde{\mathbf{p}}}^{(\lambda)*}(t_0) e^{-i\tilde{\mathbf{p}}\mathbf{x}} \right) \\ E_b^j(\mathbf{x}, t_0) &= \sqrt{-g(t_0)} g^{jk}(t_0) \int \frac{d^3 \tilde{\mathbf{p}}}{(2\pi)^3} \left(\alpha_{b, \tilde{\mathbf{p}}}^{(\lambda)} \partial_0 \xi_{k, \tilde{\mathbf{p}}}^{(\lambda)}(t_0) e^{i\tilde{\mathbf{p}}\mathbf{x}} + \alpha_{b, \tilde{\mathbf{p}}}^{(\lambda)*} \partial_0 \xi_{k, \tilde{\mathbf{p}}}^{(\lambda)*}(t_0) e^{-i\tilde{\mathbf{p}}\mathbf{x}} \right). \end{aligned} \quad (\text{B.15})$$

The conjugate momenta of the spatial coordinates $\tilde{\mathbf{p}}$ were defined in footnote 6 of Sec. 2.2.2. The mode vectors (or polarization vectors) $\xi_{j, \tilde{\mathbf{p}}}^{(\lambda)}$ with polarizations $\lambda = 1, 2, 3$ are generalizations of the mode functions $\xi_{\tilde{\mathbf{p}}}$ in scalar field theory and satisfy similar normalization conditions to Eq. (2.51)

$$g^{jk}(x^0) \left(\xi_{j, \tilde{\mathbf{p}}}^{(\lambda)}(x^0) \overleftrightarrow{\partial}_0 \xi_{k, \tilde{\mathbf{p}}}^{(\lambda')} \right) = \delta_{\lambda\lambda'} \frac{i}{\sqrt{-g(x^0)}}. \quad (\text{B.16})$$

Mode vectors with a different polarization are orthogonal to each other. We choose $\lambda = 3$ as the longitudinal polarization vector $\xi_{j, \tilde{\mathbf{p}}}^{(\lambda)} \sim \tilde{p}_j$ while $\lambda = 1, 2$ are transverse polarizations. As in the scalar case, we have Gaussian initial conditions and thus we choose the mode vectors to satisfy the free equations of motion initially. For their explicit form, we refer to the Appendices of Refs. [15, 157].

The functions $\alpha_{b, \tilde{\mathbf{p}}}^{(\lambda)}$ and $\alpha_{b, \tilde{\mathbf{p}}}^{(\lambda)*}$ also have the same conditions as for scalar theory in Eqs. (2.83) and (2.84), with an additional $\delta_{\lambda\lambda'}$ due to polarization. Since for gauge theories we only consider over-occupation initial conditions of Eq. (2.61), we neglect the quantum 1/2 in the corresponding relations for $\alpha_{b, \tilde{\mathbf{p}}}^{(\lambda)}$. For the same reason, we have not included any one-point correlation function in the initialization (B.15). Moreover, we only initialize the transverse directions $\lambda = 1, 2$ taking $\alpha_{b, \tilde{\mathbf{p}}}^{(3)} = 0$. The Gauss law constraint (B.14) is fixed at initial time by use of the Fourier acceleration method [191, 192].

Gauge-invariant observables can be computed from gauge-invariant variables such as electric fields or gauge links. For instance, the computation of the energy density and the pressures

proceeds in the same way as for scalars in Eq. (2.88) with the classical stress-energy tensor $T_{\mu\nu}$ of the gauge theory in Eq. (2.28). To cope for the discretized theory, one only needs to exchange the magnetic fields $\sum_a F_{jk}^a F_{jk}^a$ with their discretized form in footnote 1.

In contrast, the distribution function $f_g(\tilde{\mathbf{p}}, x^0)$ is a gauge-dependent quantity. The gauge condition $A_0 = 0$ that was employed so far allows for residual time-independent gauge transformations. For a proper definition of the distribution function, we fix the residual gauge dependence by employing a Coulomb type gauge fixing conditions at fixed time $x^0 = t'$

$$\sum_j (-g^{jj}(t')) \partial_j A_j^a(\mathbf{x}, t') = 0. \quad (\text{B.17})$$

As for the Gauss law constraint, we use the Fourier acceleration method [15, 157, 191, 192] to fix the Coulomb type gauge. Different from usual Coulomb gauge that is valid at all times, we can only fix this gauge at a particular time because of our temporal gauge condition. We fix this gauge at the time t' when we compute our gauge-dependent quantities.

Similar to scalar theory in Eq. (2.49) or in (2.83), we define our gauge distribution as

$$f_g(\mathbf{p}, x^0) = \frac{1}{V N_g} \sum_{b=1}^{N_c^2-1} \sum_{\lambda=1,2} \left\langle \left| \alpha_{b,\tilde{\mathbf{p}}}^{(\lambda)}(x^0) \right|^2 \right\rangle. \quad (\text{B.18})$$

To shorten the notation, we also use $f(\mathbf{p}, x^0)$ for the gauge distribution. In its definition (B.18) we used $N_g = 2(N_c^2 - 1)$ and the functions

$$\alpha_{b,\tilde{\mathbf{p}}}^{(\lambda)}(x^0) = i\sqrt{-g(x^0)} \int d^3x \sum_{j,k} g^{jk}(x^0) \left(\xi_{j,\tilde{\mathbf{p}}}^{(\lambda)*}(x^0) \overleftrightarrow{\partial}_0 (A_k^b(\mathbf{x}, x^0)) \right) e^{-i\tilde{\mathbf{p}}\mathbf{x}}, \quad (\text{B.19})$$

which can be understood as a classical analogy of the scalar annihilation operators (2.50). As for the initial conditions, the polarization vectors $\xi_{j,\tilde{\mathbf{p}}}^{(\lambda)}$ are chosen to satisfy the free equations of motion for gauge theory, which follow from taking $g \rightarrow 0$ in the classical equations of motion. They also satisfy the Coulomb type gauge condition. Their form is explicitly given in the Appendices of Refs. [15, 157]. The Coulomb type gauge condition, together with the Gauss law constraint, lead to a vanishing $\alpha_{b,\tilde{\mathbf{p}}}^{(3)}(x^0) = 0$, such that only transverse polarizations need to be taken into account in the definition of f_g in Eq. (B.18). We finally note that other definitions of distribution functions in classical gauge theory have also been employed in the literature, as for instance in Refs. [16, 19].

Appendix C

Detailed analysis of self-similarity

Systems close to nonthermal fixed points exhibit a self-similar evolution. The distribution function then evolves as in Eq. (3.1) for a static or in Eq. (5.1) for longitudinally expanding metric and is characterized by scaling exponents and a scaling function. In this Appendix we describe how we extract the scaling exponents and estimate their uncertainties from this evolution, which was first introduced in Ref. [15] and adapted in Ref. [118].

C.1 For isotropic systems

In Sec. 4.1 we observe that the nonrelativistic and relativistic $N = 2$ and $N = 4$ theories evolve in a self-similar way, characterized by Eq. (3.1). Here we describe how we extract the pair of scaling exponents (α, β) and estimate their uncertainties from this self-similar evolution. We use the same extraction method for the isotropic infrared region in longitudinally expanding scalars in Sec. 6.1.1. In that case, the time t should be substituted by the proper time τ in all equations of this section.

At first, we quantify the deviation from the self-similar evolution of the distribution function. For each pair (α, β) the spectra at several times are rescaled according to

$$f_{\text{resc}}(p, t) = (t/t_{\text{ref}})^{-\alpha} f((t/t_{\text{ref}})^{-\beta} p, t). \quad (\text{C.1})$$

We use the distribution at the earliest time t_{ref} as a reference and the distributions at the N_{com} later times for comparison. A perfectly self-similar evolution (3.1) implies $\Delta f(p, t) \equiv f_{\text{resc}}(p, t) - f(p, t_{\text{ref}}) = 0$ such that the rescaled distribution function becomes time independent. However, this equality is in general only true for the correct set of scaling exponents and is in practice violated due to statistical uncertainties of the data and systematic deviations from the perfect scaling behavior. Minimizing the deviations yields the best fit for the scaling

exponents. The study of how the deviations are distributed around the best values gives an estimate for the uncertainties of the exponents. We quantify the deviations by

$$\chi^2(\alpha, \beta) = \frac{1}{N_{\text{com}}} \sum_{k=1}^{N_{\text{com}}} \frac{1}{\int d(\log(p))} \int d(\log(p)) \left(\frac{\Delta f(p, t_k)}{f(p, t_{\text{ref}})} \right)^2, \quad (\text{C.2})$$

where we sum over all relative deviations for each comparison spectrum. We use integration over $d(\log(p))$ to increase the sensitivity at low momenta. The upper limit of integration is given by the highest momentum included in the inverse particle cascade, i.e. the last point of the approximate $1/p^{\kappa}$ power law of the reference distribution function. Since the spectra are binned in momentum space, the integrals translate to sums over momenta $\int d(\log(p)) \mapsto \sum_{i=1}^{n_k-1} \log(p_{i+1}/p_i)$, where $p_{i+1} > p_i$ are the discrete momenta of each test spectrum k with possibly a different number of bins n_k . To compute the difference $\Delta f(p_i, t_k)$, we linearly interpolate momenta of the reference spectrum to coincide with the discrete momenta of the rescaled spectra.

The deviation $\chi^2(\alpha, \beta)$ is minimal for the best fit of the scaling exponents $\bar{\alpha}$ and $\bar{\beta}$. We define the likelihood function of a given set of exponents (α, β) as

$$W(\alpha, \beta) = \frac{1}{\mathcal{N}} \exp \left[-\frac{\chi^2(\alpha, \beta)}{2 \chi^2(\bar{\alpha}, \bar{\beta})} \right], \quad (\text{C.3})$$

where \mathcal{N} is a normalization constant such that the integral $\int d\alpha d\beta W = 1$. Integrating $W(\alpha, \beta)$ over one of the exponents provides a marginal likelihood function for the other one, e.g. $W(\alpha) = \int d\beta W(\alpha, \beta)$. Approximating the marginal likelihood functions with Gaussian distributions, we obtain an estimate for the standard deviations σ_α and σ_β , while the means are still given by $\bar{\alpha}$ and $\bar{\beta}$. Our thus measured scaling exponents are finally written in the form

$$\alpha = \bar{\alpha} \pm \sigma_\alpha, \quad \beta = \bar{\beta} \pm \sigma_\beta. \quad (\text{C.4})$$

C.2 For longitudinally expanding anisotropic systems

In App. D.2 we extract the scaling exponents (α, β, γ) from the self-similar evolution of the single-particle distribution of non-Abelian plasmas. Here we provide the details of our extraction method. Our strategy is to compare the rescaled weighted distribution at different times ($Q\tau_{\text{Test}} = 1250, 1500, 1750, 2000$)

$$f_{\text{Test}}^{(n,m)}(p_T, p_z, \tau) = p_T^n p_z^m s^{-\alpha} f \left(s^{-\beta} p_T, s^{-\gamma} p_z, \tau_{\text{Test}} \right), \quad (\text{C.5})$$

with the reference values

$$f_{\text{Ref}}^{(n,m)}(p_T, p_z) = p_T^n p_z^m f(p_T, p_z, \tau_{\text{Ref}}), \quad (\text{C.6})$$

at the reference time $Q\tau_{\text{Ref}} = 1000$. The variable $s = (\tau_{\text{Test}}/\tau_{\text{Ref}})$ denotes the time scale factor in Eq. (C.5). By use of the self-similarity relation (5.1), one finds that $f_{\text{Test}}^{(n,m)} = f_{\text{Ref}}^{(n,m)}$ holds for the correct set of scaling exponents (α, β, γ) . Since this equality is in general violated for different values of the scaling exponents as well as due to systematic deviations from the scaling behavior, one can then attempt to minimize the deviation in order to determine the best fitting scaling exponents. We quantify these deviations in terms of

$$\chi_{(n,m)}^2(\alpha, \beta, \gamma) = \frac{1}{N_{\text{Test}}} \sum_{\tau_{\text{Test}}} \frac{\int dp_T dp_z \left(f_{\text{Test}}^{(n,m)} - f_{\text{Ref}}^{(n,m)} \right)^2}{\int dp_T dp_z \left(f_{\text{Ref}}^{(n,m)} \right)^2}. \quad (\text{C.7})$$

In practice, we first divide all data into equidistant bins of size $p_T^{\text{Bin}}/Q = 0.02$ and $p_z^{\text{Bin}}/Q = 12.0/(Q\tau)$ respectively for transverse and longitudinal momenta to reduce statistical uncertainties. The integral is then evaluated as a sum over momentum bins. Since in general the rescaled momenta of the (binned) test data do not coincide with the center of any reference momentum bin, we use bi-cubic Bezier patches to perform additional interpolations and smoothing of the reference data. As we are primarily interested in the behavior of hard excitations, we employ the weights $n = 1, 2, 3$ and $m = 0, 1, 2$ and impose a lower transverse momentum cut-off $0.7 Q \leq p_T$ on the integration in eq. (C.7). In addition, we also impose a higher momentum cutoff $p_T \leq 1.7 Q$ and $p_z < 0.8 Q$ to restrict the comparison to the regime of high occupancies.

The combined deviation for all weighted distributions is then evaluated as the sum

$$\chi^2(\alpha, \beta, \gamma) = \frac{1}{9} \sum_{n=1}^3 \sum_{m=0}^2 \chi_{(n,m)}^2(\alpha, \beta, \gamma), \quad (\text{C.8})$$

which we calculate for different values of the scaling exponents. Clearly, a smaller overall deviation $\chi^2(\alpha, \beta, \gamma)$ for a given set of exponents shows a better realization of the scaling relation in Eq. (5.1) and thus points to higher likelihood for that set of exponents. To quantify this behavior, we define the likelihood for a given set of scaling exponents (α, β, γ) as

$$W(\alpha, \beta, \gamma) = \frac{1}{\mathcal{N}} \exp \left[-\frac{\chi^2(\alpha, \beta, \gamma)}{2\chi_{\text{min}}^2} \right]. \quad (\text{C.9})$$

Here χ_{min}^2 denotes the smallest value of $\chi^2(\alpha, \beta, \gamma)$ obtained in the analysis and quantifies statistical fluctuations of the data set as well as systematic deviations from the scaling behavior. The smallest deviation $\chi_{\text{min}}^2 = 0.00033$ is obtained for the set of scaling exponents $\alpha - 3\beta - \gamma = -1.05$, $\beta = -0.02$, $\gamma = 0.285$.

Appendix D

Expanding non-Abelian plasmas: Scaling exponents

We will now discuss the quantitative procedure to extract the scaling exponents α, β, γ from our simulations of longitudinally expanding non-Abelian plasmas in Sec. 5.3.1.¹ This analysis is complicated by the fact that scaling only sets in at later times after the transient regime. We therefore compare simulations with different initial conditions to see at what time a common scaling behavior is realized. On the other hand, in particular at very late times, discretization errors may influence the scaling behavior, and we employ different lattice discretizations to ensure that the results are independent of the discretization for all times of interest.

An additional complication arises when comparing our results to different weak coupling thermalization scenarios in the literature [67–71]. The measured scaling exponents can receive systematic errors from finite time effects and from deviations from the scaling of the energy density $\epsilon \sim \tau^{-1}$. These effects can lead to differences to the predicted scaling behavior. Since different quantities are sensitive to finite time corrections in different ways, a comparison between different extraction methods can be used to estimate these systematic uncertainties.

D.1 Gauge invariant analysis

We first discuss the extraction of the scaling exponents from hard scales and the energy stress tensor. Hard scales are gauge invariant observables that can be constructed by considering higher dimensional operators such as covariant derivatives of the field strength tensor [19]

$$\mathcal{H}_j^j(\tau) = -4 \int \frac{d^3x}{V} D_k^{ab}(x) F_b^{kj}(x) D_{ac}^l(x) F_{lj}^c(x). \quad (\text{D.1})$$

¹The methods discussed in this Appendix have been published in Ref. [15].

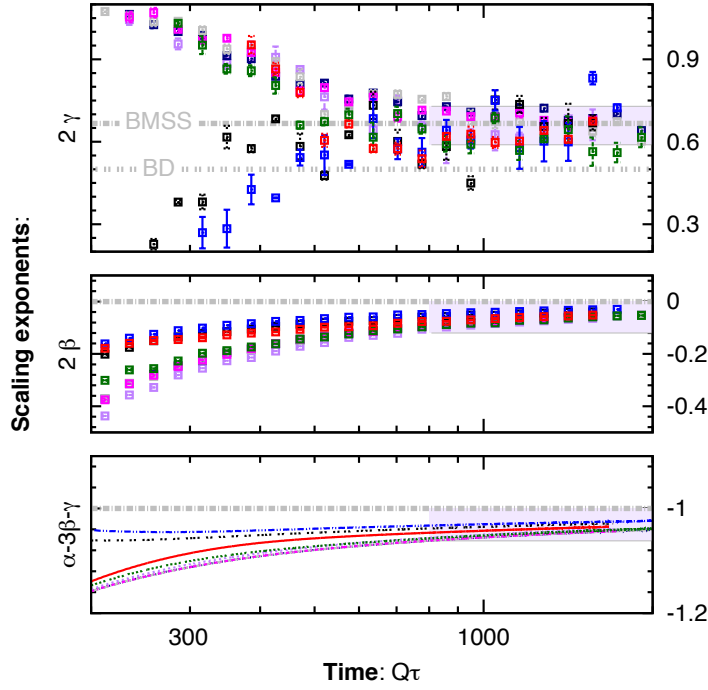


FIGURE D.1: Local scaling exponents β, γ and $\alpha - 3\beta - \gamma$ as functions of time. The results are extracted from the logarithmic derivatives of gauge invariant observables for different initial conditions and lattice discretization. In the scaling regime the results for the scaling exponent γ for different initial conditions converge to a common scaling exponent. The exponents β and $\alpha - 3\beta - \gamma$ are subject to systematic scaling corrections which decrease monotonically in time. The gray bands indicate the extracted values in the scaling regime along with their errors. The scaling exponents in the original ‘bottom-up’ scenario [67] (BMSS: $\gamma = 1/3, \beta = 0, \alpha - 3\beta - \gamma = -1$) and an instability modified version [68] (BD: $\gamma = 1/4, \beta = 0, \alpha - 3\beta - \gamma = -1$) are shown for comparison as gray dashed lines.

Here summation over spatial Lorentz indices $k, l = x, y, \eta$ and color indices $a, b, c = 1, \dots, N_c^2 - 1$ is implied while no summation over the spatial index j is assumed. By comparing the continuum equation of motion $D_k^{ab} F_b^{kj} = \partial_0 E_a^j / \sqrt{-g(x^0)}$ in (2.26), with its discretized analogy in Eq. (B.11), one obtains the corresponding expressions on the lattice [15, 157]

$$\mathcal{H}_j^j(\tau) = \frac{-g_{jj}}{\tau^2} \frac{a_j^2}{g^2} \frac{16}{N_T^2 N_\eta} \sum_{\mathbf{x}} \left(\sum_{k \neq 0, j} C_{jk} \text{Re} [\text{tr} (it^a [U_{jk}(x) + U_{j(-k)}(x)])] \right)^2. \quad (\text{D.2})$$

We will be interested in the quantities Λ_T^2 and Λ_L^2 , which are defined as the transverse and longitudinal projections of \mathcal{H}_j^j according to

$$\begin{aligned} \Lambda_T^2(\tau) &= \frac{\langle \mathcal{H}_\eta^\eta(\tau) \rangle}{\epsilon(\tau)}, \\ \Lambda_L^2(\tau) &= \frac{\langle \mathcal{H}_x^x(\tau) \rangle + \langle \mathcal{H}_y^y(\tau) \rangle - \langle \mathcal{H}_\eta^\eta(\tau) \rangle}{\epsilon(\tau)}, \end{aligned} \quad (\text{D.3})$$

with the energy density $\epsilon(\tau)$. The gauge-invariant quantities Λ_L and Λ_T are the characteristic longitudinal and transverse momentum scales of hard excitations. They contain additional information about the evolution of the system beyond what is contained in the energy-stress tensor. While this interpretation follows immediately from dimensional analysis, it is nevertheless insightful to evaluate the perturbative expressions for Λ_T^2 and Λ_L^2 . Considering only the Abelian part of the field strength tensor, one obtains the perturbative expressions in Eq. (5.7) (we refer to the Appendices of Refs. [15, 157] for details of this calculation), with scaling behavior $\Lambda_T^2 \sim \tau^{-2\beta}$, $\Lambda_L^2 \sim \tau^{-2\gamma}$.

To determine the scaling exponent γ , we investigate the scaling behavior of the longitudinal hard scale Λ_L^2 . We first divide our data in logarithmically equidistant time bins and then locally extract the scaling exponent from the logarithmic derivative

$$2\gamma(\tau) = -\frac{d \log(\Lambda_L^2(\tau))}{d \log(\tau)}. \quad (\text{D.4})$$

The result is shown in the top panel of Fig. D.1, where we present the extracted scaling exponent $2\gamma(\tau)$ as a function of time for a set of four different initial conditions in the range $\xi_0 = 1 - 6$ and $n_0 = 0.25 - 1$. After the transient regime, where the local exponents are quite different for different initial conditions and subject to large error bars, one observes a clear convergence towards a single value at later times. We also display results from the evolution for $\xi_0 = n_0 = 1$ using four different lattices in the range $N_T = 256 - 512$, $N_\eta = 1024 - 4096$ with $Qa_T = 0.5 - 1$ and $a_\eta = (0.625 - 2.5) \cdot 10^{-3}$ to take into account possible discretization dependencies. By averaging over all data points for $800 \lesssim Q\tau \lesssim 2000$ we obtain the estimate

$$2\gamma = 0.67 \pm 0.07 \text{ (stat.)}, \quad (\text{D.5})$$

as indicated by the gray band in Fig. D.1. The values of γ in the original ‘bottom-up’ thermalization scenario (BMSS) [67] ($\gamma = 1/3$) and the instability modified ‘bottom-up’ scenario by Boedeker (BD) [68] ($\gamma = 1/4$) are also indicated in Fig. D.1 as horizontal gray dashed lines.

Similarly, we extract the scaling exponent β from the scaling behavior of the transverse hard scale

$$2\beta(\tau) = -\frac{d \log(\Lambda_T^2(\tau))}{d \log(\tau)}. \quad (\text{D.6})$$

The result is shown in the middle panel of Fig. D.1, where we plot $2\beta(\tau)$ as a function of time. One observes that this local scaling exponent, extracted from the lattice data, approaches zero monotonically at late times. The residual deviation from zero is a clear manifestation of the finite time scaling corrections mentioned above. We find that this deviation is

$$|\beta(\tau)| < 0.06, \quad (\text{D.7})$$

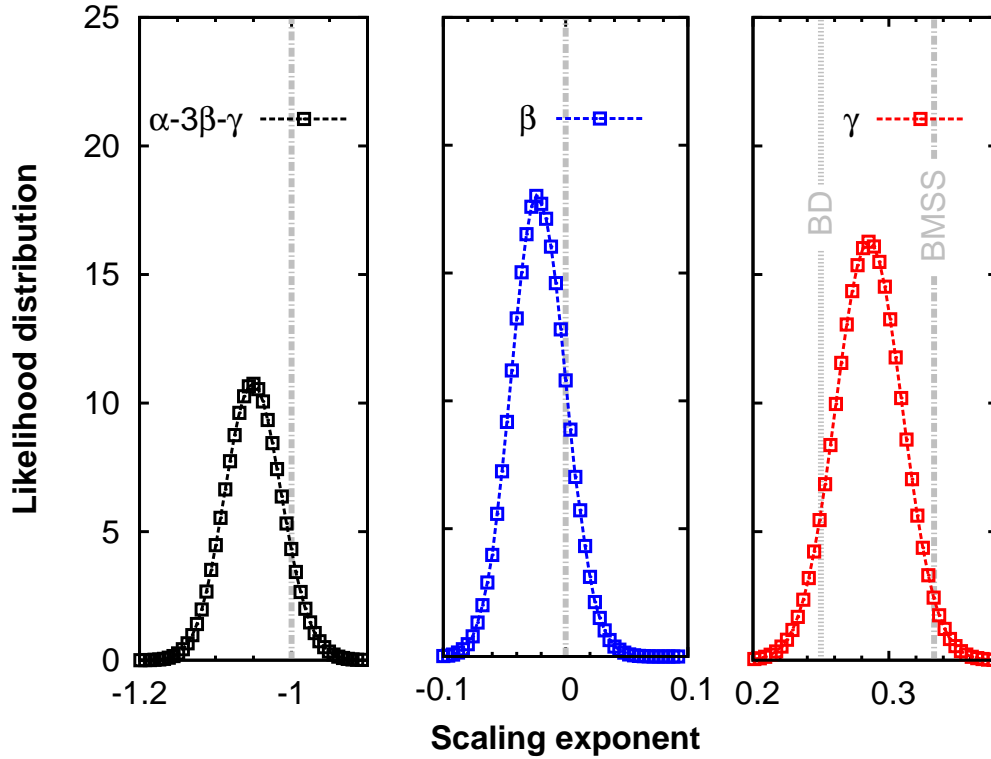


FIGURE D.2: (color online) Likelihood distribution W of the different scaling exponents. The gray vertical lines correspond to the respective values in the ‘bottom-up’ thermalization scenario (BMSS) [67] and one of its modified versions (BD) [68].

for $800 \lesssim Q\tau \lesssim 2000$ as indicated by the gray band in Fig. D.1.

Finally, we extract the linear combination of scaling exponents $\alpha - 3\beta - \gamma$ from the scaling behavior of the energy density

$$\alpha(\tau) - 3\beta(\tau) - \gamma(\tau) = \frac{d \log(\epsilon(\tau))}{d \log(\tau)}. \quad (\text{D.8})$$

According to Bjorken’s law in eq. (5.2) one can directly extract this quantity as

$$\frac{d \log(\epsilon(\tau))}{d \log(\tau)} = - \left(1 + \frac{P_L(\tau)}{\epsilon(\tau)} \right). \quad (\text{D.9})$$

In Fig. D.1, the right hand side of Eq. (D.9) is shown as a function of time. One observes that the scaling exponent approaches the anisotropic scaling limit $\alpha - 3\beta - \gamma = -1$ monotonically from below because the ratio $P_L(\tau)/\epsilon(\tau)$ decreases monotonically. The residual deviation is

$$|\alpha(\tau) - 3\beta(\tau) - \gamma(\tau) + 1| < 0.05, \quad (\text{D.10})$$

for $800 \lesssim Q\tau \lesssim 2000$ as indicated by the gray band.

D.2 Self-similarity analysis

We also perform an alternative analysis to extract the scaling exponents (α, β, γ) from the self-similar evolution of the single-particle distribution. Different from Fig. 5.5, we vary all scaling exponents and compare rescaled moments of the distribution at different times ($Q\tau_{\text{Test}} = 1250, 1500, 1750, 2000$) with those at a reference time ($Q\tau_{\text{Ref}} = 1000$). While for a perfect scaling the different curves should all give the same results, one can attempt to minimize the deviation between the rescaled curves to determine the most appropriate scaling exponents.

In practice, deviations from perfect scaling will occur even for the correct set of scaling exponents due to statistical uncertainties of the data as well as systematic deviations from the scaling behavior in Eq. (5.1). We quantify these in terms of a likelihood distribution $W(\alpha, \beta, \gamma)$ which allows us to distinguish different sets of scaling exponents. Our method is described in more detail in App. C.2.

The results of our analysis are summarized in Fig. D.2. Similarly to our gauge-invariant analysis, we analyze the combined exponents $\alpha - 3\beta - \gamma$, β and γ separately rather than α, β, γ . This choice provides a physical meaning in terms of gauge invariant quantities to each of the exponents, and reduces correlations among them. We show the likelihood distributions for the scaling exponents in Fig. D.2. The one dimensional distributions are obtained by integration of $\tilde{W}(\alpha - 3\beta - \gamma, \beta, \gamma) \equiv W(\alpha, \beta, \gamma)$ over all other exponents and normalized to yield unity upon integration. The scaling exponents we obtain from Fig. D.2 take the values

$$\begin{aligned}\alpha - 3\beta - \gamma &= -1.05 \pm 0.04 \text{ (stat.)} , \\ \beta &= -0.02 \pm 0.02 \text{ (stat.)} , \\ \gamma &= 0.285 \pm 0.025 \text{ (stat.)} .\end{aligned}\tag{D.11}$$

where the statistical errors are the widths of fitted Gauss functions. The corresponding values in the original ‘bottom-up’ thermalization scenario (BMSS) [67] ($\gamma = 1/3$) and the instability modified ‘bottom-up’ scenario by Boedeker (BD) [68] ($\gamma = 1/4$) are also indicated in Fig. D.2 as vertical gray dashed lines. Since the scaling exponents $\beta = 0$ and $\alpha - 3\beta - \gamma = -1$ are the same in both scenarios, we only show a single line in the left and central panels.

Appendix E

Range of validity of the classical approximation for expanding scalars

In this Appendix, we examine the range of validity of the classical-statistical approximation employed in our numerical simulations to study the far-from-equilibrium dynamics of a longitudinally expanding scalar theory.¹ In general, the classical-statistical approximation can be justified when the typical occupancies f of the system are large and quantum effects play a negligible role. In Sec. 2.3.1, we have discussed the ‘classicality’ condition in this context

$$f(p_T, p_z, \tau) \gg 1, \quad (\text{E.1})$$

which is a necessary condition to justify a description of the quantum dynamics in terms of a classical evolution.

On the level of kinetic equations, the validity of the classical approximation can be examined by comparing the classical and quantum contributions to the collision integral. One finds that for a perturbative $2 \leftrightarrow 2$ scattering process in scalar field theories, the classical part of the collision integral takes the form [8, 13, 106]

$$C_{\text{Classic}}[f](p_1) = \frac{\lambda^2(N+2)}{6N^2} \int d\Omega^{2\leftrightarrow 2} \left((f_1 + f_2)f_3f_4 - f_1f_2(f_3 + f_4) \right), \quad (\text{E.2})$$

with the corresponding quantum terms

$$C_{\text{Quant}}[f](p_1) = \frac{\lambda^2(N+2)}{6N^2} \int d\Omega^{2\leftrightarrow 2} \left(f_3f_4 - f_1f_2 \right), \quad (\text{E.3})$$

While the final state Bose enhancement factors are considered to be large in the classical field description, this is not the case when genuine quantum corrections are relevant. One may therefore expect that as long as the ‘classicality’ condition (E.1) is satisfied for typical

¹The arguments presented in this Appendix entered our publication in Ref. [177].

momentum modes, the quantum corrections in Eq. (E.3) are suppressed and classical scattering dominates.

However as recently argued in Ref. [176], there is potentially a caveat to this argument when the system is highly anisotropic. This is because the classical-statistical approximation restricts the phase space available for each individual scattering to states which are already occupied while the quantum terms allow one to access previously unoccupied states by a single scattering. Assuming that the typical longitudinal momenta $p_z \sim \Lambda_z$ of occupied states are much smaller than the typical transverse momenta $p_T \sim \Lambda_T$ by a factor of $\delta \sim \Lambda_z/\Lambda_T \ll 1$, one finds that a classical scattering can only lead to longitudinal momenta on the order of a few times $\sim \Lambda_z$. In contrast, the quantum contribution, while suppressed by occupancy factors, has a larger phase space and allows for states with longitudinal momenta up to $\Lambda_T \gg \Lambda_z$ to be populated by a single scattering. These could in principle give a large contribution to the longitudinal pressure.

We will show here that this is not the case in the parametric domain of validity of the classical regime. We will begin by first estimating parametrically the importance of ‘quantum’ large angle $2 \leftrightarrow 2$ scatterings into previously unoccupied phase space – in particular, for modes with longitudinal momenta $p_z \sim \Lambda_T \gg \Lambda_z$. We will subsequently investigate whether the dynamics of this process can lead to an earlier breakdown of the classical-statistical approximation than suggested by Eq. (E.1) by estimating the contribution of this process to the longitudinal pressure.

E.1 Parametric estimate of quantum large angle scattering

We begin by estimating the number density of particles at large angles, which can be defined in terms of

$$N_{\text{Large-angle}}(\tau) \sim \int_{|p_z| \gg \Lambda_z} d^3p f(p_T, p_z, \tau). \quad (\text{E.4})$$

The integral over p_z is limited to modes with longitudinal momenta p_z parametrically on the order of p_T – much bigger than the typical longitudinal momenta Λ_z . We can estimate the change in time of this quantity by considering the Boltzmann equation for $2 \leftrightarrow 2$ scatterings. Including both classical and quantum contributions, it takes the form

$$\begin{aligned} \partial_\tau N_{\text{Large-angle}}(\tau) \sim & \int_{|p_{1,z}| \gg \Lambda_z} d^3p_1 \int d^3p_2 \int d^3p_3 \int d^3p_4 \\ & \frac{\lambda^2}{2\omega_1 2\omega_2 2\omega_3 2\omega_4} \delta^{(4)}(p_1 + p_2 - p_3 - p_4) \times \\ & \left[(1 + f_1)(1 + f_2)f_3f_4 - f_1f_2(1 + f_3)(1 + f_4) \right], \end{aligned} \quad (\text{E.5})$$

with the abbreviations $f_i = f(p_{i,T}, p_{i,z}, \tau)$ and similar for ω_i . Since we require $p_{1,z}$ to be much larger than the typical longitudinal momentum of all highly occupied states, i.e. $p_{1,z} \sim \Lambda_T \gg \Lambda_z$, longitudinal momentum conservation dictates that also another longitudinal momentum is large, $p_{2,z} \sim \Lambda_T \gg \Lambda_z$, meaning that both particles fall into the phase space with $f_1, f_2 \ll 1$. We can thus neglect the Bose stimulation factors in the gain term (namely, $(1+f_1)(1+f_2) \sim 1$) such that only quantum processes contribute to occupancy at large angles. Similarly, we can neglect the loss term altogether since $f_1 f_2 \ll 1$, such that our estimate becomes

$$\begin{aligned} \partial_\tau N_{\text{Large-angle}}(\tau) &\sim \int_{|p_{1,z}| \gg \Lambda_z} dp_{1,z} \int d^2 p_{1,T} \int d^3 p_2 \times \\ &\int d^3 p_3 \int d^3 p_4 \frac{\lambda^2}{2\omega_1 2\omega_2 2\omega_3 2\omega_4} \delta^{(4)}(p_1 + p_2 - p_3 - p_4) f_3 f_4. \end{aligned} \quad (\text{E.6})$$

We expect the dominant phase space for this scattering to be when the energy of all particles is on the order of the hard transverse scale Λ_T ; therefore parametrically the energy denominator $\omega_i \sim \Lambda_T$. One thus obtains the phase space integral for this scattering to be

$$\begin{aligned} \partial_\tau N_{\text{Large-angle}}(\tau) &\sim \frac{\lambda^2}{\Lambda_T^4} \int_{|p_{1,z}| \gg \Lambda_z} dp_{1,z} \int d^2 p_{2,T} \times \\ &\int d^3 p_2 \int d^3 p_3 \int d^3 p_4 \delta^{(4)}(p_1 + p_2 - p_3 - p_4) f_3 f_4. \end{aligned} \quad (\text{E.7})$$

While at first sight it may seem that this phase space is strongly enhanced for the large angle process, a subtle point is that longitudinal momentum conservation requires $p_{1,z} + p_{2,z} = p_{3,z} + p_{4,z}$ to be on the order of $\sim \Lambda_z$, which is the typical longitudinal momentum of highly occupied particles. Implementing this momentum conservation constraint leads to

$$\begin{aligned} \partial_\tau N_{\text{Large-angle}}(\tau) &\sim \frac{\lambda^2}{\Lambda_T^4} \int d^3(p_1 - p_2) \\ &\int d^3 p_3 \int d^3 p_4 \delta(\omega_1 + \omega_2 - \omega_3 - \omega_4) f_3 f_4. \end{aligned} \quad (\text{E.8})$$

Since the typical energy of all participating scatterers is of the order of Λ_T and there are no further constraints beyond energy conservation, the phase space for the scattering should be of order Λ_T^2 . This leads us to the final estimate

$$\partial_\tau N_{\text{Large-angle}}(\tau) \sim \frac{\lambda^2}{\Lambda_T^2} N_{\text{hard}}^2(\tau), \quad (\text{E.9})$$

where $N_{\text{hard}}(\tau)$ denotes the typical density of hard particles

$$N_{\text{hard}}(\tau) \sim \int d^3 p f(p_z, p_T, \tau). \quad (\text{E.10})$$

Therefore the total number of particles found at large angles should be of the order of the scattering rate in Eq. (E.9) times a time scale on the order of the age of the system²

$$N_{Large-angle}(\tau) \sim \lambda^2 \frac{N_{hard}^2(\tau)}{\Lambda_T^3} \Lambda_T \tau . \quad (\text{E.11})$$

²An alternative way to arrive at the same parametric estimate is – following Ref. [67] – to consider the rate of large angle scatterings that a single hard particle undergoes in the medium. Since the process is not Bose enhanced, this large angle scattering rate is simply given by the density of scattering centers N_{hard} times the cross section

$$\frac{dN_{Large-angle}^{Coll}}{d\tau} \sim \sigma_{Large-angle} N_{hard}(\tau) .$$

The cross section for a large angle scattering of hard scalar particles is parametrically $\sigma_{Large-angle} \sim \lambda^2/\Lambda_T^2$. The total number of particles at large angles therefore becomes

$$N_{Large-angle}(\tau) \sim N_{hard}(\tau) \frac{dN_{Large-angle}^{Coll}}{d\tau} \tau \sim \frac{\lambda^2}{\Lambda_T^2} N_{hard}^2(\tau) \tau$$

which agrees with the more detailed estimate in the text.

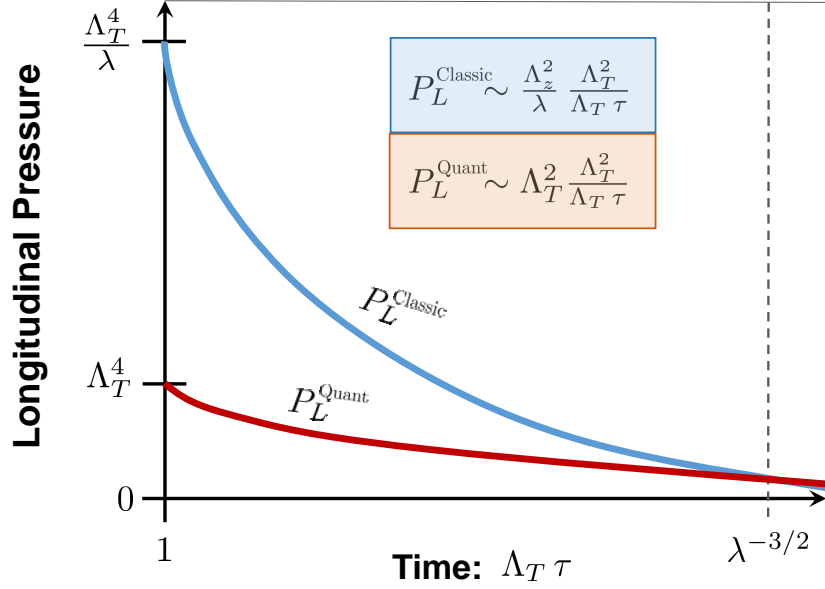


FIGURE E.1: Shown are the small angle and large-angle contributions to the longitudinal pressure as described in the text. While the large-angle contribution is suppressed initially by $1/\lambda$, it becomes important when $\Lambda_z^2 \sim \lambda \Lambda_T^2$, which occurs after the time $\lambda^{-3/2}$.

E.2 ‘Quantum’ contributions to observables

With our parametric estimate of the density of large angle particles at hand, we will now estimate the contribution of such quantum effects to the longitudinal pressure³. Since the typical longitudinal momenta of the large angle particles are on the order of the transverse hard scale Λ_T , the contribution to the pressure takes the form

$$P_L^{\text{Quant}}(\tau) \sim N_{\text{Large-angle}}(\tau) \Lambda_T \sim \lambda^2 \frac{N_{\text{hard}}^2(\tau)}{\Lambda_T^2} \Lambda_T \tau. \quad (\text{E.12})$$

which should be compared to the (perturbative) classical contribution

$$P_L^{\text{Classic}}(\tau) \sim N_{\text{hard}}(\tau) \frac{\Lambda_z^2(\tau)}{\Lambda_T}. \quad (\text{E.13})$$

³In general, the relative importance of the leading classical and subleading quantum contributions (as well as other higher order effects) depends on the observable at hand and needs to be evaluated for each observable. While certain ultraviolet sensitive observables may receive large corrections from higher order processes, the dynamics of the bulk may be perfectly well described by the leading order classical process.

Since the total number of hard particles is approximately conserved during the evolution, their density decreases as $\sim 1/\tau$ due to the longitudinal expansion, such that

$$N_{\text{hard}}(\tau) \sim \left(\frac{\tau_0}{\tau}\right) N_{\text{hard}}(\tau_0) \sim \frac{1}{\lambda} \frac{\Lambda_T^3}{\Lambda_T \tau}, \quad (\text{E.14})$$

and the ratio of the quantum contribution to the pressure over the classical contribution is given by

$$\frac{P_L^{\text{Quant}}}{P_L^{\text{Classic}}} \sim \lambda \frac{\Lambda_T^2}{\Lambda_z^2(\tau)}. \quad (\text{E.15})$$

At early times⁴ $\tau \sim \tau_0$, $\Lambda_z^2 \sim \Lambda_T^2$, hence $P_L^{\text{Quant}}/P_L^{\text{Classic}} \sim \lambda$, which is very small for $\lambda \ll 1$. With increasing time, the Λ_z^2 scale will decrease relative to Λ_T^2 as illustrated in Fig. E.1 at the example of the longitudinal pressure. Since on large time scales the longitudinal pressure is dominated by modes in the intermediate rather than hard momentum region, we will assume for this estimate *a la* BMSS that

$$\Lambda_z \sim \Lambda_T (\Lambda_T \tau)^{-1/3}. \quad (\text{E.16})$$

One then finds that the quantum contribution to the pressure becomes of the same order of magnitude as the classical contribution on the time scale

$$\Lambda_T \tau_{\text{Quant}} \sim \lambda^{-3/2}. \quad (\text{E.17})$$

Interestingly however, since $f(p_T, p_z \sim \Lambda_z) \sim (\Lambda_T \tau)^{-2/3}$ in this intermediate transverse momentum regime – the time scale obtained from Eq. (E.17) is parametrically the same as that when the occupancies in this regime become of order unity. We may therefore conclude that the ‘large angle’ quantum contribution to the pressure becomes of the order of the classical contribution only on the time scale when the classical-statistical approximation is breaking down anyway. This is indeed therefore a self-consistent criterion for when classical dynamics can be trusted. Beyond the time scale τ_{Quant} , the evolution of the system is expected to change qualitatively.

⁴Even if the initial conditions are such that the typical $p_z \sim 0$ at the instant of the collision, modes at the hard scale are very quickly populated by the instability resulting from the parametric resonance. As noted previously, the characteristic time scale for this is $\tau = \tau_0 \ln^{3/2}(\lambda^{-1})$. How rapidly this occurs is clearly visible from Fig. 5.4. A similar argument applies for gauge theories [15, 66].

Bibliography

- [1] J. Schmiedmayer and J. Berges. Cold Atom Cosmology. *Science*, 341(6151):1188–1189, 2013. doi: 10.1126/science.1243904.
- [2] J. Berges, K. Boguslavski, S. Schlichting, and R. Venugopalan. Universality far from equilibrium: From superfluid Bose gases to heavy-ion collisions. *Phys. Rev. Lett.*, 114(6):061601, 2015. doi: 10.1103/PhysRevLett.114.061601.
- [3] N. Goldenfeld. *Lectures On Phase Transitions And The Renormalization Group*. Westview Press, 1992.
- [4] S.-k. Ma. *Modern Theory of Critical Phenomena*. Westview Press, 2000.
- [5] J. Zinn-Justin. *Quantum Field Theory and Critical Phenomena*. Oxford University Press, 2002.
- [6] P. C. Hohenberg and B. I. Halperin. Theory of dynamic critical phenomena. *Rev. Mod. Phys.*, 49:435–479, Jul 1977. doi: 10.1103/RevModPhys.49.435. URL <http://link.aps.org/doi/10.1103/RevModPhys.49.435>.
- [7] Juergen Berges, Alexander Rothkopf, and Jonas Schmidt. Non-thermal fixed points: Effective weak-coupling for strongly correlated systems far from equilibrium. *Phys. Rev. Lett.*, 101:041603, 2008. doi: 10.1103/PhysRevLett.101.041603.
- [8] Raphael Micha and Igor I. Tkachev. Turbulent thermalization. *Phys. Rev.*, D70:043538, 2004. doi: 10.1103/PhysRevD.70.043538.
- [9] Juergen Berges and Gabriele Hoffmeister. Nonthermal fixed points and the functional renormalization group. *Nucl. Phys.*, B813:383–407, 2009. doi: 10.1016/j.nuclphysb.2008.12.017.
- [10] Christian Scheppach, Juergen Berges, and Thomas Gasenzer. Matter Wave Turbulence: Beyond Kinetic Scaling. *Phys. Rev.*, A81:033611, 2010. doi: 10.1103/PhysRevA.81.033611.
- [11] Gert Aarts and Juergen Berges. Classical aspects of quantum fields far from equilibrium. *Phys. Rev. Lett.*, 88:041603, 2002. doi: 10.1103/PhysRevLett.88.041603.

- [12] A. H. Mueller and D. T. Son. On the Equivalence between the Boltzmann equation and classical field theory at large occupation numbers. *Phys. Lett.*, B582:279–287, 2004. doi: 10.1016/j.physletb.2003.12.047.
- [13] Sangyong Jeon. The Boltzmann equation in classical and quantum field theory. *Phys. Rev.*, C72:014907, 2005. doi: 10.1103/PhysRevC.72.014907.
- [14] J. Berges, K. Boguslavski, S. Schlichting, and R. Venugopalan. Turbulent thermalization process in heavy-ion collisions at ultrarelativistic energies. *Phys. Rev.*, D89(7):074011, 2014. doi: 10.1103/PhysRevD.89.074011.
- [15] Juergen Berges, Kirill Boguslavski, Soeren Schlichting, and Raju Venugopalan. Universal attractor in a highly occupied non-Abelian plasma. *Phys. Rev.*, D89(11):114007, 2014. doi: 10.1103/PhysRevD.89.114007.
- [16] J. Berges, S. Scheffler, and D. Sexty. Turbulence in nonabelian gauge theory. *Phys. Lett.*, B681:362–366, 2009. doi: 10.1016/j.physletb.2009.10.032.
- [17] Juergen Berges, Soeren Schlichting, and Denes Sexty. Over-populated gauge fields on the lattice. *Phys. Rev.*, D86:074006, 2012. doi: 10.1103/PhysRevD.86.074006.
- [18] Soeren Schlichting. Turbulent thermalization of weakly coupled non-abelian plasmas. *Phys. Rev.*, D86:065008, 2012. doi: 10.1103/PhysRevD.86.065008.
- [19] Aleksi Kurkela and Guy D. Moore. UV Cascade in Classical Yang-Mills Theory. *Phys. Rev.*, D86:056008, 2012. doi: 10.1103/PhysRevD.86.056008.
- [20] S. Yu. Khlebnikov and I. I. Tkachev. Classical decay of inflaton. *Phys. Rev. Lett.*, 77: 219–222, 1996. doi: 10.1103/PhysRevLett.77.219.
- [21] Raphael Micha and Igor I. Tkachev. Relativistic turbulence: A Long way from preheating to equilibrium. *Phys. Rev. Lett.*, 90:121301, 2003. doi: 10.1103/PhysRevLett.90.121301.
- [22] Boris Nowak, Denes Sexty, and Thomas Gasenzer. Superfluid Turbulence: Nonthermal Fixed Point in an Ultracold Bose Gas. *Phys. Rev.*, B84:020506, 2011. doi: 10.1103/PhysRevB.84.020506.
- [23] Boris Nowak, Jan Schole, Denes Sexty, and Thomas Gasenzer. Nonthermal fixed points, vortex statistics, and superfluid turbulence in an ultracold Bose gas. *Phys. Rev.*, A85: 043627, 2012. doi: 10.1103/PhysRevA.85.043627.
- [24] Markus Karl, Boris Nowak, and Thomas Gasenzer. Universal scaling at nonthermal fixed points of a two-component Bose gas. *Phys. Rev.*, A88(6):063615, 2013. doi: 10.1103/PhysRevA.88.063615.

- [25] David J. Gross and Frank Wilczek. Ultraviolet behavior of non-abelian gauge theories. *Phys. Rev. Lett.*, 30:1343–1346, Jun 1973. doi: 10.1103/PhysRevLett.30.1343. URL <http://link.aps.org/doi/10.1103/PhysRevLett.30.1343>.
- [26] H. David Politzer. Reliable perturbative results for strong interactions? *Phys. Rev. Lett.*, 30:1346–1349, Jun 1973. doi: 10.1103/PhysRevLett.30.1346. URL <http://link.aps.org/doi/10.1103/PhysRevLett.30.1346>.
- [27] M. E. Peskin and D. V. Schroeder. *An Introduction To Quantum Field Theory*. Westview Press, 1995.
- [28] Y. V. Kovchegov and E. Levin. *Quantum Chromodynamics at High Energy*. Cambridge University Press, 2012.
- [29] H. J. Rothe. *Lattice Gauge Theories: An Introduction*. World Scientific Publishing Company, 2005.
- [30] Szabolcs Borsanyi, Zoltan Fodor, Christian Hoelbling, Sandor D Katz, Stefan Krieg, Claudia Ratti, and Kalman K. Szabo. Is there still any T_c mystery in lattice QCD? Results with physical masses in the continuum limit III. *JHEP*, 09:073, 2010. doi: 10.1007/JHEP09(2010)073.
- [31] John Adams et al. Experimental and theoretical challenges in the search for the quark gluon plasma: The STAR Collaboration’s critical assessment of the evidence from RHIC collisions. *Nucl. Phys.*, A757:102–183, 2005. doi: 10.1016/j.nuclphysa.2005.03.085.
- [32] K Aamodt et al. Elliptic flow of charged particles in Pb-Pb collisions at 2.76 TeV. *Phys. Rev. Lett.*, 105:252302, 2010. doi: 10.1103/PhysRevLett.105.252302.
- [33] Serguei Chatrchyan et al. Multiplicity and transverse momentum dependence of two- and four-particle correlations in pPb and PbPb collisions. *Phys. Lett.*, B724:213–240, 2013. doi: 10.1016/j.physletb.2013.06.028.
- [34] Paul Romatschke and Ulrike Romatschke. Viscosity Information from Relativistic Nuclear Collisions: How Perfect is the Fluid Observed at RHIC? *Phys. Rev. Lett.*, 99:172301, 2007. doi: 10.1103/PhysRevLett.99.172301.
- [35] Huichao Song and Ulrich W. Heinz. Causal viscous hydrodynamics in 2+1 dimensions for relativistic heavy-ion collisions. *Phys. Rev.*, C77:064901, 2008. doi: 10.1103/PhysRevC.77.064901.
- [36] Bjorn Schenke, Sangyong Jeon, and Charles Gale. Elliptic and triangular flow in event-by-event (3+1)D viscous hydrodynamics. *Phys. Rev. Lett.*, 106:042301, 2011. doi: 10.1103/PhysRevLett.106.042301.

- [37] Bjoern Schenke, Prithwish Tribedy, and Raju Venugopalan. Fluctuating Glasma initial conditions and flow in heavy ion collisions. *Phys. Rev. Lett.*, 108:252301, 2012. doi: 10.1103/PhysRevLett.108.252301.
- [38] Charles Gale, Sangyong Jeon, Bjoern Schenke, Prithwish Tribedy, and Raju Venugopalan. Event-by-event anisotropic flow in heavy-ion collisions from combined yang-mills and viscous fluid dynamics. *Phys. Rev. Lett.*, 110:012302, Jan 2013. doi: 10.1103/PhysRevLett.110.012302. URL <http://link.aps.org/doi/10.1103/PhysRevLett.110.012302>.
- [39] Juergen Berges, Jean-Paul Blaizot, and Francois Gelis. EMMI Rapid Reaction Task Force on 'Thermalization in Non-abelian Plasmas'. *J. Phys.*, G39:085115, 2012. doi: 10.1088/0954-3899/39/8/085115.
- [40] Juan Martin Maldacena. The Large N limit of superconformal field theories and supergravity. *Int. J. Theor. Phys.*, 38:1113–1133, 1999. doi: 10.1023/A:1026654312961. [Adv. Theor. Math. Phys.2,231(1998)].
- [41] Paul M. Chesler and Laurence G. Yaffe. Horizon formation and far-from-equilibrium isotropization in supersymmetric Yang-Mills plasma. *Phys. Rev. Lett.*, 102:211601, 2009. doi: 10.1103/PhysRevLett.102.211601.
- [42] Daniel Grumiller and Paul Romatschke. On the collision of two shock waves in AdS(5). *JHEP*, 08:027, 2008. doi: 10.1088/1126-6708/2008/08/027.
- [43] V. Balasubramanian, A. Bernamonti, J. de Boer, N. Copland, B. Craps, E. Keski-Vakkuri, B. Muller, A. Schafer, M. Shigemori, and W. Staessens. Holographic Thermalization. *Phys. Rev.*, D84:026010, 2011. doi: 10.1103/PhysRevD.84.026010.
- [44] Michal P. Heller, Romuald A. Janik, and Przemyslaw Witaszczyk. A numerical relativity approach to the initial value problem in asymptotically Anti-de Sitter spacetime for plasma thermalization - an ADM formulation. *Phys. Rev.*, D85:126002, 2012. doi: 10.1103/PhysRevD.85.126002.
- [45] Larry D. McLerran and Raju Venugopalan. Computing quark and gluon distribution functions for very large nuclei. *Phys. Rev.*, D49:2233–2241, 1994. doi: 10.1103/PhysRevD.49.2233.
- [46] Larry D. McLerran and Raju Venugopalan. Gluon distribution functions for very large nuclei at small transverse momentum. *Phys. Rev.*, D49:3352–3355, 1994. doi: 10.1103/PhysRevD.49.3352.
- [47] Edmond Iancu and Raju Venugopalan. The Color glass condensate and high-energy scattering in QCD. In *In *Hwa, R.C. (ed.) et al.: Quark gluon plasma* 249-3363*, 2003.

- [48] Alex Kovner, Larry D. McLerran, and Heribert Weigert. Gluon production from non-Abelian Weizsacker-Williams fields in nucleus-nucleus collisions. *Phys. Rev.*, D52:6231–6237, 1995. doi: 10.1103/PhysRevD.52.6231.
- [49] Alex Kovner, Larry D. McLerran, and Heribert Weigert. Gluon production at high transverse momentum in the McLerran-Venugopalan model of nuclear structure functions. *Phys. Rev.*, D52:3809–3814, 1995. doi: 10.1103/PhysRevD.52.3809.
- [50] Alex Krasnitz and Raju Venugopalan. Nonperturbative computation of gluon minijet production in nuclear collisions at very high-energies. *Nucl. Phys.*, B557:237, 1999. doi: 10.1016/S0550-3213(99)00366-1.
- [51] Alex Krasnitz and Raju Venugopalan. The Initial energy density of gluons produced in very high-energy nuclear collisions. *Phys. Rev. Lett.*, 84:4309–4312, 2000. doi: 10.1103/PhysRevLett.84.4309.
- [52] Alex Krasnitz and Raju Venugopalan. The Initial gluon multiplicity in heavy ion collisions. *Phys. Rev. Lett.*, 86:1717–1720, 2001. doi: 10.1103/PhysRevLett.86.1717.
- [53] Alex Krasnitz, Yasushi Nara, and Raju Venugopalan. Coherent gluon production in very high-energy heavy ion collisions. *Phys. Rev. Lett.*, 87:192302, 2001. doi: 10.1103/PhysRevLett.87.192302.
- [54] Alex Krasnitz, Yasushi Nara, and Raju Venugopalan. Gluon production in the color glass condensate model of collisions of ultrarelativistic finite nuclei. *Nucl. Phys.*, A717:268–290, 2003. doi: 10.1016/S0375-9474(03)00636-5.
- [55] T. Lappi. Production of gluons in the classical field model for heavy ion collisions. *Phys. Rev.*, C67:054903, 2003. doi: 10.1103/PhysRevC.67.054903.
- [56] T. Lappi. Energy density of the glasma. *Phys. Lett.*, B643:11–16, 2006. doi: 10.1016/j.physletb.2006.10.017.
- [57] T. Lappi and L. McLerran. Some features of the glasma. *Nucl. Phys.*, A772:200–212, 2006. doi: 10.1016/j.nuclphysa.2006.04.001.
- [58] T. Lappi, S. Srednyak, and R. Venugopalan. Non-perturbative computation of double inclusive gluon production in the Glasma. *JHEP*, 01:066, 2010. doi: 10.1007/JHEP01(2010)066.
- [59] T. Lappi. Gluon spectrum in the glasma from JIMWLK evolution. *Phys. Lett.*, B703:325–330, 2011. doi: 10.1016/j.physletb.2011.08.011.
- [60] Paul Romatschke and Raju Venugopalan. Collective non-Abelian instabilities in a melting color glass condensate. *Phys. Rev. Lett.*, 96:062302, 2006. doi: 10.1103/PhysRevLett.96.062302.

- [61] Paul Romatschke and Raju Venugopalan. The Unstable Glasma. *Phys. Rev.*, D74: 045011, 2006. doi: 10.1103/PhysRevD.74.045011.
- [62] Paul Romatschke and Raju Venugopalan. A Weibel instability in the melting color glass condensate. *Eur. Phys. J.*, A29:71–75, 2006. doi: 10.1140/epja/i2005-10304-y.
- [63] Kenji Fukushima and Francois Gelis. The evolving Glasma. *Nucl. Phys.*, A874:108–129, 2012. doi: 10.1016/j.nuclphysa.2011.11.003.
- [64] Juergen Berges and Soeren Schlichting. The nonlinear glasma. *Phys. Rev.*, D87(1): 014026, 2013. doi: 10.1103/PhysRevD.87.014026.
- [65] Thomas Epelbaum and Francois Gelis. Pressure isotropization in high energy heavy ion collisions. *Phys. Rev. Lett.*, 111:232301, 2013. doi: 10.1103/PhysRevLett.111.232301.
- [66] Juergen Berges, Bjoern Schenke, Soeren Schlichting, and Raju Venugopalan. Turbulent thermalization process in high-energy heavy-ion collisions. *Nucl. Phys.*, A931:348–353, 2014. doi: 10.1016/j.nuclphysa.2014.08.103.
- [67] R. Baier, Alfred H. Mueller, D. Schiff, and D. T. Son. 'Bottom up' thermalization in heavy ion collisions. *Phys. Lett.*, B502:51–58, 2001. doi: 10.1016/S0370-2693(01)00191-5.
- [68] Dietrich Bodeker. The Impact of QCD plasma instabilities on bottom-up thermalization. *JHEP*, 10:092, 2005. doi: 10.1088/1126-6708/2005/10/092.
- [69] A. H. Mueller, A. I. Shoshi, and S. M. H. Wong. A Possible modified 'bottom-up' thermalization in heavy ion collisions. *Phys. Lett.*, B632:257–260, 2006. doi: 10.1016/j.physletb.2005.10.047.
- [70] Aleksi Kurkela and Guy D. Moore. Thermalization in Weakly Coupled Nonabelian Plasmas. *JHEP*, 12:044, 2011. doi: 10.1007/JHEP12(2011)044.
- [71] Aleksi Kurkela and Guy D. Moore. Bjorken Flow, Plasma Instabilities, and Thermalization. *JHEP*, 11:120, 2011. doi: 10.1007/JHEP11(2011)120.
- [72] Jean-Paul Blaizot, Francois Gelis, Jin-Feng Liao, Larry McLerran, and Raju Venugopalan. Bose–Einstein Condensation and Thermalization of the Quark Gluon Plasma. *Nucl. Phys.*, A873:68–80, 2012. doi: 10.1016/j.nuclphysa.2011.10.005.
- [73] Alan H. Guth. The Inflationary Universe: A Possible Solution to the Horizon and Flatness Problems. *Phys. Rev.*, D23:347–356, 1981. doi: 10.1103/PhysRevD.23.347.
- [74] Andrei D. Linde. A New Inflationary Universe Scenario: A Possible Solution of the Horizon, Flatness, Homogeneity, Isotropy and Primordial Monopole Problems. *Phys. Lett.*, B108:389–393, 1982. doi: 10.1016/0370-2693(82)91219-9.

- [75] A. A. Penzias and R. W. Wilson. A Measurement of Excess Antenna Temperature at 4080 Mc/s. *The Astrophysical Journal*, 142:419–421, July 1965. doi: 10.1086/148307.
- [76] B. Ryden. *Introduction to Cosmology*. Addison-Wesley, 2002.
- [77] C.L. Bennett and et.al. Nine-year wilkinson microwave anisotropy probe (wmap) observations: Final maps and results. *The Astrophysical Journal Supplement Series*, 208(2): 20, 2013. URL <http://stacks.iop.org/0067-0049/208/i=2/a=20>.
- [78] Lev Kofman, Andrei D. Linde, and Alexei A. Starobinsky. Reheating after inflation. *Phys. Rev. Lett.*, 73:3195–3198, 1994. doi: 10.1103/PhysRevLett.73.3195.
- [79] D. Boyanovsky, H. J. de Vega, R. Holman, D. S. Lee, and A. Singh. Dissipation via particle production in scalar field theories. *Phys. Rev.*, D51:4419–4444, 1995. doi: 10.1103/PhysRevD.51.4419.
- [80] Lev Kofman, Andrei D. Linde, and Alexei A. Starobinsky. Towards the theory of reheating after inflation. *Phys. Rev.*, D56:3258–3295, 1997. doi: 10.1103/PhysRevD.56.3258.
- [81] Patrick B. Greene, Lev Kofman, Andrei D. Linde, and Alexei A. Starobinsky. Structure of resonance in preheating after inflation. *Phys. Rev.*, D56:6175–6192, 1997. doi: 10.1103/PhysRevD.56.6175.
- [82] D. T. Son. Reheating and thermalization in a simple scalar model. *Phys. Rev.*, D54: 3745–3761, 1996. doi: 10.1103/PhysRevD.54.3745.
- [83] Juergen Baacke, Katrin Heitmann, and Carsten Patzold. Nonequilibrium dynamics of fermions in a spatially homogeneous scalar background field. *Phys. Rev.*, D58:125013, 1998. doi: 10.1103/PhysRevD.58.125013.
- [84] Patrick B. Greene and Lev Kofman. Preheating of fermions. *Phys. Lett.*, B448:6–12, 1999. doi: 10.1016/S0370-2693(99)00020-9.
- [85] J. Berges, D. Gelfand, and J. Pruschke. Quantum theory of fermion production after inflation. *Phys. Rev. Lett.*, 107:061301, 2011. doi: 10.1103/PhysRevLett.107.061301.
- [86] J. Berges, D. Gelfand, and D. Sexty. Amplified Fermion Production from Overpopulated Bose Fields. *Phys. Rev.*, D89(2):025001, 2014. doi: 10.1103/PhysRevD.89.025001.
- [87] Juergen Berges and Julien Serreau. Parametric resonance in quantum field theory. *Phys. Rev. Lett.*, 91:111601, 2003. doi: 10.1103/PhysRevLett.91.111601.
- [88] Alejandro Arrizabalaga, Jan Smit, and Anders Tranberg. Tachyonic preheating using 2PI-1/N dynamics and the classical approximation. *JHEP*, 10:017, 2004. doi: 10.1088/1126-6708/2004/10/017.

- [89] J. Berges and D. Sexty. Bose condensation far from equilibrium. *Phys. Rev. Lett.*, 108:161601, 2012. doi: 10.1103/PhysRevLett.108.161601.
- [90] Eric Braaten and H. W. Hammer. Universality in few-body systems with large scattering length. *Phys. Rept.*, 428:259–390, 2006. doi: 10.1016/j.physrep.2006.03.001.
- [91] Jan Schole, Boris Nowak, and Thomas Gasenzer. Critical Dynamics of a Two-dimensional Superfluid near a Non-Thermal Fixed Point. *Phys. Rev.*, A 86:013624, 2012. doi: 10.1103/PhysRevA.86.013624.
- [92] Boris Nowak and Thomas Gasenzer. Universal dynamics on the way to thermalization. *New J. Phys.*, 16(9):093052, 2014. doi: 10.1088/1367-2630/16/9/093052.
- [93] Juergen Berges and Joerg Jaeckel. Far from equilibrium dynamics of bose-einstein condensation for axion dark matter. *Phys. Rev.*, D 91:025020, Jan 2015. doi: 10.1103/PhysRevD.91.025020. URL <http://link.aps.org/doi/10.1103/PhysRevD.91.025020>.
- [94] B. Svistunov. *J. Mosc. Phys. Soc.*, 1:373, 1991.
- [95] Y. Kagan, B.V. Svistunov, and G.V. Shlyapnikov. *Sov. Phys. JETP*, 74:279, 1992.
- [96] Natalia G. Berloff and Boris V. Svistunov. Scenario of strongly nonequibrated Bose-Einstein condensation. *Phys. Rev.*, A66:013603, 2002. doi: 10.1103/PhysRevA.66.013603.
- [97] Juergen Berges. Nonequilibrium Quantum Fields: From Cold Atoms to Cosmology. *arXiv*, 1503.02907 [hep-ph], 2015.
- [98] S. Weinberg. *Gravitation and cosmology: principles and applications of the general theory of relativity*. Wiley, 1972.
- [99] Alexander L. Gaunt, Tobias F. Schmidutz, Igor Gotlibovych, Robert P. Smith, and Zoran Hadzibabic. Bose-einstein condensation of atoms in a uniform potential. *Phys. Rev. Lett.*, 110:200406, May 2013. doi: 10.1103/PhysRevLett.110.200406. URL <http://link.aps.org/doi/10.1103/PhysRevLett.110.200406>.
- [100] Juergen Berges and Thomas Gasenzer. Quantum versus classical statistical dynamics of an ultracold Bose gas. *Phys. Rev.*, A76:033604, 2007. doi: 10.1103/PhysRevA.76.033604.
- [101] D. Gelfand, F. Hebenstreit, and J. Berges. Early quark production and approach to chemical equilibrium. *Phys. Rev.*, D93(8):085001, 2016. doi: 10.1103/PhysRevD.93.085001.
- [102] Juergen Berges, Daniil Gelfand, Sebastian Scheffler, and Denes Sexty. Simulating plasma instabilities in SU(3) gauge theory. *Phys. Lett.*, B677:210–213, 2009. doi: 10.1016/j.physletb.2009.05.008.

- [103] Andreas Ipp, Anton Rebhan, and Michael Strickland. Non-Abelian plasma instabilities: SU(3) vs. SU(2). *Phys. Rev.*, D84:056003, 2011. doi: 10.1103/PhysRevD.84.056003.
- [104] Mark C. Abraao York, Alekski Kurkela, Egang Lu, and Guy D. Moore. UV cascade in classical Yang-Mills theory via kinetic theory. *Phys. Rev.*, D89(7):074036, 2014. doi: 10.1103/PhysRevD.89.074036.
- [105] L. P. Kadanoff and G. Baym. *Quantum Statistical Mechanics*. W.A. Benjamin Inc, 1962.
- [106] Juergen Berges. Introduction to nonequilibrium quantum field theory. *AIP Conf. Proc.*, 739:3–62, 2005. doi: 10.1063/1.1843591. [3(2004)].
- [107] J. S. Schwinger. Brownian Motion of a Quantum Oscillator. *J. Math. Phys.*, 2:407, 1961. doi: 10.1063/1.1703727.
- [108] L. V. Keldysh. Diagram technique for nonequilibrium processes. *Zh. Eksp. Teor. Fiz.*, 47:1515, 1964.
- [109] G. Kallen. On the Definition of the Renormalization Constants in Quantum Electrodynamics. *Helv. Phys. Acta*, 25:417, 1952. doi: 10.1007/978-3-319-00627-7_90.
- [110] H. Lehmann. Uber Eigenschaften von Ausbreitungsfunktionen und Renormierungskonstanten quantisierter Felder. *Il Nuovo Cimento*, 11:342, 1954. doi: 10.1007/BF02783624.
- [111] Gert Aarts and Juergen Berges. Nonequilibrium time evolution of the spectral function in quantum field theory. *Phys. Rev.*, D64:105010, 2001. doi: 10.1103/PhysRevD.64.105010.
- [112] R. Kubo. Statistical-Mechanical Theory of Irreversible Processes. I. General Theory and Simple Applications to Magnetic and Conduction Problems. *J. Phys. Soc. Jap.*, 12:570, 1957. doi: 10.1143/JPSJ.12.570.
- [113] P. C. Martin and J. S. Schwinger. Theory of many particle systems. 1. *Phys. Rev.*, 115:1342, 1959. doi: 10.1103/PhysRev.115.1342.
- [114] Gert Aarts, Daria Ahrensmeier, Rudolf Baier, Juergen Berges, and Julien Serreau. Far from equilibrium dynamics with broken symmetries from the 2PI - 1/N expansion. *Phys. Rev.*, D66:045008, 2002. doi: 10.1103/PhysRevD.66.045008.
- [115] M. Salle, Jan Smit, and Jeroen C. Vink. Thermalization in a Hartree ensemble approximation to quantum field dynamics. *Phys. Rev.*, D64:025016, 2001. doi: 10.1103/PhysRevD.64.025016.
- [116] Andreas Elben. Nonequilibrium Dynamics and Thermalization of Inhomogeneous Quantum Fields. Master’s thesis, University of Heidelberg, February 2016.
- [117] Juergen Berges and Denes Sexty. Strong versus weak wave-turbulence in relativistic field theory. *Phys. Rev.*, D83:085004, 2011. doi: 10.1103/PhysRevD.83.085004.

- [118] A. Pineiro Orioli, K. Boguslavski, and J. Berges. Universal self-similar dynamics of relativistic and nonrelativistic field theories near nonthermal fixed points. *Phys. Rev.*, D92(2):025041, 2015. doi: 10.1103/PhysRevD.92.025041.
- [119] Kevin Dusling, Thomas Epelbaum, Francois Gelis, and Raju Venugopalan. Instability induced pressure isotropization in a longitudinally expanding system. *Phys. Rev.*, D86:085040, 2012. doi: 10.1103/PhysRevD.86.085040.
- [120] J. Berges, K. Boguslavski, S. Schlichting, and R. Venugopalan. Basin of attraction for turbulent thermalization and the range of validity of classical-statistical simulations. *JHEP*, 05:054, 2014. doi: 10.1007/JHEP05(2014)054.
- [121] Juergen Berges, Kirill Boguslavski, and Soeren Schlichting. Nonlinear amplification of instabilities with longitudinal expansion. *Phys. Rev.*, D85:076005, 2012. doi: 10.1103/PhysRevD.85.076005.
- [122] Juergen Berges, Sebastian Scheffler, and Denes Sexty. Bottom-up isotropization in classical-statistical lattice gauge theory. *Phys. Rev.*, D77:034504, 2008. doi: 10.1103/PhysRevD.77.034504.
- [123] Gert Aarts and Jan Smit. Classical approximation for time dependent quantum field theory: Diagrammatic analysis for hot scalar fields. *Nucl. Phys.*, B511:451–478, 1998. doi: 10.1016/S0550-3213(97)00723-2.
- [124] Valentin Kasper, Florian Hebenstreit, and Juergen Berges. Fermion production from real-time lattice gauge theory in the classical-statistical regime. *Phys. Rev.*, D90(2):025016, 2014. doi: 10.1103/PhysRevD.90.025016.
- [125] R. Brout. Statistical Mechanical Theory of a Random Ferromagnetic System. *Phys. Rev.*, 115:824, 1959. doi: 10.1103/PhysRev.115.824.
- [126] A. Milchev, K. Binder, and D. W. Heermann. Fluctuations and lack of self-averaging in the kinetics of domain growth. *Z. Phys. B*, 63:521, 1986. doi: 10.1007/BF01726202.
- [127] S. Wiseman and E. Domany. Lack of self-averaging in critical disordered systems. *Phys. Rev. E*, 52:3469, 1995. doi: 10.1103/PhysRevE.52.3469.
- [128] A. Aharony and A. B. Harris. Absence of Self-Averaging and Universal Fluctuations in Random Systems near Critical Points. *Phys. Rev. Lett.*, 77:3700, 1996. doi: 10.1103/PhysRevLett.77.3700.
- [129] A. Malakis and N. G. Fytas. Lack of self-averaging of the specific heat in the three-dimensional random-field Ising model. *Phys. Rev. E*, 73:016109, 2006. doi: 10.1103/PhysRevE.73.016109.

- [130] Aleksi Kurkela and Egang Lu. Approach to Equilibrium in Weakly Coupled Non-Abelian Plasmas. *Phys. Rev. Lett.*, 113(18):182301, 2014. doi: 10.1103/PhysRevLett.113.182301.
- [131] V. E. Zakharov, V. S. Lvov, and G. Falkovich. *Kolmogorov Spectra of Turbulence I: Wave Turbulence*. Springer-Verlag, 1992.
- [132] Jean-Paul Blaizot, Edmond Iancu, and Yacine Mehtar-Tani. Medium-induced QCD cascade: democratic branching and wave turbulence. *Phys. Rev. Lett.*, 111:052001, 2013. doi: 10.1103/PhysRevLett.111.052001.
- [133] Asier Pineiro Orioli. Turbulence and self-similarity in strongly correlated scalar field theories. Master's thesis, University of Heidelberg, 2014.
- [134] J. Berges and David Mesterhazy. Introduction to the nonequilibrium functional renormalization group. *Nucl. Phys. Proc. Suppl.*, 228:37–60, 2012. doi: 10.1016/j.nuclphysbps.2012.06.003.
- [135] Jan M. Pawłowski and Nils Strodthoff. Real time correlation functions and the functional renormalization group. *Phys. Rev.*, D92(9):094009, 2015. doi: 10.1103/PhysRevD.92.094009.
- [136] Per Bak, Chao Tang, and Kurt Wiesenfeld. Self-organized criticality: An explanation of the $1/f$ noise. *Phys. Rev. Lett.*, 59:381–384, Jul 1987. doi: 10.1103/PhysRevLett.59.381. URL <http://link.aps.org/doi/10.1103/PhysRevLett.59.381>.
- [137] Guy D. Moore. Problems with lattice methods for electroweak preheating. *JHEP*, 11:021, 2001. doi: 10.1088/1126-6708/2001/11/021.
- [138] Thomas Epelbaum, Francois Gelis, and Bin Wu. Nonrenormalizability of the classical statistical approximation. *Phys. Rev.*, D90(6):065029, 2014. doi: 10.1103/PhysRevD.90.065029.
- [139] Thomas Epelbaum, Francois Gelis, Naoto Tanji, and Bin Wu. Properties of the Boltzmann equation in the classical approximation. *Phys. Rev.*, D90(12):125032, 2014. doi: 10.1103/PhysRevD.90.125032.
- [140] M. Mace, S. Schlichting, and R. Venugopalan. Off-equilibrium sphaleron transitions in the Glasma. *Phys. Rev.*, D93(7):074036, 2016. doi: 10.1103/PhysRevD.93.074036.
- [141] J. Berges, Sz. Borsányi, and C. Wetterich. Prethermalization. *Phys. Rev. Lett.*, 93:142002, Sep 2004. doi: 10.1103/PhysRevLett.93.142002. URL <http://link.aps.org/doi/10.1103/PhysRevLett.93.142002>.
- [142] Dmitry Podolsky, Gary N. Felder, Lev Kofman, and Marco Peloso. Equation of state and beginning of thermalization after preheating. *Phys. Rev. D*, 73:023501, Jan 2006. doi:

- 10.1103/PhysRevD.73.023501. URL <http://link.aps.org/doi/10.1103/PhysRevD.73.023501>.
- [143] Kevin Dusling, Thomas Epelbaum, Francois Gelis, and Raju Venugopalan. Role of quantum fluctuations in a system with strong fields: Onset of hydrodynamical flow. *Nucl. Phys.*, A850:69–109, 2011. doi: 10.1016/j.nuclphysa.2010.11.009.
- [144] Guy D. Moore. Condensates in Relativistic Scalar Theories. *Phys. Rev.*, D93(6):065043, 2016. doi: 10.1103/PhysRevD.93.065043.
- [145] Kirill Boguslavski. Universality and turbulence in expanding systems. Master’s thesis, Tech. Univ. Darmstadt, September 2013.
- [146] Thomas Gasenzer, Boris Nowak, and Denes Sexty. Charge separation in Reheating after Cosmological Inflation. *Phys. Lett.*, B710:500–503, 2012. doi: 10.1016/j.physletb.2012.03.031.
- [147] S. Nazarenko. *Wave Turbulence*. Springer-Verlag, 2011.
- [148] Juergen Berges and Szabolcs Borsanyi. Range of validity of transport equations. *Phys. Rev.*, D74:045022, 2006. doi: 10.1103/PhysRevD.74.045022.
- [149] Peter Brockway Arnold, Guy D. Moore, and Laurence G. Yaffe. Effective kinetic theory for high temperature gauge theories. *JHEP*, 01:030, 2003. doi: 10.1088/1126-6708/2003/01/030.
- [150] Jean-Paul Blaizot, Jinfeng Liao, and Larry McLerran. Gluon Transport Equation in the Small Angle Approximation and the Onset of Bose-Einstein Condensation. *Nucl. Phys.*, A920:58–77, 2013. doi: 10.1016/j.nuclphysa.2013.10.010.
- [151] Alfred H. Mueller. The Boltzmann equation for gluons at early times after a heavy ion collision. *Phys. Lett.*, B475:220–224, 2000. doi: 10.1016/S0370-2693(00)00084-8.
- [152] D. V. Semikoz and I. I. Tkachev. Kinetics of Bose condensation. *Phys. Rev. Lett.*, 74:3093–3097, 1995. doi: 10.1103/PhysRevLett.74.3093.
- [153] D. V. Semikoz and I. I. Tkachev. Condensation of bosons in kinetic regime. *Phys. Rev.*, D55:489–502, 1997. doi: 10.1103/PhysRevD.55.489.
- [154] Juergen Berges. Controlled nonperturbative dynamics of quantum fields out-of-equilibrium. *Nucl. Phys.*, A699:847–886, 2002. doi: 10.1016/S0375-9474(01)01295-7.
- [155] Alexander Branschadel and Thomas Gasenzer. 2PI nonequilibrium versus transport equations for an ultracold Bose gas. *J. Phys.*, B 41:135302, 2008.

- [156] Yoshitaka Hatta and Akihiro Nishiyama. Nonequilibrium 2PI evolution of the $O(N)$ model with longitudinal expansion. *Phys. Rev.*, D86:076002, 2012. doi: 10.1103/PhysRevD.86.076002.
- [157] Soeren Schlichting. *Non-equilibrium dynamics and thermalization of weakly coupled non-Abelian plasmas*. PhD thesis, University of Heidelberg, 2013.
- [158] S. Mrowczynski. *Phys. Lett.*, B214:587, 1988.
- [159] Peter Brockway Arnold, Jonathan Lenaghan, and Guy D. Moore. QCD plasma instabilities and bottom up thermalization. *JHEP*, 08:002, 2003. doi: 10.1088/1126-6708/2003/08/002.
- [160] Paul Romatschke and Michael Strickland. Collective modes of an anisotropic quark gluon plasma. *Phys. Rev.*, D68:036004, 2003. doi: 10.1103/PhysRevD.68.036004.
- [161] Paul Romatschke and Michael Strickland. Collective modes of an anisotropic quark-gluon plasma II. *Phys. Rev.*, D70:116006, 2004. doi:10.1103/PhysRevD.70.116006.
- [162] Anton Rebhan, Paul Romatschke, and Michael Strickland. Hard-loop dynamics of non-Abelian plasma instabilities. *Phys. Rev. Lett.*, 94:102303, 2005. doi: 10.1103/PhysRevLett.94.102303.
- [163] Peter Brockway Arnold, Jonathan Lenaghan, Guy D. Moore, and Laurence G. Yaffe. Apparent thermalization due to plasma instabilities in quark-gluon plasma. *Phys. Rev. Lett.*, 94:072302, 2005. doi: 10.1103/PhysRevLett.94.072302.
- [164] Aleks Kurkela and Yan Zhu. Isotropization and hydrodynamization in weakly coupled heavy-ion collisions. *Phys. Rev. Lett.*, 115(18):182301, 2015. doi: 10.1103/PhysRevLett.115.182301.
- [165] Aleks Kurkela. Initial state of Heavy-Ion Collisions: Isotropization and thermalization. In *25th International Conference on Ultra-Relativistic Nucleus-Nucleus Collisions (Quark Matter 2015) Kobe, Japan, September 27-October 3, 2015*, 2016. URL <https://inspirehep.net/record/1415134/files/arXiv:1601.03283.pdf>.
- [166] Kenji Fukushima. Evolution to the Quark-Gluon Plasma. *arXiv*: 1603.02340 [nucl-th], 2016.
- [167] Edmond Iancu, Andrei Leonidov, and Larry McLerran. The Color glass condensate: An Introduction. In *QCD perspectives on hot and dense matter. Proceedings, NATO Advanced Study Institute, Summer School, Cargese, France, August 6-18, 2001*, pages 73–145, 2002. URL <http://alice.cern.ch/format/showfull?sysnb=2297268>.

- [168] Francois Gelis, Tuomas Lappi, and Raju Venugopalan. High energy scattering in Quantum Chromodynamics. *Int. J. Mod. Phys.*, E16:2595–2637, 2007. doi: 10.1142/S0218301307008331.
- [169] Francois Gelis, Edmond Iancu, Jamal Jalilian-Marian, and Raju Venugopalan. The Color Glass Condensate. *Ann. Rev. Nucl. Part. Sci.*, 60:463–489, 2010. doi: 10.1146/annurev.nucl.010909.083629.
- [170] Thomas Epelbaum and Francois Gelis. Fluctuations of the initial color fields in high energy heavy ion collisions. *Phys. Rev.*, D88:085015, 2013. doi: 10.1103/PhysRevD.88.085015.
- [171] Jean-Paul Blaizot, Yacine Mehtar-Tani, and Marcus A. C. Torres. Angular structure of the in-medium QCD cascade. *Phys. Rev. Lett.*, 114(22):222002, 2015. doi: 10.1103/PhysRevLett.114.222002.
- [172] Paul M. Chesler and Laurence G. Yaffe. Boost invariant flow, black hole formation, and far-from-equilibrium dynamics in $N = 4$ supersymmetric Yang-Mills theory. *Phys. Rev.*, D82:026006, 2010. doi: 10.1103/PhysRevD.82.026006.
- [173] Paul M. Chesler and Laurence G. Yaffe. Holography and colliding gravitational shock waves in asymptotically AdS 5 spacetime. *Phys. Rev. Lett.*, 106:021601, 2011. doi: 10.1103/PhysRevLett.106.021601.
- [174] V. Balasubramanian, A. Bernamonti, J. de Boer, N. Copland, B. Craps, E. Keski-Vakkuri, B. Muller, A. Schafer, M. Shigemori, and W. Staessens. Thermalization of Strongly Coupled Field Theories. *Phys. Rev. Lett.*, 106:191601, 2011. doi: 10.1103/PhysRevLett.106.191601.
- [175] Michal P. Heller, Romuald A. Janik, and Przemyslaw Witaszczyk. The characteristics of thermalization of boost-invariant plasma from holography. *Phys. Rev. Lett.*, 108:201602, 2012. doi: 10.1103/PhysRevLett.108.201602.
- [176] Thomas Epelbaum, Francois Gelis, Sangyong Jeon, Guy Moore, and Bin Wu. Kinetic theory of a longitudinally expanding system of scalar particles. *JHEP*, 09:117, 2015. doi: 10.1007/JHEP09(2015)117.
- [177] J. Berges, K. Boguslavski, S. Schlichting, and R. Venugopalan. Nonequilibrium fixed points in longitudinally expanding scalar theories: infrared cascade, Bose condensation and a challenge for kinetic theory. *Phys. Rev.*, D92(9):096006, 2015. doi: 10.1103/PhysRevD.92.096006.
- [178] Boris Nowak, Sebastian Erne, Markus Karl, Jan Schole, Dnes Sexty, and Thomas Gasenzer. Non-thermal fixed points: universality, topology, & turbulence in Bose gases. 2013. URL <https://inspirehep.net/record/1217883/files/arXiv:1302.1448.pdf>.

- [179] Thomas Gasenzer, Larry McLerran, Jan M. Pawłowski, and Dnes Sexty. Gauge turbulence, topological defect dynamics, and condensation in Higgs models. *Nucl. Phys.*, A930:163–186, 2014. doi: 10.1016/j.nuclphysa.2014.07.030.
- [180] F. Scardina, D. Perricone, S. Plumari, M. Ruggieri, and V. Greco. Relativistic Boltzmann transport approach with Bose-Einstein statistics and the onset of gluon condensation. *Phys. Rev.*, C90(5):054904, 2014. doi: 10.1103/PhysRevC.90.054904.
- [181] Zhe Xu, Kai Zhou, Pengfei Zhuang, and Carsten Greiner. Thermalization of gluons with Bose-Einstein condensation. *Phys. Rev. Lett.*, 114(18):182301, 2015. doi: 10.1103/PhysRevLett.114.182301.
- [182] Jean-Paul Blaizot, Jinfeng Liao, and Yacine Mehtar-Tani. The subtle interplay of elastic and inelastic collisions in the thermalization of the quark-gluon plasma. In *25th International Conference on Ultra-Relativistic Nucleus-Nucleus Collisions (Quark Matter 2015) Kobe, Japan, September 27-October 3, 2015*, 2016. URL <https://inspirehep.net/record/1412129/files/arXiv:1601.00308.pdf>.
- [183] A. F. de O. Falcao. Asymptotic expansions of functions related to imaginary order Bessel functions. *ZAMM*, 53:133–134, 1973.
- [184] T. M. Dunster. Bessel functions of purely imaginary order, with an application to second-order linear differential equations having a large parameter. *Siam J. Math. Anal.*, 21:995–1018, 1990.
- [185] Kenneth G. Wilson. Confinement of Quarks. *Phys. Rev.*, D10:2445–2459, 1974. doi: 10.1103/PhysRevD.10.2445. [45(1974)].
- [186] John B. Kogut and Leonard Susskind. Hamiltonian Formulation of Wilson’s Lattice Gauge Theories. *Phys. Rev.*, D11:395–408, 1975. doi: 10.1103/PhysRevD.11.395.
- [187] K. Symanzik. Continuum Limit and Improved Action in Lattice Theories. 1. Principles and ϕ^4 Theory. *Nucl. Phys.*, B226:187, 1983. doi: 10.1016/0550-3213(83)90468-6.
- [188] Jan Ambjorn, T. Askgaard, H. Porter, and M. E. Shaposhnikov. Sphaleron transitions and baryon asymmetry: A Numerical real time analysis. *Nucl. Phys.*, B353:346–378, 1991. doi: 10.1016/0550-3213(91)90341-T.
- [189] S. Scheffler. *Plasma Instabilities and Turbulence in Non-Abelian Gauge Theories*. PhD thesis, Tech. Univ. Darmstadt, 2010.
- [190] Kevin Dusling, Francois Gelis, and Raju Venugopalan. The initial spectrum of fluctuations in the little bang. *Nucl. Phys.*, A872:161–195, 2011. doi: 10.1016/j.nuclphysa.2011.09.012.

- [191] C. T. H. Davies, G. G. Batrouni, G. R. Katz, A. S. Kronfeld, G. P. Lepage, K. G. Wilson, P. Rossi, and B. Svetitsky. Fourier acceleration in lattice gauge theories. i. landau gauge fixing. *Phys. Rev. D*, 37:1581–1588, Mar 1988. doi: 10.1103/PhysRevD.37.1581. URL <http://link.aps.org/doi/10.1103/PhysRevD.37.1581>.
- [192] Attilio Cucchieri and Tereza Mendes. Critical slowing down in SU(2) Landau gauge fixing algorithms. *Nucl. Phys.*, B471:263–292, 1996. doi: 10.1016/0550-3213(96)00177-0.